



**MATERIAL  
AND MECHANICAL  
ENGINEERING  
TECHNOLOGY**

**Editorial board of the journal**

Gulnara Zhetessova (Abylkas Saginov Karaganda Technical University, Kazakhstan)  
Alexander Korsunsky (University of Oxford, England)  
Olegas Cernasejus (Vilnius Gediminas Technical University, Lithuania)  
Jaroslav Jerz (Institute of Materials & Machine Mechanics SAS, Slovakia)  
Boris Moyzes (Tomsk Polytechnic University, Russia)  
Nikolai Belov (National Research Technological University «Moscow Institute of Steel and Alloys», Russia)  
Georgi Popov (Technical University of Sofia, Bulgaria)  
Sergiy Antonyuk (University of Kaiserslautern, Germany)  
Zharkynay Christian (University of Texas at Dallas Institute of Nanotechnology, USA)  
Katica Simunovic (University of Slavonski Brod, Croatia)  
Lesley D.Frame (School of Engineering University of Connecticut, USA)  
Łukasz Gierz (Poznan University of Technology, Poland)  
Łukasz Warguła (Poznan University of Technology, Poland)  
Olga Zharkevich (Abylkas Saginov Karaganda Technical University, Kazakhstan)

## Content

<b>Soltabayev B., Yergaliuly G., Turlybekuly A., Mentbayeva A.</b> Optimization of the Properties of ZnO Films Produced by the SILAR Technique.....	3
<b>Yunusov S., Makhmudova S., Kasimova D., Agzamov M.</b> The Influence of Changes in Technological Loads on the Deflection of the Saw Cylinder Shaft of a Linting Machine.....	8
<b>Aljumaili A., Alaiwi Y., Al-Khafaji Z.</b> A Review of Solar Panel Cooling Methods and Efficiencies.....	14
<b>Zharkevich O.M., Shlyakhov S.V., Nurzhanova O.A., Imasheva K.I.</b> Development and research of a new reinforced design of the mounting block.....	28
<b>Yurov V.M., Zhangozin K.N., Portnov V.S., Rakhimova G.M., Rakhimov A.M.</b> Concrete Reinforced with Graphene and Graphene Oxide.....	36
<b>Kulikov V.Yu., Baiseitova Y.A., Kovaleva T.V., Tulegenova Sh.N., Kurypko S.A.</b> Effect of Binder Composition on Briquettes from Dust-Like Ball Bearing Steel ShKh15.....	43
<b>Andreyachshenko V.A., Toleuova A.R.</b> Effect of Boron Additive on the Formation Ferrous Phases in Alloys Al - Fe – Si.....	49
<b>Abildina A.R., Issagulov A.Z., Shcherbakova Ye.P., Kvon Sv.S</b> Using the Method of Probabilistic Deterministic Experiment to Assess the Impact of Alloying Elements on the Properties of the Quasi High-Entropy Alloy of the Fe-Cr-Ni-Co-Mn System.....	56
<b>Subramani S., Dhairiyasamy R., Gabiriel D.</b> Multi-Objective Optimization of Machining Parameters for Sustainable Turning of AISI 630 Stainless Steel using Taguchi-Based Desirability Function Analysis.....	65
<b>Abdreshov Sh., Bakyt G., Sarkynov Y., Zhakupova Zh., Imangaliyeva A., Makhimova A.</b> The Results of Experimental Studies of the Jet Thermal Module.....	78
<b>Sinelnikov K.A., Moldabaev B.G., Zhunusbekova Zh.Zh., Kukeshva A. B.</b> Theoretical and Experimental Analysis of Ultrasonic Cleaning of Internal Combustion Engine Radiators with the Development of Practical Recommendations.....	87
<b>Berg A.S., Reshetnikova O.S., Krasnov A.O.</b> Research and Optimization of Designs of External Gear Pumps.....	96
<b>Patil P.J., Pawar R.Sh., Kardekar N.B., Kamble D.A., Yadav R.Sh.</b> Investigating the Thermal Performance of Wheat Straw Insulation in Cement Hollow Blocks.....	106
<b>Muhammad Hashami, Auyelkhankyzy Moldir, Auyelkhankyzy Madina</b> Carbon Aerogels Derived from Industrial Wastes and Biomass Sources: Characteristics, Characterization, and Applications.....	114

## Optimization of the Properties of ZnO Films Produced by the SILAR Technique

Soltabayev B.<sup>1\*</sup>, Yergaliuly G.<sup>1</sup>, Turlybekuly A.<sup>1</sup>, Mentbayeva A.<sup>2</sup>

<sup>1</sup>National Laboratory Astana, Nazarbayev University, Astana, Kazakhstan

<sup>2</sup>Nazarbayev University, Astana, Kazakhstan

\*corresponding author

**Abstract.** Zinc oxide (ZnO) is a promising semiconductor material for optical and gas sensors. This study examines the influence of film thickness and solvent choice on the performance of ZnO thin films generated by SILAR at room temperature and atmospheric pressure. Ethanol and distilled water (DW) were used as solvents. Thin films of varying thicknesses were analyzed using X-ray diffraction (XRD), scanning electron microscope (SEM) atomic force microscopy (AFM), and Hall effect measurements to evaluate their morphology, crystal structure, and optical and electrical properties. X-ray diffraction analysis showed that films created using ethanol or DW have a hexagonal ZnO structure with a predominant growth orientation along the (002) plane. Films prepared with ethanol exhibited crystallinity comparable to films prepared with DW. ZnO films prepared with ethanol showed low resistivity ( $10^{-2} \Omega \text{ cm}$ ) and high electron mobility ( $750 \text{ cm}^2/\text{Vs}$ ). This highlights the potential of the SILAR method using ethanol to create high-quality ZnO thin films suitable for various applications. Thus, the study highlights the importance of thickness and solvent selection in the SILAR deposition process to optimize the properties of ZnO thin films for optical and gas sensors.

**Keywords:** zinc oxide, SILAR method, semiconductors, distilled water and ethanol, optical and electrical properties.

### Introduction

Various techniques for preparing thin film ZnO coatings such as spin coating, salt-gel, spray pyrolysis, electrochemical and chemical deposition, and magnetron sputtering are widely used to create such films [1]. Over the past three decades, SILAR has become one of the popular solution methods for thin film deposition [2]. The main advantages of SILAR include high layer growth rate, control of adsorption and reaction time, and low process temperature, which prevents oxidation and corrosion of the substrate [3]. To obtain a high-quality thin film, it is important to optimize the preparation conditions, such as the concentration of precursors, the nature of the complexing agent, the pH of the solutions, the reaction time and the deposition cycle.

The SILAR method is inexpensive, simple, and suitable for deposition over large areas, including a variety of substrates such as insulators, semiconductors, metals, and temperature-sensitive materials. It is based on sequential reactions between a substrate and a solution, where semiconductor materials are grown by immersion in various aqueous solutions [4].

The SILAR method has enabled the creation of various ZnO nanostructures such as nanorods and nanoflowers. Recent studies have created ultraviolet detectors based on ZnO nanorods and oriented nanorod films without a grain layer. The hydrophobic properties of flower-like ZnO and their excellent performance as gas sensors are also investigated [5]. The morphology and properties of the films are controlled by reaction parameters such as concentration, temperature, pH and number of deposition cycles.

The influence of the immersion cycle on the properties of thin ZnO layers has been discussed in many articles [6]-[8]. Precursors and annealing temperature play an important role. Studies show the influence of different precursors and annealing conditions on the performance of ZnO films. However, most studies used aqueous media to form ZnO films.

In some studies, solvents such as ethylene and isopropyl alcohol were used in the SILAR process, but water remained the main solvent [9]. This study reports the fabrication of ZnO thin films on glass substrates using pure ethanol as a solvent. The functionality of ZnO films grown from aqueous and alcoholic solutions was also compared, which provided new data on the effect of film thickness and solvent on surface morphology.

### 1. Materials and methods

ZnO films were deposited onto glass substrates using the SILAR method at room temperature and atmospheric pressure. The glasses were cleaned in an ultrasonic bath (first in a soap solution, then in distilled water and a 1:1 mixture of water and ethanol), and then dried in a nitrogen atmosphere for an hour and a half. Zinc chloride ( $\text{ZnCl}_2$ , Sigma Aldrich purity  $\geq 98\%$ ) was used as a source of zinc. A 0.1 M  $\text{ZnCl}_2$  solution was prepared by dissolving 1.363 g of  $\text{ZnCl}_2$  in 100 ml of distilled water or ethanol, adding ammonia solution (25-30%  $\text{NH}_4\text{OH}$ , Sigma Aldrich) drop by drop until pH 10.5 was reached.

To deposit the film, the glass substrate was immersed in a solution of zinc and ammonia for 15 seconds, then in hot ( $90^\circ\text{C}$ ) distilled water for 7 seconds. The zinc-ammonia complex was adsorbed in hot water, forming zinc hydroxide ( $\text{Zn}(\text{OH})_2$ ) on the substrate. After air drying for a minute, the samples were washed with distilled

water for 30 seconds. The cycle was repeated 30, 40, 50 and 60 times to obtain films of different thicknesses. All deposition steps and SEM images of the various cycles are shown in Figure 1.

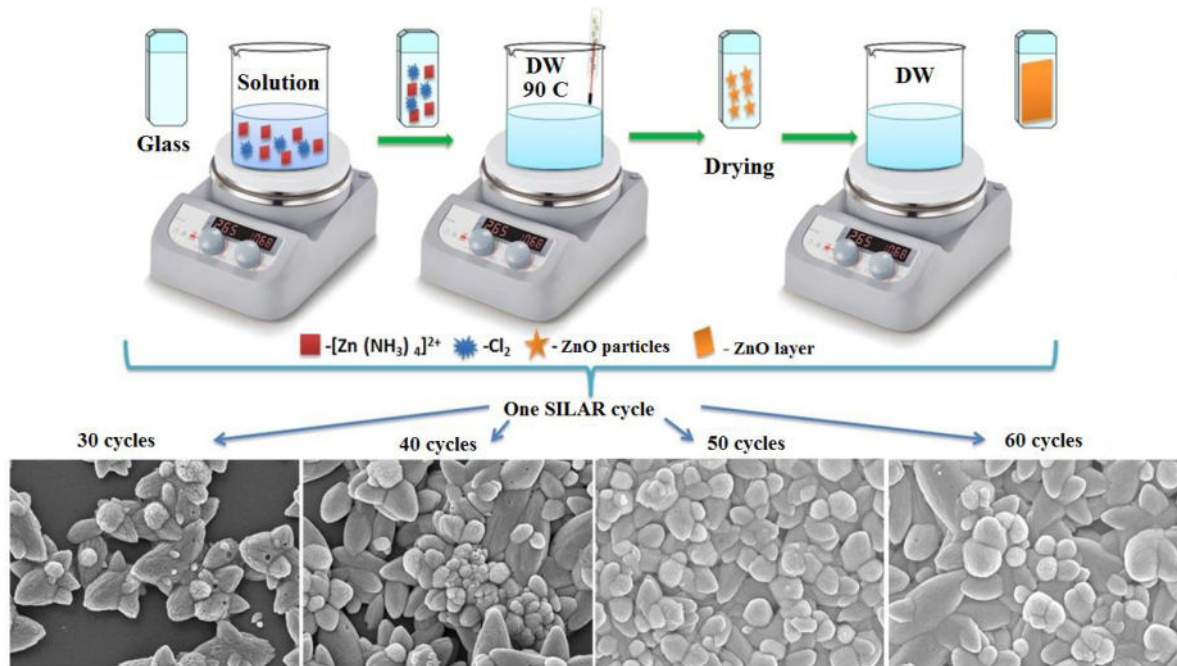


Fig. 1. – Steps for preparing ZnO thin film using SILAR and SEM images

After deposition, the ZnO samples were dried at room temperature and annealed in an  $\text{N}_2$  atmosphere at 500 °C for 2 hours. The samples were designated as ZnO: 30 (DW or ethanol), ZnO: 40 (DW or ethanol), ZnO: 50 (DW or ethanol), ZnO: 60 (DW or ethanol). The detailed procedure for deposition of films using the SILAR method was described in a previous studies [10,11]. Film thickness was measured by spectroscopic ellipsometry using SEN research 4.0 ellipsometer, fixing the incident angle at 70° and scanning the wavelength range from 330 to 1100 nm in 0.5 nm steps.

## 2. Results and their discussions

### Structural properties.

To study in more detail the influence of thickness and reaction environment on the growth of zinc oxide nanostructures, structural analysis of deposited ZnO thin films on glasses was performed using X-ray diffraction (XRD). The structural properties of ZnO films were studied using XRD on a SmartLAB Rigaku system (using  $\text{Cu K}\alpha\lambda = 1.5406 \text{ \AA}$  radiation). Figure 2 shows the X-ray diffraction patterns of ZnO thin films with different deposition cycles (30, 40, 50 and 60) that were grown using DW (Figure 2a) and ethanol (Figure 2b) solvents.

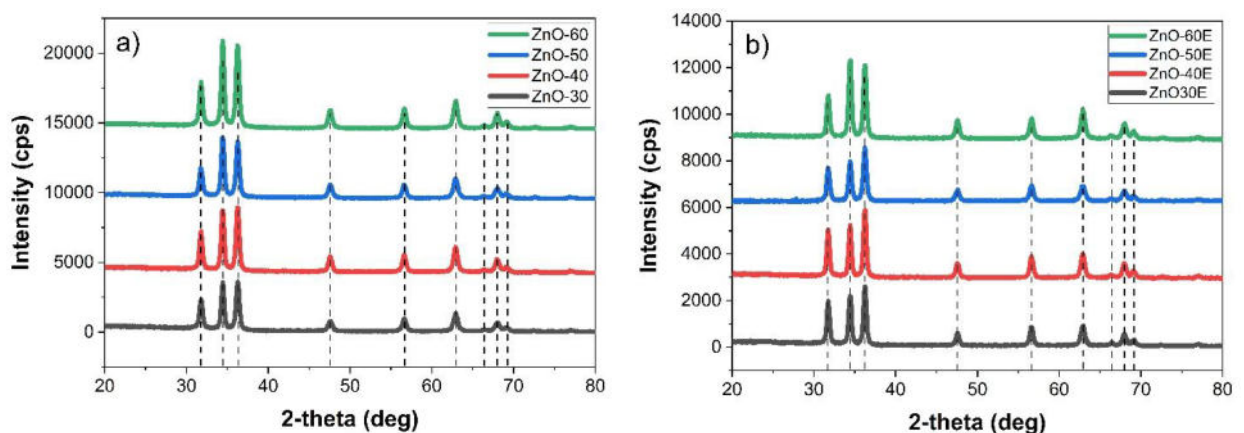


Fig. 2. – XRD patterns of ZnO thin films with different SILAR cycles: a) DW solvent and b) ethanol solvent.

All ZnO thin films exhibited high crystallinity with clear peaks corresponding to the hexagonal wurtzite crystal structure of ZnO, such as (100), (002), and (101). An increase in peak intensity was observed, especially along the c axis along the (002) plane, with increasing film thickness, regardless of the use of water or alcohol in the

process. This trend is consistent with published work [12] and data from the ICSD PDF-2 database (No. 03-065-0726).

Despite the differences in SILAR cycles and the use of various precursors, the calculated lattice parameters ( $a=3 \text{ \AA}$ ,  $c=5.2 \text{ \AA}$ ) and interplanar spacing ( $d=2.6 \text{ \AA}$ ) of the ZnO hexagonal structure remained consistent across all samples. This suggests that using ethanol as a solvent for ZnO does not compromise its crystalline structure and can be considered a suitable alternative to the conventional aqueous solution.

**Table 1.** Effect of the number of SILAR cycles on the crystallite size, half-maximum width (FWHM), dislocation density ( $\delta$ ), lattice strain ( $\epsilon$ ), interplanar distance ( $d$ ) and lattice constants ( $a, c$ ) of ZnO films along the diffraction peak (002)

Name	$2\theta$ (deg)	D (nm)	FWHM	$\delta$ ( $\text{\AA}$ ) <sup>-2</sup> $\times 10^{-6}$	$\epsilon$ ( $10^{-3}$ )	d ( $\text{\AA}$ )	Lattice constant ( $\text{\AA}$ )		Thickness (nm)
							a=b	c	
<b>DW</b>									
<b>ZnO:30</b>	34.42	22.720	0.3695	19.372	11.81	2.603	3.006	5.2069	192 $\pm$ 7
<b>ZnO:40</b>	34.41	23.182	0.3621	18.608	11.31	2.604	3.007	5.2087	217 $\pm$ 9
<b>ZnO:50</b>	34.42	20.502	0.4095	23.791	10.66	2.603	3.005	5.2063	329 $\pm$ 12
<b>ZnO:60</b>	34.42	21.395	0.3924	21.846	10.45	2.603	3.006	5.2067	498 $\pm$ 16
<b>Ethanol</b>									
<b>ZnO:30</b>	34.44	23.289	0.3605	18.437	10.62	2.602	3.007	5.2040	136 $\pm$ 6
<b>ZnO:40</b>	34.44	23.191	0.3620	18.593	10.43	2.602	3.005	5.2044	191 $\pm$ 9
<b>ZnO:50</b>	34.45	22.773	0.3687	19.282	10.39	2.601	3.004	5.2033	284 $\pm$ 9
<b>ZnO:60</b>	34.44	23.529	0.3568	18.063	10.28	2.602	3.005	5.2041	354 $\pm$ 14

#### Morphological properties.

Particle size in distilled water (Fig. 3a) shows small shifts, but no dependence on cycles is observed, while the particle size of films grown in ethanol (Fig. 3b) increases with the number of cycles.

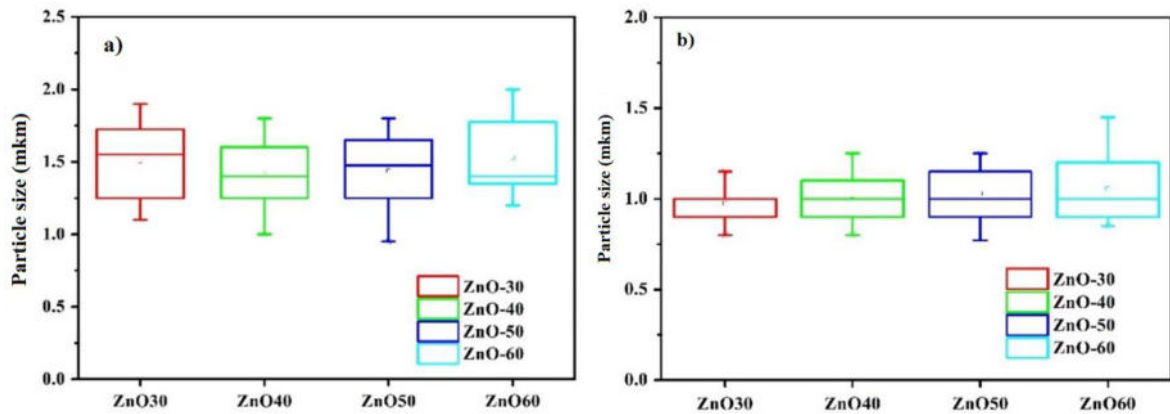


**Fig. 3.** – Film particle sizes calculated from AFM images for ZnO thin films grown in (a) DW and (b) ethanol.

#### Electrical properties.

The electrical parameters of the thin films were assessed using Ecopia Hall measurements at room temperature. Hall effect measurements were carried out to obtain the electrical parameters such as resistivity –  $\rho$  ( $\Omega \cdot \text{cm}$ ), Hall mobility –  $\mu$  ( $\text{cm}^2/\text{Vs}$ ) and carrier concentration –  $n$  ( $\text{cm}^{-3}$ ) listed in Figure 4.

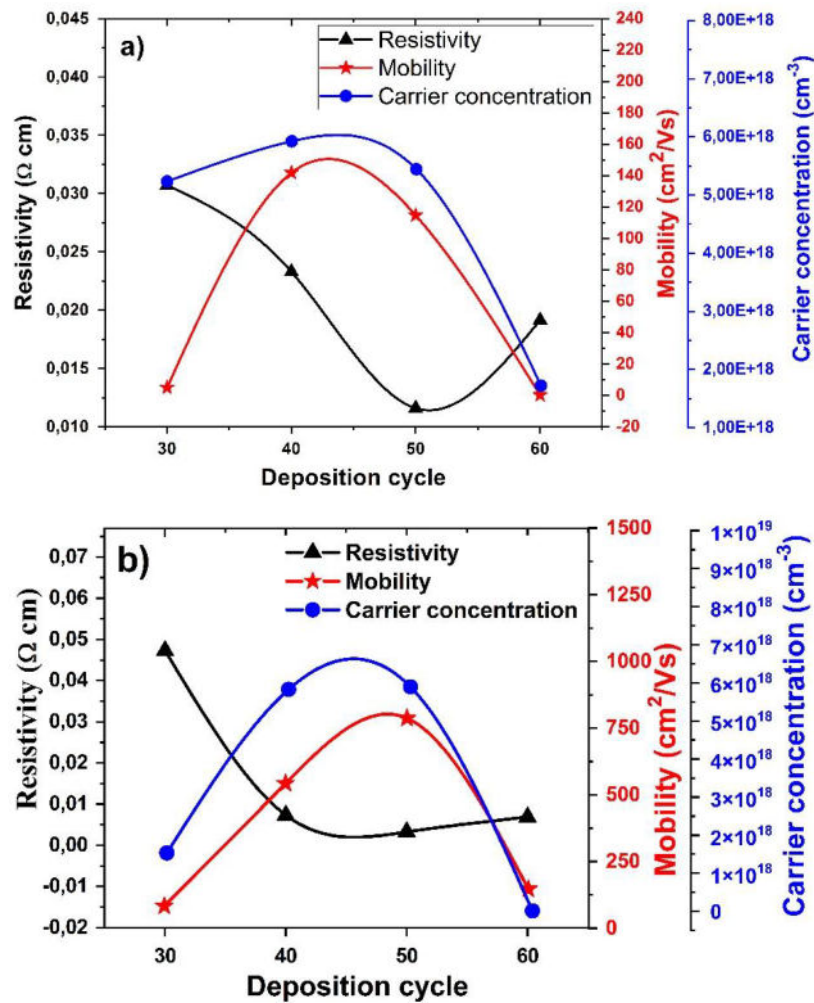


Fig. 4. – Hall measurements results of ZnO thin films grown in a) DW, and b) in ethanol.

According to these results, the carrier concentration of ZnO samples increased to a maximum at 50 deposition cycles. Then it decreased with further increase in the deposition cycle.

### Conclusion

In this study, ZnO thin films of various thicknesses were prepared on glass substrates using the SILAR method and solvents of distilled water and ethanol. The use of ethanol instead of distilled water in the SILAR method to produce ZnO thin films on glass substrates resulted in higher crystallinity and smaller grain size. Films produced with more SILAR cycles had a dense coating of nanostructures on the surface. ZnO thin films produced using ethanol also had a wider band gap and the highest charge carrier mobility. This offers potential for applications in gas sensors and dye-sensitive solar cells. Further research will be aimed at studying the gas-sensitive properties of these ZnO films.

### Acknowledgments

This research is funded by the Science Committee of the Ministry of Science and Higher Education of the Republic of Kazakhstan (*grant no. AP13067814*).

### References

- [1] Vandeginste V. A review of fabrication technologies for carbon electrode-based micro-supercapacitors //Applied Sciences. – 2022. – Vol. 12. – №. 2. – p. 862.
- [2] Pathan H. M., Lokhande C. D. Deposition of metal chalcogenide thin films by successive ionic layer adsorption and reaction (SILAR) method //Bulletin of Materials Science. – 2004. – Vol. 27. – p. 85-111.
- [3] Kumar D. K. et al. Synthesis of SnSe quantum dots by successive ionic layer adsorption and reaction (SILAR) method for efficient solar cells applications //Solar Energy. – 2020. – Vol. 199. – p. 570.
- [4] Soonmin H. Recent advances in the growth and characterizations of SILAR-deposited thin films //Applied Sciences. – 2022. – Vol. 12. – №. 16. – p. 8184.
- [5] Soltabayev B. et al. The effect of indium doping concentration on structural, morphological and gas sensing properties of IZO thin films deposited SILAR method //Materials Science in Semiconductor Processing. – 2019. – Vol. 101. – p. 28-36.

- [6] Çorlu T. et al. Low level NO gas sensing properties of Cu doped ZnO thin films prepared by SILAR method //Materials Letters. – 2018. – V. 212. – p. 292-295.
- [7] Ghosh B. et al. Fabrication and optical properties of SnS thin films by SILAR method //Applied surface science. – 2008. – V. 254. – №. 20. – p. 6436-6440.
- [8] Akaltun Y., Çayır T. Fabrication and characterization of NiO thin films prepared by SILAR method //Journal of Alloys and compounds. – 2015. – Vol. 625. – p. 144-148.
- [9] Ghos B. C. et al. Influence of substrate, process conditions, and post-annealing temperature on the properties of ZnO thin films grown by SILAR method. – 2020.
- [10] Yergaliuly G. et al. Effect of thickness and reaction media on properties of ZnO thin films by SILAR //Scientific reports. – 2022. – Vol. 12. – №. 1. – p. 851.
- [11] Soltabayev B. et al. Quick NO gas sensing by Ti-doped flower-rod-like ZnO structures synthesized by the SILAR method //ACS applied materials & interfaces. – 2022. – Vol. 14. – №. 36. – C. 41555-41570.
- [12] Desai M. A. et al. Seed-layer-free deposition of well-oriented ZnO nanorods thin films by SILAR and their photoelectrochemical studies //International Journal of Hydrogen Energy. – 2020. – Vol. 45. – №. 10. – p. 5783-5792

#### Information of the authors

**Soltabayev Baktiyar**, PhD, Head of Lab and Lead Researcher of PI «National Laboratory Astana»

e-mail: [baktiyar.soltabayev@nu.edu.kz](mailto:baktiyar.soltabayev@nu.edu.kz)

**Yergaliuly Gani**, PhD, Researcher of PI «National Laboratory Astana»

e-mail: [gani.yergaliuly@nu.edu.kz](mailto:gani.yergaliuly@nu.edu.kz)

**Turlybekuly Amanzhol**, PhD, Senior Researcher of PI «National Laboratory Astana», Astana, Kazakhstan.

e-mail: [amanzhol.turlybekuly@nu.edu.kz](mailto:amanzhol.turlybekuly@nu.edu.kz)

**Mentbayeva Almagul**, PhD, Professor, School of Engineering and Digital Sciences, Nazarbayev University

e-mail: [almagul.mentbayeva@nu.edu.kz](mailto:almagul.mentbayeva@nu.edu.kz)

## The Influence of Changes in Technological Loads on the Deflection of the Saw Cylinder Shaft of a Linting Machine

Yunusov S.<sup>1</sup>, Makhmudova S.<sup>1</sup>, Kasimova D.<sup>2</sup>, Agzamov M.<sup>3</sup>

<sup>1</sup>Tashkent State Transport University, Tashkent, Uzbekistan,

<sup>2</sup>Andijan Mechanical Engineering Institute, Andijan, Uzbekistan,

<sup>3</sup>Tashkent institute of textile and light industry

**Abstract.** In the article the calculation of the deflection of the saw cylinder shaft of the linter machine is given taking into account the technological resistance revealed due to the mass of the seed roll. For theoretical calculation of the influence of raw material roll density (mass of raw material roll, machine productivity) on the process of deformation of the saw cylinder shaft, the bending calculation of the saw cylinder shaft without taking into account the masses of saws and gaskets, with taking into account saw discs and gaskets and with taking into account the raw material roll (in static position) is made. By reducing the bending of the saw cylinder shaft, the angular speed and the productivity of the process can be increased.

**Keywords.** Shaft bending, saw cylinder, seed roller, shaft deformation, linter machine, transverse force, bending moment, equations of equilibrium, support reaction.

### Introduction.

Currently, there are more than 100 primary cotton processing plants in the country. The cotton plants' machinery and technology are gradually being upgraded. The main objective of modernisation of the plants is to increase the productivity of machines and to produce high-grade cotton fibre and lint that meets the requirements of the world market.

In the primary processing of cotton, the main process is the separation of the spinning fibre from the seeds, which produces its main products fibre and seeds. Along with the development of cotton cultivation, technology and techniques of cotton harvesting and processing there appeared the necessity to carry out other processes: preparation, storage, drying and cleaning of both raw material and its products. In addition, the range of products produced by cotton processing plants has expanded [1,2].

The history of the emergence of prodiginised seed processing processes is inextricably linked to the development of other sectors of the national economy. Until the second half of the 19th century, prodiginised seeds were used only as sowing material, which required only a small part of the produced seeds.

The cotton ginning industry produces three types of lint. The first type of lint contains fibres with a mass-length of 13/14 mm or more, the second type - from 7-8 to 12-13 mm, and the third type - 6-7 mm or less. In addition, the lint is also characterised by its grade, which is determined according to the grade of the seeds to be processed [3-5].

The process of linting of cotton seeds originated as a preparatory process necessary to maximise the compression of oil from the cotton seeds. The resulting lint had no industrial value. Seed linting was performed on linting machines developed similar to saw gins in the United States of America [6,7].

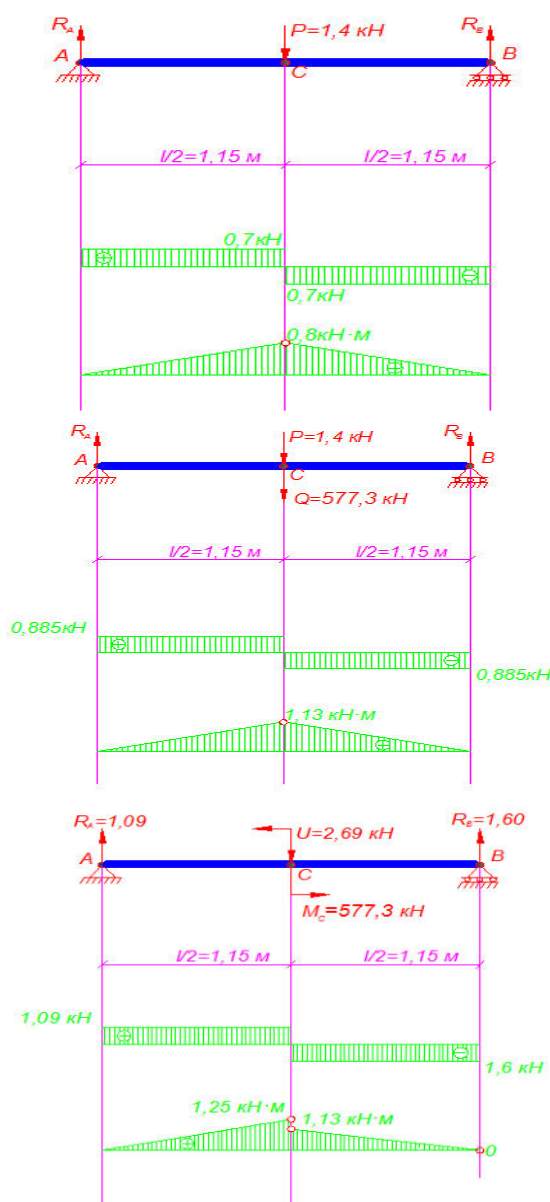
In the creation of machines for cotton ginning industry with high parameters can be realised only on the basis of deep knowledge of physical processes occurring in machines in different loading modes and development of new, more perfect methods of calculation of acting loads, which are the basis for calculation of machine parts and units for strength and endurance. Especially urgent are the issues of development and refinement of methods of calculation of drives and shafts of machines of large capacity or importance for production. This would make it possible to carry out production tests to refine the adopted parameters.

One such machine in the cotton processing industry is the linter machine. The linting process is carried out on linter machines, where the main working organ is the saw cylinder. It is the drive of the saw cylinder of linter machines 18.5 kW that consumes a significant amount of power in the machine.

### 1. Research methodology

For theoretical calculation of the influence of raw roll density (raw roll mass, machine productivity) on the process of deformation of the saw cylinder shaft, a calculation is made, which consists of several steps, which are presented in Fig. 1.

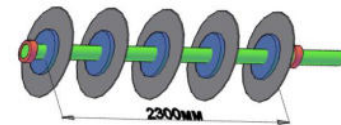
Given that the saw cylinder shafts are made from a whole shaft and are more than 2 metres long, there is an inherent bending of the shaft. Let's consider this with the help of calculations. The following data are required for the calculation: shaft length  $l=2300$  mm; gravity force  $P=m \cdot g$ , where  $m$ -mass of the shaft. The theoretical weight of steel relative to the diameter is [8,9].  $\varnothing 61,8=23,56$  kg/m,  $\varnothing 100=61,65$  kg/m. Taking into account the shaft length  $m_{sh} = \rho \cdot l = 61,65 \cdot 2,3 = 141,2$  kg. These are the values in newtons  $P=m_{sh} \cdot g = 141,2 \cdot 9,8 = 1389,6$  N. (Fig.1.a)



(a) Bending calculation of the saw cylinder shaft (not including saw and shim weights)



b) bending calculation of the saw cylinder, including saw blades and shims



c) bending calculation of the saw cylinder with regard to the raw material roll (in static position)

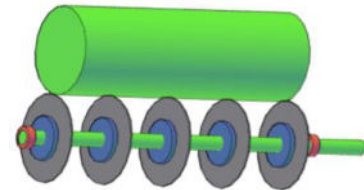


Fig. 1. - Saw cylinder shaft and calculation diagram

## 2. Results and discussion

Composing the equations of equilibrium for this system, we find the reaction forces on the bearings (supports). The reactions of the supports occur along the directions along which the rod (shaft) will not be able to move. Table 1 summarises the calculation data for all variants.

To plot the transverse forces  $Q_y$  and bending moments  $M_{U3}$  the method of sections is used. The transverse force in the section of the rod is equal to the sum of projections of external forces on the Y axis acting on the rest of the rod (shaft). The bending moment in the section of the rod (shaft) is equal to the sum of the moments of external forces acting on the remaining part of the rod (shaft), relative to the centre of gravity of the section. The obtained design data for all variants are summarised in Table 2.

**Table 1.** Reactions of the supports occur along the directions along which the rod (shaft)

$\sum M_{ia} = 0$	$\sum M_{ib} = 0$	Verification: $\sum Z_i = 0$
Saw cylinder shaft		
$P \cdot l/2 - R_B \cdot l = 0$	$R_A \cdot l - P \cdot l/2 = 0$	$R_A - P + R_B = 0$
$R_B = \frac{1400 \cdot 1,15}{2,3} = 700 \text{ H}$	$R_A = \frac{1400 \cdot 1,15}{2,3} = 700 \text{ N}$	$700 - 1400 + 700 = 0$
Saw cylinder, including saws and gaskets.		
$Q \cdot l/2 + P \cdot l/2 - R_B \cdot l = 0$	$R_A \cdot l - P \cdot l/2 - Q \cdot l/2 = 0$	$R_A - P - Q + R_B = 0$
$R_B = \frac{1977 \cdot 1,15}{2,3} = 988,5 \text{ N}$	$R_A = \frac{1977 \cdot 1,15}{2,3} = 988,5 \text{ N}$	$988,5 - 1400 - 577 - 988,5 = 0$

In order to make a mathematical description of the object of calculation and to solve the problem as simply as possible, real structures are replaced by idealised models or calculation schemes. In this case the calculation becomes approximate, with the help of this method we have carried out the bending calculation of the saw cylinder. Fig.1.b. shows the general view of the saw cylinder in the assembled version and the calculation diagram. In this step, the bending calculation of the saw cylinder shaft is carried out, taking into account the masses of saws and shims.

Fig. 1.b shows the scheme of the saw cylinder including saws and shims in the equally distributed variant in the calculation of which the transverse force is distributed along the length of the shaft ascending, and the bending moment in the flat form, this occurs directly under the influence of the equally distributed force ( $g$  - saw blades and shims (mass)). It follows that changing the mass of the spacer leads to a reduction in the bending moment of the shaft itself, as changing the mass of the saw blade is a difficult problem to solve. Then we apply the method of approximations for this case of the first approximation. And for the shaft itself we apply the second approximation and build the calculation diagram, which is shown in Fig. 1.b.

$$g_{sh} = \frac{G_s + G_d}{l} = \frac{g(m_s + m_d)}{l} \quad (1)$$

where,  $m_s, m_d$  - is the total mass of saw blades and gaskets mounted on the shaft,  $l$ -shaft length.

From reference data [10,11], the masses of which are respectively  $0.3\text{kg}$  and  $0.15\text{kg}$ . Taking into account their number on the saw cylinder, we calculate the total value of the equidistributed force.

$$g_s = \frac{9,8(39 + 20)}{2,3} = 251 \text{ H/M}$$

$$Q = g_s \cdot l \cdot l/2 = 251 \cdot \frac{2,3^2}{2} = 577 \text{ H}$$

Calculations to determine the reaction forces on the supports were carried out using the above methodology and the results obtained are summarised in Table 2.

**Table 2.** The reaction forces

Formula	1-section	2-section
Saw cylinder shaft		
$Q_y = \sum P_y$	$Q_I = R_A = 700 \text{ N}$	$Q_{II} = R_A - P = -700 \text{ N}$
$M_{be} = \sum M_c$	$M_I = R_A x_I$ At, $x_I = 0; M_I = 0;$ $x_I = 1.15; M_I = 0.8 \text{ kN-m}$	$M_{II} = R_A x_2 - P(x - 2 \cdot l/2);$ At, $x_2 = 1.15; M_{II} = 0.8;$ $x_2 = 2.3 M_I = 0.7 - 2.3 - 1.4(2.3 - 1.15) = 0$
Saw cylinder, including saws and gaskets		
$Q_y = \sum P_y$	$Q_I = R_A = 988.5 \text{ N}$	$Q_{II} = R_A - P - Q = -988.5 \text{ N}$
$M_{be} = \sum M_c$	$M_I = R_A x_I$ At, $x_I = 0; M_I = 0;$ $x_I = 1.15; M_I = 1136 \text{ N-m}$	$M = R_{IIA} x_2 - P(x - 2 \cdot l/2) - Q(x - 2 \cdot l/2);$ At, $x_2 = 1.15; M_{II} = 1136 \text{ N-m};$ $x_2 = 2.3 M = 0_{II}$

Next, we determine the internal forces of the saw cylinder shaft, taking into account the seed roller shaft (in static position). Fig. 1.c. shows the general view of the process and the calculation diagram. The calculation of which is important in the assembly and operation of the machines. Where to take into account the seed roller in the calculations consider in the following form. Considering the mass of the seed roller, we will calculate the mass force, and using the approximation method we will consider the distributed forces as concentrated forces (Fig. 1.b). Let's take the mass of the seed shaft in the following interval.  $m_m = 60 \div 90\text{kg}$  for this case,  $U = 588 \div 882\text{N}$ . Then in

this case the moment of resistance arising from the load of the seed roller on the saw cylinder  $M_{rm} = F_{tr} R$ , where,  $F_{tr} = f \cdot U$ .

The next question of interest is the influence of the seed shaft on the deformation process of the saw cylinder shaft. Let's consider the proposed calculation scheme in the following form, where the shaft gravity force  $P$  and equally distributed force  $g$  will be considered as accepted in the variant of the calculation scheme of the second approximation. Forces  $P$  and  $Q$  by substituting the geometric centre of the shaft in our case - it is point (C) Fig. 1.c. In order to take into account the seed shaft (external resistance) we will insert the force  $U$ , here from the seed shaft arises torque or the so-called moment of resistance of the system  $M_c$ . In Fig. 1.c, the calculation scheme in cross section is shown. The calculation is carried out according to the above mentioned method. Table 3 summarises the calculation data on the influence of the seed shaft mass on the deformation process of the saw cylinder shaft, taking into account the seed shaft.

**Table 3.** The influence of the seed shaft mass on the deformation process of the saw cylinder shaft

$M_{rm}$ (kg)	U (N)	$F_{fr}$ (H)	$M_{rm}$ (N-m)	P(H)	Q(H)	$R_A$ (H)	$R_B$ (H)
60	588	705,6	112,90	1400	577	1331,59	1233,41
70	686	823,2	131,71	1400	577	1388,77	1274,23
80	784	940,8	150,53	1400	577	1445,95	1315,05
90	882	1058,4	169,34	400	77	1503,13	1355,87

The shaft diameter can now be determined using the allowable stress theory [6]:

$$\sigma_{max} = \frac{M_{max}}{W_y} \leq [\sigma] \tag{2}$$

Axial moment of resistance of a cross section:

$$W_z = \frac{\pi d^3}{32} \tag{3}$$

From this we can calculate the shaft diameter for the permissible load:

$$d \geq \sqrt[3]{\frac{32 \cdot M_{max}}{\pi \cdot [\sigma]}} \tag{4}$$

Next, we determine the transverse internal forces and bending moments for each case separately using the section method (Table 4).

**Table 4.** The transverse internal forces and bending moments for each case

$M_{rm}$ (kg)	$Q_1$ (H)	$Q_2$ (H)	$M_1$ (N-m)		$M_2$ (N-m)	
			x=0	x=1,15	x=1,15	x=2,3
60	1331,59	-1233,41	0	1531,323	1418,427	0
70	1388,77	-1274,23	0	1597,081	1465,369	0
80	1445,95	-1315,05	0	1662,839	1512,311	0
90	1503,13	-1355,87	0	1728,597	1559,253	0

To determine the deflections  $Y_1, Y_2, Y_3$  in the direction of mass oscillations we apply unit forces; the epuples from these unit forces  $M_1, M_2, \text{ and } M_3$  are multiplied with the epuple of bending moments  $M$  from forces  $Q$  by the Vereshchagin method. The moments of inertia of the cross sections are calculated according to [12,13]:

$$J = \frac{\pi d^4}{64}$$

On the basis of the obtained solutions with variations of technological resistance (seed shaft mass) ( $m_{rm}$ , kg) the graphs characterising the influence of the seed shaft mass on the forces of the cross section ( $Q$ , N) and on the bending moment of the shaft ( $M_{bc}$ , N/m) are plotted in Fig.2.

The results of processing of the obtained solutions with variations of technological resistance (seed shaft mass) show that with the increase of technological resistance linearly increases the reaction forces on the bearings, the growth of which directly affects the forces of cross section and on the bending moment of the tedder shaft. The character of the obtained curves of influence of the seed roller mass on the reaction forces in the bearings corresponds to the character of the curves of influence of the seed roller mass on the cross-sectional forces ( $Q$ , N) and on the bending moment of the shaft ( $M_{bc}$ , N/m). So if at the mass of the seed shaft  $m_{rm} = 60$ kg force of the cross section  $Q = 1331$  N and bending moment of the shaft  $M_{bc} = 1531$  N/m, then at the mass of the seed shaft  $m_{rm} = 90$ kg force of the cross section and bending moment of the shaft respectively was  $Q = 1503$  N,  $M_{bc} = 1728$ N/m. It should be

noted that with the increase of the seed shaft mass from 60kg to 90kg also increases the value of the cross-sectional forces from 2565N to 2869N and the bending moment of the shaft from 112N/m to 170N/m respectively Fig. 2.

Next, we calculate the shaft deflection:

$$Z = Z_0 + \theta_0 x + \frac{1}{EJ_y} \left[ \sum M \frac{(x-a)^2}{2} + \sum P \frac{(x-b)^3}{6} + \sum q \frac{(x-c)^4}{24} \right] \quad (5)$$

Initial condition:  $x=0; \begin{cases} Z_0 \neq 0 \\ \theta_0 \neq 0 \end{cases}, a=b=c=l/2$

Taking into account the shaft arrangement and the arrangement of the masses, it can be determined as follows  $\theta_0$  as follows, if  $x = 2a$ , to  $Z_b = 0$  hence:

$$\theta_0 = \left\{ \frac{\frac{1}{EJ_y} \left[ \frac{R_A 2a^3}{6} - \frac{M(2a-a)^2}{2} - \frac{P(2a-a)^3}{6} + \frac{R_b(2a-2a)^3}{6} \right]}{2a} \right\} \quad (6)$$

After determining  $\theta_0$  the shaft deflection can be calculated for each section or for each  $x$  value. The calculations are summarised in Table 5.

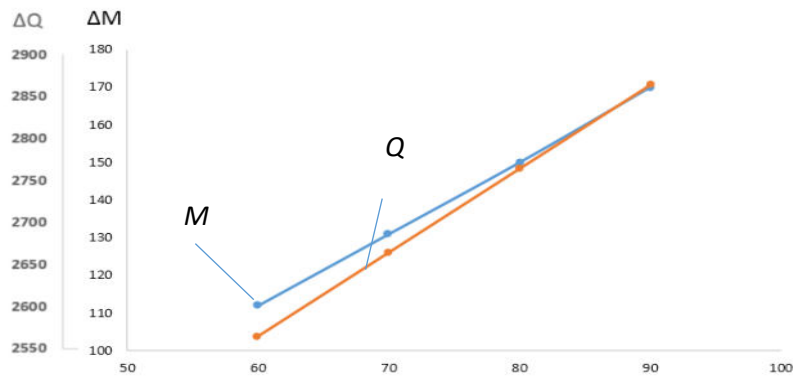


Fig. 2. - Effects of seed roll mass on the cross-sectional force differences (Q-15, N) and on the shaft bending moment ( $M_{be}$ , N/m)

For each case, the effect of changing the density or mass of the raw shaft on the saw cylinder shaft deflection was considered.

Table 5. Effect of changing the density or mass of the raw shaft

$M_{rm}$ , kg	Shaft deflection $Z$ , (mm)			
	$x = 0,58$	$x = 1,15$	$x = 1,73$	$x = 2,3$
60	-0,46413	-0,66344	-0,5526	0
70	-0,48247	-0,68879	-0,5756	0
80	-0,50082	-0,71414	-0,59859	0
90	-0,51917	-0,73949	-0,62158	0

The cross-section of the shaft and the weight of the saw cylinder in the existing design is unreasonably large ( $d=100mm$ ). If the shaft diameter is reduced, a more favourable variant in terms of energy saving can be achieved. This large mass of the saw cylinder (mainly due to the mass of the shaft) leads to the fact that the machine requires a high power consumption (17-17.5 kW) when starting the machine.

It is known [14-18] that the power consumption in the set mode of the saw cylinder is 12-12.5 kW. Inertia mass of the saw cylinder is large, in the stop mode it takes 7-12 seconds to completely stop the saw cylinder. This adversely affects the product quality.

### Conclusion

After the calculation works to identify the influence of the technological load on the saw cylinder shaft, it is suggested to reduce the inertia moment (mass) of the saw cylinder and to adjust the density of the seed shaft. The main method of mass reduction is to lighten the shaft itself or to reduce the number of saws and shims, which will reduce the length of the shaft. The adjustment of the seed roll density depends on many parameters but the most effective is the development of a new design of seed tedder for the working chamber of the linter machine.

The angular speed can be increased by reducing the bending of the saw cylinder shaft. In this way, the machine performance is not actually reduced.

## References

- [1] Sulaimonov R.Sh. et al. Improvement of the main units of the working chamber linter // *Universum: technical sciences : electronic scientific journal*. 2022. 3(96).
- [2] Azamatovich O., O'g'li A., Akramovich Q. //Determining the Optimal Parameters of an Advanced Linter Machine. *Engineering*, 810-820. doi: 10.4236/eng.2023.1512057.
- [3] Bittenbinder I.A. Productivity of linter machine, Collection of works. All-Union Congress of ITR, 1982.
- [4] Yunusov S., Sultonov A., Rakhmatov M., Bobomurotov T., Agzamov M //Results of studies on extending the time operation of gin and linter grates // *E3S Web of Conferences*, 2021, 304, 03028.
- [5] Yunusov S.Z., Kenjayev S.N., Makhmudova Sh.A., Islamova G.X. Full factorial experiment in research the parameters of a combined shaft of technological machines // *E3S Web of Conferences*, 2023, 401, 03043.
- [6] *Metalworker's Handbook in five volumes. Mashgiz - 1959. 5th volume p.3. edited by N.S.Acherkan.*
- [7] Mukhammadiev, D., Ibragimov F., Abzoirov O. /Experimental study of the bending of the linter machine saw blade // *E3S Web of Conferences* 390, AGRITECH-VIII 2023.
- [8] Mukhammadiev D.M., Ibragimov F.K., Mukhammadiev T.D. Modeling the Motion of a Saw Ginning Machine // *Journal of Machinery Manufacture and Reliability*, 49 (3), 2020, pp. 256-262.
- [9] Miroshnichenko G.I. *Fundamentals of designing machines for primary cotton processing*. M.:1972.
- [10] Gusenkov P.G. *Machine parts*. - M.: Vysshaya shkola, 1982. - 121-137 p.
- [11] Yu Wenbin Inertial and elastic properties of general composite beams // *Composite Structures-2025*, 352. doi: 10.1016/j.compstruct.2024.118690.
- [12] Cesnik, C.E.S., Hodges, D.H., Sutyryn, V.G. Cross-sectional analysis of composite beams including large initial twist and curvature effects // *AIAA Journal-1999*, 34 (9), pp. 1913-1920. doi: 10.2514/3.13325.
- [13] Martina A., Katili I., Widyatmoko S. Comparison of Higher-Order Beam Theory and First-Order Beam Theory Models on FGM Beam Element for Static Analysis // *Journal of Advanced Research in Applied Sciences and Engineering Technology-2025*, pp. 57-73, doi:10.37934/araset.53.2.5773.
- [14] Yunusov S.Z. *Dynamics of machine units with mechanisms of saw gin working organs*. Monograph, Izd. "Fan va technology" Tashkent-2013. – 143 p.
- [15] Sultonov A., Agzamov M., Rakhmatov M., Agzamov M., Nosirov Kh. Development of the saw cylinder for gins and linters with use of new elements of the design. *E3S Web Conf.* 304 03029, 2021. DOI: 10.1051/e3sconf/202130403029.
- [16] Agzamov M. M. The Influence of the Rotation Speed of the Raw Roller on Fiber Quality and Other Indicators of the Generation Process. In *Proceedings of Higher Education Institutions. Textile Industry Technology (Issue 4, pp. 88–93)*. Ivanovo State Polytechnic University, 2021, DOI: 10.47367/0021-3497\_2021\_4\_88.
- [17] Agzamov M. et al. 2021 IOP Conf. Ser.: Earth Environ. Sci. 939 012072. DOI: 10.1088/1755-1315/939/1/012072.
- [18] Agzamov M. et al. 2021 IOP Conf. Ser.: Earth Environ. Sci. 939 012073. DOI: 10.1088/1755-1315/939/1/012073.
- [19] Turakulov M., Tursunov N., Salokhiddin Y. Steeling of synthetic cast iron in induction crucible furnace taking into account consumption rate of carburizers // *E3S Web of Conferences* 401, 05012, 2023. <https://doi.org/10.1051/e3sconf/202340105012>.
- [20] Tursunov, T. , Tursunov, N., Urazbayev, T. Investigation of heat exchange processes in the lining of induction furnaces // *E3S Web of Conferences* 401, 05029, 2023. <https://doi.org/10.1051/e3sconf/202340105029>.
- [21] Turakulov M., Tursunov N., Yunusov S. New concept of cast iron melting technology in induction crucible furnace”, *E3S Web of Conferences* 401, 01060, 2023 <https://doi.org/10.1051/e3sconf/202340101060>.

## Information of the authors

**Yunusov Salokhiddin Zununovich**, d.t.s., professor, Tashkent State Transport University  
e-mail: [ysz1979@gmail.com](mailto:ysz1979@gmail.com)

**Makhmudova Shakhnoza Abduvaliyevna**, PhD, associate professor, Tashkent State Transport University  
e-mail: [maxmudovash88@mail.ru](mailto:maxmudovash88@mail.ru)

**Kasimova Dilafruz Alisherkyzy**, senior lecturer, Andijan Mechanical Engineering Institute  
e-mail: [kasimova\\_d@andmiedu.uz](mailto:kasimova_d@andmiedu.uz)

**Agzamov Mirkhosil Mirsalikhovich**, PhD, associate professor, Tashkent institute of textile and light industry

## A Review of Solar Panel Cooling Methods and Efficiencies

Aljumaili A.<sup>1</sup>, Alaiwi Y.<sup>1</sup>, Al-Khafaji Z.<sup>2,3\*</sup>

<sup>1</sup>Altinbas University, Instambul, Turkey

<sup>2</sup>Imam Ja'afar Al-Sadiq University, Baghdad, Iraq

<sup>3</sup>Universiti Kebangsaan Malaysia, Bangi, Malayisa

\*corresponding authors

**Abstract:** Photovoltaics is one of the most widely employed clean energy sources on earth. However, when the temperature of the PV cell rises, its electrical power decreases, which makes it essential to find ways to develop the module's efficiency in high-temperature situations. One of the techniques used to raise efficiency and performance is cooling. Researchers have used a variety of ways to cool solar PV panels, including active and passive methods. Researchers used a forced air stream, PCM, a heat exchanger, water, and many other methods to make a solar PV thermal system work better. The principal purpose of this chapter is to look at the significant information the researchers found in their research about how to improve the efficiency and performance of PV cells, how to cool them, and other reasons that affect the output of solar cells.

**Keywords:** solar panel; cooling methods; cooling efficiencies.

### Introduction

Clean energy refers to energy sources that regenerate spontaneously and may be utilized repeatedly [1], [2], [3]. Some energy sources are solar, wind, geothermal, hydropower, and bioenergy. In general, renewable energy sources are seen as more ecologically responsible and sustainable than non-renewable power sources, such as fossil fuels, which are limited and emit greenhouse gases when burned [4]. The use of renewable energy sources has several advantages. For instance, they can lessen our dependence on fossil fuels, which is significant in climate change [5], [6], [7], [8], [9].

Additionally, renewable energy sources can offer a more consistent and predictable energy supply and often have lower long-term operational expenses. Additionally, renewable energy may foster employment growth and local economic development [10]. Although the UN globalist agenda emphasized the necessity of developing green power and lowering pollution (CO<sub>2</sub> or NO<sub>x</sub>), facts indicate that these targets are not achievable under the existing structure. If global coal and natural gas usage continues at its present rate, the heat of the earth is expected to increase by 4–6 °C above what it was before industrialization.

A rise of this magnitude would be disastrous for food production, people's health, and biodiversity. It would jeopardize the existence of communities in so many places on the globe [11]. Solar energy has the potential to fulfill the world's energy needs if it is exploited efficiently. Energy from the sun can be converted directly to electricity by photovoltaic cells (PV) or converted thermally by concentrated solar power. PV technology has become more attractive in recent years thanks to a considerable cost reduction. Solar energy system operating costs are frequently cheaper than non-renewable energy sources. However, PV cells cannot convert all of the energy in the solar spectrum due to their inability to utilize low-energy photons and the thermal energy produced through thermalization by high-energy photons [12], [13], [14], [15], [16].

The sun produces enormous amounts of energy, and the planet receives about 1.8 x 10<sup>14</sup> kW daily, which accounts for a significant fraction of the sun's total solar power, calculated to be 3.8 x 10<sup>23</sup> kW. Solar energy is a renewable resource that may power various devices, such as solar water heaters, concentrated solar power plants, and solar panels [17].

The two crucial factors that affected a solar photovoltaic company's effectiveness were the dispersion and intensity of solar radiation. The two factors differ significantly across countries. Asia has the highest potential for solar radiation absorption compared to other warm countries since their year-round sunshine duration is more significant. Fig. (1) shows the variation of solar radiation in the Middle East. Understanding that much solar energy is wasted since it is unused [18] is essential. Using semiconducting materials that show the photovoltaic effect, the process known as photovoltaic (PV) transforms light into electricity. When photons (light particles) from the sun or other light sources dislodge electrons from their atoms, a current of electricity is produced. Typically constructed of silicon, PV cells are organized in panels or modules that may be put on buildings such as walls or roofs. Since it has been around for a while, photovoltaic PV technology has become famous for power in homes, companies, and other purposes [19]. As shown in Fig. 2.

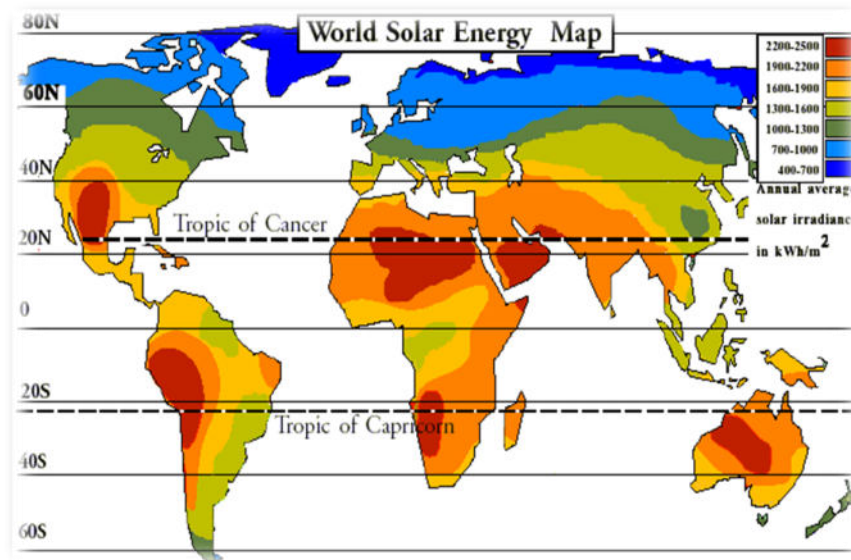


Fig. 1. - Solar radiation [20]

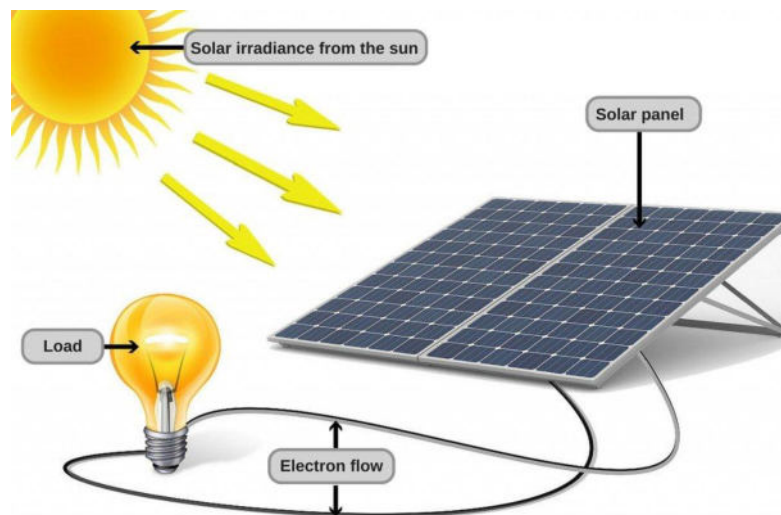


Fig. 2. - Converting sunlight into electricity [21]

PV modules are quite sensitive to rising ambient temperatures. The power and performance of PV modules are reduced when the ambient temperature rises [22]. Solar cell power output  $P$  and voltage output  $V$  are connected through the  $P$ - $V$  characteristic, assuming constant solar irradiance ( $E$ ) and panel temperature ( $T_m$ ). If  $T_m$  or  $E$  are modified in any way, the entire collection of attributes is modified. Fig. 3 shows a temperature increase in a cell. The maximum current of solar cells decreases as the temperature increases. For every 1 degree Celsius increase, the output power of the cells drops by 0.5%, which means that overheating can significantly impact the production of solar cells [23].

Solar PV cells are the primary element of PV systems and are mainly semiconductor devices that can convert solar radiation into DC electricity when exposed to sunlight. Such an optical cell consists of a P-N junction formed on a thin light-sensitive material, primarily silicon. The P-N junction of the cell is formed by doping a silicon wafer with impurities, thereby creating two layers with different electrical properties. The physical process through which solar cells convert solar radiation into electricity is known as the PV effect [24] to demonstrate the science of transforming the absorbed light from the silicon cell into a current.

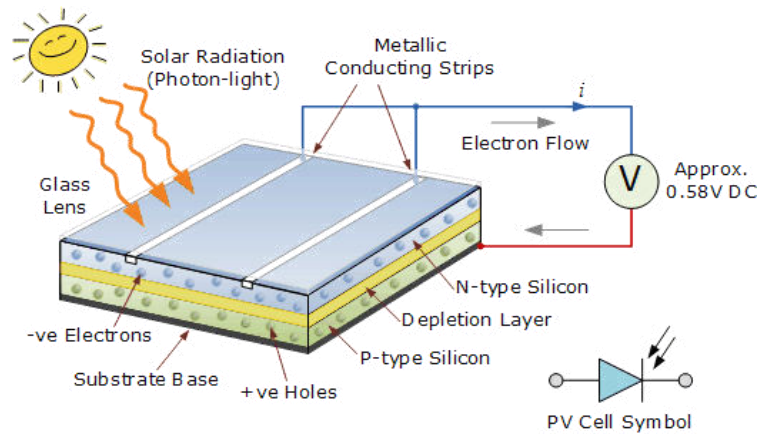


Fig. 3. - P-N junction for solar cell [25]

A typical PV panel has glass, silica, EVA, and PVF layers—Fig. 4. Predicting the amount of heat absorbed by photovoltaic cells can be difficult due to the varying absorptivity coefficients of various materials. The heat output of photovoltaic cells is complex and challenging to accurately determine due to factors such as cell efficiency, the environment in which the cells are used, and the material of the cells. Among other things, it impacts the temperature of the cells. Of day, the tilt angle, and a material's emissivity and reflectivity. The emissivity determines the amount of heat lost to the surrounding environment, but reflectivity determines how much heat is absorbed from the backside and frame of the model. The temperature of photovoltaics is generally higher than the ambient air temperature, leading to greater dissipation through heat loss rather than absorption through diffuse irradiance. Fig. 5 [26].

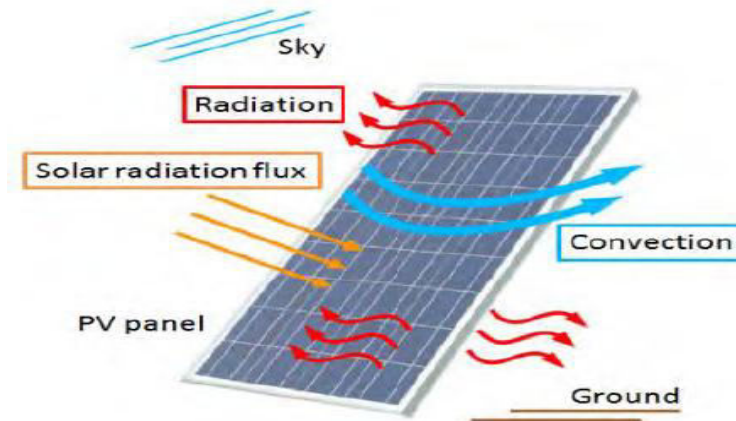


Fig. 4. - Heat transfer in PV panel [27]

Recently, the efficiency of photovoltaic panels has significantly improved, with some reaching more than 16%. However, panels with an efficiency rate of 11.7 percent are still widely available and have been shown to experience a decline in performance when their cell temperatures reach 25 °C [28].

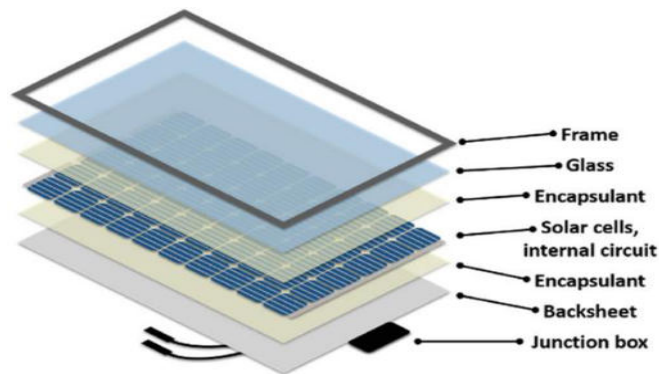


Fig. 5. - PV panel structures [29]

### 1. Phase Change Materials (PCM)

In recent years, PCM has been used in various applications, the most significant of which is cooling applications that utilize water and air because of their capacity to store enormous amounts of heat and dissipate it through melting, despite their small size. While it comes in various shapes and sizes, its primary applications include energy conservation in buildings and heat storage applications such as hot water tanks and protecting food from extreme heat during shipping and storage. Finally, it was used in photovoltaic (PV-PCM) applications to raise the efficiency of solar panels, an area in which researchers have made tremendous progress, and the rise in panel efficiency was noticed when phase-changing materials were used [30].

Phase change materials are categorized into two fundamental types of organic materials: paraffin compounds (amino acids) and non-paraffin compounds, which have high thermal stability and are employed in low-temperature applications. Inorganic materials, like salt hydrates, are more common than their predecessors. It is for use in low and moderate-temperature settings. The usage of (PCM) in house heating and cooling applications has been investigated. PCMs are adaptable, melting and solidifying across a wide temperature range, making them appropriate for various applications. Furthermore, such technologies benefit people and save energy, as shown in Fig. 6.

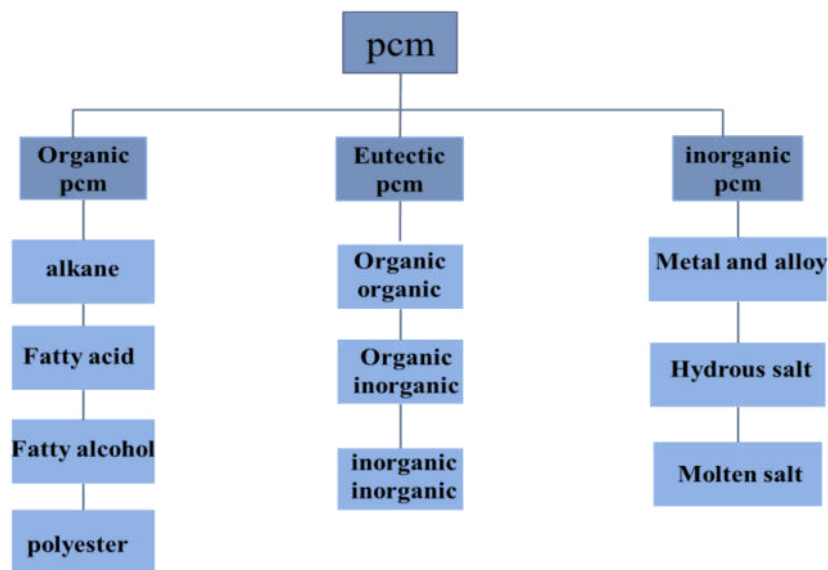


Fig. 6. - PCMs are classified according to their properties

Table 1. Type of Commercial PCM [31]

Organic	Commercial PCM
Paraffin c 18	S27
Tetradecanol	RT30
Paraffin c 16-28	TH29
Paraffin c 13	RT25
Dodecanol	STL27
Paraffin wax	RT40- RT50-RT58

PCMs are utilized for temperature regulation in several photovoltaic systems to decrease temperature-dependent photovoltaic efficiency loss. At three different degrees of insolation, the performance of each PCM was determined by evaluating four distinct PV/PCM systems. Modifying the mass and thermal conductivity of PCM was essential for adjusting PV temperature. The highest temperature drop of 18 degrees Celsius was obtained in 30 minutes, and a temperature drop of 10 degrees Celsius was maintained continuously for 5 hours [32].

A PV/PCM hybrid with two types of PCMs has been studied, and it can keep the PV at its average working temperature of 25°C, improving solar energy conversion efficiency during varying diurnal insolation. The incoming energy is captured as heat by the photovoltaic and transferred to the PCMs via the high thermal cell wall. The PCMs' thermal management properties may keep the PV temperature lower for longer [33]. (PCM) have been studied as a way to regulate the temperature of solar panels. By incorporating PCMs into the design of solar panels, it is possible to keep the cells' temperature closer to the ambient temperature for longer periods of time when exposed to high levels of solar radiation. For example, research has shown that using PCMs can allow solar panels to maintain a temperature below 40 degrees Celsius for an additional 80 minutes when subjected to 1000 W/m<sup>2</sup> of solar radiation over a prolonged period [34].

Investigated on a global scale, the yearly growth in energy production provided by a photovoltaic structure with a phase change material core. PCM functions as a heatsink. The PCM provides cooling effects in regions with slight intra-annual climatic fluctuation. When the ideal PCM melting point is used, yearly photovoltaic energy production increases by more than 6% in Mexico and eastern Africa and more than 5% in several other regions [35]. The study specifically aimed at the thermal characteristics of three separate PCM classes. The thermophysical characteristics of five solid-liquid phase transition materials were analyzed for usage in photovoltaic heat regulation applications. The components were separated into three major categories: wax, salt hydrates, and fatty acid mixtures. It is essential to examine the link between the thermophysical characteristics of PCMs and their usage as temperature managers and the external operation of PV systems [36].

The photovoltaic panel's comprehensive heat transport analysis was done with the PCM. This study determined the convection influences on the melted PCM, the wind velocity, and the PV board's slope angle. Then noted, the panel's maximum working temperature when conduction and convection effects are combined is 54.90 °C, as well as 58.5 °C when convection in melted PCM is not included (just conduction mode). Additionally, higher wind velocity or a higher tilt angle have been shown to minimize the functioning temperature of PV panels [37].

The impact of adding phase-changing materials on power conversion efficiency and increased lifetime in building-integrated photovoltaics was examined. The primary purpose is to assess the operating temperature regulation for BIPV with and without PCMs under different climate conditions. The finding showed that PCM applications have a beneficial environmental effect because they use fewer resources to make BIPV. PCMs can store heat and avoid significant damage to the BIPV early in its life cycle [38]. The computational analysis and scientific experiment demonstrate that PCM can regulate the temperature of the PV model by ten degrees Celsius for around six hours in Malaysian conditions, as shown in Fig. 7. These temperature decreases greatly enhance the productivity of the photovoltaic module [39].

The efficiency of solar panels was investigated by utilizing a variety of cooling configurations that included a variety of thermal absorber designs, coolants, and PCMs. According to this study, PV panels incorporating PCM are effective options for solar panel cooling [40]. After significant research on several natural and forced cooling methods for solar photovoltaics, previously employed systems have been deemed superior. Inactive cooling uses PCM paraffins such as wax, eutectics, natural material, and cotton wick, whereas active cooling uses gas, water, and nanofluids. Then, it has been noticed that the ambient temperature of the panel affects the conversion process, which affects both electrical performance and efficiency. As the cell's temperature rises, its performance degrades [41].



**Fig. 7.** - Melted PCM pouring on the rear part of PV [39]

The thermodynamic photovoltaic-PCM model was investigated to determine a PCM's mass, heat, and energy transfer mechanisms under a photovoltaic panel. The appropriate PCM increases the created output energy to 12.7 W. The highest functional temperature of the photovoltaic cell was lowered from 70.36 °C to 56 °C because the PCM's thickness increased from 1 cm to 3 cm [42]. To create a simplified model to calculate and analyze both the effectiveness and thermal functionality of the PCM system, they examined different PCMs' melting points and latent temperatures to select the appropriate PCM and, based on previous reviews, then discovered that the plate temperature decreased by about 10.1 °C and the efficiency increased by up to 3.73 percent [30].

PCM was applied to the backside of a photovoltaic panel. PV thermal management (PCM) is designed to absorb the PV panel's excess heat, allowing for PV thermal control and energy power efficiency enhancement. The findings show that the PV temperature differential between photovoltaic systems without PCM and PV-PCM systems can reach 23 degrees Celsius, resulting in a 5.18 percent increase in the PV-PCM system's energy production [43]. To create a model to evaluate the PCM's functionality throughout the year and under different situations. Five modules were simulated, and the findings suggest that PCM performs well in the summer with a high melting point [44]. PCM is used as a cooling technique to improve the effectiveness of photovoltaic panels.

The influence of PCM physical properties, ambient conditions, and encapsulation design has been computed and empirically investigated. It can be demonstrated that using a suitable PCM can enhance the productivity of photovoltaic panels and PV thermal systems.

Then, PCM decreased the solar plate's heat and enhanced the structure's ability to convert solar energy into usable power [45]. An analytical and experimental investigation was undertaken to calculate the impact of inclination angles on the solution's efficacy—procedure properties of a substance (PCM) when used as a heatsink behind a solar panel. Based on the data, when the angle of tilt went from 0 to 90 degrees, the melting time went down, and the plate temperature went down by 0.4% to 12.0% [46]. Then, methods for cooling a solar panel with PCM on the backside of the PV model were investigated. They discovered that free cooling is more effective in hot conditions [47].

## 2. Heatsink

Heat sinks are used to passively or actively cool a method, with or without the expenditure of other power. Heatsinks are constructed of heat-absorbing and heat-distributing materials. Because of their excellent thermal conductivity, copper and aluminum are often used in heatsinks. Heatsinks use variously sized and shaped fins to dissipate heat [48]. The dispersants were employed in conjunction with solar cells and considerably lowered the panel's temperature, as the dispersants aid in heat dispersion to the surrounding region. Fig. 8 shows one type of heatsink and its operation [49].

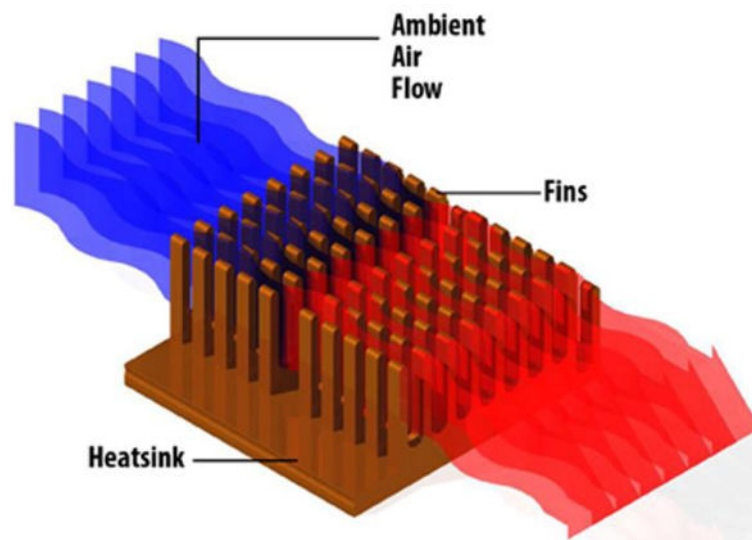


Fig. 8. - Heat sink

Researchers were able to study the impacts of four alternative thermal management methods on the thermal efficiency, point-based efficiency, and overall efficiency of a solar panel by mixing experimentally injected graphite with an externally finned heatsink. According to the findings of this study, this strategy was the most efficient way to improve the capacity of a solar panel by 12.97%. As a result, including graphite and an externally finned heatsink in the design of solar panels may be an efficient strategy to increase their performance and efficiency [50]. The effectiveness of a solar cell coupled to a thermal sink cooling system was evaluated under varying levels of solar radiation as well as passive and active air cooling over the heatsink. As compared to a solar cell cooled by natural convection, the temperature of a solar panel dropped by convective heat transfer at 500 W/m<sup>2</sup> of incoming heat flux increased as the solar irradiation increased. 5.4% of the solar panel heat is dissipated when the heatsink is cooled by natural convection. In comparison, 11% is dissipated when cooled by forced convection because forced airflow has a higher heat transfer coefficient than natural airflow [19].

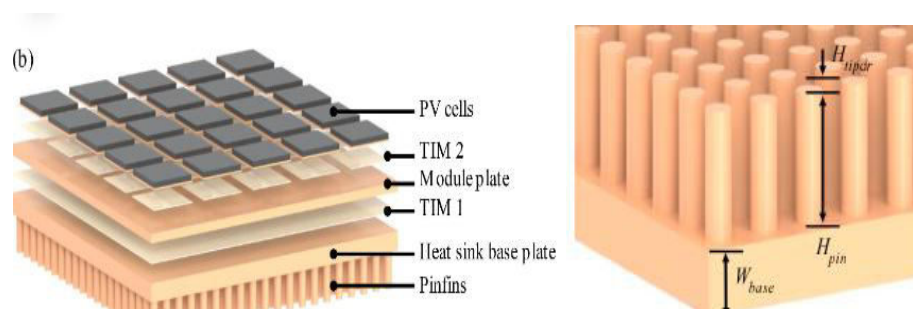


Fig. 9. - Heat sink with pin fins [51]

Looked for a link between lowering the heat of a cell and variations in its performance and productivity in cells during normal operation circumstances and those with thermoelectric panels. According to the findings, the combination of a heat sink and a thermoelectric module lowers the heat of the PV panels, increasing their efficiency as well as output power. The cooling performance was optimum. In an ideal situation, the thermoelectric heat transfer cells could increase solar panel performance and power output by 10.50% [52].

In an effort to design a more effective method for cooling the cell, they evaluated the output of a PV cell using a finned mini-channel heat sink exposed to a high concentration ratio. Introducing alumina and silicon dioxide nanoparticles improved the thermal conductivity of water. Furthermore, there was a substantial improvement when the fluid's temperature was increased. At a Re of 8.25 and a concentration level of 500, the system's overall efficiency improved by 3.82 percent [53].

Thermal control is achieved through the use of two layers of heat sink and a CPV cell. The cooling orientations of air in parallel flow and counter flow were examined. When the concentration ratio (CR) was 5, 10, 15, and 20, ethanol was used as a coolant to prevent the CPV from overheating. According to the experiments, temperatures drop significantly when the inlet flow rate is raised [54]. According to the research, a heat sink was used to cool a solar panel. Two Nanofluids cooled the heat sink. The heat sink comprises an aluminum cover and two zigzag-channeled components.

The heat sink and PV performance were evaluated for nanoparticle concentration at various Reynolds numbers. The introduction of alumina nanoparticles improves the thermal performance of solar cells. Increasing the (Re) number from 50 to 150 resulted in a 7% increase in thermal efficiency [55]. Analyzed cooling a solar cell module by increasing the back surface's heat transfer factor. The efficiency of a heat sink engaged on the backside of a panel is studied, as is the impact of fin height on heatsink performance. The panel's front and back surfaces achieved 62 °C and 51 °C, respectively, with a 20 mm heatsink fin height. When the fins were 300 mm long, temperatures dropped to 45 °C as well as 30 °C, respectively. Fig. 10 shows a heatsink with a fin length of 20 mm.

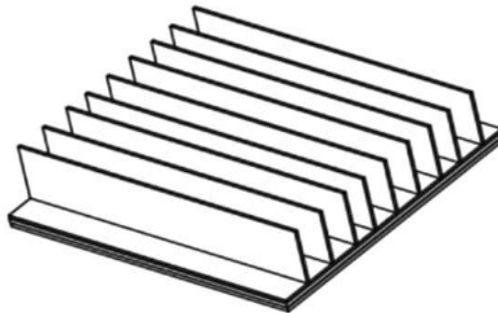


Fig. 10. - Heatsink with 20 mm fin height [56]

They looked at the effect of cooling on solar model efficiency. They tested the efficiency of PV cells using a flat cooling channel as well as a finned channel placed at the rear of the model. They discovered that the presence of fins increased the output of the model by 18.92%, and a drop in the panel temperature of 39.82 °C was recorded after it was 57.91 °C without cooling [57].

To improve thermal efficiency, a passive cooling system comprised of a heatsink with aluminum and copper fins and a number of them (5–10–15) positioned at the bottom of the panel was applied. They found that increasing the number of blades increased the thermal effectiveness of the board, with 15 blades and an aluminum base yielding the best results. Finally, the board's temperature decreased by 10.2 C, and its productivity improved by 2.74 % [48]. It is possible to enhance a solar cell's efficiency by using numerical calculations and air channels with varying airspeeds fitted with a heat sink in the shape of a hexagonal pin-fin at the bottom of the panel. Thermal efficiency increased by 60.8 percent, and electrical efficiency increased by 13.1 percent as a result [58].

### 3. Heatsink and PCM

The effect of PCMs on reducing the temperature increase in integrated PV cells in buildings was investigated. Two PCMs were used to mitigate the overheating of PV cells. Thermal performance was offered to improve the thermal conductivity of the PCM for different inner fin arrangements by using paraffin wax RT25 with inner fins. More than 30 °C could decrease the temperature rise of the PV/PCM system compared to a single flat aluminum sheet rest through a phase change [59]. Fig. 11 shows PCM and heatsink for cooling electronic devices.



Fig. 11. - PCM with heatsink [60]

The most investigated natural cooling techniques are PCM-built, air-based, liquid-based (water and nanofluids), and radiative-based. Based on the obtained results and known technical solutions, the air-based cooling option using Al fins installed on the PV plate back surface is currently the most incredible practical passive cooling alternative, both technically and economically [61]. A 2D model of the PV layers was constructed and connected with a stage change material and heatsink to forecast the transient temperature variation. Compared to single-hole and three-hole series heatsink arrangements, heatsink geometries with three and five equivalent cavities were shown to dramatically lower panel heat. Furthermore, it was discovered that using a five-parallel-hole heatsink considerably improved the solar cell's temperature uniformity [62].

In order to enhance the photovoltaic system and make the panel work better, a container with a phase-changing material and a heatsink was made and fastened to the posterior of the panel. In order to Fig. out how deep the container should be, the effects of the environment on wind speed, melting point, and ambient temperature, as well as the depth of the fin and the distance between them, were studied [63]. A new method to improve the efficiency of solar PV panels, such as TCE, was proposed, using PCMs and aluminum panels. They used two 5 W PVs; one was combined with an aluminum plate at the rear of the panel. The panel was compared to one with a naturally ventilated plate without PCM and aluminum. It was experimentally verified that the aluminum plate at the back of the panel enhanced its efficiency by an average of 24.4%. With a decrease in average temperature of 10.35 °C, the electrical efficiency of the plate increased by 2%. The maximum decrease in temperature was 13 °C for the first day and 7.7 °C for the second day [64].

Investigated Heatsinks with fins coupled with PCM substances were produced to generate an effective heat load and improve thermal conductivity efficiency. A significant drop in temperature was seen, especially when there was a lot of heat flux [65]. The research looked at the numerical enhancement in photovoltaic cooling achieved by employing finned PCM (FPCM) heatsinks. The PV, PCM, and FPCM methodologies were tested in Southeast England's atmospheric conditions. Experience has shown that PCM heatsinks may reduce the maximum PV temperature by about 13 K, while FPCM heatsinks can enhance PV cooling by 19 K.

Fig. 12 demonstrates that PCM heat sinks may boost PV output energy from 13% to 14% [66]. They assembled and examined three distinct PCM containers, including grooved, tubed, and finned containers, to increase the output power of a PV structure (PV). The finned container proved to be the best in terms of cooling. The outcome was that the heat of the PV units dropped a lot, allowing them to produce the most electricity possible [67]. A numerical study was done to lower the temperature. Electrical devices use a mixture of phase-changing materials and heat dissipators of various shapes and sizes to raise the lousy conductivity of phase-changing materials, and a significant improvement in thermal performance was observed [68].

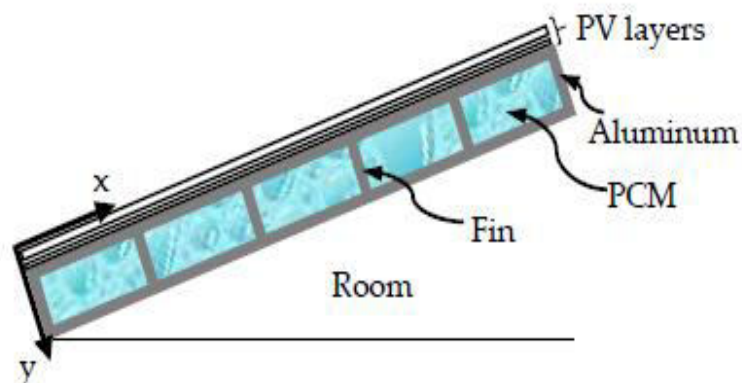


Fig. 12. - Components of the heatsink with PCM [66].

#### 4. Cooling strategies that can boost the effectiveness of PV models

Adopting a unique micro-pipe array enhances the cooling of the solar model. Natural convection cooling devices in both air and water were evaluated. When the average radiation amount is 26.3 MJ, the most significant variations in photoelectric conversion efficiency (2.6 percent), maximum temperature drop (4.7 °C), and maximum output power (8.4 percent) are observed. When the average radiation is 21.9 MJ, the water-cooled solar plate with a heat pipe surpasses the air-cooled type by a maximum of 3% in photoelectric conversion efficiency, 8% in temperature reduction, and 13.9 percent in output power increase [69].

A new study on a hybrid solar energy system combining thermal and photovoltaic technology to cool photovoltaic cells revealed that a series of channels with only an entrance and exit were placed to the back of the photovoltaic board to ensure equal airflow distribution. In specific tests, active cooling was utilized. Temperature and efficiency are linear. The module becomes extremely hot without active cooling, limiting the solar cells' efficiency to 8–9%. When solar cells operate with active cooling, their efficiency increases to 12 and 14% [68]. Then, it worked to cool the photovoltaic panel using a wind-powered roof-top turbine blower. Solar cell cooling and ventilation were accomplished in the same process. A dynamo powered the wind turbine ventilator. To improve the productivity of the solar cell, air was circulated beneath it using a blade. Along with the ventilator's regular breathing, this combination increased the output power of the photovoltaic cell by 46.54 percent [70].

Active evaporative cooling is utilized to reduce the PV heat. The increase caused by solar irradiance absorption on PV modules was tested. He coated the rear of the panel with synthetic clay and allowed a thin layer of water to evaporate. The findings indicate that the suggested technique is technically possible, as it achieves an output voltage gain of 19.4% at its maximum and 19.1% in output energy [71]. They have created a unique method to boost the effectiveness of PV plates, which entails adding a thin layer of oil to the front side to improve the quantity of sunlight the plates receive and, consequently, their efficiency. To examine several oils, including mineral oils and natural oils. The output of the photovoltaic panel has been examined. Labovac oil lets more light through than other oils, so it has been found that covering modules with a thin film of Labovac oil, about 1 mm thick, makes the model more than 20% more efficient [72].

In Egypt, an alternative cooling method for PV panels was evaluated. Instead of a compressor, a heat exchanger uses a soil heat exchanger to cool the rear of a panel. The thermally pre-cooled airflow across the back of the panel at an ideal ratio of 0.0288 m<sup>3</sup>/s successfully moderated the board's temperature from 55 °C (without cooling) to 42 °C. The photovoltaic panel's electrical output improved from 18.90% to 22.98% at this optimal flow rate [73]. The experiment to cool solar panels with saturated activated alumina and saline water is presented at varying radiation levels. In the 6-hour test, two irradiation levels of 800 W/m<sup>2</sup> and 1000 W/m<sup>2</sup> were used.

The salt influence, mainly on activated alumina tablets, was monitored for four months. Internal and exterior design changes recommended increased system cooling by 3–4 to Cover previous configurations [74]. They developed a novel cooling method that works with solar panels. The thermo-magneto-generator system operates as both a thermal dissipater and an electrical generator. The cooling technique improved efficiency by over 99%. The peak generation is 1.6 mW/m<sup>2</sup> [75]. A cotton fiber mesh is used to make the plate's back surface cooler; this mesh takes in water from a pipe and transmits it down the slope of the device by capillary action. During the experiment, the temperature decreased by 23.55 degrees Celsius. As a result, the panel's power increased by approximately 30.3 percent [76].

Hydrogel beads soaked with Al<sub>2</sub>O<sub>3</sub> liquid nanofluid are used to cool solar panels. With 0.5 percent wt., the surface temperature dropped from 17.9 degrees Celsius to 17.1 degrees Celsius. From a performance standpoint, 0.5 percent wt. Provided the best results, but due to the cost of nanomaterials, 0.25 percent wt. Concentrations are the most cost-effective option [77]. A smart water spraying approach that ineffectively solves a critical gap faced by the PV cell during hot weather situations. The use of an Arduino board to implement a microcontroller temperature control water spray device improved the effectiveness of the solar cell. The study used a temperature control feedback system and made a cooling algorithm for solar collectors, which made the PV panel array about 16.65% more efficient [78].

The effectiveness of polycrystalline photovoltaic cells when cooled by evaporation was investigated. Under similar circumstances, cooled PV panels outperformed uncooled PV panels in efficiency and output. Evaporative convective cooling uses a wet cloth on the cooling channel's bottom surface. When a 120 mm air gap was used to cool the solar model, it increased daily energy output and efficiency by about 1.7 and 1.2 percent, respectively [79]. Water-based photovoltaic systems. This technology reduces the photovoltaic panels' temperature by 5–6 °C. The solar PV absorber system is perhaps the most economically advantageous from a thermal and electrical energy production standpoint. Self-contained PV systems might benefit from water evaporation on the rear of the panels by utilizing mud and cotton wicks. Solar panels in dry climates benefit from dual cooling [80].

#### 5. Variables that influence solar cells' productivity

The impact of various reasons on the panel temperature of selected PV methods in Singapore was examined, including material, ventilation, module frame, and other ambient circumstances. The monitoring findings revealed that the temperature rose between the lowest and highest temperatures. Readings varied due to three factors. When the temperature of silicon wafer-based modules increases by one degree, power consumption decreases by 0.45% [81]. They modified initial conditions such as transparent conductors, metallic pattern conductivity, and low light

intensity, allowing for grid design and finger size optimization. The results show that a metal grid with 20- $\mu\text{m}$  broad lines would enhance the performance effectiveness of the solar board by 11.7% [82].

The impacts of external influences on the module's temperature were explored. The sun, wind, temperature, and distance between neighboring cells were all considered. The solar panel layer reached a maximum temperature of 331.76 kelvin. Additionally, lighter irradiation facilitates the solar module's thermal dissipation, increasing its temperature. When the wind speed goes from 0 meters per second to 1 meter per second, the efficiency of a solar module also goes up [83]. The influence of humidity on solar panel output was tested in a lab. After measuring PV output (voltages and currents), solar radiation incident studies show that solar irradiance and panel power production decline when humidity increases. The panel's output power decreases by 34.22 percent for every 50 percent increase in humidity [31].

The distance between the panels and the roof impacted the free airflow's ability to detect the panels' temperature. It was discovered that the natural airflow beneath them influenced the panels' performance. The amount of solar irradiation, distance between solar models, and so on were also investigated. The average temperature of a PV group without an air cavity is about 12 c greater than that of a PV array with an air gap of more than 200 millimeters and about 18 c higher, widened to 250 millimeters [84]. The influence of dust depletion on the electrical output of the SPV was examined, and an experimental examination of the output power sensitivity throughout dust depletion was performed. Sand storms, levels of pollution, and snow quantity all significantly influence SPV's performance. These difficulties reduce solar panel efficiency and have a detrimental influence on electrical performance [85].

Snowfall on photovoltaic panels can significantly reduce power output, as shown in Fig. 13. This effect must be precisely anticipated to be considered a reliable energy source. There were other topics they investigated. To examine both engaged and cumulative solar irradiance and the thermal capacitance of the PV panels [86]. Hand scrubbing, vacuuming, and electrostatic precipitation are some cleaning techniques used. This cleaning procedure can increase the panel's efficiency by 15-20% [87]. Then, it was found that dust reduces the sunlight the solar cells receive, lowering the output. So, cleaning routines are implemented to increase panel performance. The more frequently clean, the better; though this may require more energy, the gain may need to be increased [88].



Fig. 13. - The effect of the snow on the model [89]

## Conclusion

The heat of the photovoltaic modules is a crucial aspect that determines the amount of power they will produce. While more sunlight can be beneficial, it also raises the panel's temperature, which can offset some of the benefits. In reality, the most efficient solar photovoltaic panels only transform about 20% of the incident solar irradiance into straight current energy, with the majority of the remaining irradiation being reflected or absorbed by the module material as heat [85]. When the environment's temperature rises by one degree Celsius, the panel's efficiency falls by 0.5% and its voltage falls by 2.2 mV. The high heat of the cell will harm the model's ability to produce power [90]. There is a solid motivation to decrease cell base temperature through heat transfer and removal methods in the fastest and most straightforward technique possible.

## References

- [1] Radhi S. S., Al-khafaji Z. S., Falah M. W. Sustainable heating system by infrared radiators, vol. 4, no. 1, pp. 42–52, 2022, doi: 10.37868/hsd.v4i1.82.
- [2] Y. Al-Abayechi, Y. Alaiwi, and Z. Al-Khafaji, "Exploration of key approaches to enhance evacuated tube solar collector efficiency," *J. Adv. Res. Numer. Heat Transf.*, vol. 19, no. 1, pp. 1–14, 2024.
- [3] A. Aljumaili, Y. Alaiwi, and Z. Al-Khafaji, "INVESTIGATING BACK SURFACE COOLING SYSTEM USING PHASE CHANGE MATERIALS AND HEATSINK ON PHOTOVOLTAIC PERFORMANCE," *J. Eng. Sustain. Dev.*, vol. 28, no. 3, pp. 294–315, 2024.
- [4] F. Sveučilište u Zagrebu. Fakultet strojarstva i brodogradnje., S. Nižetić, and T. Giuseppe Marco, "Photovoltaic Panels: a Review of the Cooling Techniques," *Transactions of FAMENA*, vol. 40, no. SI-1, pp. 63–74,

2000.

- [5] Z. Al-Masoodi, A. Dulaimi, H. Jafer, Z. Al-Khafaji, W. Atherton, and H. Safa, "Soft Soil Treated with Waste Fluid Catalytic Cracking as a Sustainable Stabilizer Material," *Iraqi Geol. J.*, vol. 54, pp. 84–98, 2022, doi: 10.46717/igj.55.1C.4Ms-2022-03-23.
- [6] Z. O. Al-Masoodi, Z. Al-Khafaji, H. M. Jafer, A. Dulaimi, and W. Atherton, "The effect of a high alumina silica waste material on the engineering properties of a cement-stabilised soft soil," in *The 3rd BUId Doctoral Research Conference*, Dubai, AUE, 2017.
- [7] A. J. Hussain and Z. S. Al-Khafaji, "The fields of applying the recycled and used oils by the internal combustion engines for purposes of protecting the environment against pollutions," *J. Adv. Res. Dyn. Control Syst.*, vol. 12, no. 1 Special Issue, 2020, doi: 10.5373/JARDCS/V12SP1/20201119.
- [8] A. J. Hussain and Z. S. Al-Khafaji, "Reduction of environmental pollution and improving the (Mechanical, physical and chemical characteristics) of contaminated clay soil by using of recycled oil," *J. Adv. Res. Dyn. Control Syst.*, vol. 12, no. 4 Special Issue, pp. 1276–1286, 2020, doi: 10.5373/JARDCS/V12SP4/20201604.
- [9] A. J. Hussain, Z. S. Al-Khafaji, and I. Q. Al Saffar, "New recycling method of lubricant oil and the effect on the viscosity and viscous shear as an environmentally friendly," *Open Eng.*, vol. 14, no. 1, p. 20220521, 2024.
- [10] U.S. EPA, "Part One - The Multiple Benefits of Energy Efficiency and Renewable Energy," *Quantifying Mult. Benefits Energy Effic. Renew. Energy A Guid. State Local Gov.*, pp. 1–17, 2018.
- [11] N. Yoshino, F. Taghizadeh-Hesary, and M. Otsuka, "Covid-19 and Optimal Portfolio Selection for Investment in Sustainable Development Goals," *Financ. Res. Lett.*, vol. 38, no. July, p. 101695, 2021, doi: 10.1016/j.frl.2020.101695.
- [12] A. Altuwairgi, "Full-spectrum Solar Energy Harvesting for Power and Heat Production using Dichroic Mirror," no. March, 2022.
- [13] E. Mohammed and Z. Al-khafaji, "Effect of Surface Treatments by Ultrasonic on NiTi Biomaterials," *Acad. J. Manuf. Eng.*, vol. 21, no. 3, pp. 1–6, 2023.
- [14] Jasim Ahmed Jasim, A. Yaser, and Z. Al-Khafaji, "AN ANSYS SIMULATION STUDY ON THE EFFECT OF APPLYING TITA-NIUM ALLOY (TI-6AL-4V) COATING FOR WIND TURBINE GEAR," *Acad. J. Manuf. Eng.*, vol. 22, no. 4, 2024.
- [15] S. Sattar, Y. Alaiwi, N. S. Radhi, and Z. Al-khafaji, "Numerical Simulation for Effect of Composite Coating (TiO<sub>2</sub> + SiO<sub>2</sub>) Thickness on Steam Turbine Blades Thermal and Stress Distribution," *Acad. J. Manuf. Eng.*, vol. 21, no. 4, 2023.
- [16] T. AL-ABBOUDI, A. Yaser, and Z. Al-Khafaji, "REDUCING VIBRATION AND NOISE IN THE OIL SECTOR USING NANOPARTICLE-REINFORCED POLYMERS," *Acad. J. Manuf. Eng.*, vol. 2024, no. 3, 2024.
- [17] N. Kannan and D. Vakeesan, "Solar energy for future world: - A review," *Renew. Sustain. Energy Rev.*, vol. 62, pp. 1092–1105, 2016, doi: 10.1016/j.rser.2016.05.022.
- [18] G. O. G. Löf, J. A. Duffie, and C. O. Smith, "World distribution of solar radiation," *Sol. Energy*, vol. 10, no. 1, pp. 27–37, 1966, doi: 10.1016/0038-092X(66)90069-7.
- [19] A. M. A. Soliman, D. Hassan, and S. H. Ookawara, "An experimental study of the performance of the solar cell with heat sink cooling system," *Energy Procedia*, vol. 162, pp. 127–135, 2019, doi: 10.1016/j.egypro.2019.04.014.
- [20] M. Sabry, M. Nahas, and S. H. Al-Lehyani, "Simulation of a standalone, portable steam generator driven by a solar concentrator," *Energies*, vol. 8, no. 5, pp. 3867–3881, 2015, doi: 10.3390/en8053867.
- [21] A. Saleem, A. Iqbal, K. Mehmood, M. K. Panjwani, F. H. Mangi, and R. M. Larik, "The effect of environmental changes on the efficiency of the PV system," *Indones. J. Electr. Eng. Comput. Sci.*, vol. 18, no. 1, pp. 558–564, 2019, doi: 10.11591/ijeecs.v18.i1.pp558-564.
- [22] S. Dubey, J. N. Sarvaiya, and B. Seshadri, "Temperature dependent photovoltaic (PV) efficiency and its effect on PV production in the world - A review," *Energy Procedia*, vol. 33, pp. 311–321, 2013, doi: 10.1016/j.egypro.2013.05.072.
- [23] H. Peng, G. Ding, H. Hu, and W. Jiang, "Effect of nanoparticle size on nucleate pool boiling heat transfer of refrigerant/oil mixture with nanoparticles," *Int. J. Heat Mass Transf.*, vol. 54, no. 9–10, pp. 1839–1850, 2011, doi: 10.1016/j.ijheatmasstransfer.2010.12.035.
- [24] A. Makki, "Innovative Heat Pipe-Based Photovoltaic / Thermoelectric ( PV / TEG ) Generation System," 2017.
- [25] B. Bradley, "Improving PV Module Efficiency Through Cooling," *Chem. Eng. Undergrad. Honor. Theses*, 2020.
- [26] A. M. P. S. Ni zeti c , F. Grubi si c- Cabo, I. Marini c-Kragi c, "Experimental and numerical investigation of a backside convective cooling mechanism on photovoltaic panels." p. Energy 111 (2016) 211e225, 2016.
- [27] M. Sahli, "Simulation and modelling of thermal and mechanical behaviour of silicon photovoltaic panels under nominal and real-time conditions To cite this version : HAL Id : tel-02520073 Simulation and modelling of thermal and mechanical behaviour of Silicon photovo," 2020.
- [28] J. Y. Usman Jamil Rajput, "Comparison of heat sink and water type PV/T collector for polycrystalline photovoltaic panel cooling," p. Renewable Energy (2017), doi: 10.1016 /j.renene., 2017.
- [29] M. Aghaei *et al.*, "Review of degradation and failure phenomena in photovoltaic modules," *Renew. Sustain.*

*Energy Rev.*, vol. 159, no. July 2021, p. 112160, 2022, doi: 10.1016/j.rser.2022.112160.

- [30] M. Arıcı, F. Bilgin, S. Nižetić, and A. M. Papadopoulos, “Phase change material based cooling of photovoltaic panel: A simplified numerical model for the optimization of the phase change material layer and general economic evaluation,” *J. Clean. Prod.*, vol. 189, pp. 738–745, 2018, doi: 10.1016/j.jclepro.2018.04.057.
- [31] A. K. Tripathi, S. Ray, M. Aruna, and S. Prasad, “Evaluation of solar PV panel performance under humid atmosphere,” *Mater. Today Proc.*, vol. 45, no. xxxx, pp. 5916–5920, 2020, doi: 10.1016/j.matpr.2020.08.775.
- [32] S. Maiti, S. Banerjee, K. Vyas, P. Patel, and P. K. Ghosh, “Self regulation of photovoltaic module temperature in V-trough using a metal-wax composite phase change matrix,” *Sol. Energy*, vol. 85, no. 9, pp. 1805–1816, 2011, doi: 10.1016/j.solener.2011.04.021.
- [33] M. Jun Huang, “The effect of using two PCMs on the thermal regulation performance of BIPV systems,” *Sol. Energy Mater. Sol. Cells*, vol. 95, no. 3, pp. 957–963, 2011, doi: 10.1016/j.solmat.2010.11.032.
- [34] P. H. Biwole, P. Eclache, and F. Kuznik, “Phase-change materials to improve solar panel’s performance,” *Energy Build.*, vol. 62, pp. 59–67, 2013, doi: 10.1016/j.enbuild.2013.02.059.
- [35] C. J. Smith, P. M. Forster, and R. Crook, “Global analysis of photovoltaic energy output enhanced by phase change material cooling,” *Appl. Energy*, vol. 126, pp. 21–28, 2014.
- [36] A. Hasan, S. J. McCormack, M. J. Huang, and B. Norton, “Characterization of phase change materials for thermal control of photovoltaics using Differential Scanning Calorimetry and Temperature History Method,” *Energy Convers. Manag.*, vol. 81, pp. 322–329, 2014, doi: 10.1016/j.enconman.2014.02.042.
- [37] K. Kant, A. Shukla, A. Sharma, and P. H. Biwole, “Heat transfer studies of photovoltaic panel coupled with phase change material,” *Sol. Energy*, vol. 140, pp. 151–161, 2016, doi: 10.1016/j.solener.2016.11.006.
- [38] P. Royo, V. J. Ferreira, A. M. López-Sabirón, and G. Ferreira, “Hybrid diagnosis to characterise the energy and environmental enhancement of photovoltaic modules using smart materials,” *Energy*, vol. 101, pp. 174–189, 2016, doi: 10.1016/j.energy.2016.01.101.
- [39] H. Mahamudul *et al.*, “Temperature regulation of photovoltaic module using phase change material: a numerical analysis and experimental investigation,” *Int. J. Photoenergy*, vol. 2016, 2016.
- [40] S. Preet, “Water and phase change material based photovoltaic thermal management systems: A review,” *Renew. Sustain. Energy Rev.*, vol. 82, pp. 791–807, 2018.
- [41] A. K. Suresh, S. Khurana, G. Nandan, G. Dwivedi, and S. Kumar, “Role on nanofluids in cooling solar photovoltaic cell to enhance overall efficiency,” *Mater. Today Proc.*, vol. 5, no. 9, pp. 20614–20620, 2018, doi: 10.1016/j.matpr.2018.06.442.
- [42] M. Noura, “Numerical study of an inclined photovoltaic system coupled with phase change material under various operating conditions.” pp. 958–975, 2018. doi: <https://doi.org/10.1016/j.applthermaleng.2018.06.039>.
- [43] Z. Li, T. Ma, J. Zhao, A. Song, and Y. Cheng, “Experimental study and performance analysis on solar photovoltaic panel integrated with phase change material,” *Energy*, vol. 178, pp. 471–486, 2019, doi: 10.1016/j.energy.2019.04.166.
- [44] J. Zhao, T. Ma, Z. Li, and A. Song, “Year-round performance analysis of a photovoltaic panel coupled with phase change material,” *Appl. Energy*, vol. 245, pp. 51–64, 2019.
- [45] N. K. Sharma, M. K. Gaur, and C. S. Malvi, “Application of phase change materials for cooling of solar photovoltaic panels: A review,” *Mater. Today Proc.*, vol. 47, no. xxxx, pp. 6759–6765, 2020, doi: 10.1016/j.matpr.2021.05.127.
- [46] H. G. Abdulmunem R. Abdulmunem , Pakharuddin Mohd Samin , Hashimah Abdul Rahman , Hashim A. Hussien , Izhari Izmi Mazali, “Numerical and experimental analysis of the tilt angle’s effects on the characteristics of the melting process of PCM-based as PV cell’s backside heat sink.” pp. 520–530, 2021.
- [47] S. M. Ciril Arkar , Tej ~Zi~zak , Suzana Domjan, “Comparative analysis of free cooling of photovoltaics – phase change versus evaporative cooling.” p. 104162, 2022. doi: <https://doi.org/10.1016/j.est.2022.104162>.
- [48] M. R. A. P. and A. R. P. Zainal Arifi, Suyitno Suyitno , Dominicus Danardono Dwi Prija Tjahjana, Wibawa Endra Juwana, “The Effect of Heat Sink Properties on Solar Cell Cooling Systems,” *Appl. Sci.*, vol. 10, no. 21, 2020, doi: 10.3390/app10217919.
- [49] M. Alzahrani, H. Baig, K. Shanks, and T. Mallick, “Estimation of the performance limits of a concentrator solar cell coupled with a micro heat sink based on a finite element simulation,” *Appl. Therm. Eng.*, vol. 176, no. August 2019, p. 115315, 2020, doi: 10.1016/j.applthermaleng.2020.115315.
- [50] P. Atkin and M. M. Farid, “Improving the efficiency of photovoltaic cells using PCM infused graphite and aluminium fins,” *Sol. Energy*, vol. 114, pp. 217–228, 2015, doi: 10.1016/j.solener.2015.01.037.
- [51] J. H. J. Danish Ansari, “A novel variable-height-pinfin isothermal heat sink for densely-packed concentrated photovoltaic systems.” p. 115519, 2022.
- [52] R. Salehi, A. Jahanbakhshi, M. Reza Golzarian, and M. Khojastehpour, “Evaluation of solar panel cooling systems using anodized heat sink equipped with thermoelectric module through the parameters of temperature, power and efficiency,” *Energy Convers. Manag. X*, vol. 11, no. April, p. 100102, 2021, doi: 10.1016/j.ecmx.2021.100102.
- [53] A. Ahmed, G. Zhang, K. Shanks, S. Sundaram, Y. Ding, and T. Mallick, “Performance evaluation of single multi-junction solar cell for high concentrator photovoltaics using minichannel heat sink with nanofluids,” *Appl. Therm. Eng.*, vol. 182, no. August 2020, p. 115868, 2021, doi: 10.1016/j.applthermaleng.2020.115868.

- [54] H. I. Elqady *et al.*, “Concentrator photovoltaic thermal management using a new design of double-layer microchannel heat sink,” *Sol. Energy*, vol. 220, no. April 2020, pp. 552–570, 2021, doi: 10.1016/j.solener.2021.02.003.
- [55] M. Ibrahim and T. Saeed, “Designing a new heat sink containing nanofluid flow to cool a photovoltaic solar cell equipped with reflector,” *J. Taiwan Inst. Chem. Eng.*, vol. 124, pp. 9–16, 2021, doi: 10.1016/j.jtice.2021.05.015.
- [56] E. Johnston, P. S. B. Szabo, and N. S. Bennett, “Cooling silicon photovoltaic cells using finned heat sinks and the effect of inclination angle,” *Therm. Sci. Eng. Prog.*, vol. 23, no. November 2020, p. 100902, 2021, doi: 10.1016/j.tsep.2021.100902.
- [57] L. Bilir, Z. Ozcan, M. Gülgün, and S. Ecem, “Cooling channel effect on photovoltaic panel energy generation,” vol. 230, no. November, pp. 943–953, 2021, doi: 10.1016/j.solener.2021.10.086.
- [58] A. Abidi, “Evaluation of thermal, electrical and overall efficiency of an air-cooled solar panel equipped with hexagonal pin-fins,” *Sustain. Energy Technol. Assessments*, vol. 48, no. August, p. 101579, 2021, doi: 10.1016/j.seta.2021.101579.
- [59] M. J. Huang, P. C. Eames, and B. Norton, “Phase change materials for limiting temperature rise in building integrated photovoltaics,” *Sol. energy*, vol. 80, no. 9, pp. 1121–1130, 2006.
- [60] A. Chuttar and D. Banerjee, “Machine learning (ML) based thermal management for cooling of electronics chips by utilizing thermal energy storage (TES) in packaging that leverages phase change materials (PCM),” *Electron.*, vol. 10, no. 22, 2021, doi: 10.3390/electronics10222785.
- [61] S. Nizetić, A. M. Papadopoulos, and E. Giama, “Comprehensive analysis and general economic-environmental evaluation of cooling techniques for photovoltaic panels, Part I: Passive cooling techniques,” *Energy Convers. Manag.*, vol. 149, pp. 334–354, 2017.
- [62] M. Emam and M. Ahmed, “Cooling concentrator photovoltaic systems using various configurations of phase-change material heat sinks,” *Energy Convers. Manag.*, vol. 158, no. June 2017, pp. 298–314, 2018, doi: 10.1016/j.enconman.2017.12.077.
- [63] S. Khanna, S. Newar, V. Sharma, K. S. Reddy, and T. K. Mallick, “Optimization of fins fitted phase change material equipped solar photovoltaic under various working circumstances,” *Energy Convers. Manag.*, vol. 180, no. October 2018, pp. 1185–1195, 2019, doi: 10.1016/j.enconman.2018.10.105.
- [64] M. Rajvikram, S. Leponraj, S. Ramkumar, H. Akshaya, and A. Dheeraj, “Experimental investigation on the abatement of operating temperature in solar photovoltaic panel using PCM and aluminium,” *Sol. Energy*, vol. 188, pp. 327–338, 2019.
- [65] S. A. B. Al-Omari, Z. A. Qureshi, E. Elnajjar, and F. Mahmoud, “A heat sink integrating fins within high thermal conductivity phase change material to cool high heat-flux heat sources,” *Int. J. Therm. Sci.*, vol. 172, p. 107190, 2022.
- [66] P. Singh *et al.*, “Solar photovoltaic panels with finned phase change material heat sinks,” *Energies*, vol. 13, no. 10, 2020, doi: 10.3390/en13102558.
- [67] T. Wongwuttanasatian, T. Sarikarin, and A. Suksri, “Performance enhancement of a photovoltaic module by passive cooling using phase change material in a finned container heat sink,” *Sol. Energy*, vol. 195, pp. 47–53, 2020.
- [68] H. G. Teo, P. S. Lee, and M. N. A. Hawlader, “An active cooling system for photovoltaic modules,” *Appl. Energy*, vol. 90, no. 1, pp. 309–315, 2012.
- [69] H. C. Sox, “Notice of retraction,” *Ann. Intern. Med.*, vol. 139, no. 8, p. 702, 2003, doi: 10.7326/0003-4819-139-8-200310210-00017.
- [70] P. Valeh-e-sheyda, M. Rahimi, A. Parsamoghadam, and M. M. Masahi, “Acceptance,” *Energy Build.*, no. 2014, 2013, doi: 10.1016/j.enbuild.2013.12.052.
- [71] A. H. Alami, “Effects of evaporative cooling on efficiency of photovoltaic modules,” *Energy Convers. Manag.*, vol. 77, pp. 668–679, 2014, doi: 10.1016/j.enconman.2013.10.019.
- [72] M. S. Abd-Elhady, M. M. Fouad, and T. Khalil, “Improving the efficiency of photovoltaic (PV) panels by oil coating,” *Energy Convers. Manag.*, vol. 115, pp. 1–7, 2016, doi: 10.1016/j.enconman.2016.02.040.
- [73] A. A. Alrobaian, “Performance of PV panel coupled with geothermal air cooling system subjected to hot climatic,” *Appl. Therm. Eng.*, vol. 148, no. November 2017, pp. 1–9, 2019, doi: 10.1016/j.applthermaleng.2018.11.027.
- [74] S. Abdo, H. Saidani-Scott, B. Borges, and M. A. Abdelrahman, “Cooling solar panels using saturated activated alumina with saline water: Experimental study,” *Sol. Energy*, vol. 208, no. April, pp. 345–356, 2020, doi: 10.1016/j.solener.2020.07.079.
- [75] A. Homadi, T. Hall, and L. Whitman, “Study a novel hybrid system for cooling solar panels and generate power,” *Appl. Therm. Eng.*, vol. 179, p. 115503, 2020, doi: 10.1016/j.applthermaleng.2020.115503.
- [76] E. B. Agyekum, S. PraveenKumar, N. T. Alwan, V. I. Velkin, and S. E. Shekhelein, “Effect of dual surface cooling of solar photovoltaic panel on the efficiency of the module: experimental investigation,” *Heliyon*, vol. 7, no. 9, p. e07920, 2021, doi: 10.1016/j.heliyon.2021.e07920.
- [77] S. Abdo and H. Saidani-Scott, “Effect of using saturated hydrogel beads with alumina water-based nanofluid for cooling solar panels: Experimental study with economic analysis,” *Sol. Energy*, vol. 217, no. October

2020, pp. 155–164, 2021, doi: 10.1016/j.solener.2021.01.050.

- [78] O. T. Laseinde and M. D. Ramere, “Efficiency Improvement in polycrystalline solar panel using thermal control water spraying cooling,” *Procedia Comput. Sci.*, vol. 180, pp. 239–248, 2021, doi: 10.1016/j.procs.2021.01.161.
- [79] A. Almuwailhi and O. Zeitoun, “Investigating the cooling of solar photovoltaic modules under the conditions of Riyadh,” *J. King Saud Univ. - Eng. Sci.*, no. xxxx, 2021, doi: 10.1016/j.jksues.2021.03.007.
- [80] S. S. Bhakre, P. D. Sawarkar, and V. R. Kalamkar, “Performance evaluation of PV panel surfaces exposed to hydraulic cooling – A review,” *Sol. Energy*, vol. 224, no. May, pp. 1193–1209, 2021, doi: 10.1016/j.solener.2021.06.083.
- [81] T. Reindl, J. Luther, C. Reise, and Z. Ye, “On PV module temperatures in tropical regions,” vol. 88, pp. 80–87, 2013, doi: 10.1016/j.solener.2012.11.001.
- [82] J. Van Deelen, L. Klerk, and M. Barink, “Optimized grid design for thin film solar panels,” *Sol. Energy*, vol. 107, pp. 135–144, 2014, doi: 10.1016/j.solener.2014.05.028.
- [83] J. Zhou, Q. Yi, Y. Wang, and Z. Ye, “ScienceDirect Temperature distribution of photovoltaic module based on finite element simulation,” *Sol. ENERGY*, vol. 111, pp. 97–103, 2015, doi: 10.1016/j.solener.2014.10.040.
- [84] M. S. Naghavi, A. Esmailzadeh, B. Singh, B. C. Ang, T. M. Yoon, and K. S. Ong, “Experimental and numerical assessments of underlying natural air movement on PV modules temperature,” *Sol. Energy*, vol. 216, no. June 2020, pp. 610–622, 2021, doi: 10.1016/j.solener.2021.01.007.
- [85] M. Katoch, K. Kumar, and V. Dahiya, “Dust accumulation and reduction in electrical performance of solar PV panels,” *Mater. Today Proc.*, vol. 46, no. xxxx, pp. 6608–6612, 2020, doi: 10.1016/j.matpr.2021.04.082.
- [86] R. E. Pawluk, M. Rezvnpour, Y. Chen, and Y. She, “A sensitivity analysis on effective parameters for sliding/melting prediction of snow cover on solar photovoltaic panels,” *Cold Reg. Sci. Technol.*, vol. 185, no. November 2020, p. 103262, 2021, doi: 10.1016/j.coldregions.2021.103262.
- [87] K. Jaiganesh, K. Bharath Simha Reddy, B. K. D. Shobhitha, and B. Dhanush Goud, “Enhancing the efficiency of rooftop solar photovoltaic panel with simple cleaning mechanism,” *Mater. Today Proc.*, vol. 51, no. xxxx, pp. 411–415, 2022, doi: 10.1016/j.matpr.2021.05.565.
- [88] J. Kennedy, A. Lo, H. S. Rajamani, and S. Lutfi, “Solar and sand: Dust deposit mitigation in the desert for PV arrays,” *Sustain. Energy, Grids Networks*, vol. 28, p. 100531, 2021, doi: 10.1016/j.segan.2021.100531.
- [89] E. Andenæs, B. P. Jelle, K. Ramlo, T. Kolås, J. Selj, and S. E. Foss, “The influence of snow and ice coverage on the energy generation from photovoltaic solar cells,” *Sol. Energy*, vol. 159, no. September 2017, pp. 318–328, 2018, doi: 10.1016/j.solener.2017.10.078.
- [90] M. R. Maghami, H. Hizam, C. Gomes, M. A. Radzi, M. I. Rezadad, and S. Hajighorbani, “Power loss due to soiling on solar panel: A review,” *Renew. Sustain. Energy Rev.*, vol. 59, pp. 1307–1316, 2016, doi: 10.1016/j.rser.2016.01.044.

#### Information of the authors

**Aljumaili Ahmed**, Msc., lecturer, Altinbas University

e-mail: [yaser.alaiwi@altinbas.edu.tr](mailto:yaser.alaiwi@altinbas.edu.tr)

**Alaiwi Yaser**, PhD, assistance professor, Altinbas University

e-mail: [yaser.alaiwi@altinbas.edu.tr](mailto:yaser.alaiwi@altinbas.edu.tr)

**Al-Khafaji Zainab**, PhD, lecturer, Imam Ja'afar Al-Sadiq University, Universiti Kebangsaan Malaysia

e-mail: [p123005@siswa.ukm.edu.my](mailto:p123005@siswa.ukm.edu.my)

## Development and Research of a New Reinforced Design of the Mounting Block

Zharkevich O.M., Shlyakhov S.V., Nurzhanova O.A.\*, Imasheva K.I.

Abylkas Saginov Karaganda Technical University, Karaganda, Kazakhstan

\*corresponding author

**Abstract.** In connection with the modernization of coal mine equipment in the Karaganda coal basin, the customer faced the problem of installing large units: the existing installation blocks have a low load-bearing capacity. This article discusses the development of an experimental model of a reinforced installation block according to the customer's technical specifications. In accordance with the customer's requirements for dimensions, weight and load-bearing capacity, design and technological documentation for a new reinforced installation block design was developed. Mathematical calculations for the strength of the design units were verified by the APM FEM program in the KOMPAS-3D system. Steel grade 30XGSA is the optimal material for the main parts of this product under the specified loads. The nominal diameter of the rod for the "axis" and "earring" parts is 48 mm. The weight of the structure meets the requirements and does not exceed 15 kg. The minimum permissible cross-sectional area of the eye of the "earring" part is 329 mm<sup>2</sup>. Two installation blocks were manufactured according to the developed drawings, which successfully passed the tensile strength tests. This design has been found to be operational and is to be tested in coal mine conditions.

**Keywords:** mounting block, bracket, steel rope, lifting device, rigging.

### Introduction

The assembly block is widely used in assembly and disassembly work on equipping coal mine long walls with equipment and serves to transport and install the units of the complex at the work site [1, 2].

The assembly block must meet strict safety, reliability, and efficiency requirements [3].

The main requirements for the assembly block are [4-6]:

- strength and reliability of the structure;
- the quality of the material from which it is made;
- ensuring its lifting capacity with a safety margin;
- the safety of load fixation.

The block must be made of materials resistant to high loads, corrosion, abrasive wear and exposure to aggressive mine environments (dust, humidity, gases) [7, 8].

The block must be designed to lift and move loads corresponding to its lifting capacity with a safety margin [9]. Reliable grips, slings, and other fastening elements must ensure the safe fixation of the load during transportation and installation [10].

The assembly block is a structure consisting of three main elements: a bracket, an axis, and a block (Figure 1). Before carrying out work, the assembly block is fixed by the bracket with fastening elements (chain, rope, etc.) to the metal arch support of the mine workings or to the metal structures of the installed mechanized support, a branch of the rope  $\varnothing 22.5 \dots 27$  mm is passed through the block and the block is fixed with an axis. The assembled assembly block is used both to change the direction of movement of the ropes and to lift and move loads.



Fig. 1. - General view of the operating mounting block

In modern realities, new and modernized equipment is heavier and less divided into component units, which complicates the production of installation work with operation at maximum loads of installation blocks [11]. The brackets of the installation block often fail during the work. Also, in case of critical deformation of the bracket, the released rope can cause injury to workers.

In this regard, in the mines of Karaganda, there was a need to use a new reinforced design of the installation block that meets the following requirements:

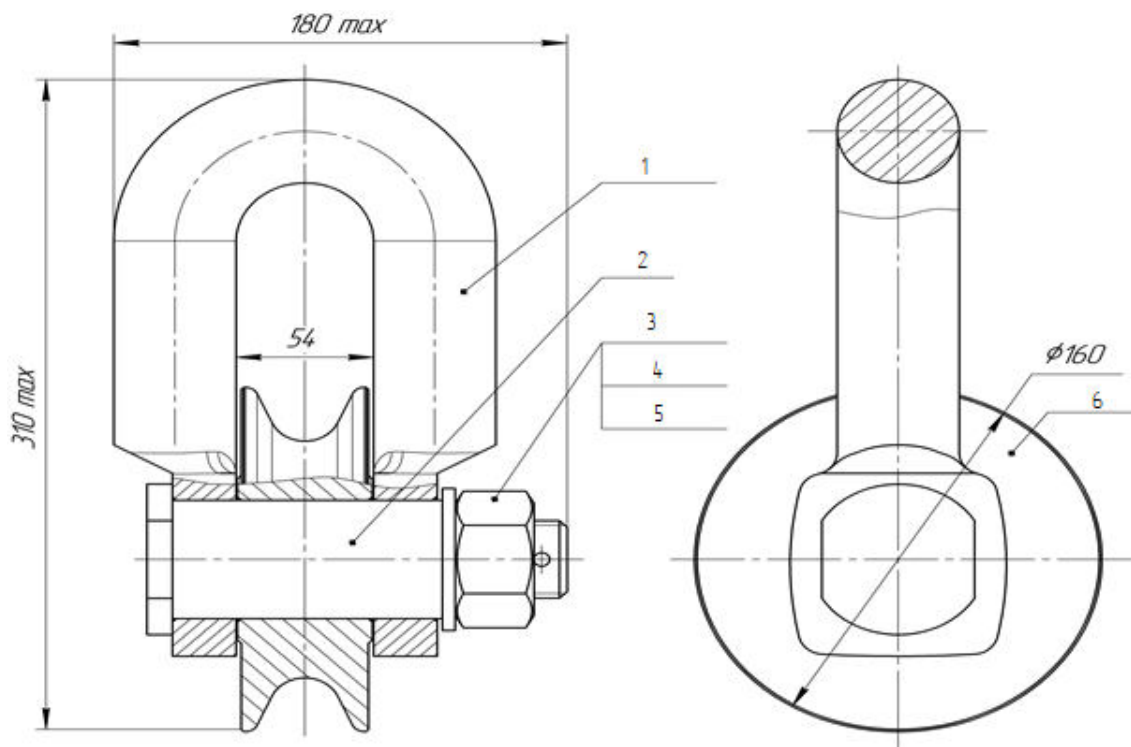
- 1) type of design - collapsible;
- 2) breaking load - not less than 320 kN;
- 3) weight - no more than 15 kg (maximum weight of the load lifted by the worker, permitted by safety requirements);
- 4) overall dimensions -  $160 \times 180 \times 310$  mm.

When monitoring the market of lifting devices, the required blocks were not identified. Most of the assembly blocks either exceed the declared dimensions and weight, or do not have the required load-bearing capacity.

The aim of the study is to develop a new reinforced design of the mounting block for assembly and dismantling works in coal mine long walls, ensuring the above requirements.

## 1. Research methodology

The main load-bearing elements of the assembly block structure are the "axle", "block" and "earring" parts (Figure 2).



1 – earring; 2 – axis; 3 – washer; 4 – nut; 5 – cotter pin; 6 – block

Fig. 2. – Scheme of the design of the reinforced mounting block

In accordance with the stated requirements, the design of the assembly block must have dimensions of  $160 \times 180 \times 310$  mm. The "axis" was previously made of 30KhGSA steel and to increase the lifting capacity it will be enough to calculate and change the working diameter upwards.

The design of the "block"  $\varnothing 160$  mm for ropes  $\varnothing 22.5 \dots 27$  mm did not change except for the diameter of the hole for the "axis". The design of the "earring" was selected for the required dimensions and the loads on the eyes were calculated using various grades of steel, since previously the "earring". At "Kurylysmet" LLC it was made of steel 20.

For comparison with steel 20, the most commonly used structural carbon high-quality and structural alloyed round steels were selected, namely: 35, 45, 30XGSA and 40C. The main criterion for optimizing the choice of material for the construction of the assembly block is the strength criterion. To assess the strength criterion of the structure, it is necessary to know the yield strength of the selected material. The yield strengths of the steel grades used are presented in Table 1.

Table 1. Yield strength of steel grades

Steel grade	Yield strength, MPa
20	250
35	320
45	360
30XGSA	850
40X	330

The safety factor of the structure is determined by the formula [12]:

$$n = \frac{\sigma_s}{\sigma_{max}}, \tag{1}$$

where  $\sigma_s$  – yield strength of material, MPa;

$\sigma_{max}$  – maximum stresses in the structure, MPa.

**2. Calculation of the geometrical dimensions of the mounting block structure**

To determine the diameter of the “axle” and “earring”, the formula for calculating the rod on shear was used [13]:

$$d = \sqrt{\frac{4 \times S}{\pi \times \tau_{sh} \times 0,3}}, \tag{2}$$

where d – axle diameter, mm;

S - нагрузка на срез, Н;

0,21 - allowable voltage coefficient;

$\tau_{sh}$  - allowable shear stress (yield strength of the rod material), MPa.

Substituting into the formula the values for steel 30XGSA and the required breaking load, the following result was obtained:

$$\sqrt{\frac{4 \times 320000}{3,14 \times 850 \times 0,21}} \approx 48 \text{ mm}$$

According to calculations, the diameter of the rod of the “axle” and “earring” was taken as 48 mm.

At the pin diameter of 48 mm, the weight of the structure is minimal.

For comparison, we made similar calculations with the previously mentioned steel grades (Figure 3).

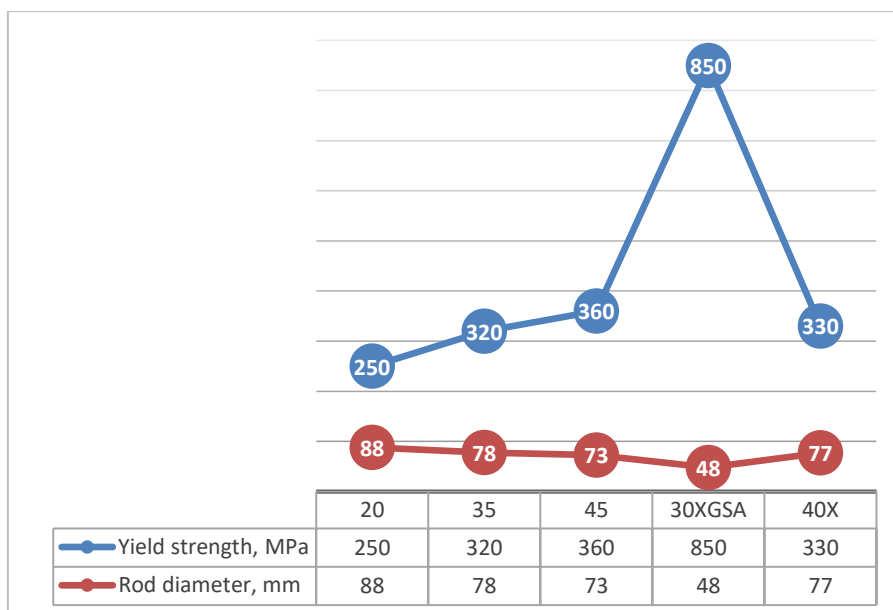


Fig. 3. - Diameter of the axis of the mounting block structure when using different steel grades

According to this table, we were convinced of the correctness of the choice of material - steel 30XGSA, which with the highest characteristics of yield strength provides the smallest diameter of the rod, necessary for the design of the structure in the given overall dimensions.

The following calculations were made for the “earring” lugs.

The permissible normal stress at break is determined by the formula [14]:

$$[\sigma_n] = \frac{\sigma_t}{n}, \quad (3)$$

where  $\sigma_t$  - tensile strength, MPa;

$n$  – safety factor.

Permissible normal stress at rupture by formula (3):

$$[\sigma_n] = \frac{1220}{3} = 406 \text{ MPa}$$

The permissible shear stress at shear is determined by the formula [15]:

$$[\tau_{ps}] = 0,6 \times [\sigma_n] = 0,6 \times 406 = 243 \text{ MPa} \quad (4)$$

The tangential stress in the vertical section at given parameters depends on the cross-sectional area of the eye  $S$  and is determined by the formula [16]:

$$\tau_{ts} = \frac{Q}{4 \times S} < [\tau_{ps}], \quad (5)$$

where  $Q$  - breaking load, N;

$S$  – cross-sectional area,  $\text{mm}^2$ .

Accordingly, the area of the eyelet must be no less than [17]:

$$S = \frac{Q}{4 \times \tau_{ps}} = \frac{320000}{4 \times 243} = 329 \text{ mm}^2 \quad (6)$$

The cross-sectional area of the eye is determined by the formula [18]:

$$S = \frac{D-d}{2} \times B, \quad (7)$$

where  $D = 85$  – eye outer diameter, mm;

$d = 49$  – diameter of the eyelet hole, mm;

$B = 25$  – eye thickness, mm.

Cross-sectional area of the eye by formula (7):

$$S = \frac{85 - 49}{2} \times 25 = 450 \text{ mm}^2$$

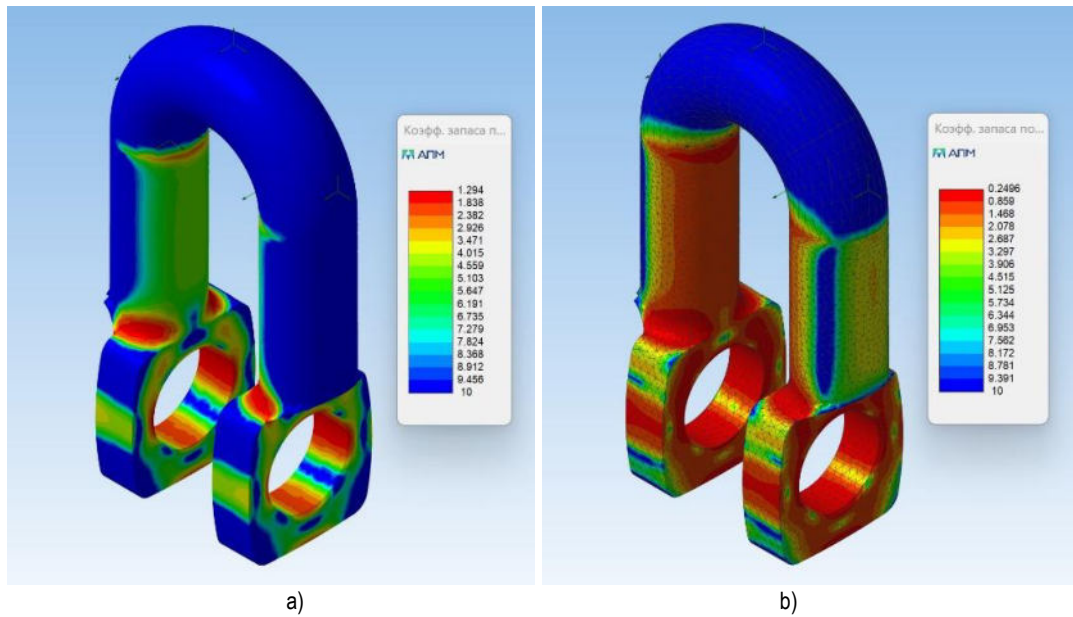
The total tangential stresses in the vertical section are equal to:

$$\tau_{ts} = \frac{Q}{4 \times S} = \frac{320000}{4 \times 450} = 178 \text{ MPa} < 243 \text{ MPa}$$

In the final version, the strength condition is fulfilled: the result of the calculation of the tangential stress in the vertical section of the “ear” lugs was lower than the permissible one, which corresponded to the stated requirements.

### 3. Engineering analysis of the mounting block design

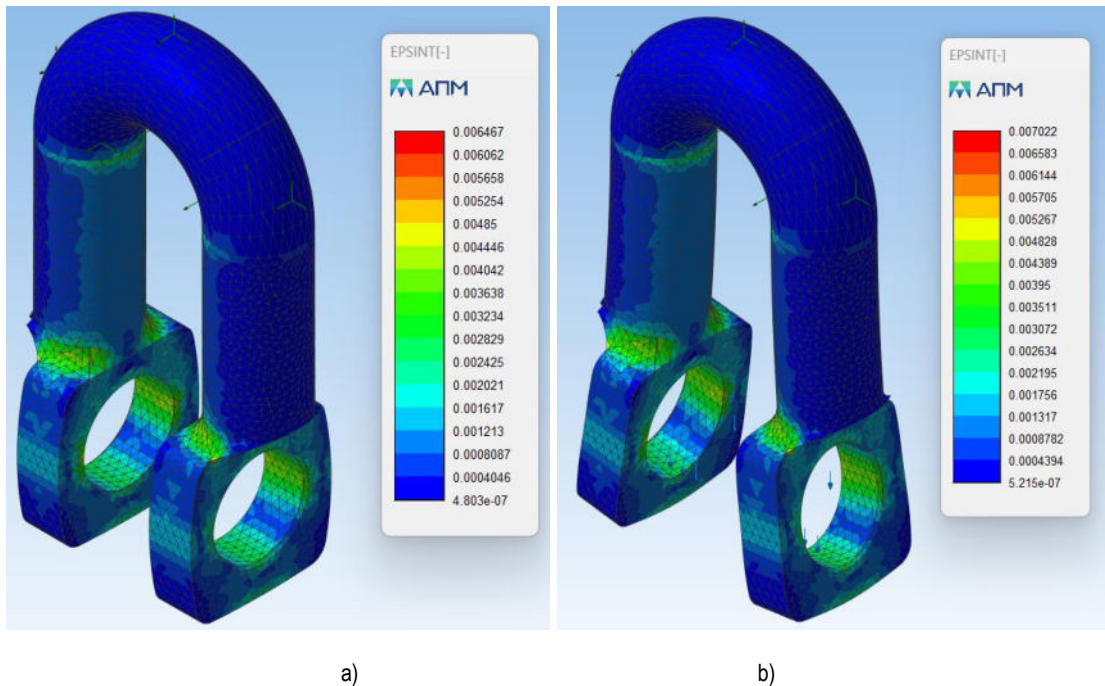
Verification of mathematical calculations of the part “bracket” was performed in the APM FEM program in the KOMPAS-3D system of ASKON LLC. The functional set of the program allowed to simulate a solid object and comprehensively analyze the behavior of the calculation model under various influences on it [19, 20]. The results of calculation of the applied loads on the lugs of the solid three-dimensional model at the fixed arc-shaped part were visually reflected in it. In addition, as a comparison for steel 30XGSA and steel 20, calculations for safety factor (Figure 4) and total deformations (Figure 5) were carried out.



a) steel 30XGSA; b) steel 20

Fig. 4. - Result of calculation of safety factor of the part “earring” in APM FEM application

The safety factor of the earring made of 30 XGSA steel ranges from 1.8 to 10 mm, the total deformation of the earring structure made of 20 steel ranges from 0.8 to 10. The most vulnerable parts of the earring are the inner diameter of the eyelet and the eyelet flanges.



a) steel 30XGSA; b) steel 20

Fig. 5. - Result of calculation of total deformations of the part “earring” in APM FEM application

The total deformations in the cross-section of the eyelet of the earring from steel 30 XGSA range from 0.004 to 4.8 mm, the total deformations of the earring structure from steel 20 - 0.005÷5.2.

All the results obtained by the program confirmed the mathematical calculations and on this basis it was decided to proceed to the manufacture of prototypes for experimental testing in laboratory conditions. This analysis allowed to avoid labor and material costs for manufacturing of physical experimental samples in case of undetected errors in calculations.

Based on the results of mathematical calculations and engineering analysis, a working set of drawings of the mounting block was developed for the manufacture of prototypes.

#### 4. Experimental studies

Two prototypes of mounting blocks were manufactured for the experimental breaking force test. The parts “earring” were made by free forging with subsequent machining, the other parts, except for standard products for axis fixation, were made on lathes. The parts “earring” and “axis” have undergone the necessary heat treatment. All parts individually and the complete assembly have been quality controlled. During the inspection, the main dimensions of the assemblies of the blocks planned for control measurements during the tests were documented, namely:

- diameter of the “axis”;
- diameter of the holes of the lugs of the “shackle”;
- width, height and thickness of the holes of the “earring”.

For the experiment was prepared universal machine with ultimate load of 100 tons type UMM-100 (hereinafter: breaking machine), which has a certificate of periodic verification. The part “block” was excluded from the test, as its strength was not questioned and separate calculations for it were not carried out. Instead of the “block” part, a fixture in the form of a rod with an eye and a threaded rod for fixing the block in the movable and fixed frames of the tensile machine was developed (Figure 6).

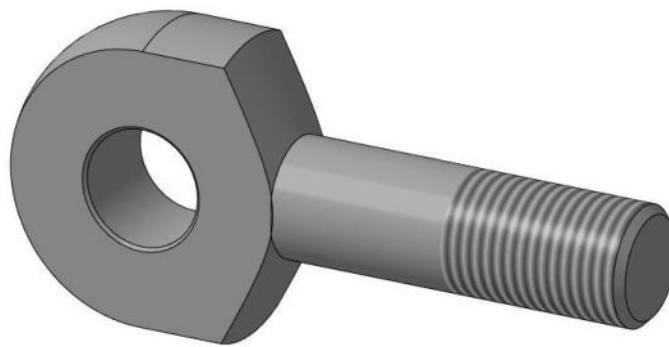


Fig. 6. - Fixture for installation of mounting blocks

It was decided to install two blocks simultaneously on the tensile machine; this allowed to save testing time and to exclude the development of an additional fixture for fixing the “earring” part in the frames of the tensile machine. For this purpose, firstly, the “earring” parts were provided with joint contact of the inner surfaces of the bending radii. Then the fixtures in the form of a rod were installed with lugs instead of parts “block” and fixed in “earrings” with “axes” and standard products, then the rods with threaded rods were installed and fixed in the frames of the rupture machine (Figure 7).

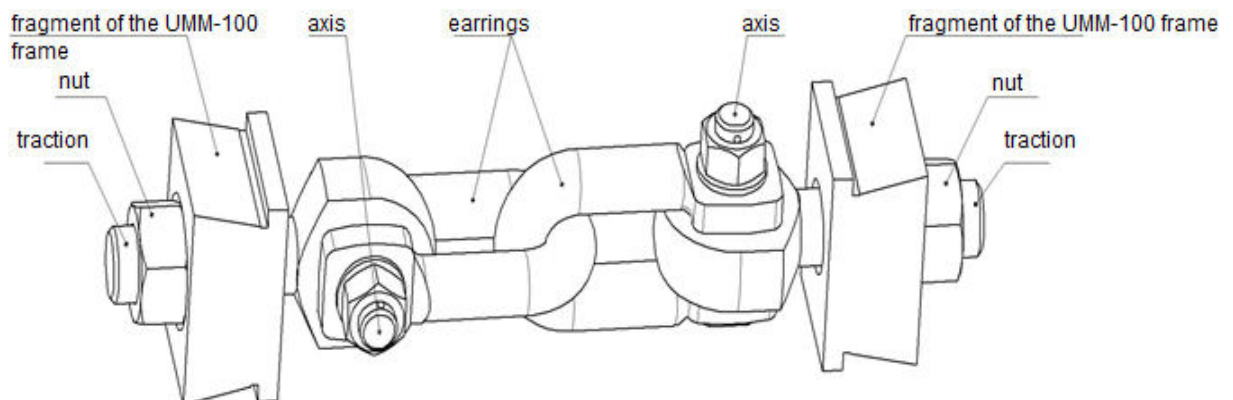


Fig. 7. - Project of mounting blocks installation on the UMM-100 machine

The tests were carried out in four stages with a gradual increase in load. After placing the prototype mounting blocks on the tensile machine (Figure 8), they were subjected to a load of 26000 kgf for 5 minutes. After that, the assembly blocks were dismantled from the tensile machine, visually inspected for deformations and disassembled into assemblies, over which a control measurement of the main dimensions was carried out.



Рис. 8. – Installed mounting blocks on the UMM-100 machine

The mounting blocks were then reinstalled and tested under loads of 32000 kgf, 40000 kgf and 48000 kgf. Each load was applied to the mounting blocks for 5 minutes. After each test, disassembly and measurements of the main dimensions were taken.

During the whole experiment, none of the dimensions of the mounting blocks were changed, which means that they were fully tested by the tensile testing machine and the experiment can be considered a success.

In the future, based on the conducted experiment, each newly manufactured mounting block before acceptance by the department of technical control of “Kurylysmet” LLP will be subjected to load testing in laboratory conditions on the breaking machine UMM-100 in 40000 kgf for 5 minutes with recording the test results in the product passport.

### Conclusions

The results of mathematical calculations, engineering analysis and experimental tests proved the performance of the design. As a result of the conducted researches the following was established:

- 1) Steel grade of the main parts, taking into account the loads acting on them - 30XGSA;
- 2) The diameter of the rod of the parts “axle” and “earring” - 48 mm;
- 3) The minimum permissible cross-section of the eye of the part “earring” - 329 mm<sup>2</sup>;
- 4) The developed design did not exceed the required weight limit of 15 kg;
- 5) The conducted experiment proved that actually the assembly block is able to withstand a short-term load of  $\approx 470$  kN.

This design is made in strict accordance with the stated requirements for the mines of Karaganda coal basin.

### References

- [1] Matsui K. Underground mining transportation systems: Chapter 2. Civil Engineering – Vol. II - Underground Mining Transportation Systems, 2020. – P.1 - 22
- [2] Krauze K., Mucha K., Wydro T., Kutnik A., Hałas W., Ruda P. Operational Tests of a Modular Installation and Transport Assembly of Steel Arch Support in Underground Excavations //MAPE 2021, volume 4, issue 1, pp. 343-354
- [3] Volkov P. V., Kulsaitov R.V., Magitov A. M. Technology for fixing mine workings with friction anchors of the SZA type with a new type of anticorrosive coating //IOP Conf. Series: Materials Science and Engineering, 966, 2020) 012017
- [4] Amosov A. G. Comparative analysis of materials of loading devices of machine building //Proceedings of the international conference on advances in materials, systems and technologies: (CAMSTech-II 2021), June 2022, AIP Conference Proceedings, 2467(1), 030033
- [5] Westover L.M., Jacek Olearczyk J., Hermann U., Adeeb S., Mohamed Ya. Analysis of rigging assembly for lifting heavy industrial modules //Canadian Journal of Civil Engineering, 41(6), 2014. – P. 131-140

- [6] Wieczorek, A.N.; Wójcicki, M.; Drwięga, A.; Tuszyński, W.; Nuckowski, P.M.; Nędzka, J. Abrasive Wear of Mining Chain Drums Made of Austempered Ductile Iron in Different Operating Modes //Materials, 2022, 15, 2709.
- [7] Hango S.I., Chown L.H., Merwel J.W., Kavishe F.P.L., Cornish L.A. Corrosion of Selected Hard Facing Materials Exposed to Mine Water //ISTJN 2014, 4:90-105.
- [8] Volodymyr B., Kovalevska I., Sheka I. A., Sachko R. Results of research on the stability of mine workings, fixed by arched supports made of composite materials, in the conditions of the Pokrovske Mine Administration //IOP Conference Series: Earth and Environmental Science, Vol. 1156, Iss: 1,2023, P. 012011-012018
- [9] Arpana Sawant A., N. Deshmukh N.N., Chauhan S., Dabhadkar M., Deore R. Design and analysis of lifting tool assemblies to lift different engine block //AIP Conference Proceedings, 1859(1), 2017, 020057
- [10] Wheatley T., Chong P.L., Habibi H., Djawad W. Automating the Optimal Selection Process of Subassembly Sections of a Modular Spreader Beam Used in Lifting Operations //Machines, Vol.10, Issue 9, 2022, Article 808. <https://doi.org/10.3390/machines10090808>
- [11] Demin V.F., Kamarov R.K. Developing the Technology and Bench Testing Methods of Supporting the Rock Massif //Material and Mechanical Engineering Technology, №3, 2023. – P. 23 - 33
- [12] Zharkevich, O.; Nikonova, T.; Gierz, Ł.; Berg, A.; Berg, A.; Zhunuspekov, D.; Warguła, Ł.; Łykowski, W.; Fryczyński, K. Parametric Optimization of a New Gear Pump Casing Based on Weight Using a Finite Element Method //Applied Science, 2023, 13, 12154
- [13] Ruchwa M. Fundamental formulae for the calculation of shear flexible rod structures and some applications In book: Research and Modelling in Civil Engineering. - Publisher: Koszalin University of Technology Publishing House, 2018. – 259 p.
- [14] Hance B. M. Huang L. A simplified stress-based forming limit criterion for advanced high strength steel (AHSS) //IOP Conf. Series: Materials Science and Engineering, 418, 2018, 012037
- [15] Mafaniso S. Mechanics of Materials I An Introduction to the Mechanics of Elastic and Plastic Deformation of Solids and Structural Materials, Third edition, Oxford. – 1997, 481 p.
- [16] Nurova O.S. Calculation of Rod Bolt Strength //American Journal of Engineering, Mechanics and Architecture, Volume 2, Issue 3, 2024, P.165-171
- [17] Vityunin M.A., Chikova O.A. Strength of materials: a tutorial. – Ekaterinburg: Ural. state ped. university, 2014. – 136 p.
- [18] Kravchenko G., Dmitry Durov D., Kravchenko K., Linkov N. Assessment of the load-loading capacity of bolted joints during bolt bending and the combination of materials used //BIO Web of Conferences 93, 04021, 2024. – P. 1 - 9
- [19] Raschet konstruktsiy metodom konechnykh elementov s ispol'zovaniyem prilozheniya APM FEM: uchebno-metod. posobiye / ZH.A. Starostina, R.V. Morozov. – M.: MADI, 2022. – 100 s.
- [20] APM FEM Sistema prochnostnogo analiza dlya KOMPAS-3D.Versiya dlya KOMPAS-3D v21. Rukovodstvo Pol'zovatelya. – Korolev: Nauchno-tekhnicheskiiy tsentr «APM», 2022. – 71 s.

**Information of the authors:**

**Zharkevich Olga Mikhailovna**, c.t.s., professor, Abylkas Saginov Karaganda Technical University  
e-mail: [zharkevich82@mail.ru](mailto:zharkevich82@mail.ru)

**Shlyakhov Sergey Vladimirovich**, master student, Abylkas Saginov Karaganda Technical University  
e-mail: [sergey.shlyakhov@yandex.kz](mailto:sergey.shlyakhov@yandex.kz)

**Nurzhanova Oxana Amangeldyevna**, PhD, acting associate professor, Abylkas Saginov Karaganda Technical University  
e-mail: [nurzhanova\\_o@mail.ru](mailto:nurzhanova_o@mail.ru)

**Imasheva Kulzhan Imashevna**, master, senior lecturer, Abylkas Saginov Karaganda Technical University  
e-mail: [imasheva-gulzhan@mail.ru](mailto:imasheva-gulzhan@mail.ru)

## Concrete Reinforced with Graphene and Graphene Oxide

Yurov V.M.<sup>1</sup>, Zhangozin K.N.<sup>1</sup>, Portnov V.S.<sup>2</sup>, Rakhimova G.M.<sup>2\*</sup>, Rakhimov A.M.<sup>2</sup>.

<sup>1</sup>"Vostok" LLP, Astana, Kazakhstan

<sup>2</sup>Abylkas Saginov Karaganda Technical University, Karaganda, Kazakhstan

\*corresponding author

**Abstract.** In this paper, we propose a model of concrete reinforced with graphene and graphene oxide. The thickness of the surface layer of the C–S–H gel is  $R(I) = 60.3 \text{ nm}$  ( $< 100 \text{ nm}$ ), i.e. it is a nanostructure according to Gleiter. The equation we obtained shows that the higher the adhesion energy  $W_a$ , the more difficult it is to destroy a solid. This means that concrete is easier to destroy by bending than by compression ( $W_{aa} > W_{ac}$ ). The  $R(II)$  layer, which we called the mesolayer, is stronger than the  $R(I)$  layer, since  $\gamma_2 = 3\gamma_1$ . It differs from the nanolayer and the bulk phase in that the size effects in it occur according to a different type. Here, size effects of the kinetic type are present, associated with temperature, the mean free path of elementary excitations, etc., but they do not exceed 1 micron. At  $h = R(I)$ , a second-order phase transition (according to Ehrenfest) occurs, the nature of which is described by us using the Landau mean field method. There are no size effects in the bulk phase (larger than 1 micron). It is shown that graphene and graphene oxide are introduced into the interlayer space. Graphene and GO, limited in the interlayer region of the C–S–H gel, demonstrate different morphology. In graphene, carbon atoms, ordered in the  $xy$  plane, are distributed far from the C–S–H surface. No expansion along the  $z$ -direction is observed. The C–C bonds in GO are stretched in the  $z$ -direction, and the graphene sheet is somewhat damaged. Compared to standard concrete, the  $R(I)$  and  $R(II)$  values decrease by half and the elastic parameters of concrete change. The article shows that the addition of graphene and graphene oxide to cement mortar significantly strengthens (by 4-5 times) standard concrete.

**Keywords:** concrete, graphene, nanolayer, mesolayer, size effect, strength

### Introduction

Reference [1] (see bibliography therein) presents graphene (G) reinforced concrete. It shows an extraordinary increase in compressive strength of up to 146%, flexural strength of up to 79.5% and a 78% reduction in maximum displacement due to compressive load. At the same time, improved electrical and thermal performance is found with an 88% increase in heat capacity. A significant reduction in water permeability of almost 400% compared to standard concrete, which is an extremely desirable property for the long-term durability of concrete structures, makes this new composite material ideal for construction in flood-prone areas. Finally, it is shown that the incorporation of G into modern concrete will result in a 50% reduction in the required concrete material, while still meeting building load specifications. This will result in a significant reduction in carbon emissions from cement production of 446 kg/tonne.

In the work [2] (see bibliography therein) graphene oxide (GO) reinforced concrete was presented. The current study showed that the inclusion of GO even with 0.02% by weight of cement increased the strength by 12-24% and durability properties. The inclusion of GO can accelerate the hydration process of cement as it provides nucleation sites for cement hydrates. But the workability was reduced by 4% due to the agglomeration of GO, causing the water molecule to remain trapped. The water permeability properties tend to decrease with increasing GO content. And the quality of concrete mixtures was improved as the microstructural analysis of the mixtures actually indicates that GO acts as a filler of the material, healing the microcracks at the nanoscale, helping to transport water to the unreacted cement particles.

A review of all previous studies on G and GO reinforced concrete was made in [3]. It was shown that there are four forms of graphene products, namely graphene (G), graphene oxide (GO), reduced graphene oxide (rGO) and graphene nanoplatelets (GNPs), as shown in Fig. 1. These forms of graphene products have been used in numerous studies including [1, 2]. Emphasis is placed on the problems associated with G, GO, rGO and GNP reinforced concrete. These problems are as follows: G, GO reduce the workability of concrete and the mechanisms for its reduction are unclear; there remains a problem of the quality of carbon nanostructures leading to the development of microcracks; the production of graphene with controlled quality at low cost on an industrial scale is a big challenge; the inability of graphene to achieve high dispersion can potentially have an adverse effect on the properties of concrete due to the formation of agglomerates and weak pockets; graphene oxide can be a hazardous material since it can cause an explosion under certain conditions.

## 1. Methods and Materials

### 1.1 Experimental methodology

This study utilized a combination of experimental and theoretical approaches to examine the structure and

properties of concrete reinforced with graphene and graphene oxide. The research aimed to assess how these nanomaterials influence the mechanical and microstructural characteristics of concrete. The methodology was divided into two main components: experimental investigations and theoretical modeling.

The experimental portion of the study involved the preparation of concrete samples with varying concentrations of graphene and graphene oxide. The mixing process followed standardized procedures to ensure homogeneous dispersion of the nanomaterials. To evaluate their impact, multiple tests were conducted:

Compression and flexural strength tests were performed using a hydraulic press to assess load-bearing capacity and durability. Atomic force microscopy (AFM) and scanning electron microscopy (SEM) were employed to observe the dispersion of graphene within the concrete matrix and its interaction with calcium silicate hydrate (C–S–H) gel. X-ray diffraction (XRD) and energy-dispersive spectroscopy (EDS) were utilized to study phase composition and elemental distribution, ensuring proper integration of graphene-based additives. A slump test was conducted to examine the effects of graphene on the fluidity and workability of fresh concrete mixtures.

Concrete sample preparation followed GOST 10180-2012 standards to ensure reliable and reproducible results.

## 1.2 Materials

The primary materials used in this study included:

- cement: Portland cement CEM I 42.5N, chosen for its high compressive strength and optimal hydration characteristics;
- graphene and Graphene Oxide: These nanomaterials were introduced in concentrations ranging from 0.02% to 0.15% by cement mass, carefully dispersed to prevent agglomeration;
- aggregates: Natural sand (0.1–4 mm particle size), gravel, and crushed stone were used as fillers;
- water: Distilled water was utilized to eliminate the influence of impurities on hydration reactions;
- chemical Additives: In selected trials, plasticizers and superplasticizers were added to optimize the rheology and workability of the concrete mixture.

Theoretical analysis was conducted using molecular dynamics simulations to investigate the interaction of graphene and graphene oxide with C–S–H gel at the nanoscale.

The combined experimental and theoretical approaches provided valuable insights into the reinforcing effect of graphene and graphene oxide on concrete. The integration of these nanomaterials was shown to enhance mechanical strength, reduce crack formation, and improve durability. The findings contribute to the ongoing development of advanced, high-performance concrete materials with superior structural properties.

## 2. Results and discussion

The above issues include production consistency, cost of graphene-based additives, dispersion of graphene in concrete, workability and flowability of graphene-based concrete, sustainability, and safety issues.

We also reported in [4] on improving the properties of graphene-added concrete obtained by liquid-phase exfoliation of graphite [5].

**The aim** of this paper is to propose a model of graphene and graphene oxide reinforced concrete.

### Nano-meso-macrostructure of concrete

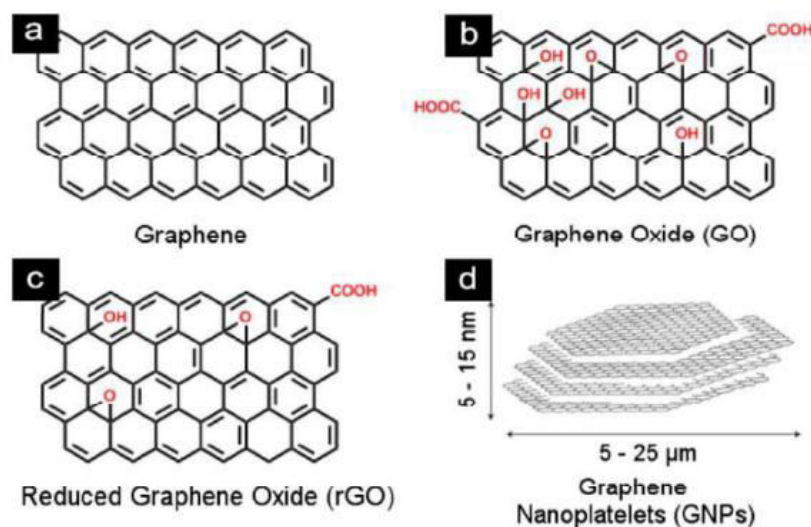
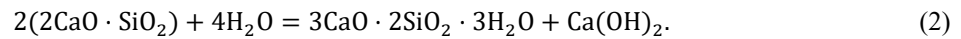
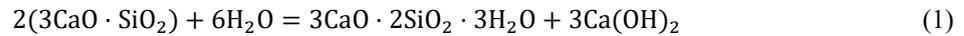


Fig. 1. - Illustration of (a) graphene (G), (b) graphene oxide (GO), (c) reduced graphene oxide (rGO), and (d) graphene nanoplatelets (GNPs) [3]

Concrete consists of cement paste, which is a porous and hierarchical material with different phases. When cement powder is mixed with water, a hydration reaction results in the formation of the main chemical products: calcium silicate hydrate (C–S–H), calcium hydroxide (CH), ettringite, and monosulfoaluminates. C–S–H accounts for approximately 70% of the fully hydrated products and is the main contributor to the mechanical strength of the material [6]. The silicate phases react with water to form calcium hydroxide and a rigid calcium silicate hydrate gel, the C–S–H gel [7]:



The thickness of the surface layer of a solid body R(I) is given by the formula [8]:

$$R(I) = 0,17 \cdot 10^{-9} \cdot \alpha \cdot \nu [m]. \quad (3)$$

In equation (3) it is necessary to know one parameter – the molar volume of the element, which is equal to  $\nu = M/\rho$  (M is the molar mass,  $\rho$  is its density),  $\alpha = 1 \text{ m}^{-2}$  is a constant to maintain the dimensionality (R(I) [m]). Considering that the rigid calcium silicate gel of the C–S–H hydrate is a homogeneous solid solution, it is easy to estimate the molar mass from equations (1) and (2) –  $M_1 = 1070 \text{ g/mol}$ ;  $M_2 = 922 \text{ g/mol}$ . The crystal structure obtained from equation (2) is closer to the mineral tobermorite [9], which is a layered crystalline form of calcium silicate. The density of the C–S–H gel is closely related to the water content in the pores of the gel. Neutron and X-ray scattering methods were used to determine with high accuracy [10] the density and water content in saturated globules. The density is  $2.604 \text{ g/cm}^3$ ,

The thickness of the surface layer of the C–S–H gel according to equation (3) is -  $R(I) = 60.3 \text{ nm}$ , and the number of layers is  $n = R(I)/a$  (a is the interlayer distance, equal to  $a = 1.4 \text{ nm}$  [7]). This means that the number of C–S–H layers is  $n = 43$ . According to our work [8], the diagram of the crystalline form of calcium silicate will look like that shown in Fig. 2a, and the silicate chain (monolayer of calcium silicate) is shown in Fig. 2b.

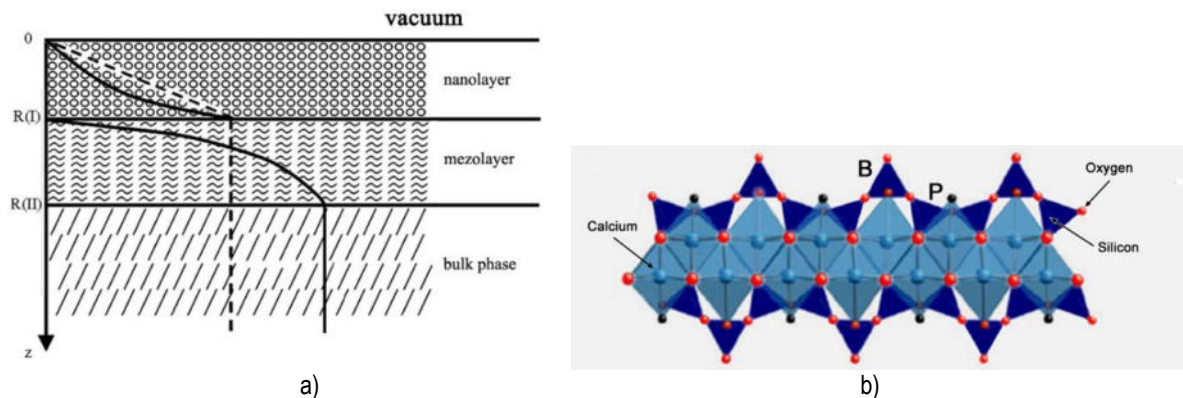


**Fig. 2.** - Schematic diagram of a solid: nanolayer → mezolayer → bulk phase (a); schematic diagram of a C–S–H layer showing a Ca–O core layer with a silicate tetrahedron attached on both sides. The silicate chain, calcium octahedron and oxygen atoms are shown as dark blue, light blue tetrahedron and red spheres, respectively (b) [7].

The thickness of the surface layer of the C–S–H gel is  $R(I) = 60.3 \text{ nm}$  ( $< 100 \text{ nm}$ ), i.e. it represents a nanostructure according to Gleiter [11]. The C–S–H gel in water forms crystalline nuclei with a critical radius [12]:

$$r_c = 2 M \gamma_{12} T_0 / \rho q \Delta T, \quad (4)$$

where M is the molar mass;  $\gamma_{12}$  is the surface tension at the boundary; T is the temperature;  $\rho$  is the density; q is the heat of fusion. Our estimate gives  $r_c = 5 \text{ nm}$ , which means that the R(I) layer contains  $n\Gamma = R(I)/r_c \approx 12$  globules. This situation is shown using atomic force microscopy (AFM) in Fig. 3.

Size effects in the R(I) layer are determined by a collective of atoms (collective processes). Such “semi-classical” size effects are observed only in nanostructures [13].

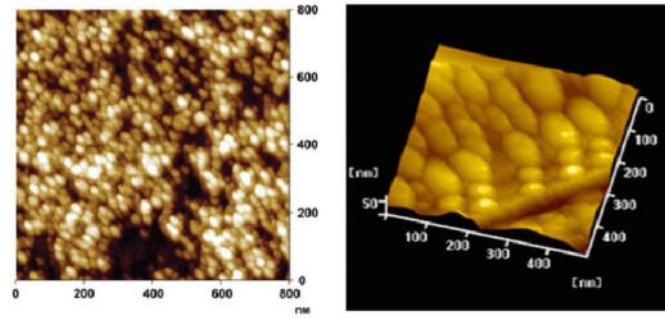


Fig. 3. - AFM photographs of C-S-H particles [7].

This means that the R(I) layer is a nanolayer (Fig. 2a). The surface energy of a bulk crystal  $\gamma_2$  is equal to [14]:

$$\gamma_2 = 0,7 \cdot 10^{-3} \cdot T_m [\text{J/m}^2], \quad (5)$$

where  $T_m$  is the melting temperature (K).

In the R(I) layer, the size effect must be taken into account and the surface energy becomes equal to  $\gamma_1$  [14]:

$$\gamma_1 = \gamma_2(1 - R(I)/R(I) + h) \approx 0,3\gamma_2. \quad (6)$$

Equation (6) shows that the surface energy of the R(I) layer is three times less than the surface energy of the main crystal. To separate the R(I) layer from the rest of the crystal, energy must be expended, which is called the adhesion energy [15]:

$$W_a = \gamma_1 + \gamma_2 - \gamma_{12} \approx \gamma_1 + \gamma_2 = 1,3\gamma_2, \quad (7)$$

where  $\gamma_{12}$  is the surface energy at the phase boundary, which is negligibly small due to the second-order phase transition.

The internal stresses  $\sigma_{is}$  between phases  $\gamma_1$  and  $\gamma_2$  can be calculated using the formula [16]:

$$\sigma_{is} = \sqrt{W_a \cdot E/R(I)}, \quad (8)$$

where  $E$  is the Young's modulus of elasticity. Using equations (5)–(8), we calculate the elastic parameters for standard concrete using a layered structure such as tobermorite or calcium silicate.

Table 1. Elastic parameters of standard concrete

Concrete	$W_{aa}$ , J/m <sup>2</sup>	$W_{ac}$ , J/m <sup>2</sup>	$\sigma_{isa}$ , MPa	$\sigma_{isc}$ , MPa	$E_a$ , GPa	$E_c$ , GPa
C-S-H ( $\rho = 2,604$ )	4,517	1,654	5589	1334	142	65

The melting point of calcium silicate is  $T_m = 1817$  K and  $\gamma_2 = 1272$  mJ/m<sup>2</sup>, Young's modulus  $E = 65$  GPa for C-S-H [7]. Significant elastic stresses in the R(I) layer lead to the creation of nanocracks, the length of which is  $L_{nm} = R(I)$  [14].

For the destruction of a solid, force, deformation and energy criteria of destruction were developed. There is the following relationship between them [17]:

$$\frac{K_{1c}^2(1-\mu^2)}{E} = 2\delta_{1c}\sigma_B = G_{1c} = J_{1c} = 2\gamma = W_a, \quad (9)$$

where  $K_{1c}$  is the critical stress intensity factor, the force criterion of destruction;  $E$  is the elastic modulus;  $\mu$  is Poisson's ratio;  $\delta_{1c}$  is the critical opening at the crack tip, the deformation criterion of destruction;  $\sigma_B$  is the ultimate strength;  $G_{1c}$  is the critical intensity of the released energy, the energy criterion of destruction;  $J_{1c}$  is the critical J-integral, the energy criterion of destruction;  $\gamma$  is the surface energy,  $W_a$  is the adhesion energy.

Equation (9) shows that the greater  $W_a$ , the more difficult it is to destroy a solid. This means that concrete is easier to destroy by bending than by compression ( $W_{aa} > W_{ac}$ ).

The R(II) layer, which we called the mesolayer (Fig. 2a), is stronger than the R(I) layer, since  $\gamma_2 = 3\gamma_1$ . It differs from the nanolayer and the bulk phase in that the size effects in it occur in a different way. Here, size effects of the kinetic type are present, related to temperature, the mean free path of elementary excitations, etc., but do not exceed

1 micron. At  $h = R(I)$ , a second-order phase transition occurs (according to Ehrenfest), the nature of which we described in [18] using the Landau mean field method. In the bulk phase (larger than 1 micron), there are no size effects.

**Concrete reinforced with graphene and graphene oxide.**

The structure of C–S–H obtained by molecular dynamics (MD) [7] with graphene (G) and graphene oxide (GO) is shown in Fig. 4a, b.

It can be seen from Fig. 4 that graphene and graphene oxide are embedded in the interlayer space. Graphene and GO confined in the interlayer region of C–S–H gel exhibit different morphologies.

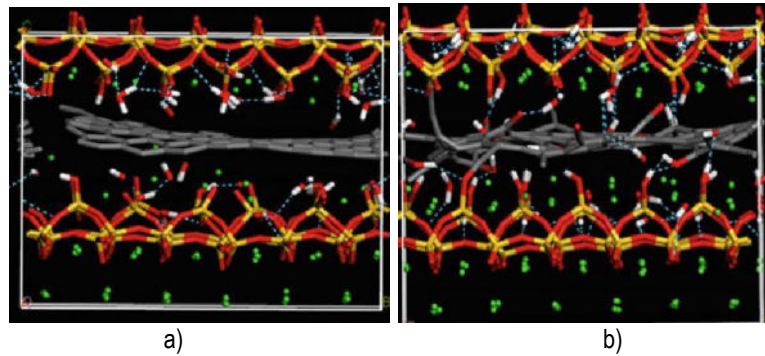


Fig. 4. - Structure of G/C–S–H and GO/ C–S–H [7].

In graphene, the carbon atoms, which are ordered in the xy plane, are distributed away from the C–S–H surface. No expansion along the z-direction is observed at the graphene/C–S–H interface in Fig. 4a. On the other hand, as shown in Fig. 4b, the protruding hydroxyls on both sides of GO indicate the C–S–H interface. The C–C bonds in GO are stretched in the z-direction, and the graphene sheet is somewhat disrupted. Compared with standard concrete, the  $R(I)$  and  $R(II)$  values are halved and the elastic parameters of concrete change. These changes are shown in Table 2. Concrete consists of components in the following weight proportions: water 10%, cement 20%, fillers (sand, gravel, crushed stone) 70%. The concentration of graphene during the formation of the concrete mixture drops by 3 times, i.e., in an aqueous solution, the concentration of graphene will be 0.15%. For  $1\text{m}^3$  of concrete (= 2 tons) we get 300 g of graphene.

Table 2. Elastic parameters of concrete with graphene and graphene oxide.

Concrete	$W_{aa}, \text{J/m}^2$	$W_{ac}, \text{J/m}^2$	$\sigma_{isa}, \text{MPa}$	$\sigma_{isc}, \text{MPa}$	$E_a, \text{GPa}$	$E_c, \text{GPa}$
graphene	17,243	6,314	25000	6250	1100	525
graphene oxide	14,629	5,418	10392	2598	430	197

Comparison of Tables 1 and 2, as well as equation (9), we conclude that the addition of graphene and graphene oxide to cement mortar significantly strengthens (by 4-5 times) standard concrete. In Table 2,  $T_m = 4510 \text{ K}$  is chosen for the melting temperature of graphene [19].

Due to the compositional, structural and physical complexity of the C–S–H gel, the main building blocks of cement hydrate have not yet been fully understood [7].

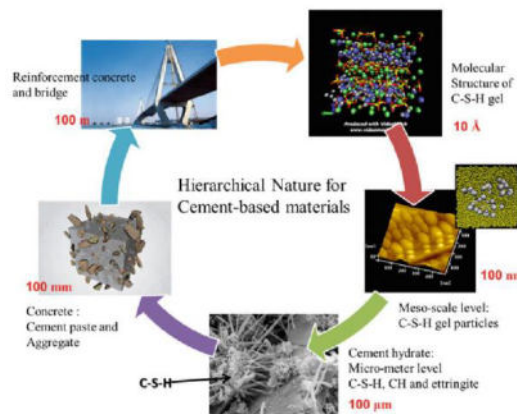


Fig. 5.- Hierarchical structure of concrete [7]

As shown in Fig. 5, at the macroscale ( $>10^{-3}$  m), concrete can be regarded as a material consisting mainly of two phases: aggregate and cement matrix. At the microscale ( $10^{-3} - 10^{-6}$  m), different hydration products and different C–S–H gel morphologies form a heterogeneous structure of cement paste. At the mesoscale, less than 1  $\mu\text{m}$ , the C–S–H gel can be observed as elliptical-shaped particles packed with different densities. At the nanoscale ( $<10^{-9}$  m), the distribution and arrangement of Ca, Si, OH form the basic C–S–H structure. Concrete, the most widely used building material, has been applied to pavements, architectural structures, foundations, highways, roads, overpasses, parking structures, brick, block walls, and foundations for gates, fences, and pillars. And its use is not comparable with other materials [20].

### Conclusion

One of the pressing issues in the mining industry of Kazakhstan is the processing of technogenic mineral formations (TMF). Currently, more than 60 billion tons of TMF have been accumulated in Kazakhstan [21]. At the same time, the total annual level of TMF processing is about 11% of the annual output, while in developed industrial countries the level of industrial waste use reaches 70–80% [22]. In our opinion, TMF processing should be carried out by creating modified concrete from TMF with an admixture of graphene or graphene oxide, the most widely used building material.

### Acknowledgments

This scientific article was published as part of the grant funding for 2024–2026 IRN No. AR32488258 "Development of an innovative technology for obtaining graphene by intercalating graphite with microcluster water and modifying HTSC ceramics with graphene" (the study is funded by the Science Committee of the Ministry of Science and Higher Education of the Republic of Kazakhstan).

### References

- [1] Dimov D., Amit I., Gorrie O., Barnes M.D., Townsend N.J., Neves A.I.S., Withers F., Russo S. and Craciun M.F. Ultrahigh Performance Nanoengineered Graphene-Concrete Composites for Multifunctional Applications // *J. Advanced Functional Materials*, 2018, V. 28, № 23. - P. 1705183. h DOI: <http://hdl.handle.net/10871/32568>
- [2] Devi S.Ch., Khan R.A. Mechanical and durability performance of concrete incorporating graphene oxide // *Journal of Materials and Engineering structures*, 2019, Vol. 6. – P. 201–214.
- [3] Fayyad T.M., Abdalqader A.F., Sonebi M. An insight into graphene as an additive for the use in concrete // *Civil Engineering Research in Irtland*, 2022. – P. 67-72.
- [4] Zhangozin K.N. *Methodus nova graphene producendi cum aqua microcluster intercalata.* – Almaty : Darkhan, 2023. – 102 p.
- [5] Zhangozin K.N., Zhanabergenov T.K., Kargin D.B. Circa novam methodum producendi pulveris graphene // *Nomenclator ENU dictus est. L. Gumileva*, 2021, tomi CXXXVI, N. III. - P. 8-16. DOI: <https://doi.org/10.32523/2616-6836-2021-136-3-8-16>
- [6] Richardson I.G. The calcium silicate hydrates // *Cement and Concrete Research*, 2008, Vol. 38(2). – P. 137–158. doi:10.1016/j.cemconres.2007.11.005
- [7] Hou D. *Molecular Simulation on Cement-Based Materials. From Theory to Application.* - Science Press and Springer Nature Singapore Pte Ltd. 2020. – 197 p. <https://doi.org/10.1007/978-981-13-8711-1>
- [8] Yurov V.M., Portnov V.S., Maussymbayeva, A.D. Thickness of the surface layer as-class hydrocarbons// *Aspectibus physico-chemicis investigandi racemis, nanostructuris et nanomaterialibus.* — 2022. — Soboles. 14. - pp. 331-341. DOI: 10.26456/pcascnn/2022.14.331.
- [9] Hamid S. The crystal structure of the 11 A natural tobermorite  $\text{Ca}_2.25\text{Si}_3\text{O}_7.5(\text{OH})1.5\cdot\text{H}_2\text{O}$  // *Zeitschrift für Kristallographie*, 1981, Vol. 154. - P. 189–198 DOI:10.1524/zkri.1981.154.14.189.
- [10] Allen A.J., Thomas J.J. and Jennings H.M. Composition and density of nanoscale calcium silicate hydrate in cement // *Nature Material*, 2007, Vol. 6. – P. 311–316. DOI:10.1038/nmat1871
- [11] Gleiter H. Nanostructured materials: basic concepts and microstructure // *Acta mater.*, 2000, V. 48. - P. 1-29. DOI:10.1016/S1359-6454(99)00285-2
- [12] Volmer M. *Kinetics formationis novi periodi.* - M.: Nauka, 1986. - 208 p.
- [13] Uvarov N.F., Boldyrev V.V. Magnitudo effectus in chymiae systemata heterogeneorum // *Uspekhi khimii*, 2001, T. 70 (4). - pp. 307-329. (In Russian). DOI: <https://doi.org/10.1070/RC2001v070n04ABEH000638>
- [14] Yurov V.M., Goncharenko V.I., Oleshko V.S. Studium primarium nanocracks in atomicis metallis levibus // *Physica Technical Epistolae.* - 2023. - Volumen 49. - Quaestio. 8. - pp. 35-38. DOI: 10.21883/PJTF.2023.08.55136.19504
- [15] Yurov V., Zhangozin K. Surface layer thickness, defects and strength of graphite // *The scientific heritage*, 2023, No 128. – P. 20-27. DOI:10.53939/1560-5655\_2024\_1\_19
- [16] Yurov V., Zhangozin K. About the mechanism of graphite splitting // *International independent scientific journal*, 2024, №58. – P. 29-40. DOI:10.53939/1560-5655\_2024\_1\_19

- [17] Erasov V.S., Oreshko E.I. Rationes dependentiae notarum mechanicarum rimae resistentiae materialis in magnitudine materiae Aviation specimen // Aviation materials and technologies, 2018, n. 3(52). - P. 56-64. DOI: 10.18577/2071-9140-2018-0-3-56-64
- [18] Yurov V.M., Guchenko S.A., Laurinas V.Ch., Zavatskaya O.N. Structural phase transition in a surface layer of metals // Bulletin of KarSU, 2019, – №1. – С. 50-60. DOI:10.31489/2019PH1/50-60
- [19] Los J.H., Zakharchenko K.V., Katsnelson M.I. and Fasolino A. Melting temperature of graphene // Phys. Rev., 2015, B91, 045415. DOI: <https://doi.org/10.1103/PhysRevB.91.045415>
- [20] Rakhimova G., Slavcheva G., Aisanova M., Rakhimov M., Tkach E. The influence of a complex additive on the strength characteristics of concrete for road construction // International Journal of GEOMATE. – 2023. 25 (110), pp.243-250. DOI: <https://doi.org/10.21660/2023.110.3934>
- [21] Mashkin N.A., Esirkepova A.B., Sherov K.T., Rakhimova G.M., Zharkevich O.M., Mussayev M.M. Activation of Cement Binder in Heavy Concrete Technology //Material and Mechanical Engineering Technology, 2020 (3), 9–12.
- [22] Fakhrullin R. F., Tursunbayeva A., Portnov V. S., L'vov Yu. M. Ceramic Nanotubes for Polymer Composites with Stable Anticorrosion Properties // Crystallography Reports, 2014 (7) Vol. 59, 1107–1113. DOI: <https://doi.org/10.1134/S1063774514070104>

#### Information of the authors

**Yurov Viktor Mikhailovich**, Candidate of Physical and Mathematical Sciences, Associate Professor, leading construction manager of LLP “Vostok”  
e-mail: [exciton@list.ru](mailto:exciton@list.ru)

**Zhangozin Kanat Nakoshevich**, Director, Leading Researcher of TSK-Vostok LLP, Candidate of Physical and Mathematical Sciences, Associate Professor, e-mail: [4kzh@mail.ru](mailto:4kzh@mail.ru),

**Portnov Vassily Sergeevich**, Doctor of Technical Sciences, Professor, Abylkas Saginov Karaganda Technical University  
e-mail: [vs.portnov@mail.ru](mailto:vs.portnov@mail.ru)

**Rakhimova Galiya Mukhamedievna**, Candidate of Technical Sciences, Associate Professor of the Department of Construction Materials and Technologies of the Abylkas Saginov Karaganda Technical University  
e-mail: [g.rakhimova@kstu.kz](mailto:g.rakhimova@kstu.kz)

**Rakhimov Askhat Muratovich**, PhD, senior lecturer of the Department of Construction Materials and Technologies of the Abylkas Saginov Karaganda Technical University  
e-mail: [rakhimov.askhat@gmail.com](mailto:rakhimov.askhat@gmail.com)

## Effect of Binder Composition on Briquettes from Dust-Like Ball Bearing Steel ShKh15

<sup>1</sup>Kulikov V.Yu., <sup>1</sup>Baiseitova Y.A., <sup>1</sup>Kovaleva T.V., <sup>1</sup>Tulegenova Sh.N.\*, <sup>1</sup>Kurypko S.A., <sup>2</sup>Kovalev P.V.

<sup>1</sup>Abylkas Saginov Karaganda Technical University, Karaganda, Kazakhstan

<sup>2</sup>Peter the Great St. Petersburg Polytechnic University

\*corresponding author

**Abstract.** In the work, it was studied how the composition of the binder affects the characteristics of briquettes from ball bearing waste, steel. The goal is to find an efficient way of recycling metal waste, in order to reduce the damage to nature and better use resources.

The briquettes were pressed in the laboratory, choosing optimal conditions. The influence of different binders on the strength of briquettes, important for metal melting and recovery was investigated. It was found that the binder composition greatly affects the strength, gas permeability and heat resistance of briquettes, which determines the recycling efficiency.

This work is important for the creation of new technologies for metal recycling, improvement of product quality and increase of profitability of steel processing.

The study will help to optimize the choice of binders, reducing costs and improving the performance of the briquettes. More durable and resilient briquettes will extend the life of metal smelting and recovery equipment. In the future, the results can be used to introduce technology in enterprises that will increase recycling opportunities and reduce waste. Developments can be widely applied in metallurgy.

**Keywords:** industrial waste, briquettes, chips, metal chips, components, drying, complex compositions.

### Introduction

Increased competition, increasing environmental requirements, as well as the complexity of extraction and pre-preparation of raw materials - these and other factors impose higher demands on the country's metallurgical industry. Therefore, the improvement of traditional and development of new technologies is a necessary condition for sustainable development of metallurgy. New intensive technologies and processes not only place high demands on the quality of raw materials, but also demand new types of them. With the increasing shortage of low-carbon coking coals and the intensification of processes, complex ore-fuel materials will become increasingly important, and pre-partial recovery processes will be applied more widely in raw material preparation. Traditional methods of raw material canning by agglomeration and crushing have largely exhausted their reserves and capabilities. Thus, at the current technical level it is difficult to obtain a metallized agglomerate or solid pellets with high free carbon content. At the same time, such materials are obtained by briquetting.

At present, waste is generated in the processing of castings made from ShKh15 ball bearing steel. Pulverized wastes from milling and drilling lose their productive and material value as opposed to bulk products, and are usually waste. The recycling of industrial wastes generated by mechanical processing is becoming increasingly important. One of the tasks at such enterprises of the Karaganda region as a KMZ Parchomenko, LLC «Maker» is the production of briquettes from scrap of bearing steel ShKh15. For the briquettes, one of the main indicators of quality is durability. In turn, one of the important factors ensuring strength performance, along with technological regimes of pressing and sintering, is the choice of optimal binder. Liquid glass is commonly used as a binder, however, there are a number of experiments to investigate the use of various components as a binder.

For example, the paper [1-3] presents studies on the technological properties of briquettes with peat, bentonite and marshall as binders.

The use of hot pressing when liquid glass is used as a binder is also addressed in work [3-5].

It is known that briquetting is a technological process of interaction of different solid components and is based on the property of loose material to be compacted and strengthened under the influence of applied pressure. In this case, the resulting adhesion forces between the close particles ensure the formation of a briquette. Therefore, the formation of a briquette is the result of compaction and hardening of loose material under the influence of pressing. The main technological parameters of the briquette as a component of metal scrap are: strength, bulk mass, content of harmful impurities [6-7].

In the work [8-10], it is proposed to use sludge from steelworks as a binder additive. This increases briquetting performance and reduces the cost of briquette production.

The key points related to the control of particle formation, particle crushing, cleaning and briquetting are discussed in this paper [11-13].

In the proposed study used a mixture of the following composition: S15 steel waste - 85%, liquid glass - 5%, bentonite clay - 10%. Briquette manufacturing regimes: drying temperature - 90 °C for 90 minutes, pressing pressure 50-70 kN.

## 1. Materials and Methods

The object of research was used pulverized chips, arising from machining parts of steel ShKh15 in the plant of KMZ IT. Parchomenko» (Karaganda). Chemical composition of steel chips ShKh15 is given in table 1.

After machining of steel parts from ShKh15 steel on the grinding machines, chips are formed. This chip is sent to the retention system and then to the engineering networks for disposal through pipelines. In the engineering network, the chip undergoes a filtration process, after which it is collected into special containers and transported to the retention area for storage. In order to obtain high-quality bars, samples of chips are taken from the storage areas for briquetting and subsequent processing of fusing modes. The chemical analysis carried out on the spectrometer revealed an increased content of carbon and sulphur in the powder of the chip compared to the original steel ShKh15. This is due to the contamination of the chip with the residual coolant used in the grinding process [14, 15].

**Table 1.** Chemical composition of powder chips ShKh15

Element	C	Cr	Si	Mn	Ni	S	P	Fe
Content	1,01	1,52	0,24	0,25	0,12	0,01	0,02	96,83

Retsch analytical sieving machine was used to analyze the fraction composition of the swarf sludge, which showed that the bulk of the particles (70%) refers to the fraction 0-0.6 mkm. The fraction 0.7-3.0  $\mu\text{m}$  constituted 25% of all particles. The particle content  $>1$  mm was less than 5%. The bentonite clay analysis showed that the bulk of the particles is 0-0.7  $\mu\text{m}$ , the fraction 0.7-1.0  $\mu\text{m}$  was 20% of all the particles.

To determine the feasibility of manufacturing briquettes from Table 1 - Chemical Composition of Powder Chips steel chip processing in industrial conditions, identical laboratory studies of briquettes with different binder composition were carried out. The criterion of conditioning of such briquettes was their strength and chemical composition of carbon and chromium.

The briquette components (Table 2) were mixed in laboratory roller-type runners. The compound of liquid glass and bentonite clay is proposed as a binder. Various ratios of these additives were investigated.

**Table 2.** Complex Briquette sample compositions

Component	Content of sample					
	№ 1	№ 2	№ 3	№ 4	№ 5	№ 6
Steel Chip S15	84,5	84,5	84,5	89,5	89,5	89,5
Water	0,5	0,5	0,5	0,5	0,5	0,5
Liquid glass	10	8	5	7	5	3
Bentonite clay	5	7	10	3	5	7

The pressing was carried out in a press (Figure 1) with a diameter of 20 mm, using a laboratory press at a pressure of up to 500 kN.



**Fig. 1.** - Punch and press prepared for briquette production

Briquettes sintering was carried out in the drying cabinet SNOL-67/350. In order to determine the optimal briquette drying regime, a briquette drying was carried out - 3 briquettes at each selected temperature in the Snol-67/350 oven, with the mass of the briquettes being determined every half hour to determine the amount of water evaporation. The most optimal briquette drying regime was found to be sample 4 (table 3), where at an initial temperature of 600C, the briquette is heated up to 60 minutes and dried out to 900C for 90 minutes.

**Table 3.** Selection of the optimal time and drying modes for briquettes

Sample briquettes	Drying time, min		Drying temperature, °C		Evaporation of water, g	
	primary	final	primary	final	primary	final
sample № 1	40	80	50	100	0,3	0,39
sample № 2	45	75	65	80	0,26	0,3
sample № 3	50	75	55	90	0,3	0,35
sample № 4	60	90	60	80	0,2	0,25
sample № 5	45	65	65	85	0,27	0,32
sample № 6	40	70	60	80	0,28	0,31

Briquette drying speed depends on the surface area as well as the briquette drying temperature. Also due to the evaporation of water during drying changes drying time. That is, the drying time is reduced at a higher temperature. We conclude that the optimum time for drying briquettes is 90 minutes and the drying temperature 80 °C (table 3). Because these modes show more optimal strength properties of the briquettes, which promote safe transportation and further loyal melting of the briquettes in induction furnaces.

**Fig. 2.** - Samples after drying

The briquettes were produced in two modes with the same temperature and different pressure (Table 4).

**Table 4.** Briquette modes

Type of binder	Mode	Temperature drying, °C	Duration drying, min	Pressure, kN
sample № 1	A	90	90	50
	B	90	90	60
	C	90	90	70
sample № 2	A	90	90	50
	B	90	90	60
	C	90	90	70
sample № 3	A	90	90	50
	B	90	90	60
	C	90	90	70
sample № 4	A	90	90	50
	B	90	90	60
	C	90	90	70
sample № 5	A	90	90	50
	B	90	90	60
	C	90	90	70
sample № 6	A	90	90	50
	B	90	90	60
	C	90	90	70

Strength was determined on the floor installation to determine the tensile strength of the Instron-100. The chemical composition was evaluated using an Olympus Vanta Element-S metal analyzer. The gas permeability of samples (Figure 3) was determined on a gas permeability measuring instrument type 04315M.



Fig. 3. - Samples of briquettes made from CH15 steel dust chips

## 2. Research results

The strength and gas permeability characteristics of the manufactured briquettes (Figure 2) are shown in table 5. The strength characteristics are affected by the oxide inclusions and the content of some blanks.

Table 5. Results of sample studies

Sample/mode	Characteristic			
	Compressive strength, MPa	Compressive strength, MPa	Content, %	
			C	Cr
№ 1 A	492	76	1,03	1,48
№ 1 B	504	74	1,04	1,47
№ 1 C	509	72	1,02	1,47
№ 2 A	514	78	1,01	1,46
№ 2 B	518	77	1,03	1,44
№ 2 C	521	74	1,00	1,45
№ 3 A	526	82	1,01	1,49
№ 3 B	537	80	1,02	1,47
№ 3 C	539	78	1,02	1,47
№ 4 A	517	73	1,00	1,51
№ 4 B	524	72	1,03	1,50
№ 4 C	526	71	0,99	1,50
№ 5 A	519	75	1,02	1,49
№ 5 B	526	71	1,00	1,48
№ 5 C	527	69	0,98	1,50
№ 6 A	524	75	1,01	1,50
№ 6 B	527	72	1,00	1,51
№ 6 C	529	70	1,01	1,52

Thus, it has been determined that the use of bentonite clay in a mixture together with liquid glass increases the strength of ShKh15 ball bearing steel briquette while maintaining the pressing and sintering modes. It is obvious that the partial use of bentonite clay in volume 10% with application of liquid glass in volume 5%. Probable mechanism of strengthening is wrapping (plating) the dispersed particles of clay dust and their good adhesion bond in liquid glass medium. The optimum total is a binder content of about 15%, but exceeding it is not advisable, as this results in a thicker binder layer between the particles which can be subject to brittle destruction as a result of loading. In addition, the increase of the binder content negatively affects the silicon content in the briquette. With

increasing content of liquid glass in the mixture, gas permeability of briquette is reduced. Also the increase of pressure leads to a decrease in gas penetration [16-17].

The content of chromium and carbon in the briquettes is comparable to that of ShKh15 steel casting, which means that the binder components used do not have a significant effect on the chemical composition of the briquette.

The optimum pressing pressure for briquettes with complex binder composition has been determined to be 60 kN. Further pressure increase is not advisable, because at increased energy costs, almost does not affect the strength of the briquette.

In the study of the microstructure of a briquette, we concluded that fine grain gives the best mechanical properties at output (Figure 4).

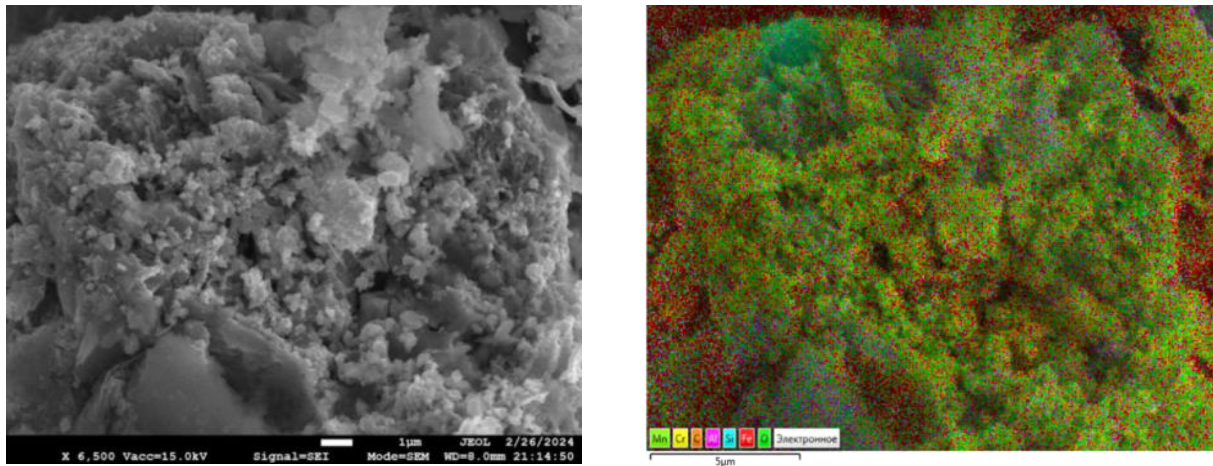


Fig. 4. - Microstructure of the briquette and multi-layer chemical element distribution map, 6500

Studies have shown that the distribution of chromium and carbon along the briquette volume is uniform.

Multicilo on the distribution map of chemical elements is obtained from the surface of the sample briquette. The distribution of carbon and chromium is uneven due to the briquette sintering processes, so they are more concentrated in the upper layers. The oxides are also less localized in certain areas of the briquette, which improves the strength and wear resistance of the briquettes.

## Conclusion

The metal dust chip as a component of the metal sheet for the introduction of the further smelting process requires prior preparation at the expense of low strength. As a result, cold briquetting with binder components was used to improve the process properties.

According to the results of experimental studies, it was determined that the most optimal composition of briquettes obtained is: ShKh15 steel slag - 85%, liquid glass - 5%, bentonite clay - 10%. Briquette manufacturing regimes: drying temperature - 90 °C for 90 minutes, Press pressure 60 kN.

It was determined that the chemical composition of the briquette corresponds to the chemical composition of the main material according to GOST 801-78 «Ball bearing steel».

This briquetting method allows to obtain briquettes with chromium and carbon content comparable to the content of the main product and to produce a technologically necessary strength of the briquette (about 540 MPa). Based on the studies carried out, it can be concluded that the production of high-quality briquettes from scrap ShKh15 steel metal chips is the initial stage on the way to the production of high-quality steel ingot.

The study gives the start to the rational recycling of chip waste and its reuse in production, which allows to actualize complex activities aimed at reducing material losses and including involving it in a new technological cycle, and also provides ways to reduce pollution.

## References

- [1] Kurunov I.F., Titov V.N., Bolshakova O.G. Analysis of the efficiency of alternative ways of recycling iron-bearing metallurgical wastes //Metallurgy, 2006, 11, 39-42.
- [2] Murray J.W., Jin X., Cleaver C.J. A review of principles and options for the re-use of machining chips by solid, semi-solid or melt-based processing // Journal of Materials Processing Technology, v, October 2024, 118514.
- [3] Cooper D.R., Song J., Gerard R. Metal recovery during melting of extruded machining chips //Journal of Cleaner Production, v, 1 November 2018, 282-292.
- [4] Valica O.M. Technological characteristics of metal shavings/ O.M. Valica, M.P. Selycka //Engineering and mechanical science/ The Herald of GSTU IM. P.O. DRY 1. - 2010.- C. 23-32.
- [5] Rietdorf Ch., Ziehn S., Giunta M., Mieke R., Sauer A. Environmental Assessment of Metal Chip Recycling – Quantification of Mechanical Processing's Global Warming Potential // Procedia CIRP, volume 122, 2024, 241-246.

- [6] Sidelnikov S., Zagirov N., Loginov Yu. and others. Investigation the structure and properties of deformed semi-finished products produced from chips of Al–Mg alloys system alloyed with scandium // International Journal of Lightweight Materials and Manufacture, 2023, volume 6, Issue 1, 46-58.
- [7] Diakonov O.M. Production of metallurgical briquettes based on particle-powder compositions by hot pressing. // Casting and metallurgy, 2011, 4, 129-137.
- [8] Zlotnikov E.G. Modern technologies of processing and briquetting of metal shavings in automated production // Notes of the Mining Institute SPB. - 2014. - P. 37-40.
- [9] Bizhanov A.M., Kurunov I.F., Durov N.M. et al. Research of the mechanical strength of the crack. Ch. 2 // Metallurg, 2012, 10, P. 36.
- [10] Maymur B.N. Petrenko V.I. Metallurgical raw material briquetting. Relevance and development of the method // Ferrous metallurgy, 2016, 3, P. 74-80.
- [11] Dalmia J. K., Kurunov I.F., Steel R.B., Bazhanov A. M. Production and application in the blast furnace of new generation briquettes // Metallurgy, 2012, 3, 39-41.
- [12] Babanin V.I., Yeregin A.Y. Briquetting of fine-grained materials in ferroalloy production: experience and opportunities // Metallurgy, 2006, 5, 45-49.
- [13] Ravich B.M. Briquetting in the color and iron metallurgy. - M.: Metallurgy, 2011. - 232 p.
- [14] Volokitina I.E., Volokitin A.V. Evolution of the Microstructure and Mechanical Properties of Copper during the Pressing–Drawing Process // Physics of Metals and Metallography, 2018, 119(9), 917–921.
- [15] Issagulov A.Z., Kim V.A., Kvon S.S., Kulikov V.Y., Tussupova A.U. Production of technical silicon and silicon carbide from rice-husk // Metalurgija, 2014, 53(4), 685-688.
- [16] Kovalev P.V., Popova, S.D., Issagulov A.Z., Kulikov V.Y., Kvon S.S. Investigation of the effect of high strength strips steel modification with rare-earth metal (REM) // Metalurgija, 2017, 56(3-4), 393–395.
- [17] Issagulov A.Z., Kvon S.S., Kulikov V.Y., Sakbossynova A.A. Cr - Ni system alloys composition impact on durability value // Metalurgija, 2014, 53(4), 621–623

#### Information of the authors

**Kulikov Vitaliy Yurievich, c.t.s.**, professor, Abylkas Saginov Karaganda Technical University, Republic of Kazakhstan

e-mail: [mlpikm@mail.ru](mailto:mlpikm@mail.ru)

**Baiseitova Yerkenaz Aglanovna**, doctoral student, Abylkas Saginov Karaganda Technical University

e-mail: [aglanovna@mail.ru](mailto:aglanovna@mail.ru)

**Kovalyova Tatyana Victorovna**, PhD, lecturer, Abylkas Saginov Karaganda Technical University

e-mail: [sagilit@mail.ru](mailto:sagilit@mail.ru)

**Tulegenova Sholpan Nygmetovna**, senior lecturer, Abylkas Saginov Karaganda Technical University

e-mail: [sholpan.tulegenova.65@mail.ru](mailto:sholpan.tulegenova.65@mail.ru)

**Kurypko Stanislav Aleksandrovich**, chief designer of KMZ Parkhomenko LLP, Abylkas Saginov Karaganda Technical University

e-mail: [stanislavkuriipko@mail.ru](mailto:stanislavkuriipko@mail.ru)

**Kovalev Pavel Valeryevich**, associate Professor, Peter the Great St. Petersburg Polytechnic University

e-mail: [kovalev\\_pv@spbstu.ru](mailto:kovalev_pv@spbstu.ru)

## Effect of Boron Additive on the Formation Ferrous Phases in Alloys Al - Fe - Si

Andreyachshenko V.A., Toleuova A.R.\*

Abylkas Saginov Karaganda Technical University, Karaganda, Kazakhstan

\*corresponding author

**Abstract.** The article presents an analysis of the diagram of the state of the Al – Fe – Si system using the Thermo-Calc program: polythermal sections were constructed and analyzed in order to determine the concentration limits of the appearance of primary crystals of Fe-containing phases, the mass fractions of phases at certain temperatures were calculated. A search was performed for optimal concentrations and temperatures at which the formation of a highly symmetric  $\text{Al}_8\text{Fe}_2\text{Si}$  phase capable of perceiving plastic deformation takes place. The Al-30Fe-9Si-1B system was also investigated. Based on the calculation of the parameters of the primary crystallization of iron in Al – Fe – Si alloys, the possibility of evaluating the effectiveness of modifying this alloy with boron is shown. The boron additive was considered as a modifier contributing to the grinding of aluminium grains and the formation of a wide area of existence of the  $\text{Al}_8\text{Fe}_2\text{Si}$  phase. The concentration and temperature ranges at which the maximum number of phases  $\text{Al}_8\text{Fe}_2\text{Si}$  and  $\text{AlB}_2$  can be achieved have been determined. The minimum amount of the  $\text{Al}_9\text{Fe}_2\text{Si}_2$  phase has been calculated, which is undesirable because it leads to a decrease in the mechanical properties of the alloy. From a practical point of view, the complex of proposed studies will allow to scientifically substantiate and develop new technologies for the production and processing of semi-finished products and finished products from aluminium-based alloys and functional materials with a given structure.

**Keywords:** aluminium, crystallization, boron, phase, polythermic section, modification.

### Introduction

Aluminum is one of the key export products of Kazakhstan. The country holds a leading position in Central Asia for its production. However, there are problems associated with this industry (high world market value, high energy costs) [1]. Nevertheless, the prospects for the development of the aluminum industry in Kazakhstan remain quite high. Kazakh companies are actively working to modernize their production facilities and introduce new technologies. This increases production efficiency and reduces energy costs [1].

In the conditions of saving material and energy resources, the issue of recycling aluminum alloys becomes especially relevant, which inevitably leads to an increase in the content of such poorly removed impurities as iron and silicon [2-5]. The increased content of the latter limits the possibility of obtaining such grades of aluminum alloys that are capable of deep drawing, and some operational properties are also reduced. At the same time, recycled aluminum alloys can be very effectively used as raw materials for the production of metal-ceramic materials based on aluminum with an increased content of both iron and silicon. Such metal-ceramic materials have high hardness values and can be used to manufacture products operating under high wear conditions. A distinctive feature of the alloy considered in this paper is the possibility of forming the  $\alpha$ -phase, which is characterized by high symmetry of the crystal lattice, which predicts its susceptibility to plastic deformation to a greater extent compared to the  $\beta$  and  $\theta$  phases, which have monoclinic crystal lattices [6-10].

Considering the increased content of alloying elements in the alloy, significantly exceeding the solubility limits in aluminum, it is quite labor-intensive to obtain such materials by traditional melting. For this purpose, the use of additive manufacturing methods can solve the problem of obtaining metal-ceramic materials.

Often, to ensure the formation of a favorable microstructure, small additives of modifiers are used in aluminum alloys, among which the most common are Ti, Zr, V, TiC,  $\text{TiB}_2$ , Na, Sr, Sb, Ba [11-15].

Boron is also a well-known modifier of aluminum alloys, which helps to grind the primary crystallizing phases in aluminum alloys, improving the quality of mechanical processing. Aluminum-matrix composite materials alloyed with boron have low specific density, strength, corrosion resistance, good thermal conductivity, and the ability to absorb thermal neutrons. At the same time, there is insufficient literary data showing the effect of boron on the phase composition of aluminum alloys rich in both iron and silicon, and they are mainly fragmentary.

One of the promising areas for producing high-quality aluminum alloys is the additive method of composite material synthesis. The aim of the work was a fundamental study of the Al-Fe-Si system. Search for optimal concentrations and temperatures at which a highly symmetric phase of  $\text{Al}_8\text{Fe}_2\text{Si}$  is formed, capable of receiving plastic deformation. Al-30Fe-9Si-1B was also investigated. The boron additive was seen as a modifier, contributing to the grinding of aluminum grains and the formation of a wide range of phase  $\text{Al}_8\text{Fe}_2\text{Si}$ . Aluminum alloys, in which boron is used as a modifier (up to 0.04% at melt temperature 690-710°C immediately before casting) and grain shredder are used in the electrical industry. Boron is also introduced to increase electrical conductivity and as a refining additive in aluminum alloys, which are used in the nuclear power industry in the amount of 0095 - 0.1% [16].

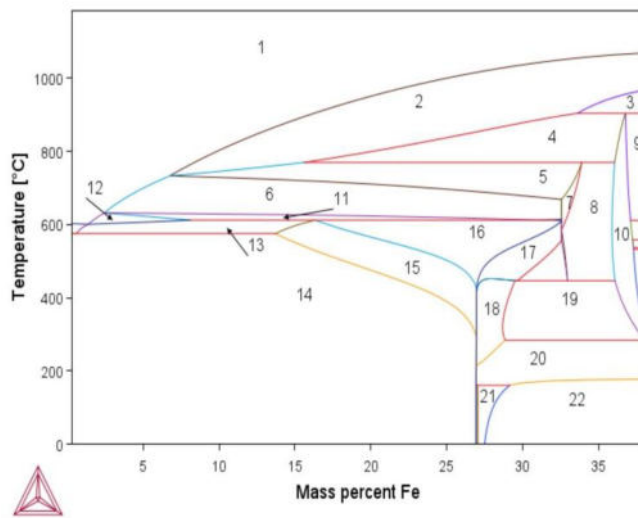
## 1. Research methodology

At the initial stage, the Al-Fe-Si system from the side of the iron corner was considered. This analysis was carried out using the modern computer program Thermo-Calc.

The Thermo-Calc computer product is a program for calculating phase equilibrium, the basic principle of operation: the algorithm of global minimization of Gibbs energy of multicomponent systems. It is also possible to calculate thermodynamic properties of phases (Gibbs energy, enthalpy, etc.), metastable equilibrium. The main characteristic of this program is its modularity, extensibility, replenishment of the databank of various elements for different systems (metal, salt, oxide, aqueous solutions, etc.). This program also allows the calculation of phase diagrams of multicomponent systems (construction of polythermic and isothermal sections, phase composition calculation, calculation of cooling curves), which was done in this work.

Using the Thermo-Calc program (version TCW8, database TTAL8.2) the aluminum-based system was analyzed to determine the concentration limits of the appearance of primary Fe-containing phase.

The Al-Fe-Si aluminum corner state diagram (Figure 1) is considered as an example. In equilibrium with (Al), in addition to the phases from double systems, there can be two triple connections:  $\text{Al}_8\text{Fe}_2\text{Si}$  ( $\alpha$ ) and  $\text{Al}_9\text{Fe}_2\text{Si}_2$  ( $\beta$ ). In this system there are three three-phase reactions involving (Al):  $(\text{Al}): \text{L} + \text{Al}_9\text{Fe}_2\text{Si}_2 \rightarrow \text{L} + \text{Al}_9\text{Fe}_2\text{Si}_2 + (\text{Al})$ ;  $\text{L} + \text{Al}_9\text{Fe}_2\text{Si}_2 + (\text{Al}) \rightarrow \text{Al}_8\text{Fe}_2\text{Si} + \text{Al}_9\text{Fe}_2\text{Si}_2 + (\text{Al})$ ;  $\text{Al}_9\text{Fe}_2\text{Si}_2 + (\text{Al}) \rightarrow \text{Al}_9\text{Fe}_2\text{Si}_2 + (\text{Si}) + (\text{Al})$ , three three-phase reactions involving liquid phase L and phase  $\theta$ :  $\text{L} + \theta + \tau_2 \rightarrow \text{L} + \theta + \text{Al}_8\text{Fe}_2\text{Si}$ ;  $\text{L} + \theta + \text{Al}_8\text{Fe}_2\text{Si} \rightarrow \text{L} + \text{Al}_8\text{Fe}_2\text{Si}$ ;  $\text{L} + \text{Al}_8\text{Fe}_2\text{Si} \rightarrow \text{L} + \text{Al}_8\text{Fe}_2\text{Si} + \text{Al}_9\text{Fe}_2\text{Si}_2$ , the formulations of each phase at a certain temperature are given in the table 1.



Region number	Phase region
1	L
2	L + $\theta$
3	L + $\theta$ + $\tau_{11}$
4	L + $\theta$ + $\tau_2$
5	L + $\theta$ + $\text{Al}_8\text{Fe}_2\text{Si}$
6	L + $\text{Al}_8\text{Fe}_2\text{Si}$
11	L + $\text{Al}_8\text{Fe}_2\text{Si}$ + $\text{Al}_9\text{Fe}_2\text{Si}_2$
12	L + $\text{Al}_9\text{Fe}_2\text{Si}_2$
13	L + $\text{Al}_9\text{Fe}_2\text{Si}_2$ + (Al)
16	$\text{Al}_8\text{Fe}_2\text{Si}$ + $\text{Al}_9\text{Fe}_2\text{Si}_2$ + (Al)
15	$\text{Al}_9\text{Fe}_2\text{Si}_2$ + (Al)
14	$\text{Al}_9\text{Fe}_2\text{Si}_2$ + (Si) + (Al)
17	$\text{Al}_8\text{Fe}_2\text{Si}$ + $\text{Al}_9\text{Fe}_2\text{Si}_2$
18	$\theta$ + $\text{Al}_9\text{Fe}_2\text{Si}_2$
7	$\theta$ + $\text{Al}_8\text{Fe}_2\text{Si}$
8	$\theta$ + $\text{Al}_8\text{Fe}_2\text{Si}$ + $\tau_2$
9	$\theta$ + $\tau_{11}$ + $\tau_2$
10	$\theta$ + $\tau_2$
19	$\theta$ + $\text{Al}_9\text{Fe}_2\text{Si}_2$ + $\tau_2$
20	$\theta$ + $\text{Al}_9\text{Fe}_2\text{Si}_2$ + (Si)
21	$\theta$ + $\text{Al}_9\text{Fe}_2\text{Si}_2$ + $\tau_8$
22	$\theta$ + $\text{Al}_9\text{Fe}_2\text{Si}_2$

Fig. 1. – Polythermic section of the system Al - 32Fe - 9Si on the side of the iron corner

Primary crystals  $\theta$  - phase, tend to grow along the orientation [010], forming coarse needles, scales and plate shapes in Al-Fe hypereutectic alloys, which seriously impairs the mechanical properties of alloys [17], [18].

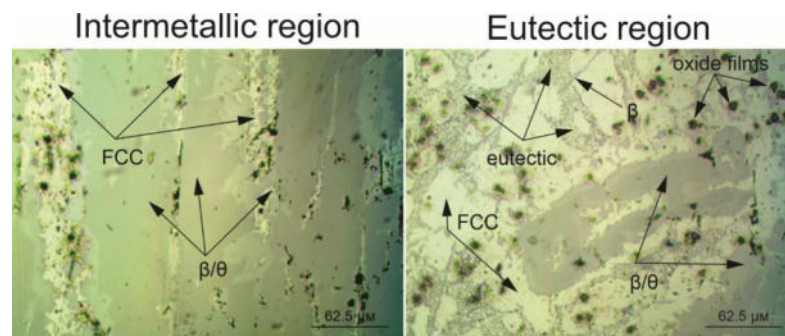
The  $\text{Al}_8\text{Fe}_2\text{Si}$  phase has a rather narrow crystallization interval and is suppressed by  $\text{Al}_9\text{Fe}_2\text{Si}_2$  phase formation, which is a very undesirable process, as the presence of  $\text{Al}_9\text{Fe}_2\text{Si}_2$  phase in the structure causes deterioration of the mechanical properties of the material [19], [20].

**Table 1.** Phase composition of the system Al-32Fe-9Si

Phase	% mass	Content of the components, %		
		Al	Fe	Si
t = 1072 °C (1 region)				
L	100	81,20	9,75	9,00
t = 925 °C (2 region)				
L	84,5	69,71	19,52	10,63
θ	15,5	59,51	39,60	0,82
t = 928 °C (3 region)				
L	31,27	53,21	29,33	17,38
θ	28,63	58,77	39,71	1,51
τ <sub>11</sub>	40,09	51,11	40,69	8,18
t = 831 °C (4 region)				
L	24,93	71,37	14,99	13,63
θ	40,25	59,17	39,39	1,42
τ <sub>2</sub>	34,80	51,05	33,89	15,05
t = 730 °C (5 region)				
L	8,88	84,45	6,63	8,90
θ	12,79	59,60	39,21	1,17
Al <sub>8</sub> Fe <sub>2</sub> Si	78,23	57,11	32,55	10,33
t = 671 °C (6 region)				
L	70,61	87,71	3,75	8,53
Al <sub>8</sub> Fe <sub>2</sub> Si	29,38	57,50	32,55	9,94
t = 665 °C (7 region)				
θ	6,08	59,64	39,15	1,19
Al <sub>8</sub> Fe <sub>2</sub> Si	93,91	57,91	32,56	9,52
t = 648 °C (8 region)				
θ	23,96	59,34	39,16	1,49
Al <sub>8</sub> Fe <sub>2</sub> Si	43,25	57,67	32,55	9,76
τ <sub>2</sub>	32,77	52,44	33,91	13,64
t = 828 °C (9 region)				
θ	41,76	58,53	39,57	1,89
τ <sub>11</sub>	16,63	51,11	40,69	8,18
τ <sub>2</sub>	41,60	49,44	33,87	16,68
t = 571 °C (10 region)				
θ	51,97	58,00	39,23	2,75
τ <sub>2</sub>	48,02	50,16	33,88	15,94
t = 618 °C (11 region)				
L	61,99	90,20	1,97	7,81
Al <sub>8</sub> Fe <sub>2</sub> Si	28,91	58,07	32,56	9,36
Al <sub>9</sub> Fe <sub>2</sub> Si <sub>2</sub>	9,08	58,28	26,90	14,81

Phase	% mass	Content of the components, %		
		Al	Fe	Si
t = 624 °C (12 region)				
L	97,37	89,03	2,16	8,79
Al <sub>9</sub> Fe <sub>2</sub> Si <sub>2</sub>	2,62	57,64	26,89	15,45
t = 589 °C (13 region)				
L	25,09	88,17	1,12	10,7
Al <sub>9</sub> Fe <sub>2</sub> Si <sub>2</sub>	34,68	57,46	26,89	15,64
(Al)	40,22	98,76	0,00	1,22
t = 379 °C (14 region)				
Al <sub>9</sub> Fe <sub>2</sub> Si <sub>2</sub>	52,15	63,49	26,95	9,54
(Si)	3,74	0,00	0,00	100
(Al)	44,10	99,79	0,00	0,20
t = 491 °C (15 region)				
Al <sub>9</sub> Fe <sub>2</sub> Si <sub>2</sub>	81,11	62,32	26,94	10,73
(Al)	18,88	99,68	0,00	0,31
t = 550 °C (16 region)				
Al <sub>8</sub> Fe <sub>2</sub> Si	30,58	60,35	32,59	7,05
Al <sub>9</sub> Fe <sub>2</sub> Si <sub>2</sub>	59,49	61,78	26,94	11,27
(Al)	9,91	99,67	0,31	0,00
t = 494 °C (17 region)				
Al <sub>8</sub> Fe <sub>2</sub> Si	49,72	60,32	32,59	7,08
Al <sub>9</sub> Fe <sub>2</sub> Si <sub>2</sub>	50,27	62,09	26,94	10,96
t = 362 °C (18 region)				
θ	6,38	57,98	38,99	3,02
Al <sub>9</sub> Fe <sub>2</sub> Si <sub>2</sub>	93,61	63,60	26,96	9,43
t = 367 °C (19 region)				
θ	33,68	56,72	38,96	4,31
Al <sub>9</sub> Fe <sub>2</sub> Si <sub>2</sub>	46,53	63,16	26,95	9,88
τ <sub>2</sub>	19,78	50,88	33,89	12,55
t = 229 °C (20 region)				
θ	30,66	53,03	38,82	8,14
Al <sub>9</sub> Fe <sub>2</sub> Si <sub>2</sub>	69,01	64,00	26,96	9,03
(Si)	0,31	0,00	0,00	100
t = 120 °C (21 region)				
θ	6,70	51,64	38,75	9,59
Al <sub>9</sub> Fe <sub>2</sub> Si <sub>2</sub>	93,18	64,11	26,96	8,92
τ <sub>8</sub>	0,11	20,10	50,26	29,62
t = 93 °C (22 region)				
θ	49,58	52,15	38,77	9,07
Al <sub>9</sub> Fe <sub>2</sub> Si <sub>2</sub>	50,41	64,11	26,96	8,92

To evaluate the morphology of the obtained phases, an alloy of the Al-Fe-Si system with a basic composition was synthesized. The technological conditions of the synthesis are presented in detail in [21, 22]. For metallographic analysis, microsections were prepared using a standard technique, using cutting, grinding, and polishing operations. The microstructure was studied immediately after synthesis, without additional processing in the "as prepared" state. The synthesized ingot has two main regions: the intermetallic region, which occupies the bulk of the material, and the eutectic region (Figure 2).

**Fig. 2.** – Microstructure of the alloy system Al-Fe-Si

Metallographic analysis shows that the structure of the material predominantly contains a combination of  $\beta/\theta$  phases, with the growth of the  $\beta$  phase occurring on the primary crystals of the  $\theta$  phase, which is in good agreement with the results of computer modeling for region 22 (Figure 1). At the same time, thin sections of the FCC solid solution of silicon and iron in aluminum were detected, formed as products of decomposition and phase transformation as a result of nonequilibrium cooling conditions during synthesis. The obtained results demonstrate the validity of using this approach to modeling for the purpose of predicting the phase composition of the alloy during its modification.

In this connection, the effect of boron on the formation and formation of the  $\text{Al}_8\text{Fe}_2\text{Si}$  phase was further considered. As an example, a diagram of the state of Al-Fe-Si-B (Figure 3) was constructed.

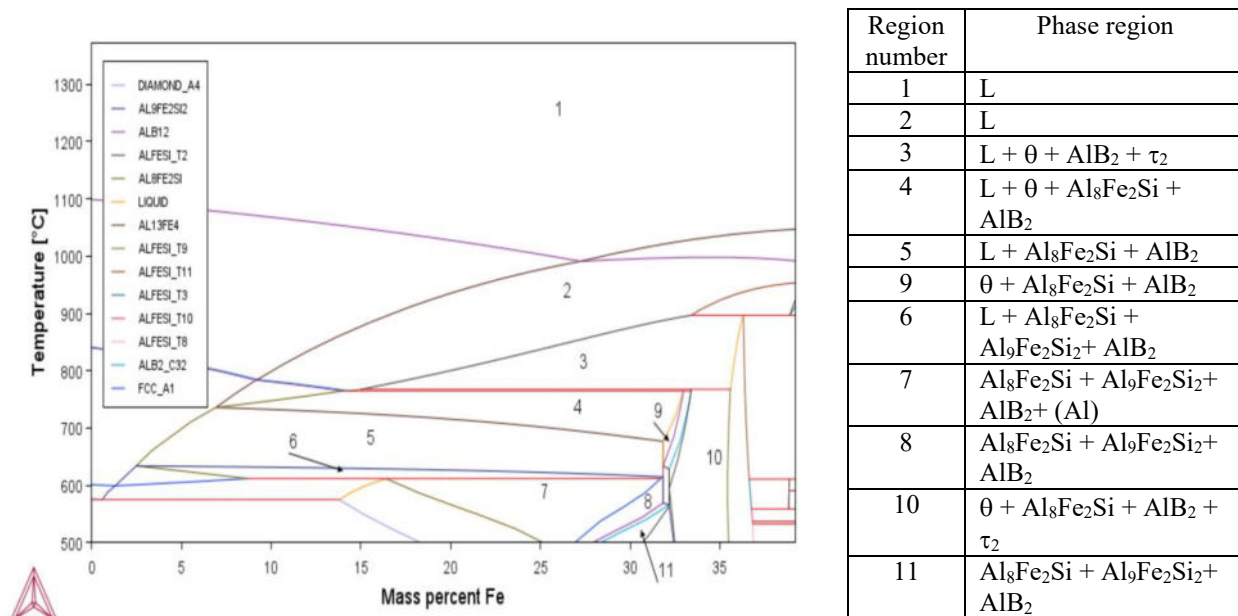


Fig. 3. – Polythermic section of the system Al-30Fe-9Si-1B

In this system, with the participation of the  $\theta$  phase, there are four three-phase reactions with the formation of  $\text{Al}_8\text{Fe}_2\text{Si}$  and  $\text{AlB}_2$ :  $\text{L} + \theta + \text{AlB}_2 + \tau_2 \rightarrow \text{L} + \theta + \text{Al}_8\text{Fe}_2\text{Si} + \text{AlB}_2$ ;  $\text{L} + \theta + \text{Al}_8\text{Fe}_2\text{Si} + \text{AlB}_2 \rightarrow \text{L} + \text{Al}_8\text{Fe}_2\text{Si} + \text{AlB}_2$ ;  $\text{L} + \text{Al}_8\text{Fe}_2\text{Si} + \text{AlB}_2 \rightarrow \theta + \text{Al}_8\text{Fe}_2\text{Si} + \text{AlB}_2$ . There is one four-phase reaction involving (Al):  $\text{L} + \text{Al}_8\text{Fe}_2\text{Si} + \text{Al}_9\text{Fe}_2\text{Si}_2 + \text{AlB}_2 \rightarrow \text{Al}_8\text{Fe}_2\text{Si} + \text{Al}_9\text{Fe}_2\text{Si}_2 + \text{AlB}_2 + (\text{Al})$ . The  $\text{Al}_8\text{Fe}_2\text{Si}$  phase has three three-phase reactions:  $\text{Al}_8\text{Fe}_2\text{Si} + \text{Al}_9\text{Fe}_2\text{Si}_2 + \text{AlB}_2 \rightarrow \theta + \text{Al}_8\text{Fe}_2\text{Si} + \text{AlB}_2 + \tau_2$ ;  $\theta + \text{Al}_8\text{Fe}_2\text{Si} + \text{AlB}_2 + \tau_2 \rightarrow \text{Al}_8\text{Fe}_2\text{Si} + \text{Al}_9\text{Fe}_2\text{Si}_2 + \text{AlB}_2$ . The formulations of each phase at a certain temperature are given in table 2. As seen from the reactions, the separation of phase  $\text{Al}_8\text{Fe}_2\text{Si}$  and  $\text{AlB}_2$  goes through the entire temperature range.

Table 2. Phase composition of the system Al-30Fe-9Si-1B

Phase	% mass	Content of the components, %			
		Al	Fe	Si	B
t = 1236 °C (1 region)					
L	100	64,21	25,78	9,00	1,00
t = 1236 °C (2 region)					
L	100	64,21	25,78	9,00	1,00
t = 818 °C (3 region)					
L	44,65	72,57	14,10	13,12	1,89
$\theta$	33,80	59,21	39,37	14,1	0,00
$\text{AlB}_2$	2,85	17,21	0,00	0,00	82,78
$\tau_2$	18,68	51,20	33,9	14,89	0,00
t = 730 °C (4 region)					
L	23,54	84,25	6,73	8,93	0,07
$\theta$	8,13	59,6	39,21	1,18	0,00
$\text{Al}_8\text{Fe}_2\text{Si}$	64,09	57,1	32,55	10,34	0,00
$\text{AlB}_2$	4,22	55,51	0,00	0,00	4,48
t = 685 °C (5 region)					

Phase	% mass	Content of the components, %			
		Al	Fe	Si	B
t = 568 °C (7 region)					
$\text{Al}_8\text{Fe}_2\text{Si}$	30,53	59,72	32,58	7,69	0,00
$\text{Al}_9\text{Fe}_2\text{Si}_2$	51,75	60,97	26,93	12,08	0,00
$\text{AlB}_2$	4,24	55,51	0,00	0,00	44,48
(Al)	13,46	99,56	0,01	0,41	0,00
t = 568 °C (8 region)					
$\text{Al}_8\text{Fe}_2\text{Si}$	79,22	58,98	32,57	8,44	0,00
$\text{Al}_9\text{Fe}_2\text{Si}_2$	16,38	60,04	26,92	13,02	0,00
$\text{AlB}_2$	4,39	55,51	0,00	0,00	44,48
t = 677 °C (9 region)					
$\theta$	4,64	59,66	39,16	1,17	0,00
$\text{Al}_8\text{Fe}_2\text{Si}$	90,92	57,8	32,55	9,63	0,00
$\text{AlB}_2$	4,42	55,51	0,00	0,00	44,48
t = 628 °C (10 region)					
$\theta$	22,45	59,31	39,15	1,54	0,00

L	61,31	86,94	4,37	8,63	0,04
Al <sub>8</sub> Fe <sub>2</sub> Si	34,76	57,39	32,55	10,05	0,00
AlB <sub>2</sub>	3,91	55,51	0,00	0,00	44,48
t = 625 °C (6 region)					
L	60,90	89,26	2,23	8,47	0,02
Al <sub>8</sub> Fe <sub>2</sub> Si	31,08	57,80	32,55	9,63	0,00
Al <sub>9</sub> Fe <sub>2</sub> Si <sub>2</sub>	4,06	57,79	26,89	15,31	0,00
AlB <sub>2</sub>	3,93	55,51	0,00	0,00	44,48

Al <sub>8</sub> Fe <sub>2</sub> Si	38,90	57,9	32,56	9,53	0,00
AlB <sub>12</sub>	3,23	17,21	0,00	0,00	82,78
τ <sub>2</sub>	35,40	52,49	33,91	13,58	0,00
t = 520 °C (11 region)					
Al <sub>8</sub> Fe <sub>2</sub> Si	68,86	59,46	32,58	7,95	0,00
Al <sub>9</sub> Fe <sub>2</sub> Si <sub>2</sub>	27,97	61,02	26,93	12,04	0,00
AlB <sub>12</sub>	3,16	17,21	0,00	0,00	82,78

## 2. Results and Discussing

One of the main criteria for producing alloys based on aluminium is the process of modification (grinding of grains of cast aluminium with the introduction of special additives). The process of grinding aluminum grain at crystallization is the result of special interaction of transition metals with aluminium [23], [24]. The ideal modifier is a particle that satisfies the following requirements: it should be effectively crushed grain at a minimum concentration; in the melt is thermally stable and dispersed; it has a minimum structural difference with the lattice of the modifying alloy; do not lose their modifying properties when melting. None of the modifiers currently known have a complete set of these properties [16], [25], [26]. One such modifier in aluminum alloys is boron, which is a transition metal. It has good refining effect on Al-Si alloys [27], [28].

Analyzing the polythermic section of the system Al - 32Fe - 9Si on the side of the iron angle sections, we can conclude that the phase of interest to us Al<sub>8</sub>Fe<sub>2</sub>Si has a fairly wide crystallization interval at a temperature from 730 C to 490 °C, but its formation is suppressed by the formation of phase Al<sub>9</sub>Fe<sub>2</sub>Si<sub>2</sub>. For example, at 494 °C (table 2, 17 region), the phase region consists of Al<sub>8</sub>Fe<sub>2</sub>Si (49.72%) and Al<sub>9</sub>Fe<sub>2</sub>Si<sub>2</sub> (50.27%). However, with the drop in temperature, a phase transition is underway with the disappearance of the Al<sub>8</sub>Fe<sub>2</sub>Si phase, which is completely transitioned to the Al<sub>9</sub>Fe<sub>2</sub>Si<sub>2</sub> phase.

The Al<sub>9</sub>Fe<sub>2</sub>Si<sub>2</sub> phase is known to be the most harmful, reducing the mechanical properties of aluminum alloys. In particular, the plate or needle phase of Al<sub>9</sub>Fe<sub>2</sub>Si<sub>2</sub> not only cleaves the matrix, but also contributes to the formation of casting defects such as pores and shrink pores. These phases easily cause stress concentration and crack propagation, thus becoming the weakest sites in the alloys Al-Si [29], [30], [31]. Therefore, a section of the system Al-30Fe-9Si-1B was built and the main optimal phase compositions were determined.

Boron is an effective grain shredder in Al-Si alloys, but the mechanism responsible for the effect of boron on the formation and growth of phases rich in iron is still under discussion [31]. The mechanism of primary grinding of boron grains in the Al matrix in the alloy is based on the formation of particles AlB<sub>2</sub> as a result of eutectic reaction (table 3, region 3). And the formation of this phase has a fairly wide temperature crystallization interval (818 - 520 °C). It can also be concluded that this phase contributes to the formation of the Al<sub>8</sub>Fe<sub>2</sub>Si phase with a fairly good phase composition (min 31.08%, max 90.92%). Phase AlB<sub>2</sub> is crystallized by eutectic reaction at 818 C (table 4, area 3). Since the AlB<sub>2</sub> and Al<sub>8</sub>Fe<sub>2</sub>Si phases have different crystallographic lattices, it can be assumed that the AlB<sub>2</sub> phase is the catalyst for the onset of phase Al<sub>8</sub>Fe<sub>2</sub>Si [32], [33], [34].

## Conclusions

Quantitative analysis of the phase diagram Al - Fe - Si as the basis of the high-strength alloy was carried out using the program Thermo-Calc (version TCW8, database TTAL8.2). The standard alloy Al - 32Fe - 9Si was considered, built a polythermic section, calculated the temperature of phase transformations. The phase composition obtained during modeling was compared with the real phase composition, and the microstructure of the alloy was studied. Optimum concentrations of iron and silicon were determined for Al<sub>8</sub>Fe<sub>2</sub>Si phase crystallization. The mass fractions of each phase are calculated at certain temperatures.

A polythermic cut Al-30Fe-9Si-1B was also calculated. The concentration and temperature regions at which the maximum number of Al<sub>8</sub>Fe<sub>2</sub>Si and AlB<sub>2</sub> phases can be achieved have been determined. The minimum number of phase Al<sub>9</sub>Fe<sub>2</sub>Si<sub>2</sub> is calculated, which is undesirable because it leads to a decrease in the mechanical properties of the alloy.

The data presented in this article are the initial stage in carrying out research on the development of technology for the synthesis of composite ceramic materials of the Al<sub>x</sub>Fe<sub>y</sub>Si system using an additive method to improve the quality of the structure of materials based on them. In the future, a complete thermodynamic analysis will be carried out to select the optimal concentrations of alloying elements in order to develop a rational mode of heat treatment of the alloy under study.

In the future, using the above described thermodynamic calculations to identify and modify phases rich in iron in Al-Fe-Si alloys, it is planned to experiment with the addition of boron by the method of additive synthesis.

**Acknowledgement.** The work was done with the support of the Ministry of Science and Higher Education of the Republic of Kazakhstan (Grant AP19675471)

## References

- [1] Kazakhstan guide in the country. <https://kazakhstangid.ru/ao-alyuminiy-kazahstana>, 2024
- [2] Zhou B, Liu B, Zhang S, Lin R, Jiang Y, Lan X. Microstructure evolution of recycled 7075 aluminum alloy and its mechanical and corrosion properties. *Journal of Alloys and Compounds*, 2021; 879. – p. 160407. <https://doi.org/10.1016/j.jallcom.2021.160407>
- [3] Sun Y. The use of aluminum alloys in structures: Review and outlook // *Structures*. 2023. 57. – p. 105290. <https://doi.org/10.1016/j.istruc.2023.105290>
- [4] Yu Y, Zhang X, Wang C, Hu J, Zhou D, Yang C, Zhang D. The influence of deformation-dependent prior chip boundary on microstructure and tensile properties in a solid-state recycled AA6063 aluminum alloy. *Journal of Materials Processing Technology*, 2025, 336 – p. 118693. <https://doi.org/10.1016/j.jmatprotec.2024.118693>
- [5] Krolo J, Špada V, Bilušić M, Čatipović N. Welding of Solid-State-Recycled Aluminum Alloy: Comparative Analysis of the Mechanical and Microstructural Properties. *Applied Sciences*, 2025, 15(3) – p. 1222. <https://doi.org/10.3390/app15031222>
- [6] Andreyachshenko V, Toleuova A. On the influence of iron and silicon content on the phase composition of the Al-Fe-Si system. *Kompleksnoe Ispolzovanie Mineralnogo Syra= Complex use of mineral resources*, 2025, 332(1), pp. 98-107. <https://doi.org/10.31643/2025/6445.09>
- [7] Andreyachshenko V, Naizabekov A. The technology of equal channel angle backpressure extrusion for deformation iron and aluminium alloys. In *Proceedings of the 3rd International Conference on NANOCON-2011*, 2011. – pp. 246-252.
- [8] Andreyachshenko V, Isheva Y, Mazhit A, Imangazinova D. ECAP-treated aluminium alloy AA2030: microstructure and mechanical properties. *Materials & Technologies/Materiali in Tehnologije*, 2019. 53(6). – pp. 805-810. [10.17222/mit.2018.250](https://doi.org/10.17222/mit.2018.250)
- [9] Andreyachshenko V.A. Evolution of the AA2030 alloy microstructure in the ECAP process. *Metallic Materials/Kovové Materiály*, 2022. 60(2) – 79-87. [10.31577/km.2022.2.79](https://doi.org/10.31577/km.2022.2.79)
- [10] Andreyachshenko V, Bartenev I, Malashkevichute-Brillant Y. Synthesis of an aluminum alloy rich in iron and silicon by surfacing with a consumable electrode. *Acta Metallurgica Slovaca*, 2024, 30(3) – 133-136. <https://doi.org/10.36547/ams.30.3.2065>
- [11] Ammar HR, Samuel E, Elsharkawi E, Doty HW, Songmene V, Samuel FH. Effect of Be, Sr, Mn, Mg, Cr and Si Addition on Neutralization and Fragmentation of  $\beta$ -Al<sub>5</sub>SiFe Phase in Al-(6–10)% Si Alloys. *International Journal of Metalcasting*, 2025 – pp. 1-24. <https://doi.org/10.1007/s40962-024-01540-0>
- [12] Nagaraj C, Dutt KM, Manjunath GK, Sharath PC, Sollapur SB, Arunkumar DT. Effect of multidirectional forging on grain structure and mechanical properties of hypereutectic Al–20% Si alloys with added refiners and modifiers. *Canadian Metallurgical Quarterly*, 2024 – pp. 1-15. <https://doi.org/10.1080/00084433.2024.2413245>
- [13] Man'ko T. Influence of Modification of Cast and Deformed Alloys on Mechanical Properties of Compositions. *Journal of Rocket-Space Technology*, 2024, 33(4-28) – pp. 94-97. <https://doi.org/10.15421/452430>
- [14] Zheng Q, Chen T, Li D, Wu J. Synergistic optimization of  $\alpha$ -Al grain and eutectic Si structures for Al-Si alloys via a newly designed Al-Ce-B alloy. *Materials Science and Engineering: A*, 2025, 925 – p. 147867. <https://doi.org/10.1016/j.msea.2025.147867>
- [15] Grejtak T, Shyam A, Blau PJ, Qu J. Additively manufactured and cast high-temperature aluminum alloys for electric vehicle brake rotor application. *Wear*, 2025 – p. 205961. <https://doi.org/10.1016/j.wear.2025.205961>
- [16] Aluminum alloy modification. [https://studref.com/519893/tehnika/modifitsirovanie\\_alyuminiyevyh\\_splavov](https://studref.com/519893/tehnika/modifitsirovanie_alyuminiyevyh_splavov)
- [17] Zhongping Q, Changming F, Chamini L. M, Yun W, Zhongyun F. Effects of Si solution in  $\theta$ -Al<sub>13</sub>Fe<sub>4</sub> on phase transformation between Fe-containing intermetallic compounds in Al alloys. *Journal of Alloys and Compounds*, 2023. – p. 1-13. <https://doi.org/10.1016/j.jallcom.2022.167587>
- [18] Que Zh, Fang Ch, Mendis ChL., Wang Yu., Fan Zh. Effects of Si solution in  $\theta$ -Al<sub>13</sub>Fe<sub>4</sub> on phase transformation between Fe-containing intermetallic compounds in Al alloys. *Journal of Alloys and Compounds*, 2023 <https://doi.org/10.1016/j.jallcom.2022.167587>.
- [19] Jin L, Liu K, Chen XG. Evolution of Fe-Rich Intermetallics in Al-Si-Cu 319 Cast Alloy with Various Fe, Mo, and Mn Contents. *Metall Mater Trans B*, 2019. – p. 1896–1907. <https://doi.org/10.1007/s11663-019-01584-2>
- [20] Nová K, Novák P, Průša F, Kopeček J, Čech J. Synthesis of Intermetallics in Fe-Al-Si System by Mechanical Alloying. *Metals*, 2019 <https://doi.org/10.3390/met9010020>
- [21] Aiken AZ, Andreyachshenko VA. Evolution of microstructure and properties in Fe, Si-Rich Al-Fe-Si alloy. *AIP Conference Proceedings*, 2024, 3251(1) – p. 040006 <https://doi.org/10.1063/5.0234067>
- [22] Andreyachshenko V, Ulyeva G. Heat treatment effect on the intermetallic Al-Fe-Si alloy microstructure. *Acta Metallurgica Slovaca*, 2024, 30(4) – pp. 156–160. <https://doi.org/10.36547/ams.30.4.2092>
- [23] Yang W, Gao F, Ji Sh. Formation and sedimentation of Fe-rich intermetallics in Al–Si–Cu–Fe alloy. *Transactions of Nonferrous Metals Society of China*, 2015. – p. 1704-1714 [https://doi.org/10.1016/S1003-6326\(15\)63776-1](https://doi.org/10.1016/S1003-6326(15)63776-1)
- [24] Lan X, Kai L, Wang J, Yang M, Lu Q, Du Y. Developing Al–Fe–Si alloys with high thermal stability through tuning Fe, Si contents and cooling rates. *Intermetallics*, 2022 <https://doi.org/10.1016/j.intermet.2022.107505>.

- [25] Becker H, Bergh T, Vullum PE, Leineweber A, Li Y. Effect of Mn and cooling rates on  $\alpha$ -,  $\beta$ - and  $\delta$ -Al-Fe-Si intermetallic phase formation in a secondary Al-Si alloy. *Materialia*, 2019 <https://doi.org/10.1016/j.mtla.2018.100198>
- [26] Song DF, Zhao YL, Wang Z et al. 3D Fe-Rich Phases Evolution and Its Effects on the Fracture Behavior of Al-7.0Si-1.2Fe Alloys by Mn Neutralization. *Acta Metall. Sin. (Engl. Lett.)*, 2022. – p. 163–175 <https://doi.org/10.1007/s40195-021-01299-x>
- [27] Fang CM, Que ZP, Fan Z. Crystal chemistry and electronic structure of the  $\beta$ -AlFeSi phase from first-principles. *Journal of Solid State Chemistry*, 2021 <https://doi.org/10.1016/j.jssc.2021.122199>
- [28] Orozco-González P, Castro-Román M, Muñoz-Valdez R, Luna-Álvarez S, Equihua-Guillén F, Hernández-Rodríguez A, Baltazar-Hernández VH, Alvarado-Hernández F. Formation and crystal structure of the  $\tau$  phase in the Al-Fe-Mn-Si system. *Materials Letters*, 2016. – p. 277-279 <https://doi.org/10.1016/j.matlet.2016.05.139>
- [29] Naizabekov A.B., Andreyachshenko V.A. Evaluation of possible mechanical property improvement for alloy of the Al-Fe-Si-Mn system by equal-channel angular pressing. *Metallurgist*, 2013; 57(1-2) – pp.159-163. doi 10.1007/s11015-013-9706-0
- [30] Yu JM, Wanderka N, Rack A, Daudin R, Boller E, Markötter H, Manzoni A, Vogel F, Arlt T, Manke I, Banhart J. Influence of impurities, strontium addition and cooling rate on microstructure evolution in Al-10Si-0.3Fe casting alloys. *Journal of Alloys and Compounds*, 2018. – p. 818-827. <https://doi.org/10.1016/j.jallcom.2018.06.372>
- [31] Song D, Zhao Y, Jia Y, Huang G, Zhang Z, Zhou N, Li X, Zheng K, Fu Y, Zhang W. Effect of B addition on the formation of Fe-rich phases in Al-Si-Fe alloys. *Journal of Alloys and Compounds*, 2022 <https://doi.org/10.1016/j.jallcom.2022.167426>
- [32] Toleuova A.R., Dostayeva A.M., Zharkevich O.M., Abdullina S.A., Adilkanova M.A., Serikbayev D. Calculating and experimental studying phase transformations in the Al-Zr-Fe-Si system alloys // *Metallurgija*, 2020. – p. 543 – 546
- [33] Jiang H, Liu YC, Wei C, Zhang YH, Gao ZM. Influence of minor Co on the formation of intermetallic phases in the Al91Fe7Si2 alloy. *Journal of Alloys and Compounds*, 2008. – p. 92-97 <https://doi.org/10.1016/j.jallcom.2007.11.019>.
- [34] Kishor M., Chopra K., Ayyagari K.P.R. Tackling Fe-rich Intermetallics in Al-Si Alloy: A Critical Review. *Trans Indian Inst Met*, 2023 <https://doi.org/10.1007/s12666-023-03205-8>

#### Information of the authors

**Andreyachshenko Violetta Alexandrovna**, PhD, associate professor, Head of the Testing Laboratory Engineering Profile “Comprehensive Development of Mineral Resources”, Abylkas Saginov Karaganda Technical University  
e-mail: [Vi-ta.z@mail.ru](mailto:Vi-ta.z@mail.ru)

**Toleuova Ainagul Rymkulovna**, PhD, associate professor, docent of the department Nanotechnology and metallurgy, Abylkas Saginov Karaganda Technical University  
e-mail: [rymkul.ainagul@gmail.com](mailto:rymkul.ainagul@gmail.com)

## Using the Method of Probabilistic Deterministic Experiment to Assess the Impact of Alloying Elements on the Properties of the Quasi High-Entropy Alloy of the Fe-Cr-Ni-Co-Mn System

Abildina A.R.<sup>1\*</sup>, Issagulov A.Z.<sup>1</sup>, Shcherbakova Ye.P.<sup>2</sup>, Kvon Sv.S.<sup>1</sup>

<sup>1</sup>Abylkas Saginov Karaganda Technical University, Karaganda, Kazakhstan

<sup>2</sup> Kaliningrad State Technical University, Kaliningrad, Russia

\*corresponding author

**Abstract.** This article considers the issues of planning experiments in testing wear resistance, hardness and tensile strength of the Cantor alloy. Basic experiments were carried out and an experimental matrix was developed. An experimental planning matrix was developed and calculated to conduct the basic experiments. The input and output parameters of the experiment were determined. The following were selected as input parameters: the niobium content from 14 to 18%; the carbon content from 1.5 to 2.5%; press pressure from 80 to 100 MPa. The output parameters were wear resistance, hardness and tensile strength. As a result, a six-factor matrix of experiments on five levels was used, in which three factors were vacant. Based on the data obtained, experiments were carried out on smelting an experimental quasi high-entropy alloy of the CoCrFeMnNi system with different niobium contents under laboratory conditions.

**Keywords:** experiment planning, wear resistance, hardness, press pressure, alloying elements, Cantor alloy, factors, correlation, high-entropy alloy.

### Introduction

High-entropy alloys (HEA) are a current trend in improving structural metallic materials [1]. Currently, there is a significant number of studies focused on the development of high-entropy alloys based on various technologies [2-6]. Study [4] presents a traditional composition of the CoCrFeMnNi system material (Cantor alloy) that demonstrates the potential for using such materials for subsequent experiments. The study reveals that the CoCrFeMnNi system forms a homogeneous solid solution with a face-centered cubic lattice. Study [5] demonstrates that the addition of such alloying elements as Ti, Nb, V and B provides improved mechanical properties, which makes this HEA suitable for real use. The main disadvantage of all high-entropy alloys is their high price compared to traditional materials. This is due to both the composition of the charge, since high-entropy alloys are produced using pure metals, and the characteristics of the technological process, which includes mandatory remelting, accelerated crystal formation and the other methods aimed at increasing the structure homogeneity. In recent years, the development of so-called quasi high-entropy alloys (QHEA), for which the requirements to the structure are less stringent, has become popular [6].

The basic principle of developing quasi high-entropy alloys is similar to that used for high-entropy alloys (HEA). In this case, a multi-component system consisting of at least five elements is used. However, in quasi high-entropy alloys, the equiatomic concentration of components is less strictly observed, and the criteria for the charge and smelting technology are much simpler. This circumstance makes quasi high-entropy alloys more commercially attractive, while their characteristics can be comparable with the parameters of high-entropy alloys.

### 1. Experimental part and discussion of results

To determine wear resistance, hardness and compressive strength of the Cantor alloy, the method of probabilistic deterministic experiment was used [7, 8].

To use the method of probabilistic deterministic experiment, experiments were previously conducted to select input and output parameters. The following input parameters are selected: niobium content from 14 to 18%; carbon content from 1.5 to 2.5%; pressing pressure from 80 to 100 MPa (deterministic).

The output parameters were assumed to be wear resistance, hardness, and ultimate strength (probabilistic). These studies aim to determine the dependence of the mechanical properties, in particular, the wear resistance and hardness of the casting on various factors of its manufacture – chemical composition, melting temperature, casting configuration, heat treatment, impact of pressing, etc. The simultaneous effect of all factors at a certain value gives some specific and practically reproducible result, therefore, we can talk about the existence of an objective fundamental multifactorial dependence [9-11]. However, the type of such dependence is not defined [12-13]. Therefore, the final result of the casting properties can be determined only by several, usually two or three, factors [14-15]. Therefore, the use of the method of probabilistic deterministic experiment is very relevant.

Table 1 shows the experimental factors for the content of alloying elements and press pressure and their numerical values. Table 2 shows the plan of the 6-factor experiment at 5 levels.

The decomposition process was modeled using the method of six-factor probabilistically deterministic experimental planning. So, with 6 factors (k) influencing the process, varying at 5 levels (n), the following number of calculations and experiments (N) have to be performed:  $N = n^k = 5^6 = 15,625$ . For this reason, the mathematical

planning method is used in both numerical and physical modeling of the process under study, which makes it possible to reduce the number of experiments by tens and hundreds of times.

**Table 1.** Experimental factors for the content of alloying elements and press pressure

Factors		Factor levels				
		1	2	3	4	5
$X_1$	Nb content, %	14	15	16	17	18
$X_2$	C content, %	1.5	1.7	2	2.3	2.5
$X_3$	Press pressure, MPa	80	85	90	95	100
$X_4$	Vacant factor	1	2	3	4	5
$X_5$	Vacant factor	1	2	3	4	5
$X_6$	Vacant factor	1	2	3	4	5

**Table 2.** Plan of the 6-factor experiment at 5 levels

$X_1$	$X_2$	$X_3$	$X_4$	$X_5$	$X_6$	Wear resistance, %	Hardness, HV	Compressive strength limit, MPa
14	1.5	80	1	1	1	88	370	630
14	2	90	3	3	3	72.6	360	630
14	1.7	85	2	2	2	78	290	650
14	2.5	100	5	5	5	72.5	300	670
14	2.3	95	4	4	4	88	360	625
16	1.5	90	2	5	4	93.2	310	680
16	2	85	5	4	1	94	360	630
16	1.7	100	4	1	3	87	360	570
16	2.5	95	1	3	2	82	390	680
16	2.3	80	3	2	5	78	370	665
15	1.5	85	4	3	5	76	360	690
15	2	100	1	2	4	86.5	370	640
15	1.7	95	3	5	1	93	330	690
15	2.5	80	2	4	3	82	300	550
15	2.3	90	5	1	2	82	340	655
15	1.5	100	3	4	2	87.1	360	660
15	2	95	2	1	5	82	360	670
15	1.7	80	5	3	4	72	330	640
15	2.5	90	4	2	1	87.3	330	660
15	2.3	85	1	5	3	81	335	635
17	1.5	95	5	2	3	75	320	630
17	2	80	4	5	2	89	330	660
17	1.7	90	1	4	5	93	430	690
17	2.5	85	3	1	4	93	390	660
17	2.3	100	2	3	1	91	370	645

The data in Table 2 were processed using the least squares method and partial dependences were obtained in the form of linear and polynomial functions of the type:

$$Y(X) = a + bX, \quad (1)$$

$$Y(X) = c_0 + c_1X^l + \dots + c_nX^m, \quad (2)$$

where  $a, b, c_i$  are fixed coefficients;

$X$  is a variable (factor).

Partial dependences of the optimization parameter are wear resistance, hardness and compressive strength:

1) on factor  $X_1$  ( $p_{\text{niobium}}$ , Nb content, %), equations of the form:

$$\begin{aligned}
 Y_{wear.1} &= -1.67x_1^2 + 54.362 x_1 - 354.5 \\
 Y_{hard.1} &= -4.7143x_1^2 + 155.06x_1 - 915.63 \\
 Y_{str.1} &= 3.2x_1 + 629.4
 \end{aligned}
 \tag{3}$$

2) on factor  $X_2$  (p<sub>carbon</sub>, C content, %):

$$\begin{aligned}
 Y_{wear.2} &= -2.6691 x_2^2 + 9.3383 x_2 + 76.791 \\
 Y_{hard.2} &= -52.34x_2^2 + 210.98x_2 + 143.52 \\
 Y_{str.2} &= 22.455x_2^2 - 101.44x_2 + 758.2
 \end{aligned}
 \tag{4}$$

3) in factor  $X_3$  (p<sub>pressure</sub>, press pressure, MPa):

$$\begin{aligned}
 Y_{wear3} &= -0.0226 x_3^2 + 4.2057 x_3 - 110.12 \\
 Y_{hard.3} &= -0.0657x_3^2 + 12.409x_3 - 232.2 \\
 Y_{проч.3} &= -0.3029x_3^2 + 54.954x_3 - 1829.4
 \end{aligned}
 \tag{5}$$

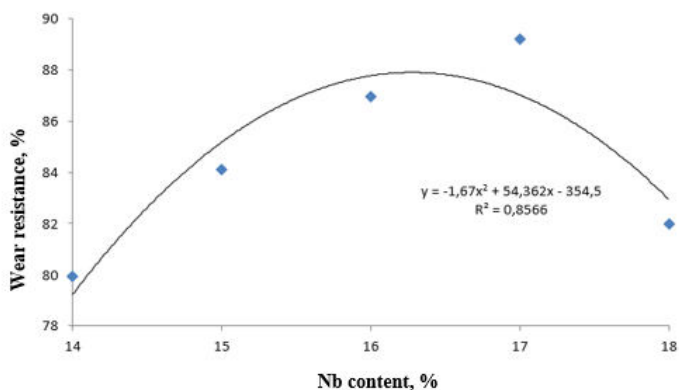
Table 3 shows the experimental values of wear resistance, hardness and compressive strength of the Cantor alloy.

**Table 3.** Calculated values of partial functions

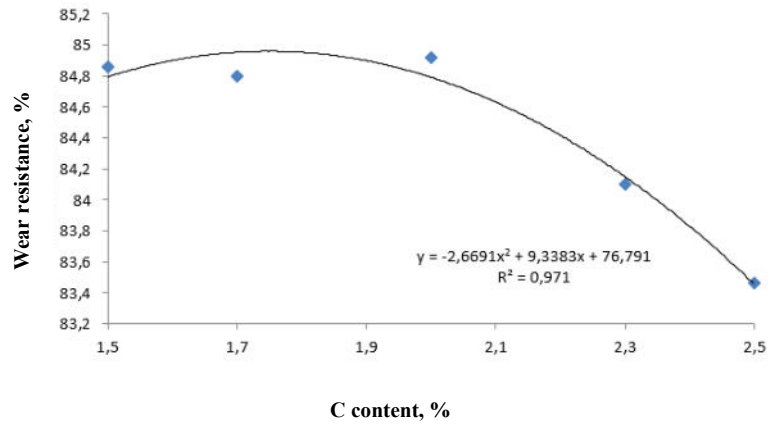
Function	Level					Average value, $\bar{Y}_{av.}$
	1	2	3	4	5	
Wear resistance						
$y = -1.67x_1^2 + 54.362 x_1 - 354.5$	79.82	83.9	86.84	88.2	81.88	84.128
$y = -2.6691 x_2^2 + 9.3383 x_2 + 76.791$	83.86	84.6	84.82	84	83.36	84.128
$y = -0.0226 x_3^2 + 4.2057 x_3 - 110.12$	81.8	84.4	85.62	84	84.82	84.128
Hardness						
$y = -4.7143x_1^2 + 155.06x_1 - 915.63$	336	340	358	68	343	349
$y = -52.34x_2^2 + 210.98x_2 + 143.52$	344	348	356	55	342	349
$y = -0.0657x_3^2 + 12.409x_3 - 232.2$	340	347	354	52	352	349
Compressive strength limit						
$y = 3.2x_1 + 629.4$	641	645	645	657	653	648.2
$y = 22.455x_2^2 - 101.44x_2 + 758.2$	658	648	646	645	644	648.2
$y = -0.3029x_3^2 + 54.954x_3 - 1829.4$	629	653	663	659	637	648.2

It is seen from Table 3 that the average values for each function coincide with the overall average value, which is the evidence of the absence of an error.

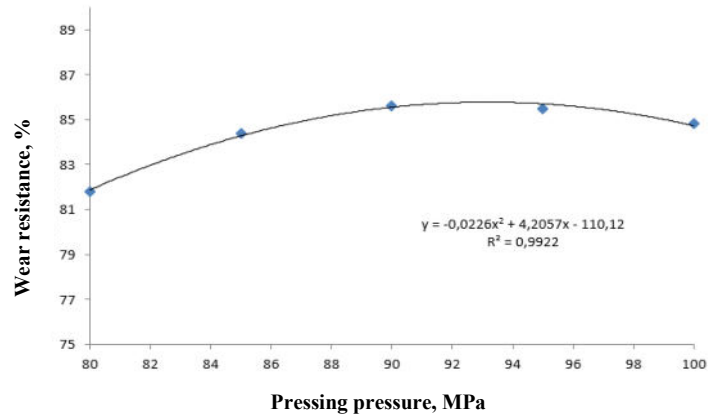
Figure 1 shows the graphs of the obtained partial dependences, constructed according to the data in Table 3.



a)



b)

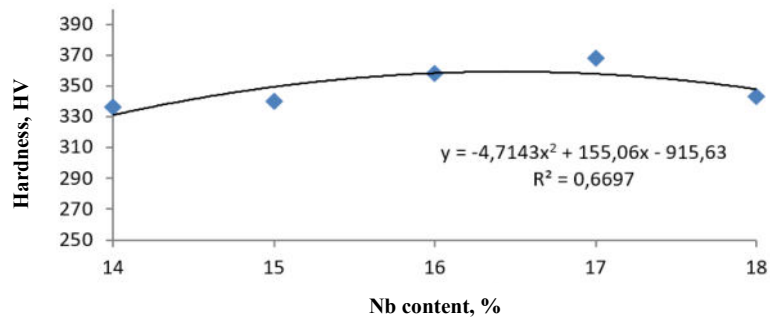


c)

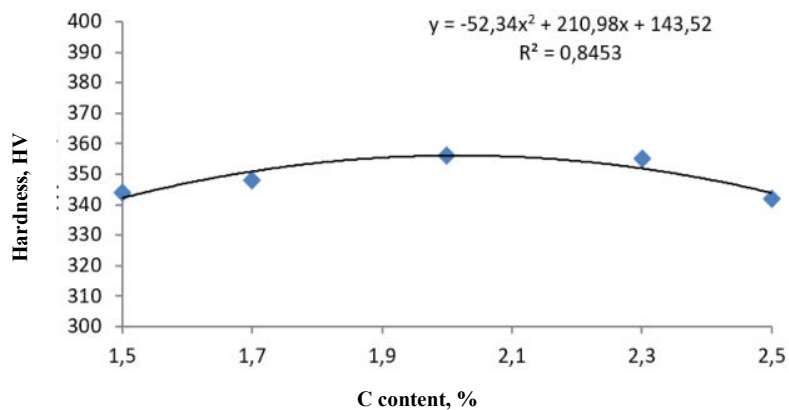
Fig.1. – Partial dependences of wear resistance of Cantor alloy: a) on the niobium content, b) on the carbon content, c) on press pressure

The correlation coefficient for each equation was  $R < 1$ . The correlation coefficient for comparison with experimental data for the first equation was  $R = 0.8566$ , for the second equation  $R = 0.971$  and for the third equation  $R=0.9922$ . These values indicate the influence of the factor on the result.

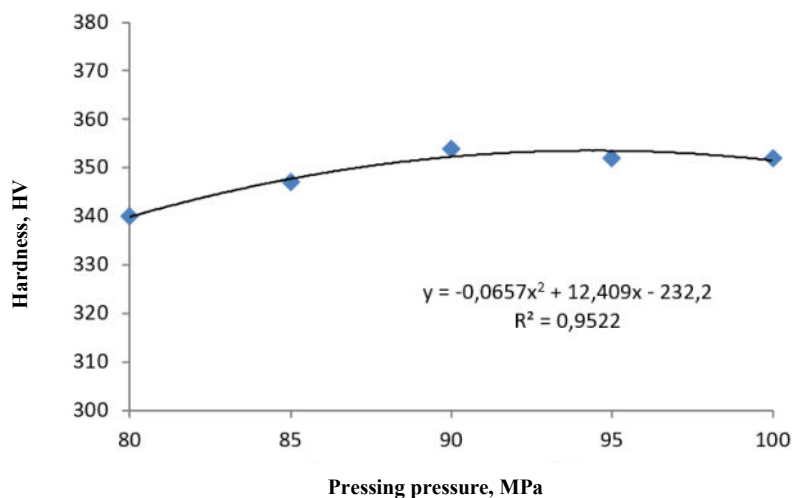
Figure 2 shows the partial dependencies of the hardness of the Cantor alloy.



a)



b)



c)

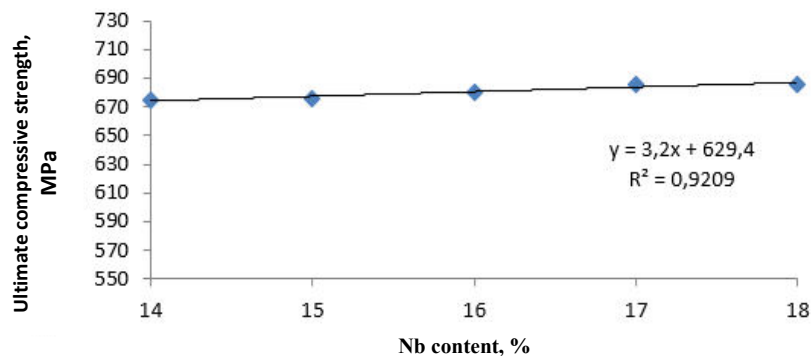
Fig. 2. – Partial dependences of the Cantor alloy hardness: a) on the niobium content, b) on the carbon content, c) on press pressure

The correlation coefficient for each equation was  $R < 1$ . The value of the correlation coefficient is selected automatically in Excel when constructing curves, calculated using formulas (6):

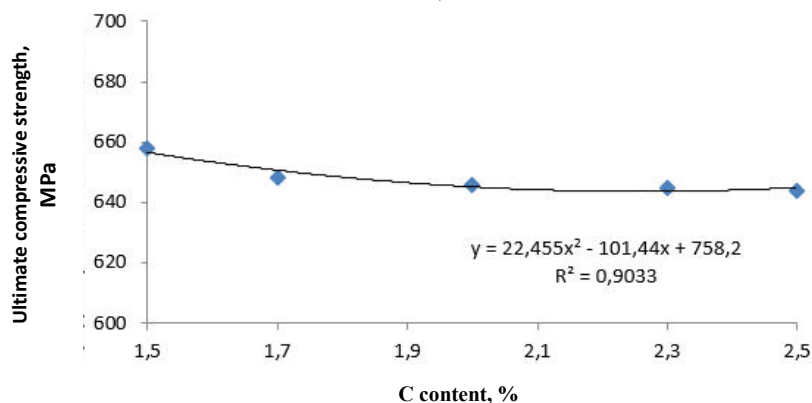
$$a_0 = \frac{\sum_{u=1}^N \bar{y}_u}{N} \qquad a_i = \frac{\sum_{u=1}^N x_{ui} \bar{y}_u}{N} \qquad (6)$$

The correlation coefficient for comparison with experimental data for the first equation was  $R=0.6697$ , for the second equation  $R=0.8453$  and for the third equation  $R=0.9522$ . These values indicate the influence of the factor on the result.

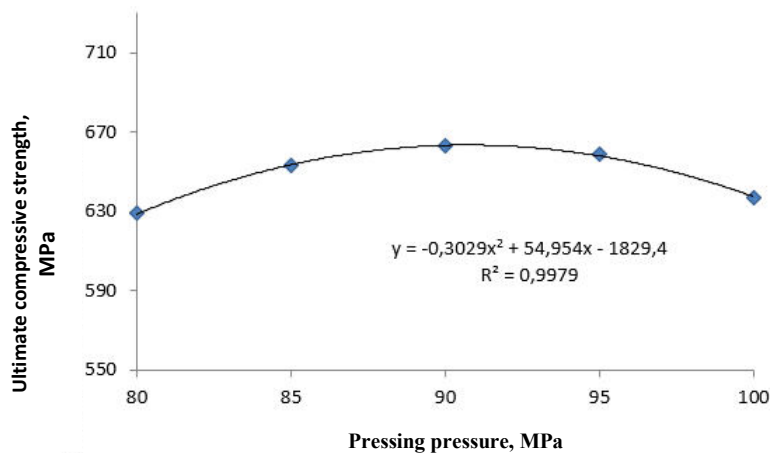
Figure 3 shows the partial dependences of the compressive strength of the Cantor alloy.



a)



b)



c)

a) on the niobium content, b) on the carbon content, c) on press pressure

Fig. 3. – Partial dependences of the compressive strength of Cantor alloy

The correlation coefficient for each equation was  $R < 1$ .

The correlation coefficient for comparison with the experimental data for the first equation was  $R = 0.9209$ , for the second equation  $R = 0.9033$  and for the third equation  $R = 0.9979$ . These values indicate the influence of the factor on the result.

Since the average values of the calculated values of the functions completely coincided with the experimental data, the selection of private dependencies was carried out correctly.

$$Y_{n(wear)} = \frac{(-1.67x_1^2 + 54.362x_1 - 354.5)(-2.6691x_2^2 + 9.3383x_2 + 76.791)(-0.0226x_3^2 + 4.2057x_3 - 110.12)}{84.128^{3-1}} =$$

$$= -0.000014x_1^2x_2^2x_3^2 + 0.00265x_1^2x_2^2x_3 - 0.0694x_1^2x_2^2 + 0.00047x_1x_2^2x_3^2 -$$

$$-0.086x_1x_2^2x_3 + 2.26x_1x_2^2 - 0.003x_2^2x_3^2 + 0.56x_2^2x_3 - 14.7x_2^2 + 0.00005x_1^2x_2x_3^2 -$$

$$-0.009 x_1^2 x_2 x_3 + 0.24 x_1^2 x_2 + 0.0016 x_1 x_2 x_3^2 + 0.3 x_1 x_2 x_3 - 7.9 x_1 x_2 + 0.01 x_2 x_3^2 - 1.97 x_2 x_3 + 51.5 x_2 + 0.0004 x_1^2 x_3^2 - 0.076 x_1^2 x_3 + 1.99 x_1^2 - 0.013 x_1 x_3^2 + 2.48 x_1 x_3 - 64.95 x_1 + 0.09 x_3^2 - 16.18 x_3 + 361.7$$

$$Y_{n(hard.)} = \frac{(-4.7143x_1^2 + 155.06x_1 - 915.63)(-52.34x_2^2 + 210.98x_2 + 143.52)(-0.0657x_3^2 + 12.409x_3 - 232.2)}{349^{3-1}} =$$

$$= -0.00013x_1^2 x_2^2 x_3^2 + 0.03x_1^2 x_2^2 x_3 - 0.47x_1^2 x_2^2 + 0.0005x_1^2 x_2 x_3^2 - 0.1x_1^2 x_2 x_3 + 1.9x_1^2 x_2 + 0.00036x_1^2 x_3^2 - 0.069x_1^2 x_3 + 1.29x_1^2 + 0.004x_1 x_2^2 x_3^2 - 0.8x_1 x_2^2 x_3 + 15.5x_1 x_2^2 - 0.018x_1 x_2 x_3^2 + 3.3x_1 x_2 x_3 + 62.4x_1 x_2 - 0.012x_1 x_3^2 + 2.27x_1 x_3 - 42.4x_1 - 0.026x_2^2 x_3^2 + 4.88x_2^2 x_3 - 91.36x_2^2 + 0.1x_2 x_3^2 - 19.68x_2 x_3 + 368.3x_2 + 0.07x_3^2 - 13.4x_3 + 250.5$$

$$Y_{str.} = \frac{(3.2x_1 + 629.4)(22.455x_2^2 - 101.44x_2 + 758.2)(-0.3029x_3^2 + 54.954x_3 - 1829.4)}{648.2^{3-1}} =$$

$$= -0.00005x_1 x_2^2 x_3^2 + 0.009x_1 x_2^2 x_3 - 0.3x_1 x_2^2 + 0.0002x_1 x_2 x_3^2 - 0.04x_1 x_2 x_3 + 1.4x_1 x_2 - 0.0017x_1 x_3^2 + 0.3x_1 x_3 - 10.56x_1 - 0.01x_2^2 x_3^2 + 1.85x_2^2 x_3 - 61.5x_2^2 + 0.04x_2 x_3^2 - 8.35x_2 x_3 + 278x_2 - 0.34x_3^2 + 62.4x_3 + 2077.8$$

(7)

After transformation there is obtained:

$$L = -0.000014C_{Nb}^2 C_c^2 p_{np}^2 + 0.00265C_{Nb}^2 C_c^2 p_{np} - 0.0694C_{Nb} C_c^2 + 0.00047C_{Nb} C_c^2 p_{np}^2 - 0.086C_{Nb} C_c^2 p_{np} + 2.26C_{Nb} C_c^2 - 0.003C_c^2 p_{np}^2 + 0.56C_c^2 p_{np} - 4.7C_c^2 + 0.00005C_{Nb}^2 C_c p_{np}^2 - 0.009C_{Nb}^2 C_c p_{np} + 0.24C_{Nb}^2 C_c + 0.0016C_{Nb} C_c p_{np}^2 + 0.3C_{Nb} C_c p_{np} - 7.9C_{Nb} C_c + 0.01C_c p_{np}^2 - 1.97C_c x_3 + 51.5C_c + 0.0004C_{Nb}^2 p_{np}^2 - 0.076C_{Nb}^2 p_{np} + 1.99C_{Nb}^2 - 0.013C_{Nb} p_{np}^2 + 2.48C_{Nb} p_{np} - 64.95C_{Nb} + 0.09p_{np}^2 - 16.18p_{np} + 361.7$$

$$HV = -0.00013C_{Nb}^2 C_c^2 p_{np}^2 + 0.03C_{Nb}^2 C_c^2 p_{np} - 0.47C_{Nb}^2 C_c^2 + 0.0005C_{Nb}^2 C_c p_{np}^2 - 0.1C_{Nb}^2 C_c p_{np} + 1.9C_{Nb}^2 C_c + 0.00036C_{Nb}^2 p_{np}^2 - 0.069C_{Nb}^2 p_{np} + 1.29C_{Nb}^2 + 0.004C_{Nb} C_c^2 p_{np}^2 - 0.8C_{Nb} C_c^2 x_3 + 15.5C_{Nb} C_c^2 - 0.018C_{Nb} C_c p_{np}^2 + 3.3C_{Nb} C_c p_{np} + 62.4C_{Nb} C_c - 0.012C_{Nb} p_{np}^2 + 2.27C_{Nb} p_{np} - 42.4C_{Nb} - 0.026C_c^2 p_{np}^2 + 4.88C_c^2 p_{np} - 91.36C_c^2 + 0.1C_c p_{np}^2 - 19.68C_c p_{np} + 368.3C_c + 0.07p_{np}^2 - 13.4p_{np} + 250.5$$

$$R = -0.00005C_{Nb} C_c^2 p_{np}^2 + 0.009C_{Nb} C_c^2 p_{np} - 0.3C_{Nb} x_3^2 + 0.0002C_{Nb} C_c p_{np}^2 - 0.04C_{Nb} C_c p_{np} + 1.4C_{Nb} C_c - 0.0017C_{Nb} p_{np}^2 + 0.3C_{Nb} p_{np} - 10.56C_{Nb} - 0.01C_c^2 p_{np}^2 + 1.85C_c^2 p_{np} - 61.5C_c^2 + 0.04C_c p_{np}^2 - 8.35C_c p_{np} + 278C_c - 0.34p_{np}^2 + 62.4p_{np} + 2077.8$$

The obtained dependence was compared with some experimental values of the wear resistance and hardness of the samples. The samples shown in Table 4 were compared.

Table 4. Conditions for obtaining samples

Sample	Nb content, %	C content, %	Pressing pressure, MPa
1	14	1,5	80
2	15	2	100
3	16	2,5	95
4	17	1,5	95

Table 5. Comparison of research results obtained by computational and experimental methods

Sample	Wear resistance			Hardness		
	Experiment	Calculation	The discrepancy	Experiment	Calculation	The discrepancy
1	88,9	87,4	1,69	373	385	3,12
2	86,7	85,2	1,74	376	370	1,60
3	82,3	81,1	1,46	391	379	3,07
4	75,9	75,2	0,92	328	337	2,67

As can be seen from the comparative data, the discrepancy between the calculated and experimental values of wear resistance and hardness is about 1.5-3.0%.

The obtained generalized equation is adequate and can be used to determine the wear resistance ( $L_{NbCP}$ ), hardness ( $HV_{NbCP}$ ) and compressive strength ( $R_{NbCP}$ ) of the Cantor alloy castings with the niobium content of 14-18%, the carbon content of 1.5-2.5%, and press pressure of 80-100 MPa.

The increase in wear resistance, hardness and compressive strength of the Cantor alloy with increasing the niobium content occurs in the form of a polynomial curve, that is, with the niobium content of 17%, they have higher wear resistance that is equal to  $\approx 89.2\%$ , hardness that is equal to  $\approx 368$  HV and compressive strength that is equal to  $\approx 657$  MPa. The greatest increase in wear resistance, hardness and compressive strength occurs with the carbon content of 84.92%, 356 HV and 658 MPa, respectively.

The content of the Cantor alloy press pressure also affects wear resistance, hardness and compressive strength: maximum values of wear resistance  $\approx 85.62\%$ , hardness  $\approx 354$  HV and compressive strength  $\approx 663$  MPa with press pressure of 90 MPa.

### Conclusions

The calculated dependence obtained was compared with the experimental values of wear resistance and hardness of the samples. The discrepancy between the calculated and experimental values of wear resistance and hardness is about 1.5-3.0%. Based on this, the dependencies obtained by the method of probabilistically deterministic experiment can be considered adequate in the indicated ranges of initial factors. The most rational, from the point of view of identifying the optimal level of wear resistance and hardness, is proposed: niobium content – 17%, carbon content – 2%, pressing pressure – 90 MPa. Under these conditions, maximum values of wear resistance, hardness, and compressive strength are observed.

**Aknowlegment.** The work was carried out within the framework of the implementation of the IRN Program BR21882240 “Developing a quasi high-entropy alloy using Kazakhstani raw materials and technology of producing precision parts based on it” (agreement with the Committee of Science of the Ministry of Education and Science of the Republic of Kazakhstan No. 378-PTsF-23-25 dated November 15, 2023), funded by the Ministry of Science and Higher Education of the Republic of Kazakhstan.

### References

- [1] Murty B.S., Yeh J.W., Ranganathan S. High-Entropy Alloys / Butterworth-Heinemann (Elsevier), 2014, p.218.
- [2] Bataeva Z.B., Ruktuev A.A., Ivanov I.V., Yurgin A.B., Bataev I.A. Review of studies of alloys developed based on the entropy approach // Metal processing (technology, equipment, tools). 2021. Vol. 23, No. 2. P. 116-146. DOI: 10.17212/1994-6309-2021-23.2-116-146.
- [3] Yeh J.-W., Chen S.-K., Lin S.-J., Gan J.-Y., Chin Ts.-Sh., Shun T.-Ts., Tsau Ch.-H., Chang Sh.-Y. Nanostructured High-Entropy Alloys with Multiple Principle Elements: Novel Alloy Design Concepts and Outcomes //Advanced Engineering Materials, 2004, №8, 299-303
- [4] Cantor B., Chang I.T.H., Knight P., Vincent A.J.B. Microstructural development in equiatomic multicomponent alloys. Materials Science and Engineering: A, 2004, vol. 375–377, pp. 213–218. DOI: 10.1016/j.msea.2003.10.257.
- [5] Bazlov A., Stochko I., Ubyivovk E., Parkhomenko M., Magomedova D., Zanaeva E. Structure and Properties of Amorphous Quasi-High-Entropy Fe-Co-Ni-Cr-(Mo,V)-B Alloys with Various Boron Content //Metals, 2023, 13, 1464. <https://doi.org/10.3390/met13081464>
- [6] Yang L., Li Y., Wang Z., Zhao W., Qin C. Nanoporous Quasi-High-Entropy Alloy Microspheres //Metals, 2019, 9, 345. <https://doi.org/10.3390/met9030345>
- [7] Malyshev V.P. Descriptio Mathematica eventus experimenti multifactorii experimenti Seidel-Gauss methodo probato utens. Bulletin of the Academy of the Sciences of KazSSR, 1978, 4, 31-38.
- [8] Akberdin A.A., Kim A.S., Sultangaziev R.B. Consilium de experimentis numeralibus et physicis in processibus technologicis imitandis // News altiorum institutionum educationis //Ferrous Metallurgy, 2018, 61(9).
- [9] Kobi A., Indmeskine F-E., Saintis L. Chapter 22 - Life testing plan for electronic components based on design of experiments //Advances in Reliability Science, 2024, 661-685.
- [10] Zheng P., Wang H., Wei D., Pu C., He Zh. Environmental governance capability and water quality: A quasi-natural experiment based on the Ten-point Water Plan //Urban Climate, volume 41, 2022, 101050.
- [11] Yin X., Liang J., Liu Ch., Chen S., Shang Sh., Liu Ch. Accelerating the design of multivariate Nb-Si based alloys with excellent strength and toughness matching through machine learning //Next Materials, volume 6, 2025, 100294.
- [12] Prus M. Optimal designs for prediction of random effects in two-groups models with multivariate response //Journal of Multivariate Analysis, volume 198, November 2023, 105212.
- [13] Taji J., Farughi H., Rasay H. Economic-statistical design of fully adaptive multivariate control charts under effects of multiple assignable causes //Computers & Industrial Engineering, volume 173, 2022, 108676.
- [14] Issagulov A.Z., Kim V.A., Kvon S.S., Kulikov V.Y., Tussupova A.U. Production of technical silicon and silicon carbide from rice-husk // Metalurgija, 2014, 53(4), 685-688.
- [15] Kovalev, P.V., Popova, S.D., Issagulov, A.Z., Kulikov, V.Y., Kvon, S.S. Investigation of the effect of high strength strips steel modification with rare-earth metal (REM) //Metalurgija, 2017, 56(3-4), 393-395.

- [16] Issagulov A., Kovalev P., Melnik S., Kulikov V., Kvon S., Arinova S. The effect of complex extra-furnace treatment of metal melts on the formation of non-metallic inclusions in large-sized ingots //Materials Research Express, Volume 11, Issue 11, 1 November 2024, № 116502. DOI: 10.1088/2053-1591/ad898c
- [17] Kvon S., Issagulov A., Kulikov V., Arinova S. Niobium's Effect on the Properties of a Quasi-High-Entropy Alloy of the CoCrFeMnNi System // Metals, Швейцария: MDPI AG, 10.05.2024, 14, 564. <https://doi.org/10.3390/met14050564>
- [18] Aubakirov D.R., Issagulov A.Z., Akberdin A.A., Kvon Sv.S., Kulikov V.Yu., Arinova S.K., Dostaeva A.M., Chsherbakova Ye.P., Sarkenov B.B., Narembekova A.K. Influence of boron- and barium-containing modifiers on the structure of low-chromium cast iron // Heliyon, 2022, 8(11), e11496
- [19] Kovalyova T., Eremin E., Arinova S., Medvedeva I., Dostayeva A. Enhancing surface roughness of castings when sand-resin mold casting //Metalurgija, 2017, 56(1-2), 135–138

#### Information of the authors

**Abildina Aizhan Rymkulkyzy**, Doctoral student, Abylkas Saginov Karaganda Technical University  
e-mail: [aizhan--1984@mail.ru](mailto:aizhan--1984@mail.ru)

**Issagulov Aristotle Zeinullinovich**, Doctor of Engineering, Professor, Abylkas Saginov Karaganda Technical University  
e-mail: [aristotel@kstu.kz](mailto:aristotel@kstu.kz)

**Shcherbakova Yelena Petrovna**, PhD, Associate Professor, Kaliningrad State Technical University  
e-mail: [sherbakova\\_1984@mail.ru](mailto:sherbakova_1984@mail.ru)

**Kvon Svetlana Sergeyevna**, PhD, Professor, Abylkas Saginov Karaganda Technical University  
e-mail: [svetlana.1311@mail.ru](mailto:svetlana.1311@mail.ru)

## Multi-Objective Optimization of Machining Parameters for Sustainable Turning of AISI 630 Stainless Steel using Taguchi-Based Desirability Function Analysis

Subramani S.<sup>1</sup>, Dhairiyasamy R.<sup>2</sup>, Gabriel D.<sup>3\*</sup>

<sup>1</sup>Department of Mechanical Engineering, National Institute of Technology Puducherry, Karaikal, India

<sup>2</sup>Department of Electronics and Communication Engineering, Saveetha School of Engineering, Saveetha Institute of Medical and Technical Sciences, Saveetha University, Chennai, Tamilnadu, India

<sup>2</sup>Centre of Research Impact and Outcome, Chitkara University Institute of Engineering and Technology, Punjab, Rajpura, India

<sup>3</sup>College of Engineering and Technology, Aksum University, Ethiopia.

<sup>3</sup>Chitkara Centre for Research and Development, Chitkara University, Himachal Pradesh, India.

\*corresponding author

**Abstract.** Dry machining has a good association with ecological and economic control. Even though dry machining is environment-friendly, it produces poor surface quality with excessive tool wear due to a vast amount of heat generation at the machining interface. This paper aims to determine the optimum machining parameters for enhanced machining performance. The turning process was performed under a dry environment on AISI 630 steel by varying the machining parameters. The experimental run for three factors, each at three levels, was framed with the help of Taguchi's technique. Machining responses such as tool-work interface temperature, surface roughness, and material removal rate were measured online and offline with corresponding measuring devices. A temperature measuring system was developed indigenously to measure temperature. The effect of machining parameters on machining response, determination of optimum machining parameters for individual machining response, the influence of machining parameters on machining responses, and mathematical model for individual machining response were discussed. Taguchi-Desirability Function Analysis was employed to determine the optimum machining parameters for enhancing the machining performance. Enhanced machining performance was obtained at the optimum parameters of 800 rpm, 0.12 mm/rev, and 0.70 mm.

**Keywords:** Dry machining, AISI 630, Steel, Optimization, Taguchi, Desirability Function Analysis, Temperature

### Introduction

Stainless steel is often used in many engineering applications for its properties such as high strength, hardness, and corrosion resistance [1,2]. One of the most widely used materials in the stainless-steel group is AISI 630 steel. It is often known as a difficult-to-machine material by its composition and properties [3]. In addition, AISI 630 steel has superior corrosion resistance compared to 304 and 316L steel. It is used to make fasteners, reactor components, missile fittings, jet engine parts [4], safety valves, studs, nuts [5], sailboat propeller shafts [6] and implantation [7]. However, the machining of such material requires higher cutting force, resulting in higher friction at the machining interface, thus generating considerable heat. Its lower thermal conductivity nature retains the generated heat at the machining interface. It affects the quality of the machined surface and tool life, resulting in lower productivity and high production cost [8,9]. These problems are mitigated by selecting suitable cutting fluid and cooling techniques.

The flood cooling system uses plenty of cutting fluid to reduce the cutting temperature and friction. Generally, the cutting fluid used in the machining industry is a conventional fluid, i.e., a mineral oil that contains chemical components harming the environment and workers' health. It also might cause damage to the workpiece surface due to chemical reactions. The quality of the fluid degrades rapidly and gets contaminated due to bacterial growth [10,11]. Further, the disposal of conventional cutting fluid is a difficult task that severely impacts the environment. Contamination of soil and water, environmental pollution, health issues for workers, and high-cost disposal processes are the limitations of conventional cutting fluids [12]. In addition, the cost of the cutting fluid during machining under a conventional environment account for approximately 8 to 16% of the total manufacturing cost [13]. Approximately 1.2 million workers have been affected by cutting fluids that are too toxic and hazardous to the environment [14].

The adverse effect of the conventional cutting fluid can be minimized by using it at a minimum level, and it can be avoided by introducing alternate cutting fluids. The primary factor in sustainable manufacturing is the process parameters, the tool's geometry and material, the workpiece's material and geometry, and the cooling method [15]. Recently, many researchers and practitioners are showing keen interest in implementing alternatives to conventional cutting fluid, which would reduce the quantity of the cutting fluid. Thereby, reduction in environmental effects and machining costs can be reduced. Some alternatives, such as dry machining, minimum quantity lubrication, cryogenic cooling, nanofluids, and vegetable oils, are better alternatives for conventional cutting fluids [16,17].

The gaseous cutting fluid is a substance that is used as a cooled-pressurized liquid, and it contains air, nitrogen, argon, helium, and carbon dioxide. The commonly used gas-based cutting fluid is air [18]. Gas-based cutting fluid has higher corrosion resistance and cooling ability, which can be performed and utilized even at elevated temperatures. Sivaiah and Chakradhar investigated the machining performance of turning 17-4 PH stainless steel under various machining environments such as flood, MQL, cryogenic, and dry. Compared to other machining environments, reductions in temperature, surface roughness and tool wear were observed under cryogenic machining [19]. However, it cannot be used as a lubricant at the tool-work interface because of its poor viscosity. Poor viscous cutting fluid is not conducive to better lubrication, therein leading to poor surface roughness [20,21]. Moreover, the utilization of cryogenic cooling systems is a threat to ecology, and their installation requires high capital and operational cost [22].

Minimum Quantity Lubrication (MQL) is in demand in various industries due to its environment-friendly nature. The essential functions of cutting fluid are obtained significantly through MQL machining. MQL system also provides superior cooling and better lubrication. It produces tiny oil droplets with excellent flowability and penetrability [23,24]. It is an efficient technique adopted for better performance, as it uses a small quantity of cutting fluid. It also reduces the issues associated with excessive use of coolant [25]. MQL machining method utilises cutting fluid in the form of mist in the machining zone. The generated mist can float in the air and would be inhaled by the worker. Thus, it leads to lung disease, respiratory issues, and the oesophagus, stomach, pancreas, prostate, colon, and rectal cancer [18].

Dry machining nullifies the cutting fluid usage, thus eliminating the polluted environment. Compared to conventional machining, dry machining makes the environment green and pollution free. It appeals to more fabulous eco-friendly, and cost-effective environments than wet and MQL machining [26]. Selvam and Sivaram (2018) experimented to investigate the surface roughness during the turning of AISI 4340 steel under dry, near-dry, and flood environments. It was noted that the highest surface quality of the machined workpiece was achieved by flood machining. It was also found that flood and near-dry machining outperformed dry machining by improving the surface roughness, with contributions of 13% and 4.11%, respectively [27].

Ali Khan (2019) studied the effect of machining parameters and cryogenic environment during the turning of Titanium alloy, and machining responses were compared with dry and flood machining. Cryogenic machining reduced the tool wear, surface roughness, and energy consumption by 4%, 9% and 10%, respectively than dry machining [28]. Recently, Khan et al. (2020, 2022) studied the effect of flood, cryogenic and dry environments on Titanium alloy. The machining responses were enhanced by cryogenic and flood machining compared to dry machining. Despite this, they have used a dual nozzle to supply the LN<sub>2</sub> with a flow rate of 4 L/min and 6 L/min for flood machining. This leads to the disappearance of cost-effective machining [29, 30].

It has been observed from the literature that only some alternate machining environments have been implemented, and only tenuous improvements in machining performance have been obtained compared to dry machining. Further, an alternate machining method would deteriorate the environment by utilizing the cutting fluid. In this view, machining parameter optimization would improve the dry machining performance. Very few researchers have investigated the machining of AISI 630 steel so far. Furthermore, it has been observed that more studies are needed in machining the chosen material. In the present study, multi-response optimization was performed using Taguchi-based desirability function analysis to enhance machining performance.

## 1. Materials and Methods

All the experiments were conducted to measure the machining responses under a dry environment using Kirloskar make Turmmaster-35 model centre lathe with variable speed and feed drive. The stainless-steel grade of AISI 630 was chosen as a workpiece material for the current study. It was used in the form of a cylindrical shape with dimensions of 50 mm diameter and 150 mm length. A pictorial view of the workpiece with dimensions is shown in Figure 1. The cutting tool insert and holder were chosen based on the workpiece hardness and machining conditions. In addition, the cutting tool insert was chosen based on its utility in the machining industry and availability on the market. Ceratizit makes coated carbide inserts used as a cutting tool and has an ISO designation CNMG 120408EN-M70 with a nose radius of 0.8 mm. A new cutting edge was used for each level of process parameters and it is mounted on a tool holder with ISO designation PCLNR 2020 K12 WIDIA. The cutting tool insert and tool holder are shown in Figure 2.



Fig. 1. - Workpiece material used during the experiment



Fig. 2. - Pictorial view of tool insert and tool holder

## 2. Measuring devices for machining responses

The machining responses, such as tool-work interface temperature, surface roughness and material removal rate, were measured with appropriate measuring equipment. The machining responses were measured online and offline during and after turning under variable machining parameters. All the mechanical works are converted into thermal energy during the machining process. A considerable amount of heat is generated in the machining zone. It affects productivity, surface quality, workpiece dimensions, tool wear and other machining responses. Due to this, investigations of measuring tool-work interface temperature are of utmost importance.

Temperature was measured using a K-type thermocouple, and it is positioned in the modified tool insert. A pictorial view of the modified tool inserts and thermocouple is shown in Figure 3. An electric spark discharge machine made a hole in the tool insert with a 1.5 mm diameter and 3.76 mm depth. The hole was positioned 1 mm from the cutting edge and 1 mm below the rack surface. Thermocouple was inserted in the tool insert where the hole was made. The criteria for selecting thermocouples were the measuring temperature range and accuracy; availability in the market and cost were also considered.

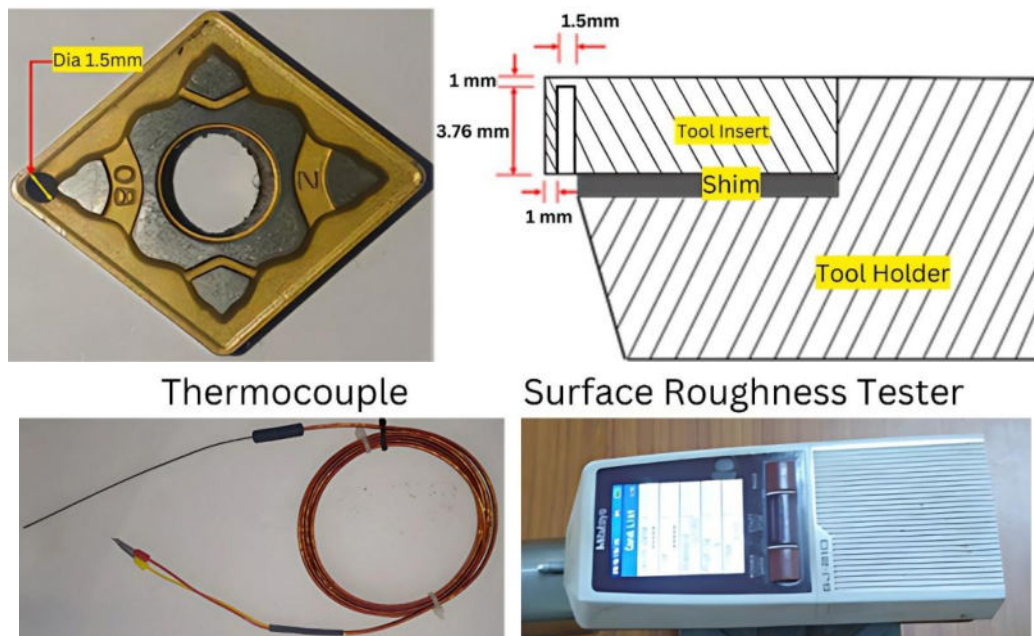


Fig.3. - Pictorial view of modified tool insert and thermocouple

Tool-work interface temperature was measured using an in-house developed temperature measuring system (TMS). A thermocouple, amplifier, UNO Arduino, and personal computer are the components utilised to develop TMS. The components are connected, as shown in Figure 4. The processor was programmed with code for measuring the temperature, which assisted the TMS in simultaneously measuring the temperature and machining time.

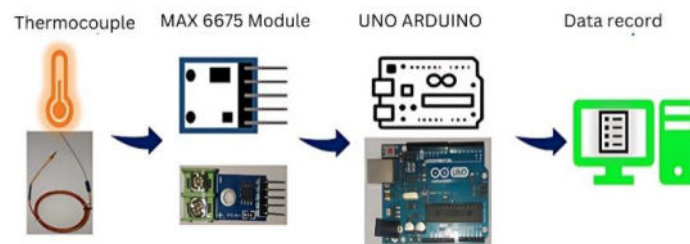


Fig. 4. - Temperature measuring system

The quality of the product is identified with the value of surface roughness. The surface roughness of the machined parts was measured offline using Mitutoyo make SJ-210 model after the turning process. Surface roughness was measured around the machined workpiece at different locations, and the average value was taken into account. The material removal rate identifies the productivity of the machining process. It was determined using the conventional method. The measurement of the material removal rate is done offline. The weight of the workpiece was measured using a weighing machine before and after the machining at each level of machining parameters. The material removal rate is defined as the ratio of the difference between the weight of the workpiece before and after the turning process to the time taken. Equation (1) represents the material removal rate at each level of machining parameters:

$$MRR = \frac{W_i - W_f}{t} (g/min) \quad (1)$$

where  $W_i$ ,  $W_f$  and  $t$  are represented as the weight of the workpiece before and after the machining and time of cutting, respectively.

### 3. Taguchi's technique

Taguchi's technique is an excellent tool for optimizing the parameters of any machining process. Depending on the type of procedure, the approach is typically conducted utilizing  $L_9$ ,  $L_{18}$ , or  $L_{27}$  orthogonal array system. Primarily,  $L_9$  orthogonal array was used to carry out the experimental design in most situations where the process was built with three machining parameters. The design of the experiment under the general full factorial method sets a total of twenty-seven experiments for three factors at three different levels. As the number of experimental runs increases, so does the cost and effort require. The experiment design is more economical when setting it up using the Taguchi technique because it reduces the experimental setup substantially compared to the conventional experimental design approach.

This study performed the turning process on AISI 630 stainless steel in a dry environment. Taguchi  $L_9$  orthogonal array design was selected for designing the experiments. The experiments were conducted by varying the machining parameters such as cutting velocity, feed rate and depth of cut. Each machining parameter varied at three levels. Nine experiments were employed to determine the optimum machining parameters for enhanced turning performance in terms of lower temperature and surface roughness (Ra) and higher material removal rate (MRR). The machining parameters at different levels are presented in Table 1.

**Table 1.** Machining parameters and their levels for the turning process

Symbol	Machining parameters	Level 1	Level 2	Level 3
$v$	Cutting speed (rpm)	700	800	900
$f$	Feed rate (mm/rev)	0.06	0.12	0.18
$a_p$	Depth of cut (mm)	0.35	0.70	1.05

The Signal to Noise (S/N) ratio is the mean and standard deviation ratio. The process is considered good in any machining process when the temperature and surface roughness are smaller and the material removal rate is larger. The mean S/N ratio for tool-work interface temperature and surface roughness was calculated using the 'lower the better' response, and 'larger the better' was used for the material removal rate:

$$S/N \text{ ratio}_{\text{smaller the better}} = -10 \log \frac{1}{n} \sum R^2 \quad (2)$$

$$S/N \text{ ratio}_{\text{Larger the better}} = -10 \log \frac{1}{n} \sum \frac{1}{R^2} \quad (3)$$

where  $n$  - number of observed data;

$R$  - observed data for each response

The value of the S/N ratio for the temperature and Ra was calculated using Equation (2). Equation (3) calculates the S/N ratio for the MRR. Minitab 19.1 is the statistical analysis tool utilized for performing the Taguchi technique.

### 4. Desirability Function Analysis

Desirability Function Analysis (DFA) is a multi-criteria decision-making statistical tool. It is used to determine the optimum input parameters for the output responses. DFA is a well-known technique adopted in the industry to simultaneously determine the optimum independent variable. The objective of the current study is to estimate the best among the given set of experiments with optimal multi-responses. The responses have conflicting criteria, such as smaller, nominal, or better. DFA is implemented to avoid such conflicting criteria.

Harrington was the one who first introduced DFA in 1967. Further, the modification has been extended by Derringer and Suich. It is implemented to estimate the machining responses of many researchers in different machining processes, namely EDM, end milling, and turning. In this methodology, a set of experiments is

undesirable if any of the output responses falls outside the desired boundary. The objective is to identify the optimum machining parameters that produce the highest desirable index value for the responses. The desirability value lies between zero to one. The value near 1 indicates that the response is within the desirable and ideal limits. The value near zero represents the response being outside the desired limit and considered undesirable.

In the present study, tool-work interface temperature, Ra and MRR are considered performance characteristics of the turning process. Machining performance is enhanced by reducing the temperature and Ra and increasing the MRR. All the machining responses are normalized using the desirability function. Therefore, the 'smaller the better' desirability function is applied for temperature and Ra, whereas the 'larger the better' is used for MRR. Individual desirability values for the machining response to be maximized are estimated using Equation (4). Individual desirability values for minimizing machining response are estimated using Equation (5):

$$d_{i \text{ (larger the better)}} = \left( \frac{y_i - y_{\min}}{y_{\max} - y_{\min}} \right)^r \quad (4)$$

$$d_{i \text{ (smaller the better)}} = \left( \frac{y_{\max} - y_i}{y_{\max} - y_{\min}} \right)^r \quad (5)$$

$$\text{Composite desirability (CD)} = [d_1^{r_1} \times d_2^{r_2} \times d_3^{r_3} \times \dots]^{\frac{1}{w}} \quad (6)$$

where  $d_i$  - individual desirability value;

$y_i$  - current value of the machining response;

$y_{\min}$  - minimum value of the machining response;

$y_{\max}$  - maximum value of the machining response;

$r$  - weightage to the individual machining response,  $w$  = number of machining responses

The composite desirability value for all sets of experiments is calculated using Equation (6). It is estimated as the geometric mean of the individual desirability values of the machining responses. The maximum composite desirability value indicates optimal machining parameters for multiple machining responses.

**Table 2.** Experimental plan and machining responses under dry turning

S. No	Machining Parameters			Machining responses		
	$v$ (rpm)	$f$ (mm/rev)	$a_p$ (mm)	$T$ (°C)	Ra ( $\mu\text{m}$ )	MRR (g/min)
1	700	0.06	0.35	140.50	0.454	16.056
2	700	0.12	0.7	196.25	0.936	72.000
3	700	0.18	1.05	244.25	2.114	132.300
4	800	0.06	0.7	210.25	0.963	49.524
5	800	0.12	1.05	274.25	1.634	100.800
6	800	0.18	0.35	192.00	1.268	77.143
7	900	0.06	1.05	293.50	1.726	56.786
8	900	0.12	0.35	215.25	1.099	49.286
9	900	0.18	0.7	236.75	2.076	113.400

Machining responses for enhanced machining performance during AISI 630 stainless steel turning are investigated under a dry environment. The machining responses are measured online and offline. The tool-work interface temperature is measured during the turning process (online). Surface roughness and material removal rate are measured after turning (offline). The machining parameters for the process and its resultant machining responses are presented in Table 2.

## 5. Results and discussion

Machining responses depend on several factors, such as cutting tool and workpiece material, machining environment, and parameters. Among all of these, the machining parameter is the one that can be controlled during the turning process. The effect of cutting speed, feed rate, and depth of cut on tool-work interface temperature is shown in Figure 4. It is observed that the tool-work interface temperature increased with the increase in the levels of all machining parameters. The rotary movement of the workpiece resists the cutting tool's linear movement, which results in heat generation at the machining zone. Friction between the tool and workpiece is further increased when the cutting speed, feed rate, and depth of cut is increased. Hence the temperature at the interface increased. In the current study, tool-work interface temperature was increased when the cutting speed, feed rate and depth of cut increased, respectively.

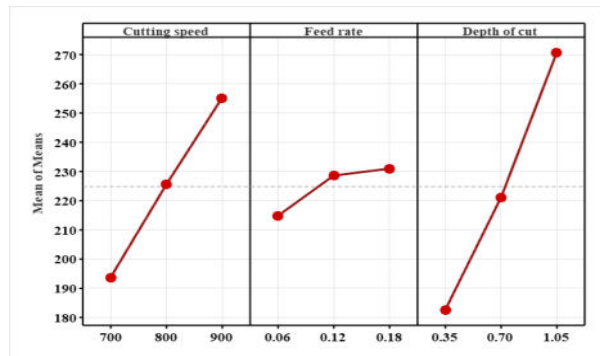


Fig. 4. - Effect of machining parameters on tool-work interface temperature

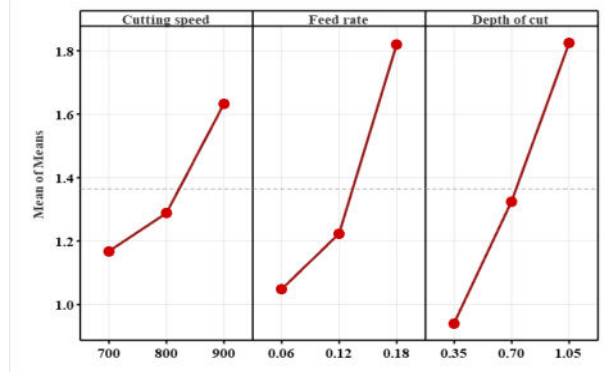


Fig. 5. - Effect of machining parameters on surface roughness

Surface roughness is the common term used in the manufacturing industry to measure the quality of the machined surface. In this study, the surface roughness of the machined workpiece was measured by varying machining parameters. Variations in surface roughness by cutting velocity, feed rate, and depth of cut are depicted in Figure 5. It was noticed that the surface roughness of the workpiece increased with increasing cutting speed. An increment in the cutting speed increases the friction between the tool and workpiece, thus resulting generation of higher tool-work interface temperature. The surface of the workpiece becomes softer due to higher temperature at the machining interface and, consequently, more adhesion of workpiece particles on the tool flank faces. This results in more tool marks on the workpiece, leading to a poor surface finish. Therefore, higher surface roughness was obtained.

It was also observed that the surface roughness value was found to increase in trend as the feed rate and depth of cut are increased, respectively. Higher cutting force and generation of heat at the machining interface caused tool marks on the machined workpiece when increasing the feed rate [31]. Surface roughness is also increased due to a built-up edge (BUE) on the cutting tool. Movement of the cutting tool is resisted by the workpiece when the depth of the cut is increased, resulting in a more BUE formation. Thus, the machined workpiece's surface roughness increased as the cut depth increased. The trends obtained from this study for surface roughness at different turning parameters concurred with the machining theory [19,32].

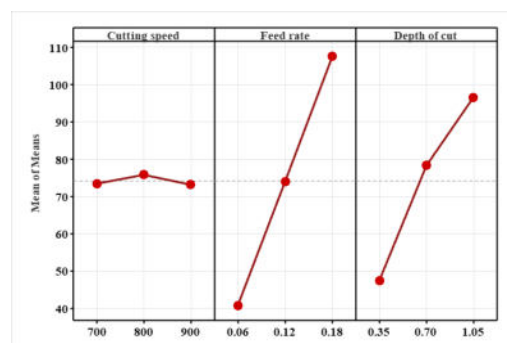


Fig. 6. - Effect of machining parameters on material removal rate

The material removal rate is the key control parameter for machining time and productivity. Higher productivity at lower machining time is achieved with higher material removal rate. The effect of cutting speed, feed rate and depth of cut on the material removal rate is shown in Figure 6. The material removal rate was found to increase when the levels of all the machining parameters increased. It is well-known that material removal rate is a function of machining parameters ( $MRR = f(\text{cutting speed}, \text{feed rate}, \text{depth of cut})$ ). Thus, higher MRR was

obtained by increasing the machining parameters. Higher material removal rate is possible when the chip reduction coefficient is lower [31,33]. This can be achieved when increasing the machining parameters.

#### 6. Identification of optimum machining parameters for individual machining responses

In any machining process, improved performance is obtained at optimum parameters. Prediction of optimum machining parameters is necessary for any machining process. Minitab 19.1 was employed to examine the machining responses, and the results of the mean S/N ratio at all levels of machining parameters were tabulated and presented. A higher value of the S/N ratio denotes the minimum changes in the difference between the expected and measured output of the process. A higher S/N ratio for the responses at each level of machining parameters is highlighted. Also, the rank for the machining parameters was awarded based on the difference between the maximum and minimum value of the S/N ratio. The rank preference was given for the machining parameters having a higher difference in the S/N ratio value. A higher mean S/N ratio for the machining parameters represents a better machining response. Based on that, the levels of machining parameters are chosen to obtain improved machining performance.

**Table 3.** Mean S/N ratio for tool-work interface temperature

Symbol	Machining parameters	Mean S/N ratio			Delta	Rank
		Level 1	Level 2	Level 3		
$v$	Cutting speed (rpm)	-45.52	-46.96	-48.07	2.55	2
$f$	Feed rate (mm/rev)	-46.25	-47.09	-47.20	0.95	3
$d$	Depth of cut (mm)	-45.09	-46.83	-48.62	3.53	1

The results of the mean S/N ratio for the tool-work interface temperature at all levels of process parameters are presented in Table 3. It is observed that the value of delta was decreased in the order of depth of cut, cutting speed, and feed rate, respectively. The depth of cut is considered the predominant parameter for the temperature. A graphical representation of the means of S/N ratio for the tool-work interface temperature at various levels of machining parameters is shown in Figure 7. It is clearly seen that the maximum S/N ratio was found at the cutting speed of 700 rpm, feed rate of 0.06 mm/rev, and depth of cut of 0.35 mm. Hence, the levels of machining parameters  $v_1 - f_1 - d_1$  were chosen as the predicted optimum machining parameter at which lower tool-work interface temperature was obtained.

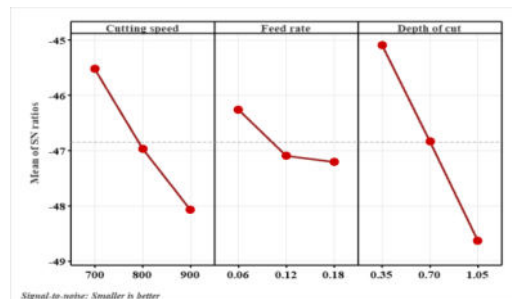


**Fig.7.** - Mean of S/N ratio of tool-work interface temperature

The results of the mean S/N ratio for the surface roughness at all levels of machining parameters are presented in Table 4. It was observed that the value of delta is decreased in the order of depth of cut, feed rate, and cutting speed, respectively. The depth of cut was considered the most predominant machining parameter for surface roughness. The means of the S/N ratio for surface roughness at various levels of machining parameters is shown graphically in Figure 8. It is seen that a cutting speed of 700 rpm, feed rate of 0.06 mm/rev, and depth of cut of 0.35 mm is found as the level of machining parameters where the maximum S/N ratio was obtained. Hence,  $v_1 - f_1 - d_1$  was chosen as levels of machining parameters and considered as the predicted optimum machining parameter, which provided lower surface roughness.

**Table 4.** Mean S/N ratio for surface roughness

Symbol	Machining parameters	Mean S/N ratio			Delta	Rank
		Level 1	Level 2	Level 3		
$v$	Cutting speed (rpm)	0.3104	-2.0000	-3.9684	4.2789	3
$f$	Feed rate (mm/rev)	0.8152	-1.5035	-4.9697	5.7849	2
$d$	Depth of cut (mm)	1.3255	-1.8142	-5.1693	6.4948	1

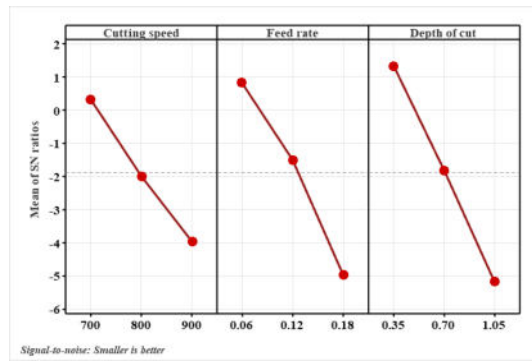


Fig. 8. - Mean of S/N ratio of surface roughness

Table 5. Mean of S/N ratio for material removal rate

Symbol	Machining parameters	Mean S/N ratio			Delta	Rank
		Level 1	Level 2	Level 3		
$v$	Cutting speed (rpm)	34.56	37.24	36.68	2.67	3
$f$	Feed rate (mm/rev)	31.03	37.02	40.42	9.39	1
$d$	Depth of cut (mm)	31.90	37.38	39.20	7.29	2

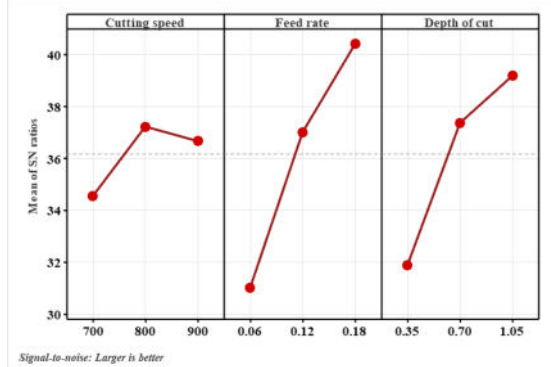


Fig. 9. - Mean of S/N ratio of material removal rate

The response table of the means of the S/N ratio for the material removal rate at all levels of machining parameters is presented in Table 5. It was found that the value of delta decreased in the order of feed rate, depth of cut, and cutting speed, respectively. The feed rate was the most predominant machining parameter, which gives a more significant delta value for the material removal rate. The means of the S/N ratio for the material removal rate for machining parameters are represented graphically in Figure 9. It is seen that the maximum S/N ratio was found at 800 rpm, 0.18 mm/rev, 1.05 mm, and it was considered as the level of machining parameters for MRR. Therefore, the levels of machining parameter  $v_2 - f_3 - d_3$  were chosen as the predicted optimum machining parameter to obtain a higher material removal rate.

### 7. Analysis of Variance

Analysis of Variance (ANOVA) is one of the statistical tools. Sir Ronald A Fisher is a British biologist who first introduced the ANOVA. It determines the most dominating independent variables on the dependent variable. It comprises the sum of squares, means squares and percentage contribution-related calculations. Identification of the dominant parameter is an essential task because it alters the machining performance of any machining process. The most dominant machining parameters on the machining are evaluated with the help of the ANOVA technique. The number of levels minus one (n-1) is the formula adopted to determine the degrees of freedom of all the machining parameters. The sum of the square was obtained when adding the square value of the difference between the machining response's mean value and the current response's value ( $\sum (y_{\text{mean}} - y_{\text{current}})^2$ ). The mean sum of the square was arrived at when taking the ratio between the sum of the square and the degrees of freedom.

The results obtained from the ANOVA for tool-work interface temperature, surface roughness and material removal rate are shown in Table 6. Among all the machining parameters, depth of cut and feed rate was found to be the most dominating parameter on the tool work interface temperature, surface roughness, and material removal rate, respectively. Depth of cut was involved in the control of temperature and surface roughness, with the highest contribution of 61.72% and 44.08%, respectively. Feed rate was involved in the control of MRR, with the highest contribution of 56.73%. In addition, cutting speed and feed rate also considerably affect temperature and surface roughness, with contributions of 32.24% and 35.42%, respectively. Hence, it is confirmed from the ANOVA results

that the depth of cut and feed rate was considered as the machining parameters which highly influence the machining responses during the turning of AISI 630 steel.

**Table 6.** ANOVA response table for the machining responses

Machining parameters	DoF	Sum of squares	Mean square	p-value	% contribution
<b>Tool-work interface temperature</b>					
Cutting speed (rpm)	2	9.7706	4.8853	0.021	32.24
Feed rate (mm/rev)	2	1.6208	0.8104	0.113	5.35
Depth of cut (mm)	2	18.7045	9.3522	0.011	61.72
Residual Error	2	0.2072	0.1036		0.68
Total	8	30.3031			100.00
<b>Surface roughness</b>					
Cutting speed (rpm)	2	27.521	13.761	0.065	19.17
Feed rate (mm/rev)	2	50.855	25.428	0.036	35.42
Depth of cut (mm)	2	63.297	31.649	0.029	44.08
Residual Error	2	1.917	0.9583		1.34
Total	8	143.591			100.00
<b>Material removal rate</b>					
Cutting speed (rpm)	2	11.929	5.965	0.301	4.99
Feed rate (mm/rev)	2	135.67	67.835	0.036	56.73
Depth of cut (mm)	2	86.419	43.21	0.056	36.13
Residual Error	2	5.139	2.569		2.15
Total	8	239.158			100.00

### 8. Regression model

The dependent variable and independent variables form the structure of the mathematical model. In a mathematical model, the independent variables evaluate the dependent variable. A mathematical model for the response was developed with the help of linear regression analysis in Minitab 19.1. The predictive mathematical model for the temperature, surface roughness and material removal rate developed by regression analysis is represented as a series of Equation 7, 8, and 9 respectively:

$$T = -125.6 + 0.3075 * v + 135.4 * f + 125.83 * d \quad (7)$$

$$R^2 = 0.9912; R^2 (\text{adj.}) = 0.9859$$

$$Ra = -2.155 + 0.002328 * v + 6.43 * f + 1.263 * d \quad (8)$$

$$R^2 = 0.9472; R^2 (\text{adj.}) = 0.9155$$

$$MRR = -40.6 - 0.0015 * v + 556.9 * f + 70.19 * d \quad (9)$$

$$R^2 = 0.9785; R^2 (\text{adj.}) = 0.9656$$

The accuracy of the predictive mathematical model was verified by the coefficient of determination  $R^2$ . The range of  $R^2$  values varies from 0 to 1. The independent and dependent variables are a good fit when the  $R^2$  value is close to unity. Equation (7) represents the predicted mathematical model for tool-work interface temperature. The  $R^2$  and adjusted  $R^2$  values were obtained as 0.9912 and 0.9859, respectively. Equation 8 represents the predicted mathematical model for surface roughness.  $R^2$  and adjusted  $R^2$  values are found as 0.9472 and 0.9155, respectively. Material removal rate at any level of machining parameters is determined using Equation 9. The  $R^2$  and adjusted  $R^2$  values for the material removal were found as 0.9758 and 0.9656, respectively. The obtained  $R^2$  value for all three machining responses is close to the unit, and the variables fit well.

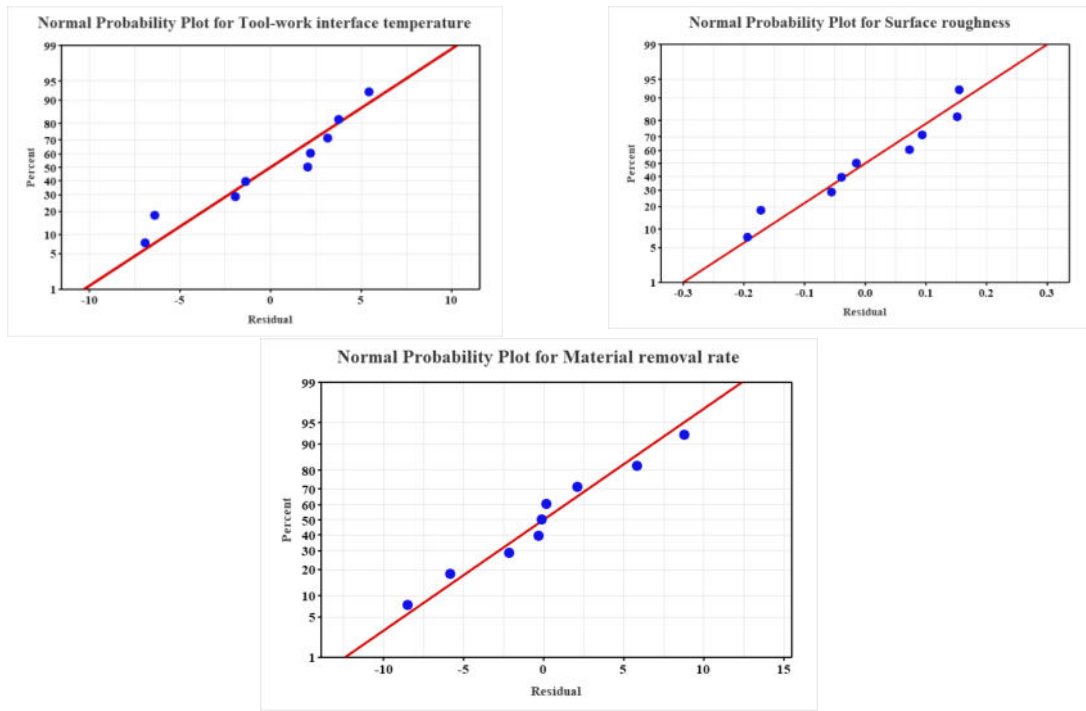


Fig. 10. - Residual plot for all the machining responses

The implication of the coefficients in the predicted model was verified by using a residual plot. The straight-line residual plot represents the residue errors in the predicted model following normal distribution, and the coefficients are significant. The residual plots for tool-work interface temperature, surface roughness and material removal rate are depicted in Figure 10. It is noticed from the plot that residuals are accumulated near the straight line in the plot for surface roughness. Hence, the coefficients in the mathematical model are valid for corresponding process parameters.

**9. Confirmation test**

A confirmation test has to be performed to examine the predicted model. The results of all the machining responses obtained during the confirmation test are given in Table 7.

**Table 7.** Confirmation test results

Run	TWIT (°C)		Ra (µm)		MRR (g/s)		Error (%)		
	Exp.	Reg.	Exp.	Reg.	Exp.	Reg.	TWIT	Ra	MRR
3	244.25	246.144	2.114	1.958	132.3	132.292	-0.775	7.372	0.006
5	274.25	268.770	1.634	1.805	100.8	98.728	1.998	-10.474	2.056
6	192.00	188.813	1.268	1.307	77.143	83.009	1.660	-3.064	-7.603
8	215.25	211.439	1.099	1.154	49.286	49.445	1.771	-4.991	-0.322

The test was conducted by choosing the response randomly from the design of the experiments. It is seen from Table 10 that variation in the percentage of residual error among the experimental and predicted model was observed within 10%. Hence, machining responses obtained from experiments had good agreement with the results determined by the predicted model.

**10. Determination of optimum machining parameter**

Each level of machining parameter and its response sets up the desired objective for the machining process. The desired objective (enhanced machining performance) of the process is achieved through optimization. The objective is obtained in a specific range by setting the machining parameters from low to high. Lower tool-work interface temperature, surface roughness, and higher material removal rate are the quality characteristics that enhance machining performance. It is necessary to combine all three machining responses for better performance. Taguchi-desirability function analysis (DFA) determines the optimum machining parameters for multiple responses.

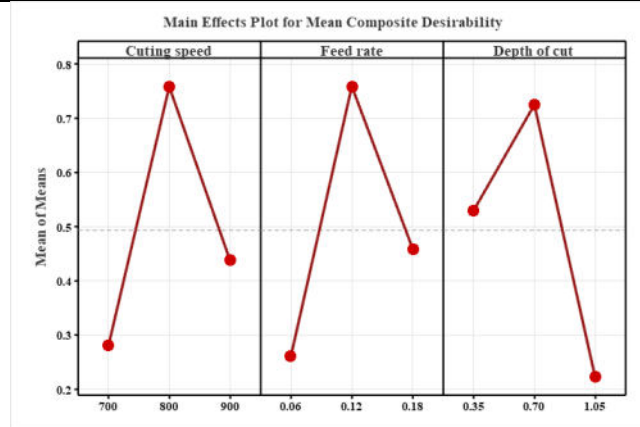
**Table 8.** Composite desirability values for experimental run

Run	Machining responses			Individual desirability			Composite Desirability	Rank
	T	Ra	MRR	T	Ra	MRR		
1	140.50	0.454	16.056	1.0000	1.0000	0.0000	0.0000	7
2	196.25	0.936	72.000	0.8599	0.8921	0.7839	0.8440	1
3	244.25	2.114	132.300	0.6856	0.0000	1.0000	0.0000	7
4	210.25	0.963	49.524	0.8166	0.8852	0.6606	0.7816	3
5	274.25	1.634	100.800	0.5014	0.6615	0.9001	0.6684	5
6	192.00	1.268	77.143	0.8723	0.7989	0.8071	0.8255	2
7	293.50	1.726	56.786	0.0000	0.6163	0.7052	0.0000	7
8	215.25	1.099	49.286	0.7999	0.8489	0.6590	0.7649	4
9	256.75	2.076	113.400	0.6219	0.2843	0.9426	0.5503	6

Minimum tool-work interface temperature and surface roughness were obtained at  $v_1 - f_1 - d_1$ , whereas the maximum material removal rate was at  $v_2 - f_3 - d_3$ . The levels of machining parameters satisfy the requirement for temperature and surface roughness but do not meet for material removal rate. Hence, Taguchi-DFA was implemented to optimize the machining parameter, improving the machining performance. Machining responses for all experimental design and their corresponding desirability values, followed by composite desirability values, is presented in Table 8.

**Table 9.** Response values for mean composite desirability

Symbol	Machining parameters	Mean composite Desirability			Delta	Rank
		Level 1	Level 2	Level 3		
$v$	Cutting speed (rpm)	0.2813	0.7585	0.4384	0.4771	3
$f$	Feed rate (mm/rev)	0.2605	0.7591	0.4586	0.4986	2
$d$	Depth of cut (mm)	0.5301	0.7253	0.2228	0.5025	1

**Fig. 11.** - Mean composite desirability values for optimum machining parameters

The highest composite desirability was found in experiment 2, with a value of 0.844. The corresponding individual desirability values for temperature, surface roughness and material removal rate were obtained as 0.8599, 0.8921 and 0.7839, respectively. Experiment 2 was considered the optimum machining parameter, enhancing the machining performance. Further, it was verified by employing the Taguchi technique. Means of composite desirability values were determined for all the experimental runs and presented in Table 9. The effect of the machining parameter on mean composite desirability is illustrated in Figure 11. It is clearly seen that the highest mean desirability value for cutting speed, feed rate and depth of cut was observed at parameter levels 2, 2 and 2, respectively. Hence, the optimum machining parameter for simultaneous optimization of multiple machining responses in the current study was obtained as  $v_2 - f_2 - d_2$ , i.e., 800 rpm, 0.12 mm/rev and 0.7 mm.

## Conclusions

The study experimentally investigated temperature, surface roughness, and material removal rate by varying the machining parameters in turning AISI 630 steel in a dry environment. The optimum machining parameter was determined using Taguchi-based desirability function analysis to enhance the machining performance. The following conclusions are drawn based on the statistical analysis carried out for experimental results:

- Depth of cut was found as the most influencing parameter on the tool-work interface temperature and surface roughness. Depth of cut influenced the temperature and surface roughness with contributions of 61.72% and 44.08%, respectively.
- Feed rate was observed as the most influencing parameter on the material removal rate, contributing to 56.73%.
- Individual optimum machining parameter for tool-work interface temperature and surface roughness was identified as  $v_1 - f_1 - d_1$ , whereas  $v_2 - f_3 - d_3$  was noted for material removal rate.
- Mathematical models were developed for tool-work interface temperature, surface roughness, and material removal rate. All models were found to be significant, with the value of  $R^2$  as 0.9912, 0.9472, and 0.9758, respectively.
- Taguchi-Desirability Function Analysis confirmed the optimum machining parameter as 800 rpm, 0.12 mm/rev, and 0.7 mm ( $v_2 - f_2 - d_2$ ) at a desirability value of 0.844.

## References

- [1] Molaei, R., Fatemi, A. and Phan, N., 2020. Multiaxial fatigue of LB-PBF additive manufactured 17-4 PH stainless steel including the effects of surface roughness and HIP treatment and comparisons with the wrought alloy. *International Journal of Fatigue*, 137, p.105646.
- [2] Saha, N., Basu, J., Sen, P. and Majumdar, G., 2020. Electrochemical behaviour of martensitic stainless steel with blood. *Materials Today: Proceedings*, 26, pp.677-680.
- [3] Bressan, J.D., Daros, D.P., Sokolowski, A., Mesquita, R.A. and Barbosa, C.A., 2008. Influence of hardness on the wear resistance of 17-4 PH stainless steel evaluated by the pin-on-disc testing. *Journal of materials processing technology*, 205(1-3), pp.353-359.
- [4] Sathyanath, A. and Meena, A., 2020. Microstructural evolution and strain hardening behavior of heat-treated 17-4 PH stainless steel. *Materials Today Communications*, 25, p.101416.
- [5] Coseglio, M.S.D.R., 2017. Sulphide stress cracking of 17-4 PH for applications in oilfield components. *Materials Science and Technology*, 33(16), pp.1863-1878.
- [6] Arisoy, C.F., Başman, G. and Şeşen, M.K., 2003. Failure of a 17-4 PH stainless steel sailboat propeller shaft. *Engineering Failure Analysis*, 10(6), pp.711-717.
- [7] Mutlu, I. and Oktay, E., 2013. Characterization of 17-4 PH stainless steel foam for biomedical applications in simulated body fluid and artificial saliva environments. *Materials Science and Engineering: C*, 33(3), pp.1125-1131.
- [8] Leksycki, K., Feldshtein, E., Królczyk, G.M. and Legutko, S., 2020. On the chip shaping and surface topography when finish cutting 17-4 PH precipitation-hardening stainless steel under near-dry cutting conditions. *Materials*, 13(9), p.2188.
- [9] Fernando, W.L.R., Sarmilan, N., Wickramasinghe, K.C., Herath, H.M.C.M. and Perera, G.I.P., 2020. Experimental investigation of minimum quantity lubrication (MQL) of coconut oil based metal working fluid. *Materials Today: Proceedings*, 23, pp.23-26.
- [10] Sivaiah, P. and Chakradhar, D., 2017. Machinability studies on 17-4 PH stainless steel under cryogenic cooling environment. *Materials and Manufacturing Processes*, 32(15), pp.1775-1788.
- [11] Sivaiah, P. and Chakradhar, D., 2018. Comparative evaluations of machining performance during turning of 17-4 PH stainless steel under cryogenic and wet machining conditions. *Machining Science and Technology*, 22(1), pp.147-162.
- [12] Kuram, E., Ozcelik, B. and Demirbas, E., 2012. Environmentally friendly machining: vegetable based cutting fluids. In *Green manufacturing processes and systems* (pp. 23-47). Berlin, Heidelberg: Springer Berlin Heidelberg.
- [13] Sarhan, A.A., Sayuti, M. and Hamdi, M., 2012. Reduction of power and lubricant oil consumption in milling process using a new SiO<sub>2</sub> nanolubrication system. *The International Journal of Advanced Manufacturing Technology*, 63, pp.505-512.
- [14] Marksberry, P.W. and Jawahir, I.S., 2008. A comprehensive tool-wear/tool-life performance model in the evaluation of NDM (near dry machining) for sustainable manufacturing. *International Journal of Machine Tools and Manufacture*, 48(7-8), pp.878-886.
- [15] Gupta, K. and Laubscher, R.F., 2017. Sustainable machining of titanium alloys: a critical review. *Proceedings of the Institution of Mechanical Engineers, Part B: Journal of Engineering Manufacture*, 231(14), pp.2543-2560.
- [16] Padmini, R., Krishna, P.V. and Mohana Rao, G.K., 2016. Experimental evaluation of nano-molybdenum disulphide and nano-boric acid suspensions in vegetable oils as prospective cutting fluids during turning of AISI 1040 steel. *Proceedings of the Institution of Mechanical Engineers, Part J: Journal of Engineering*

*Tribology*, 230(5), pp.493-505.

- [17] Amrita, M., Revuru, R.S., Siva, B. and Kamesh, B., 2021. Sustainability Analysis of Machining Inconel 718 Using Graphene-Based Nanofluids and Self-Lubricating Tools. *Smart and Sustainable Manufacturing Systems*, 5(1), pp.219-241.
- [18] Shokrani, A., Dhokia, V. and Newman, S.T., 2012. Environmentally conscious machining of difficult-to-machine materials with regard to cutting fluids. *International Journal of machine Tools and manufacture*, 57, pp.83-101.
- [19] Sivaiah, P. and Chakradhar, D., 2018. Effect of cryogenic coolant on turning performance characteristics during machining of 17-4 PH stainless steel: A comparison with MQL, wet, dry machining. *CIRP Journal of Manufacturing Science and Technology*, 21, pp.86-96.
- [20] Gajrani, K.K. and Sankar, M.R., 2020. Role of eco-friendly cutting fluids and cooling techniques in machining. *Materials forming, machining and post processing*, pp.159-181.
- [21] Debnath, S., Reddy, M.M. and Yi, Q.S., 2014. Environmental friendly cutting fluids and cooling techniques in machining: a review. *Journal of cleaner production*, 83, pp.33-47.
- [22] Duchosal, A., Werda, S., Serra, R., Courbon, C. and Leroy, R., 2016. Experimental method to analyze the oil mist impingement over an insert used in MQL milling process. *Measurement*, 86, pp.283-292.
- [23] Chuangwen, X., Ting, X., Huaiyuan, L., Zhicheng, S., Hongbing, J. and Mandong, L., 2017. Friction, wear, and cutting tests on 022Cr17Ni12Mo2 stainless steel under minimum quantity lubrication conditions. *The International Journal of Advanced Manufacturing Technology*, 90, pp.677-689.
- [24] Yan, L., Yuan, S. and Liu, Q., 2012. Influence of minimum quantity lubrication parameters on tool wear and surface roughness in milling of forged steel. *Chinese Journal of Mechanical Engineering*, 25(3), pp.419-429.
- [25] Zaman, P.B. and Dhar, N.R., 2019. Design and evaluation of an embedded double jet nozzle for MQL delivery intending machinability improvement in turning operation. *Journal of Manufacturing Processes*, 44, pp.179-196.
- [26] Gürbüz, H. and Emre Gönülaçar, Y., 2021. Optimization and evaluation of dry and minimum quantity lubricating methods on machinability of AISI 4140 using Taguchi design and ANOVA. *Proceedings of the Institution of Mechanical Engineers, Part C: Journal of Mechanical Engineering Science*, 235(7), pp.1211-1227.
- [27] Selvam, M.D. and Sivaram, N.M., 2020. A comparative study on the surface finish achieved during turning operation of AISI 4340 steel in flooded, near-dry and dry conditions. *Australian Journal of Mechanical Engineering*, 18(3), pp.457-466.
- [28] Khan, M.A., Jaffery, S.H.I., Khan, M. and Butt, S.I., 2019, November. Wear and surface roughness analysis of machining of Ti-6Al-4V under dry, wet and cryogenic conditions. In *IOP Conference Series: Materials Science and Engineering* (Vol. 689, No. 1, p. 012006). IOP Publishing.
- [29] Khan, M.A., Jaffery, S.H.I., Khan, M., Younas, M., Butt, S.I., Ahmad, R. and Warsi, S.S., 2020. Multi-objective optimization of turning titanium-based alloy Ti-6Al-4V under dry, wet, and cryogenic conditions using gray relational analysis (GRA). *The International Journal of Advanced Manufacturing Technology*, 106, pp.3897-3911.
- [30] Khan, M.A., Jaffery, S.H.I., Baqai, A.A. and Khan, M., 2022. Comparative analysis of tool wear progression of dry and cryogenic turning of titanium alloy Ti-6Al-4V under low, moderate and high tool wear conditions. *The International Journal of Advanced Manufacturing Technology*, 121(1-2), pp.1269-1287.
- [31] Sivaiah, P. and Chakradhar, D., 2018. Multi performance characteristics optimization in cryogenic turning of 17-4 PH stainless steel using Taguchi coupled grey relational analysis. *Advances in Materials and Processing Technologies*, 4(3), pp.431-447.
- [32] Sivaiah, P. and Chakradhar, D., 2019. Modeling and optimization of sustainable manufacturing process in machining of 17-4 PH stainless steel. *Measurement*, 134, pp.142-152.
- [33] Sivaiah, P. and Chakradhar, D., 2017. Multi-objective optimisation of cryogenic turning process using Taguchi-based grey relational analysis. *International Journal of Machining and Machinability of Materials*, 19(4), pp.297-312.

#### Information of the authors

**Sivakumar Subramani**, PhD, Department of Mechanical Engineering, National Institute of Technology Puducherry  
e-mail: [gabirieldee@gmail.com](mailto:gabirieldee@gmail.com)

**Ratchagaraja Dhairiyasamy**, PhD, associate professor, Department of Electronics and Communication Engineering, Saveetha School of Engineering, Saveetha Institute of Medical and Technical Sciences, Saveetha University, Centre of Research Impact and Outcome, Chitkara University Institute of Engineering and Technology  
e-mail: [ratchagaraja@gmail.com](mailto:ratchagaraja@gmail.com)

**Deepika Gabiriel**, PhD, associate professor, College of Engineering and Technology, Aksum University, Chitkara Centre for Research and Development, Chitkara University  
e-mail: [gabirieldee@gmail.com](mailto:gabirieldee@gmail.com)

## The Results of Experimental Studies of the Jet Thermal Module

Abdreshov Sh. <sup>1</sup>, Bakyt G. <sup>1\*</sup>, Sarkynov E. <sup>2</sup>, Zhakupova Zh. <sup>2</sup>, Imangaliyeva A. <sup>1</sup>, Makhimova A. <sup>1</sup>

<sup>1</sup>Mukhametzhan Tynyshbayev ALT University, Almaty, Kazakhstan

<sup>2</sup>Kazakh National Agrarian Research University, Almaty, Kazakhstan

\*corresponding author

**Abstract.** An improved design and technological scheme of a jet thermal module for efficient water heating for use in autonomous heat supply and technological processes at agricultural facilities with a brief description of its device and technological process is presented. Positive results of experimental studies and laboratory tests of the jet thermal module are given, the main parameters of which were: productivity - 1120-2145 kCal/h, water heating temperature – 34–61.5 °C (maximum - 72.7 °C), duration of water heating to operating mode – 1 - 1.5 h, water supply – 18 – 25 m<sup>3</sup>/h, the pressure of the supplied water is 25-37 m, the power consumed is 2.1 kW, the efficiency of the heat generator and the heat generating device is 0.85 – 0.95, the efficiency of the jet thermal module is 0.6 - 0.7.

**Keywords:** improved design, technological scheme, jet thermal module, experimental study, laboratory test, heat supply, positive result.

### Introduction

The article is aimed at improving the efficiency of alternative, energy-saving and environmentally friendly water heating technology for autonomous heat supply and technological processes at agricultural facilities using a jet thermal module, which, compared with analogues - electrode water heaters (boilers), reduces energy consumption by 30-50% and improves ambient air quality [1-3, 10].

In modern heat engineering systems it is important to increase the efficiency of heat exchange, reduce energy costs and increase the reliability of equipment operation. Jet heat modules represent a promising direction in the field of heat and mass transfer, as they provide high intensity of heat transfer due to the directional effect of gas or liquid jets. Their application is possible in aviation and space technology, power engineering, metallurgy, mechanical engineering and other industries where precise control of thermal processes is required [1, 2].

Despite significant progress in the development of jet thermal systems, the issues of optimisation of module design, regulation of jet flow parameters and increase of heat transfer coefficient remain relevant. Experimental studies provide accurate data on the characteristics of such modules, which contributes to the improvement of heat transfer technologies and the development of energy-efficient solutions [2].

The issues of heat transfer using jet technologies are widely studied in domestic and foreign scientific literature. Classical studies of heat transfer under the influence of gas and liquid jets are presented in the works [2, 3]. These studies consider the mechanisms of turbulent transport and heat transfer peculiarities at different modes of jet flow.

The works [2, 5] analyse the influence of flow parameters (velocity, pressure, temperature) on heat transfer efficiency. The authors note that the use of jet systems allows to significantly increase the heat transfer coefficient compared to traditional cooling and heating methods.

Current research [3, 7] focuses on numerical modelling and experimental methods for the study of jet thermal modules. They show that the choice of nozzle geometry and characteristics of the supplied flow plays a decisive role in the heat transfer efficiency. However, despite the considerable amount of theoretical and experimental work, there is still a need for a detailed study of the performance of jet heat modules under varying external conditions and different operating modes.

The present work is aimed at expanding the existing knowledge on the operation of jet thermal modules by conducting comprehensive experimental studies. In contrast to earlier works, the study considers [4]:

The influence of geometrical parameters of the nozzle system on the uniformity of heat flux distribution.

Optimal operating modes of the jet thermal module depending on the pressure and temperature of the working body.

Stability analysis of thermal characteristics under different operating conditions.

The obtained experimental data allow more accurately assess the efficiency of the jet thermal module and form recommendations for its application in various technical systems. The results of the study can be useful in the development of new energy-efficient heat exchange technologies.

The object of research is the technology of hydroheating water using a jet thermal module, technological and hydrodynamic processes occurring in a jet thermal module.

The research method. The work uses analytical and experimental studies and laboratory tests of a prototype development.

## 1. Materials and methods

A jet thermal module is a device in which a directed flow acts on a heated surface, providing intensive heat exchange. This study investigated the operation of the module using compressed air as a working body [5, 8].

The module design included the following elements[6]:

Nozzle system, providing the formation of gas flow with certain characteristics (velocity, directionality, turbulence). Nozzles of different geometry (cylindrical, conical, Laval nozzles) were used during the experiment.

A gas supply chamber stabilising the pressure and ensuring uniformity of the flow.

Fixing and guiding elements allowing to change the position of the module relative to the examined surface.

The material of the module construction is stainless steel with high temperature and corrosion resistance.

Experimental studies of the jet thermal module were carried out in several stages, including preparation of the setup, measurements, data processing and analyses of the results. This section details the methods applied in each stage of the experiment [6, 9].

Before starting the tests, the equipment was set up and calibrated [10]:

- air supply system leak check.
- calibration of the thermocouples and thermal imaging camera.
- adjustment of air supply parameters (pressure, flow rate, temperature).
- setting the heated plate in a fixed position.
- determination of reference points for temperature measurement.

Experimental studies included variation of the main parameters of the module operation and registration of thermal and aerodynamic characteristics.

The applied methods allowed to obtain accurate data on heat transfer in the jet heat module, to reveal dependences between flow parameters and heat transfer efficiency. The data can be used to optimise the design and operating modes of such systems.

Verification and refinement of the calculated parameters of the thermal module was carried out in accordance with the program, the purpose of which is to clarify the calculated limit and accept their rational values.

The inner diameter of the active ejector nozzle. The maximum vacuum created and the maximum flow rate of the sucked air by the ejector are accepted as the criterion of verification and refinement.

According to the calculation, the diameter of the active nozzle was assumed to be 8.5-21 mm, a value of 19 mm was experimentally obtained, at which a maximum vacuum of 8.4 m is created and the intake air flow rate (supply) is 210 m<sup>3</sup>/h, which is accepted as a refined parameter [4, 13].

The required flow of the centrifugal pump. According to the calculation, the pump supply is 0.00102-0.0044 m<sup>3</sup>/s, experimentally 0.003-0.0039 m<sup>3</sup>/s (11-14 m<sup>3</sup>/h), which corresponds to the calculated values and satisfies the performance of the technological process of heating water with a thermal module [8, 11].

The useful, expended power and efficiency of the jet thermal module. According to calculations, the useful power is 403.4 - 868.8 kW, the consumed power is 718.2 - 541.6 Watts and the efficiency is 0.56. Experimentally, 573 - 1479 watts, 2100 W efficiency of 0.60-0.70, which in terms of useful and expended power satisfy the calculated values, in terms of efficiency, higher values can be obtained experimentally with specified useful power for heating the room.

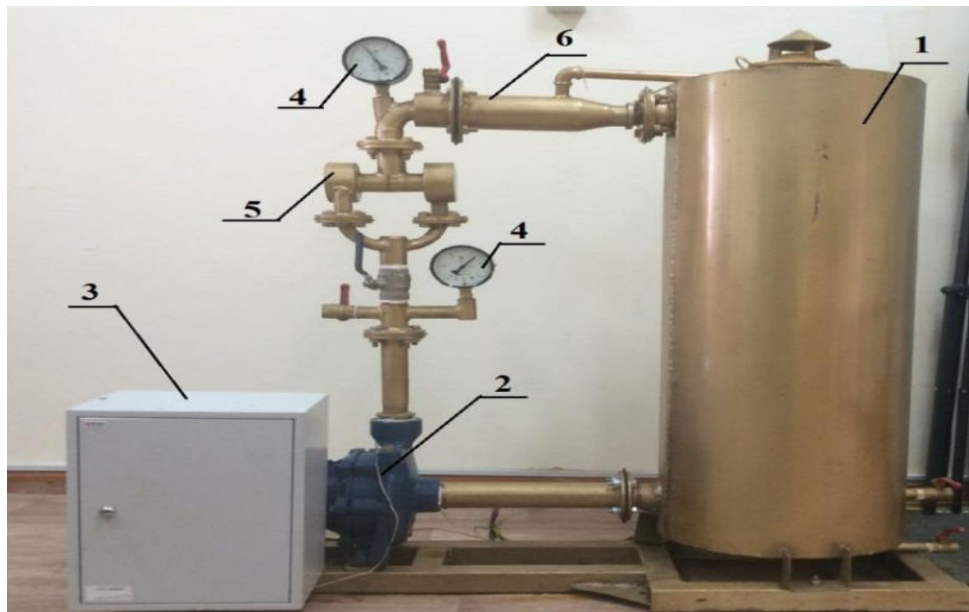
The tests of the prototype of the jet thermal module were carried out in laboratory conditions with the following initial parameters: the room is not heated with a volume of 170 m<sup>3</sup>; the volume of heated water is 70 dm<sup>3</sup>; the capacity of heated water is not insulated; the initial temperature of heated water is 18 -19.6 °C and indoor air is 15 °C; ejector parameters: the inner diameter of the active nozzle is 25mm and the mixing chamber – 34 mm; the diameter of the L-shaped passive nozzle of the heat generating device is 15 mm; the diameter of the heat generator twist chamber is 86 mm; parameters of the centrifugal pump: supply 18...25 m<sup>3</sup>/h, nominal head  $H_p = 25 -35$  m, power consumption – 1.8 – 2.1 kW [10, 12].

A general view of the prototype of the jet thermal module is shown in Figure 1.

Laboratory tests of the jet thermal module to determine its main parameters were carried out in the following sequence:

1. the thermal module assembly was installed in an unheated room, the electrical part of the centrifugal pump was connected to a single-phase electric meter, the heated water tank was filled with tap water to the level of the lower mark of the diffuser of the mixing chamber of the ejector and using a control valve on the discharge nozzle of the centrifugal pump, the pressure was set and fixed by a pressure gauge, starting with the valve fully open, and then changing upward pressure with an interval of 1-2 m [13].

after stabilization of the technological process of the thermal module at the set pressure parameter, with a time interval of 0.5 - 1 hour, the following measurements were carried out in 3-fold repetition: the temperature of the heated water in the tank according to the readings of the thermometer, the readings of the three-phase energy meter, the volume of heated water in the tank and the pump rotation speed in rpm according to the tachometer readings. The



1 – tank for heated water; 2 – centrifugal electric pump; 3 - control panel; 4 – pressure gauge; 5 – heat generator; 6 – heat generating device.

Fig. 4. - General view of the prototype of the jet thermal module

2. processing of test results based on the obtained measurements was determined using the following formulas.

The supply of the centrifugal pump was determined by the formula [14]:

$$Q_i = \frac{\sum_{i=1}^m V_i}{\sum_{i=1}^m t_i},$$

(1)

The amount of heat obtained by heating water is determined from experimental data according to the formula (9), the useful power according to (12), the consumed power according to (14) and the efficiency of the thermal module according to (16).

The power consumption of the centrifugal pump was determined by the formula [14]:

$$N_p = \frac{1}{m} \cdot k \cdot \sum_{i=1}^m (Ua + Ub + Uc), \text{ W} \quad (2)$$

The efficiency of a centrifugal pump is determined by the formula [14]:

$$\eta_p = \rho \cdot g \cdot Q_p \cdot H_p / N_p. \quad (3)$$

The efficiency of the thermal module: was determined by the formula [14]:

$$\eta = \frac{P_u}{P_s} = \frac{W_u}{W_c}. \quad (4)$$

The tests carried out on the prototype of the jet thermal module according to the developed methodology showed positive results – the thermal module is operational and meets the requirements of the technical specification for the prototype according to the main indicators obtained [15].

Laboratory tests were carried out with positive results, the main parameters of which were: productivity - 1120 - 2145 kCal/h, water heating temperature – 34 – 61.5 °C (maximum -72.7 °C), duration of water heating to operating mode – 1 - 1.5 hours, water supply – 18 – 25 m<sup>3</sup>/h, pressure of supplied water – 25-37 m, power consumption – 2.1 kW, efficiency of the heat generator and heat generating device – 0.85 – 0.95, efficiency of the jet thermal module – 0.6 - 0.7.

**Table 1.** Test results of a prototype jet thermal module

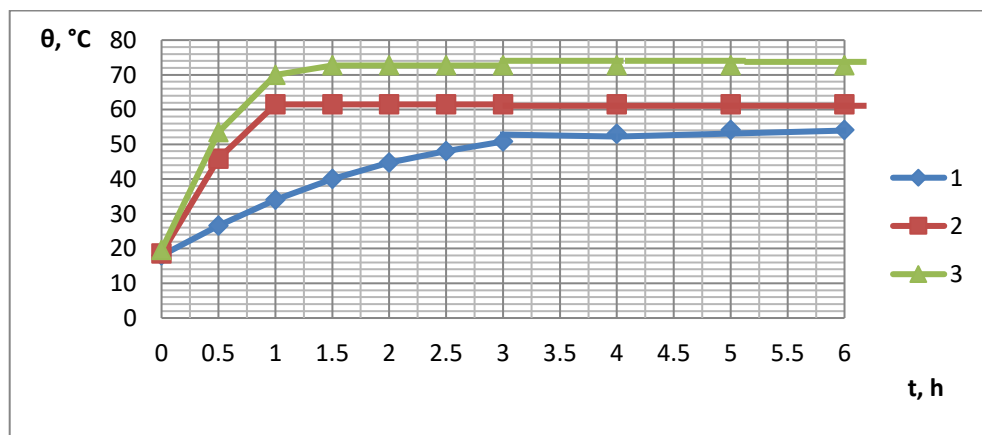
Name of indicators	Designation	Unit of measurement	The value of the indicators
Initial parameters for water heating			
The initial temperature of the heated water	$\theta$	°C	14-15
Initial indoor air temperature	$\theta_a$	°C	15-16
The volume of heated water	V	dm <sup>3</sup>	70
The main indicators of the jet thermal module			
The final temperature of the heated water	$\theta_f$	°C	54-72.7
The heat generated by heating the water	$Q_h$	kCal	602-2527
Useful thermal power	$P_u$	kW	1.47 – 1.276
Useful thermal energy	$W_u$	kWh	0.7 – 2.95
Spent thermal power	$P_s$	kW	2.1
Spent thermal energy	$W_s$	kWh	1.05 – 4.2
The vacuum created by the ejector	$H_{vac}$	m	2.8 – 8.4
Intake air flow rate (supply) by the ejector	$Q_a$	m <sup>3</sup> /h	100 – 210
Water pressure in the ejector	$H_e$	m	7 – 17.5
Efficiency of the thermal module	$\eta_{tm}$		0.7 – 0.6

## 2. Results and discussion

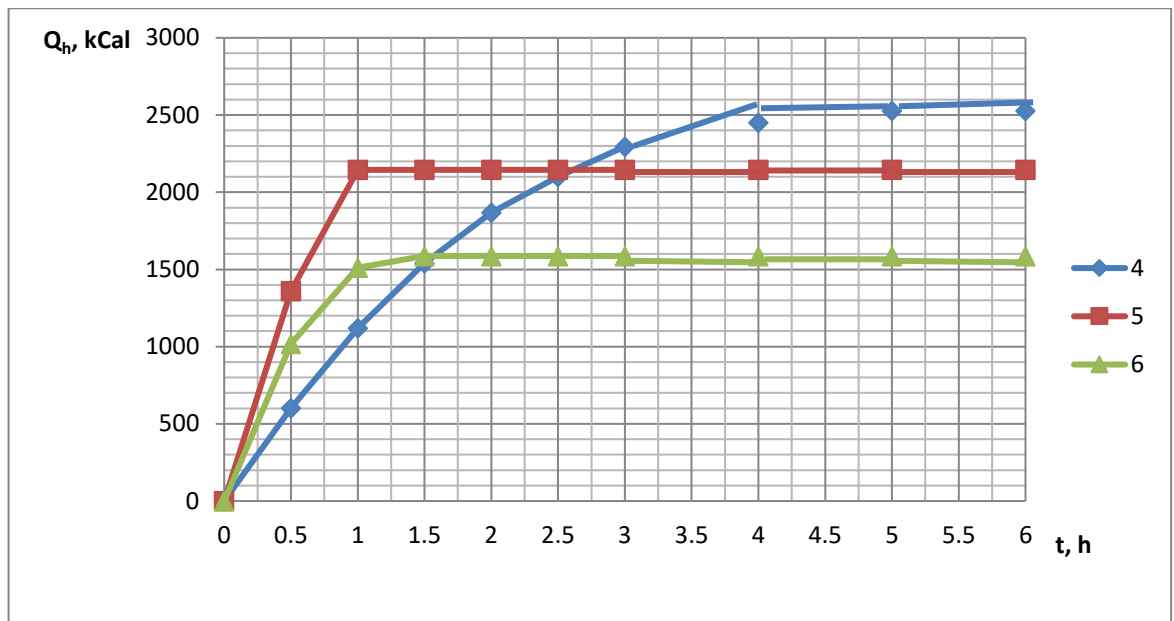
The main research of the jet thermal module was aimed at studying the technological process of the proposed jet–vacuum method of water heating, determining the essential factors affecting water heating: ejector parameters – the internal diameters of the active and passive nozzles, the amount of vacuum created in the chambers of the active and passive nozzles, air flow (gas-air mixture); parameters of the pump used – feed, pressure and efficiency; changes in technological parameters: water heating temperature, heat received, useful and expended power and useful and expended energy from the duration of water heating (operation of the thermal module) [3, 6].

We present the results obtained from experimental studies of the jet-vacuum heating method: the dependence of the temperature of the heated water, the heat received, useful and expended power, useful and expended energy on the duration of water heating, that is  $\theta_f, Q_h, P_u, P_s, W_u, W_e = f(t)$ , which are represented by graphs (Figures 2 and 3) with an optimal value of the diameter of the active nozzle of the ejector = 25 mm.

The graph (Figure 1) shows the dependences of the temperature of the heated water and the heat received on the duration of heating the water at a volume of heated water of 70 dm<sup>3</sup> (1), 50 dm<sup>3</sup> (2) and 30 (3) dm<sup>3</sup> [7].



a) 1, 2 and 3 are curves of dependence of the water heating temperature at the diameter of the active ejector nozzle of 25 mm on the heating time at the volume of heated water of 70 dm<sup>3</sup> (1), 50 dm<sup>3</sup> (2) and 30 (3) dm<sup>3</sup>;



b) 4, 5 and 6 are curves of dependence of the heat obtained when heating water at an ejector of 25 mm on the heating time at a volume of heated water of 70 dm<sup>3</sup> (4), 50 dm<sup>3</sup> (5) and 30 (6) dm<sup>3</sup>

**Fig. 2.** - Dependences of the temperature of the heated water and the heat received on the duration of water heating (operation of the thermal module) with a volume of heated water of 70 dm<sup>3</sup>, 50 dm<sup>3</sup> and 30 dm<sup>3</sup>.

During the experiments, the initial water temperature was – 18 - 19.6 °C and the final at  $V = 70 \text{ dm}^3$  (1) – 54.1 °C, at  $V = 50 \text{ dm}^3$  (2) – 61.5 °C and at  $V = 30 \text{ dm}^3$  (3) – 72.7 °C, with a decrease in the volume of heated water, the temperature of its heating. The operating time of the laboratory unit increased from 5 hours to 1.5 hours at lower costs. The total duration of the thermal module is 0.5...6 hours, depending on the installed technological and technical parameters and external influences. The thermal module was tested in an unheated room with a volume of 170 m<sup>3</sup>, the capacity of the heated water was not insulated, and therefore, simultaneously with the heating of the water, the air in the room was heated from 18 ... 19.5 °C to 23 °C [4, 8].

Curves 1, 2 and 3 (Figure 2 a) in the graph are based on experimental data, and 4, 5 and 6 (Figure 2 b) were determined using a formula using experimental data [9]:

$$Q_h = C \cdot m \cdot \Delta\theta = C \cdot V \cdot \rho \cdot \Delta\theta, \text{ kCal} \quad (5)$$

where  $C$  – specific heat capacity, kCal/kg·deg (for water  $C=1$  kCal/kg·deg);  
 $m$  – mass of heated water, kg:

$$m = V \cdot \rho, \quad (6)$$

where  $V$  – volume of heated water, m<sup>3</sup>;  
 $\rho = 1000 \text{ kg/m}^3$  – the density of the heated water;  
 $\Delta\theta$  – increasing the water heating temperature, °C:

$$\Delta\theta = \theta_f - \theta_i, \quad (7)$$

where  $\theta_i, \theta_f$  – the temperature of the heated water is initial and final, °C.

The nature of the curve changes can be clearly seen on the graphs.

It follows from the graph (Figure 1) that with increasing heating time, the temperature of the heated water and the heat received increase, the intensity of the increase is higher for the variant of the thermal module with a smaller volume of heated water, for example, during the first 0.5 hours of heating, the temperature of the heated water increases for the first variant at  $V=70 \text{ dm}^3$  - by 8.6 °C, for the second at  $V = 50 \text{ dm}^3$  - at 27.2 °C and for the third option at  $V = 30 \text{ dm}^3$  - at 33.9°C, and in 1.5 hours of operation, the water of the corresponding volume is heated by 40.0°C, 61.5 °C and 72.7 °C, reaching its maximum value, except for the option at  $V = 70 \text{ dm}^3$ , which is achieved with 5 hours of operation of the thermal module [5, 7].

At the same time, the heat obtained from the water heating is: at the volume of heated water  $V=70 \text{ dm}^3$   $Q_h = 2527 \text{ kCal}$  (at a capacity of 1120 kCal/h), at  $V=50 \text{ dm}^3$   $Q_h = 2145 \text{ kCal}$  (at a capacity of 2145 kCal/h) and at  $V=30 \text{ dm}^3$   $Q_h = 1587 \text{ kCal}$  (at capacity 11512 kCal/h), i.e. the efficiency of the technological process of water heating by

the jet-vacuum method depends on the optimization of the technological and technical parameters of the jet thermal module.

Numerical parameter data for constructing dependency curves  $P_u$  and  $W_u=f(t)$  were determined by the formula (4) and (5) using experimental data on  $Q_T$  or from the graph (Figure 3) [10]:

$$P_u = \frac{Q_h \cdot A}{t}, \text{ W} \quad (8)$$

where  $A$  – the mechanical equivalent of heat ( $A=4.2$  j/kCal);

$t$  – duration of water heating (operation of the thermal module), s.

$Q_h$  – the amount of heat obtained by heating water, kCal;

$$W_u = P_u \cdot T, \text{ kW}\cdot\text{h} \quad (9)$$

where  $P_u$  – useful power, kW;

$T$  – operating time of the thermal module, h.

The numerical values of the consumed power and energy are determined from experimental data using the formulas [10]:

$$P_s = \frac{\rho \cdot g \cdot Q_p \cdot H_p}{\eta_p}, \text{ W} \quad (10)$$

where  $\rho = 1000$  kg/m<sup>3</sup> is the density of the heated water;

$g = 9.81$  m/s<sup>2</sup> – acceleration of free fall;

$Q_p$  – heat module pump supply at operating pressure  $H_p$ , m<sup>3</sup>/s;

$H_p$  – working pressure of the pump, m;

$\eta_p$  – the efficiency of the pump used in the thermal module;

$$W_c = P_s \cdot T, \text{ kWh} \quad (11)$$

where  $P_s$  – power consumption, kW;

$T$  – operating time of the thermal module, h

Curves  $P_u$  and  $P_c$  (Figure 2)  $P=f(t)$  and curves  $W_u$ ,  $W_c$   $W=f(t)$  the graph is based on experimental data using formulas (6), (7) or obtained from the readings of a three-phase active energy meter, the heat module installed on the electric drive of the centrifugal pump, in terms of full capacity, taking into account  $\cos\varphi = 0.8$  according to the formula [10]:

$$W_c = W_a / \cos\varphi, \quad (12)$$

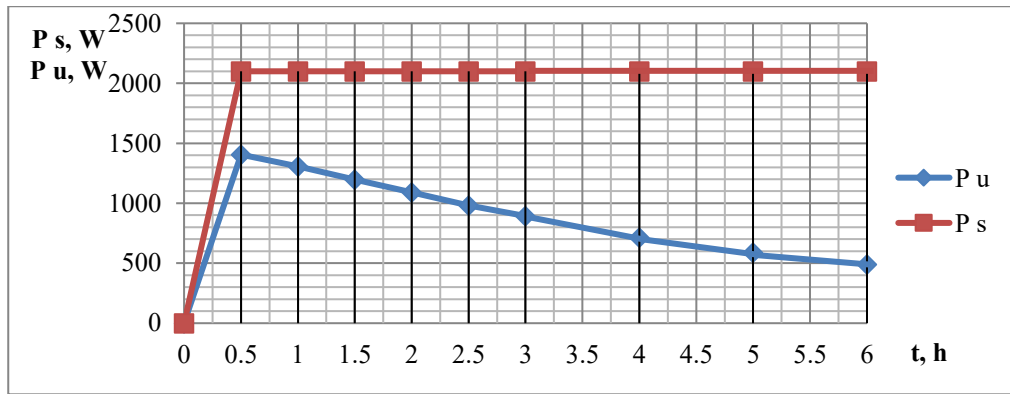
where  $W_a$  – useful active energy according to the readings of a three-phase active energy meter, kW·h.

It can be seen from the graph (Figure 3) that the curves of useful thermal power and energy  $P_u$ ,  $W_u=f(t)$  they have a curvilinear dependence with a maximum in the first hour of heating, and the remaining curves  $P_s$  and  $W_c=f(t)$  they have straightforward dependencies.

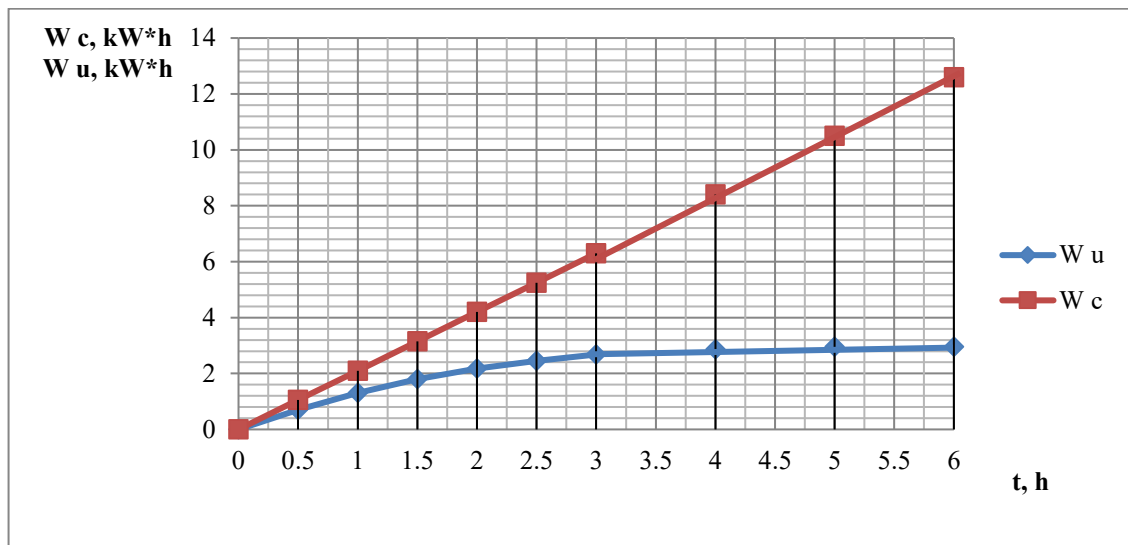
On the graph (Figure 3) dependencies  $P_s=f(t)$  and  $W_c=f(t)$  they show the total energy costs of the entire jet thermal module, which amount to 2100 W of power or 1.05- 12.6 kW·h of energy, and dependencies  $P_u=f(t)$  and  $W_u=f(t)$  they show the useful thermal power - 0.49 – 1.4 kW and useful thermal energy – 0.70 – 2.95 kW·h only for heating water without taking into account the useful costs of heating a room in the volume of 170 m<sup>3</sup>, which was heated due to an unheated water heating tank [1, 6].

It follows from the graph (Figure 4) that the indoor air heating temperature increases in a straight-line relationship with an increase interval of 1 °C per hour of operation of the heating module with a small useful power in the range of 61 - 82 Watts, and the total useful power when heating water and indoor air varies according to curvilinear dependence with a maximum in the first 1 - 1.5 hours of operation of the thermal module with an efficiency of 0.7 – 0.6.

The pressure losses in the discharge pipeline were experimentally determined: for the variant of the thermal module with an internal diameter of the active nozzle of 25 mm, the losses were 2.3-3.1 m; at 15 mm, 4.7-5.1 mm, which correspond to the calculated data.



a) — curves of the dependence of the useful thermal power and the expended one with a diameter of the active nozzle of the ejector of 25 mm on the heating time with a volume of heated water of 70 dm<sup>3</sup>



b) — curves of the dependence of the useful thermal energy and the spent at the ejector of 25 mm on the heating time at a volume of heated water of 70 dm<sup>3</sup>.

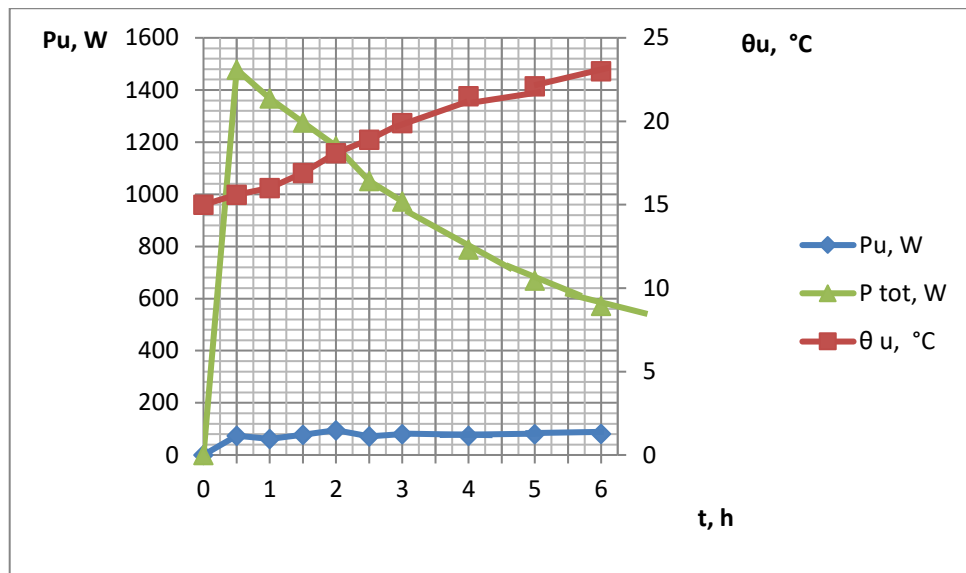
**Fig. 3.** - Dependences of useful thermal power and spent and useful and spent energy on the duration of water heating (operation of the thermal module)

The graph (Figure 4) shows the dependences of the temperature of the heated indoor air, the useful thermal power when heating the air and the total useful power when heating water and indoor air on the duration of heating the indoor air (operation of the thermal module) with a volume of heated water of 70 dm<sup>3</sup> and a volume of 170 m<sup>3</sup> [11].

As a result of studies of the technological process of heating water with a jet thermal module, it was found that the heating process is carried out in all modes of operation of the centrifugal pump with a supply from 18 m<sup>3</sup>/h at a nominal head of 35 m of a water column to 21.5 m<sup>3</sup>/h at H<sub>P</sub> = 25 m, as well as at a head of 6-8 m and the main parameters of the ejector: internal the diameter of the active nozzle is 8-25mm and the vacuum created in the chamber of the active nozzle is 0.8–2.8 m, the passive nozzle is 2.0-8.5 m and the mixing chamber is 0.2-1.2 m.

However, the heating intensity of an equal volume of water is higher with a larger pump supply and a larger amount of vacuum created, as well as the use of heat extraction from the heated air in the upper part of the tank.

Investigation of the ejector vacuuming process [10, 11] in accordance with the accepted program of experimental studies, the purpose of which is to determine the vacuum pressure created by the ejector in an additional passive nozzle, a passive nozzle of the ejector housing and mixing chamber depending on the inner diameter of the active ejector nozzle and the water pressure in the ejector; determination of the flow rate (supply) of the sucked air by the ejector through the air inlet pipes of the additional passive nozzle and the passive nozzle of the housing, depending on the water pressure in the ejector and the vacuum created by the ejector.



$\theta_{ha}$  - the curve of dependence of the temperature of the heated air in the room on the duration of heating (operation of the thermal module), °C;  $P_{ha}$  - the curve of the dependence of the useful thermal power when heating indoor air on the heating time, W;

**Fig. 4.** - Dependences of the temperature of the heated indoor air, the useful thermal power when heating the air and the total useful power when heating water and indoor air on the duration of heating the indoor air (operation of the thermal module) with a volume of heated water of 70 dm<sup>3</sup> and a volume of 170 m<sup>3</sup>

The need for these studies is to determine the possibility of using water heating by heat extraction from air sucked in by the ejector or gas-air mixtures, as well as cleaning polluted indoor air from dust, solid particles and odors.

The research results showed that with an increase in the supplied water pressure into the ejector, the vacuum pressure created in the ejector increases for all values of the diameter of the active nozzles of the ejector, however, the greatest vacuum pressure is created with a nozzle with a diameter of 19 mm, its value reaches 8.4 m at a pressure of 14.5 m. At the same time, the maximum consumption of the sucked air by the ejector is 210 m<sup>3</sup>/h through the air inlet of the additional passive nozzle and 160 m<sup>3</sup>/h through the air inlet of the passive nozzle of the ejector body [12].

Thus, the obtained results of studies of the thermal module for the created vacuum and the received supply confirm the need for its use both to increase the efficiency of water heating from the use of heat extraction of sucked air or gas-air mixtures, and to expand the scope of its use for cleaning indoor air from dust, solid particles and odors.

## Conclusions

In the course of experimental studies of the jet heat module, important results have been obtained, allowing to evaluate its efficiency and prospects of application in various heat engineering systems. The tests have shown that this module provides uniform distribution of heat flow, high degree of heat transfer and stability of operation in a wide range of parameters.

The analysis of thermal characteristics has shown that optimisation of nozzle element geometry and modes of working substance supply allows to significantly increase the heat transfer coefficient. Experiments have confirmed that the use of a jet thermal module contributes to the reduction of temperature gradients on the heated surface, which is especially important for precision thermal processes.

Experimental studies were carried out, experimental and experimental samples of the jet thermal module were developed and manufactured, and laboratory tests were carried out with positive results, the parameters of which were: productivity - 1120 - 2145 kCal/h, water heating temperature - 34 - 61.5 °C (maximum -72.7 °C), the duration of water heating to operating mode - 1 - 1.5 hours, water supply - 18-25 m<sup>3</sup>/h, pressure of the supplied water - 25-37 m, power consumption - 2.1 kW, efficiency of the heat generator and heat-generating device - 0.85 - 0.95, efficiency of the jet thermal module - 0.6 - 0.7.

The results obtained can be used to improve heat exchange technologies in power systems, industry and transport. Further research will be aimed at developing new design solutions, improving energy efficiency and expanding the application areas of jet heat modules.

## References

- [1] Robert D. Plant, Jacob Friedman, M. Ziad Saghir, A review of jet impingement cooling, *International Journal of Thermofluids*, Vol. 17, 2023, 100312, <https://doi.org/10.1016/j.ijft.2023.100312>.
- [2] Zhao X., Zhang B., Yang Z., Zhao Y. Surface orientation effects on heat transfer performance of spray cooling. *Int. J. Heat Mass Transf.*, 147 (2020), Article 118960, <https://doi.org/10.1016/j.ijheatmasstransfer.2019.118960>.
- [3] Abdullayeva, A., Kalabayeva, A., Ivanov, A., Abdullayev, S., Bakyt, G. *Methods for identification of complex industrial control objects on their accelerating characteristics*. *Communications - Scientific Letters of the University of Žilina*, 2022, 24(3), pp. B239–B246. <https://doi.org/10.26552/com.C.2022.3.B239-B246>.
- [4] Mishra A., Yadav H., Djenidi, L., Agrawa, A. Experimental study of ow characteristics of an oblique impinging jet. *Experiments in Fluids* (2020) 61:90 <https://doi.org/10.1007/s00348-020-2923-y>.
- [5] Chen, J. Wang, X., Shi, H., Si, J. Experimental investigation on flow characteristics of vertical and oblique circular impinging jet. *Physics of Fluids*, 2023, 35(5), <https://doi.org/10.1063/5.0152514>.
- [6] Azilkiyasheva M.M., Shayakhmetov, S.B., Bakyt G.B., Kopenov B.T., Baubekov Ye.Ye., Zhauyt A. Development of a method for calculating the degree of use of the plasticity resource (Dupr) when rolling on a new continuous mill. *Metalurgija*, 2021, 60(3-4), pp. 362–364.
- [7] Abdelaziz A. and Khayat R. E. On the non-circular hydraulic jump for an impinging inclined jet,” *Phys. Fluids* 34(2), 023603 (2022). <https://doi.org/10.1063/5.0079563>.
- [8] Pak I., Experimental study of the ultrasonic muffler efficiency for improving the exhaust gas cleaning system of internal combustion engines of automobiles. *Material and Mechanical Engineering Technology*, №2, 2024, 53–63. [https://doi.org/10.52209/2706-977X\\_2024\\_2\\_5](https://doi.org/10.52209/2706-977X_2024_2_5).
- [9] Cafiero G. Obligado M., Vassilicos, J. C. Length scales in turbulent free shear flows, *J. Turbul.* 21(4), 243–257 (2020). <https://doi.org/10.1080/14685248.2020.1752376>.
- [10] Abdullayev S., Tokmurzina-Kobernyak N., Ashirbayev G., Bakyt G., Izbaïrova A. (2024). Simulation of spring-friction set of freight car truck, taking into account track profile. *International Journal of Innovative Research and Scientific Studies*, 7(2), 755–763. <https://doi.org/10.53894/ijirss.v7i2.2883>
- [11] Chee M. , Chauhan P. , Georgiou J., Wilson D. Flow distribution in the liquid film created by a coherent circular water jet impinging obliquely on a plane wall, *Exp. Therm. Fluid Sci.* 140, 110748 (2023). <https://doi.org/10.1016/j.exptthermflusci.2022.110748>.
- [12] Mishra A. , Djenidi L., Agrawal, A. Flow characterization in the uphill region of pulsed oblique round jet, *Phys. Fluids* 34(3), 035113 (2022). <https://doi.org/10.1063/5.0084329>.
- [13] Shalbayev K., Abdullayev S., Mazhitov S., Bakyt G. Hydrogen Generator for internal Combustion Engine. *Journal of Applied Research and Technology*, 21(4), 535–541. <https://doi.org/10.22201/icat.24486736e.2023.21.4.1963>.
- [14] Raizner M., Rinsky V., Grossman G., Van Hout R. The effect of jet pulsation on the flow field of a round impinging jet and the radially expanding wall jet,” *Int. J. Heat Mass Transfer* 140, 606–619 (2019). <https://doi.org/10.1016/j.ijheatmasstransfer.2019.06.024>.
- [15] Abdullayev S., Bakyt G., Abdullayeva A., Duisembayeva B., Askenov Y., Ashirbayev G., Besekenov R. Testing of railway equipment for the impact on the track and turnouts. *Communications - Scientific Letters of the University of Žilina* [online]. 2024, 26(2), p. B99-B107. ISSN 1335-4205, eISSN 2585-7878. <https://doi.org/10.26552/com.C.2024.020>.

## Information of the authors

**Abdreshov Shamil**, PhD, assistant professor, Mukhametzhan Tynyshbayev ALT University  
e-mail: [a\\_shamil-80@mail.ru](mailto:a_shamil-80@mail.ru)

**Bakyt Gabit**, PhD, associate professor, Mukhametzhan Tynyshbayev ALT University  
e-mail: [gaba\\_b@bk.ru](mailto:gaba_b@bk.ru)

**Sarkynov Erbol**, candidate of technical sciences, associate Professor, Mukhametzhan Tynyshbayev ALT University  
e-mail: [verbol.sarkynov@kaznaru.edu.kz](mailto:verbol.sarkynov@kaznaru.edu.kz)

**Zhakupova Zhanar**, PhD, assistant professor, Mukhametzhan Tynyshbayev ALT University  
e-mail: [zhakupova.zhanar@kaznaru.edu.kz](mailto:zhakupova.zhanar@kaznaru.edu.kz)

**Imangaliyeva Aizhan**, candidate of technical sciences, associate professor, Mukhametzhan Tynyshbayev ALT University  
e-mail: [kiraiya@mail.ru](mailto:kiraiya@mail.ru)

**Makhimova Almira**, PhD, teaching assistant, Mukhametzhan Tynyshbayev ALT University  
e-mail: [almira\\_88s@mail.ru](mailto:almira_88s@mail.ru)

## Theoretical and Experimental Analysis of Ultrasonic Cleaning of Internal Combustion Engine Radiators with the Development of Practical Recommendations

Sinelnikov K.A., Moldabaev B.G., Zhunusbekova Zh.Zh., Kukesheva A.B.\*

Abylkas Saginov Karaganda Technical University, Karaganda, Kazakhstan

\* corresponding author

**Abstract.** The article presents the results of studies on ultrasonic cleaning of radiators in internal combustion engine cooling systems. The aim of the research is to identify the dependencies affecting the efficiency of ultrasonic cleaning of internal combustion engine radiators, as well as to develop recommendations for further research. Using the theory of similarity and dimensional analysis, critical dependencies were established, allowing for the determination of the energy efficiency of the cavitation process and the assessment of the cleaning effectiveness of the radiator using ultrasound. The obtained theoretical dependencies were experimentally validated, and their numerical values were determined. Based on these recommendations, a flowchart was developed that outlines the sequence of the radiator tube cleaning process using ultrasound, taking into account improvements in design and changes in the testing methodology.

**Keywords:** car, internal combustion engine, cooling system, radiator, cavitation, similarity theory and dimensional analysis.

### Introduction

Cleaning the cooling systems of internal combustion engines remains a relevant task, especially when vehicles are operated in conditions that promote the formation of scale and contamination. It is known that traditional cleaning methods, such as mechanical and chemical approaches, have a number of drawbacks. Mechanical methods can lead to damage to the tubes and other radiator components. Chemical compounds do not always provide complete cleaning and also damage the radiators due to their corrosive effects.

Ultrasonic treatment, based on the phenomenon of cavitation, generates microscopic bubbles in the liquid that release high energy in the form of shockwaves and microjets when they collapse. This process effectively removes scale and other contaminants from the internal surfaces of radiator tubes without damaging their structure. Unlike mechanical methods, ultrasound penetrates difficult-to-reach areas, such as tube bends and small channels, ensuring a more uniform and thorough cleaning.

Ultrasonic cleaning is also environmentally friendly, as it does not require the use of aggressive chemical reagents, and the process can be adjusted to minimize the impact on radiator materials. By regulating the parameters of ultrasonic treatment, the method can be adapted to different types of radiators and contamination levels, ensuring high cleaning efficiency without the risk of damage.

The hypothesis of the study is the probability of radiator cleaning through ultrasonic treatment.

The aim of the study is to establish the dependencies that determine the effectiveness of the ultrasonic cleaning process for internal combustion engine radiators and to develop recommendations for further research.

To achieve the research goal, the following tasks were addressed: the physical essence of the cavitation process was considered; critical dependencies were derived to evaluate the energy efficiency of the cavitation process when cleaning radiators with ultrasound; an analysis of existing results was conducted, and recommendations were made for improving the experimental setup for radiator cleaning.

The scientific novelty lies in obtaining dependencies that allow evaluating the efficiency of radiator cleaning with ultrasound.

The practical significance of the research lies in the development of recommendations and standard protocols that will improve the conduct of experimental studies and ensure reliable results. The implementation of this method in auto repair and service enterprises will increase the availability and effectiveness of innovative radiator cleaning methods, contributing to an increase in their durability and reliability.

### 1. Materials and methods

Cavitation is the process of formation, growth, and collapse of gas or vapor bubbles in a liquid, occurring due to significant pressure fluctuations, such as those induced by ultrasound waves or the movement of objects like propellers and turbines.

The main stages of cavitation include bubble formation under conditions of low pressure, their growth by capturing surrounding gas and accumulating energy, and then rapid collapse due to compression. During the cavitation process, chemically active radicals, such as hydroxyl ( $\bullet\text{OH}$ ) and hydrogen ( $\bullet\text{H}$ ) radicals, are also formed, which interact with contaminants, breaking down their structure. This effect is particularly useful for cleaning wastewater and exhaust gases, where the radicals initiate the decomposition of organic substances, enhancing the efficiency of the cleaning process [1-4].

Acoustic cavitation in liquids also triggers various physicochemical phenomena, such as sonoluminescence (the emission of light by liquids), sono-chemical reactions (the chemical effects of cavitation), dispersion (the grinding of solid particles in a liquid), emulsification (mixing and homogenization of immiscible liquids), and mechanical erosion (surface destruction), as shown in Figure 1 [5-8].

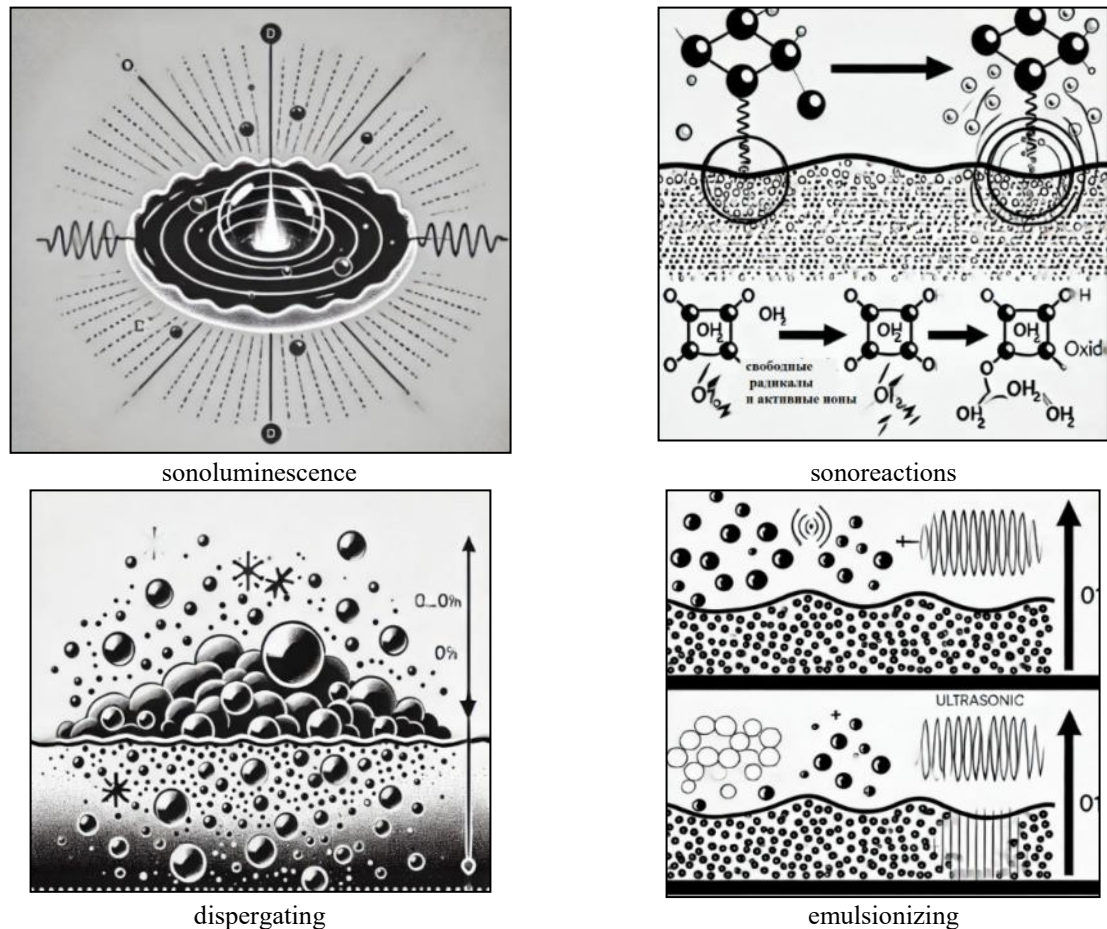


Fig. 1. – Physical and chemical phenomena of the cavitation process

Sonoreactions (chemical effects of cavitation) are chemical processes initiated by the collapse of cavitation bubbles in a liquid with releasing significant energy. This process leads to the formation of free radicals and active ions, which promotes oxidation, reduction and decomposition reactions of molecules. Dispergating (grinding of solid particles) is the process of mechanical destruction of solid particles in a liquid under the impact of cavitation. Collapsing bubbles provide intense forces that crush particles and agglomerates. Dispergating is used in the production of paints, pharmaceuticals and in the other industries where the homogeneity of particles is important [9-12]. Emulsionizing (homogenization of immiscible liquids) is the process of forming stable emulsions, where ultrasound allows mixing liquids (for example, oil and water), forming small drops and ensuring uniform distribution of phases. It is used in the food, cosmetic and pharmaceutical industries.

Mechanical erosion (surface destruction) is the process of destruction of solid material surfaces as a result of ultrasonic cavitation. When cavitation bubbles collapse on the surface of a solid material, they generate powerful shock waves and microjets that destroy the surface of the material. This process can be used to clean surfaces from dirt and scale, as well as in metalworking processes [13-16].

A number of mathematical dependencies are used to describe and quantify these processes, each of which reflects certain aspects of cavitation dynamics

The Rayleigh-Plesset equation is used to describe cavitation, which models the change in the bubble radius  $R(t)$  over time under the influence of such factors as density, surface tension and viscosity of the liquid. When the bubble collapses, the pressure inside it increases adiabatically, and its maximum value  $P_{max}$  can be expressed through the initial radius  $R_0$  and the minimum radius  $R_{min}$ :

$$P_{max} = P_0 \left( \frac{R_0}{R_{min}} \right)^3, \quad (1)$$

where  $P_{max}$  is maximal pressure innnnnsude the bubble at the momment of collapse;

$P_0$  is the initial (static) pressure of the liquid;

$R_0$  is the initial radius of the bubble;

$R_{min}$  is the minimum radius of the bubble at the moment of collapse.

Energy  $E$  released at the moment of the bubble collapse is calculated as work done on a volume from  $R$  to  $R_{min}$ :

$$E \approx \int_{R_{min}}^{R_0} P(r) \cdot 4\pi r^2 dr, \quad (2)$$

where  $P(r)$  is pressure inside the bubble as the function of the radius;

$r$  is the current radius of the bubble [17-18].

The cavitation number  $\sigma$  determines the tendency of a liquid to cavitation and reflects the relationship between the external pressure and the saturated vapor pressure of the liquid:

$$\sigma = \frac{P_\infty - P_\vartheta}{\frac{1}{2}\rho\vartheta^2}. \quad (3)$$

The ultrasound frequency also affects the bubble dynamics: at the resonant frequency, the oscillation amplitude is maximum, which leads to stronger cavitation effects and erosive action. The radius of the resonant bubble  $R_{res}$  at a given ultrasound frequency is expressed as:

$$\sigma = \frac{P_\infty - P_\vartheta}{\frac{1}{2}\rho\vartheta^2}, \quad (4)$$

where  $\sigma$  is the cavitation number, a dimensionless parameter indicating the liquid tendency to cavitation;

$P_\infty$  is pressure in the liquid far from the bubble;

$P_\vartheta$  is the saturated vapor pressure of the liquid (depends on the liquid temperature);

$\rho$  is the liquid density;

$\vartheta$  is the rate flow of the liquid.

$$\varepsilon = \frac{E_m}{E_y}, \quad (5)$$

where  $E_m$  is the energy released in the form of shock waves at the moment if the bubble collapse;

$E_y$  is the ultrasonic impact energy [19-22].

Thus, regulating the ultrasound frequency and pressure parameters allows enhancing cavitation effects and increasing erosive activity, which contributes to effective cleaning.

Currently, there is no universal model that can accurately describe the process of ultrasonic cavitation in radiator tubes. This is due to the high complexity of the phenomenon, which is influenced by many factors. Cavitation is a complex nonlinear process that depends on parameters such as the intensity and frequency of ultrasound waves, the shape and size of the tubes, the characteristics of the working liquid, and the duration of exposure. Taking all these variables into account within a single model proves to be extremely difficult.

Due to these challenges, the method of similarity theory and dimensional analysis was applied. This method allows reducing the number of variables affecting the process and identifying dimensionless criteria that describe the main patterns. The similarity theory approach is particularly effective when analyzing complex processes for which constructing a mathematical model is challenging. The application of this approach enables the identification of key parameters affecting the cleaning process and allows for an assessment of their impact on cleaning efficiency. The physical meaning and significance of the obtained similarity criteria are presented in Table 1.

Based on the physical meaning and values of the criteria, the following conclusions can be drawn:

- criterion  $k_1$  helps determine the optimal tube radius or assess the allowable thickness of the contaminant layer for effective cleaning.
- criterion  $k_2$  evaluates the efficiency of energy transfer into the liquid and enables adjustments to the power of the ultrasonic emitter.
- criterion  $k_3$  determines the efficiency of utilizing the liquid volume and system energy for contaminant removal, as well as the relationship between the liquid's characteristics, system geometry, and the mass of contaminants removed.

**Table 1.** The physical meaning and significance of the obtained similarity criteria

Criterion	Physical Meaning	Value
$k_1 = \frac{r}{\Delta}$	Characterizes the influence of tube geometry and contaminant layer thickness on the penetration of ultrasonic waves to contaminants.	Indicates that the tube radius significantly exceeds the thickness of the contaminant layer, promoting effective ultrasonic wave penetration. The cleaning process becomes more localized and intensive.
		Indicates that the contaminant layer thickness is large relative to the tube radius, making ultrasonic wave penetration more challenging and reducing cleaning efficiency. Additional measures, such as increasing power or duration of ultrasonic exposure, are required.
$k_2 = \frac{E_m}{E_y}$	Evaluates the efficiency of converting ultrasonic energy into cavitation effects through the energy transferred to shock waves.	A significant portion of ultrasonic energy is efficiently converted into shock waves. This indicates high energy efficiency of the system and an intense cavitation process, leading to active contaminant removal.
		Only a small fraction of ultrasonic energy is used to generate shock waves, indicating energy losses or insufficient power. The system requires improvements to enhance efficiency.
$k_3 = \frac{m}{r^2 \rho l}$	Indicates the relative efficiency of contaminant removal from the tube.	The volume of liquid involved in the process is significantly larger than the mass of contaminants removed. This may indicate low cleaning efficiency, as only a small amount of contamination was removed relative to the liquid volume.
		Low values of the criterion indicate high cleaning efficiency: a significant amount of contamination is removed even with a small liquid volume.

The combined analysis of all criteria allows for a detailed evaluation of the balance between energy consumption, tube geometry, and the mass of contaminants removed. The dimensionless criteria derived using the similarity theory provide essential relationships for assessing the efficiency of cavitation processes, which is crucial for understanding the mechanical impact of ultrasonic vibrations on contaminants.

Thus, the application of the similarity theory was justified for such complex processes as cavitation, as a complete mathematical analysis of cavitation bubble behavior is challenging due to the numerous factors influencing the process. The derived criteria not only describe the cleaning process but also define the conditions for effective contaminant removal.

## 2. Analysis and Discussion

An analysis of the results from experimental studies presented in the works of K.A. Sinelnikov has been conducted, where a method for cleaning car radiator tubes using cavitation generated by ultrasound waves is proposed [23-26]. As part of the dissertation work, an experimental setup for radiator tube cleaning was developed, and the process of conducting experiments aimed at evaluating the effectiveness of ultrasonic cleaning was described (Figure 2).

**Fig. 2.** – Experimental Setup for Ultrasonic Cleaning of Automotive Radiators

The experiment followed these steps:

1. Preparation Stage: The experimental setup was assembled and connected. The test bench was then filled with clean water, and its initial parameters were measured.
2. Heating Stage: The water was heated to 50°C;
3. Ultrasonic Treatment: Ultrasonic exposure was applied to the radiator for three different time intervals: 600, 1200, and 1800 seconds;
4. Parameter Measurement: After each treatment, key parameters of the liquid were measured, including volume, mass, and outflow time;
5. Final Stage: The water was aerated (saturated with air) before ultrasonic exposure, and the experimental results were analyzed [25,26].

The results of the study demonstrate that ultrasonic treatment effectively removes scale and contaminants from the walls of radiator tubes, positively impacting the performance of the cooling system and extending its service life (Table 2).

**Table 2.** Results of Experimental Studies

Exposure time (s)	Liquid mass (g)	Density (g/cm <sup>3</sup> )	Drain time (s)	Drain speed (ml/s)
0	44,57	0,9904	9,93	100,7
600	44,60	0,9911	9,73	102,7
1200	44,63	0,9917	9,22	108,45
1800	44,69	0,9931	9,20	108,69

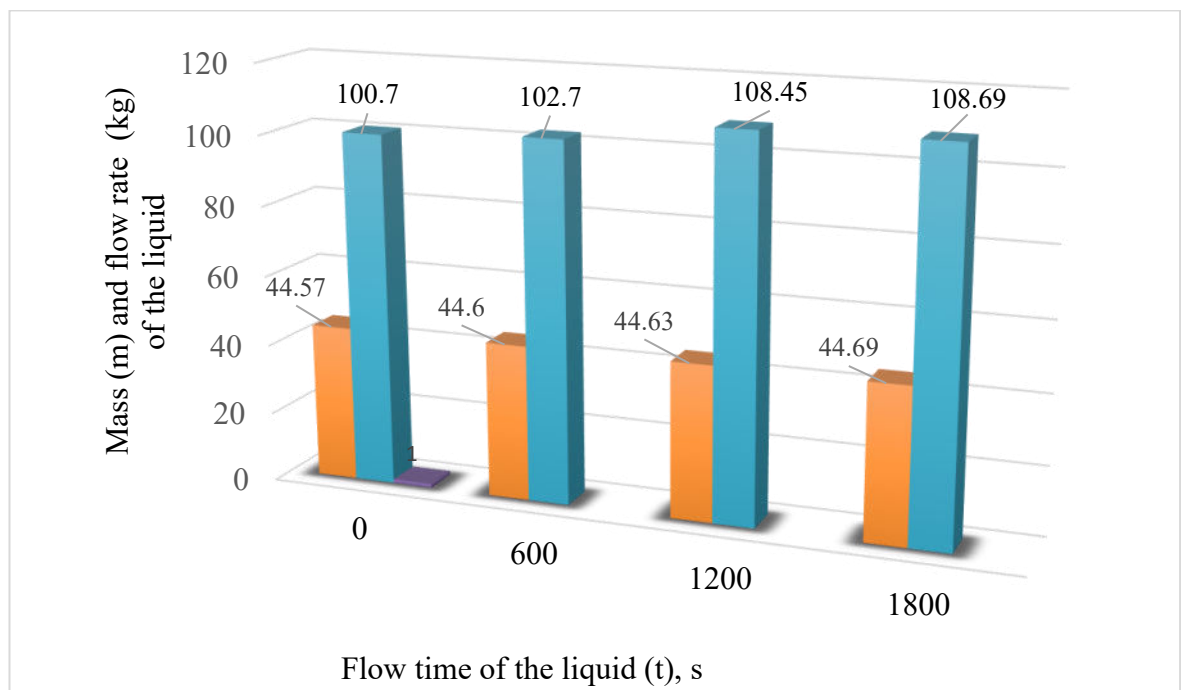


**Fig. 3.** – Changing the mass and the flow rate of liquid (g) Depending on the time of exposure to ultrasound (t)

In Figure 3, it can be observed that as the duration of ultrasonic exposure increases, both the mass and outflow rate of the liquid with removed scale increase compared to the initial parameters of untreated liquid. This phenomenon is explained by the significant amount of energy transferred to the liquid through ultrasonic waves, which induces cavitation.

As a result, microbubbles form, and their collapse generates powerful microjets. These microjets effectively clean the inner walls of radiator tubes from scale, contributing to the increase in both mass and outflow rate of the liquid. Ultrasonic exposure thus not only enhances the cleaning of the radiator but also improves the fluid's flow properties by removing deposits, as evidenced by the increase in measurable parameters.

Based on the experimental results, an assessment of the efficiency of the ultrasonic cavitation process was conducted using the derived criteria listed in Table 3.

**Table 3.** Results of Criteria Calculations

Exposure time (s)	$E_{kin}$ ( $\mu$ J)	$E_u$ (kJ)	$E_m$ (kJ)	$k_2$	$k_3$
0	225,98	0	-225,98	-	-
600	235,2	30	29	0,96	0,3
1200	262,45	60	59	0,98	0,295
1800	263,97	90	89	0,99	0,286

The numerical values of the criteria indicate high cleaning efficiency: even with a minimal liquid volume, a significant amount of contaminants was removed, confirming the effectiveness of ultrasonic waves on contaminated radiator tube surfaces.

Although K.A. Sinelnikov's dissertation involved substantial research on ultrasonic cleaning of radiator tubes, certain limitations in the experimental methodology may have affected the accuracy of the results.

We conducted an analysis of K.A. Sinelnikov's dissertation, addressing unexplored aspects and developing recommendations and suggestions for further research. The results of this analysis are presented in Table 4.

**Table 4.** Analysis Results, Recommendations, and Suggestions

Unexplored Aspects of the Dissertation	Recommendations and Suggestions
Lack of analysis of the influence of the ultrasonic emitter's position on the uniformity of cavitation along the entire length of the radiator tubes.	Conduct studies with different emitter positions to evaluate the uniformity of cavitation and its impact on cleaning efficiency.
Insufficient detail in controlling the saturation of the liquid with air, which could have affected the intensity of cavitation.	Implement a system for controlling the saturation of the liquid with air to ensure the stability of cavitation along the entire length of the tubes.
Lack of description regarding the accuracy of maintaining the liquid temperature during the experiments.	Utilize precise liquid temperature control systems and record temperature variations to analyze their impact on the process.
Insufficient attention to the types of contaminants (scale, organic deposits), which require different cavitation intensities.	Investigate the impact of different types of contaminants on cleaning efficiency and determine the optimal cavitation parameters for each type.
Lack of cavitation level control to ensure stable experimental conditions.	Develop a methodology for real-time cavitation level monitoring to ensure the reproducibility of experiments.
Insufficient analysis of the impact of ultrasonic exposure time and vibration amplitude on the cleaning process and the mass of removed contaminants.	Study the influence of ultrasonic exposure time and vibration amplitude on the dynamics of cavitation and the mechanism of contaminant removal, as well as determine their optimal values for various conditions.

According to the analysis of the research results presented in Table 4, it was determined that one of the key factors influencing the effectiveness of ultrasonic cleaning is the optimal placement of the emitter and the method of water supply [31]. It is hypothesized that using an ultrasonic emitter with directed action from bottom to top, combined with water supplied by a pump, can significantly enhance the efficiency of the process.

The proposed placement and method of liquid supply offer several important advantages. Firstly, this configuration allows cavitation bubbles to rise upward, effectively interacting with contaminants along the entire length of the radiator tubes. The bubbles accumulate at contaminated areas and, upon collapsing, destroy scale and other deposits, ensuring thorough and uniform cleaning. The pumped water supply further enhances this process by creating a turbulent flow that evenly distributes the liquid and saturates it with air, promoting the formation of cavitation bubbles. A continuous water flow also maintains a stable liquid temperature, enabling more intense cavitation, especially at elevated temperatures. All these factors together ensure effective breakdown and removal of contaminants, making the cleaning process more environmentally friendly and cost-effective by reducing the need for chemical agents and mechanical cleaning. Based on the above, the gas cleaning process on the experimental setup is presented, which will be carried out according to the flowchart in Figure 4.

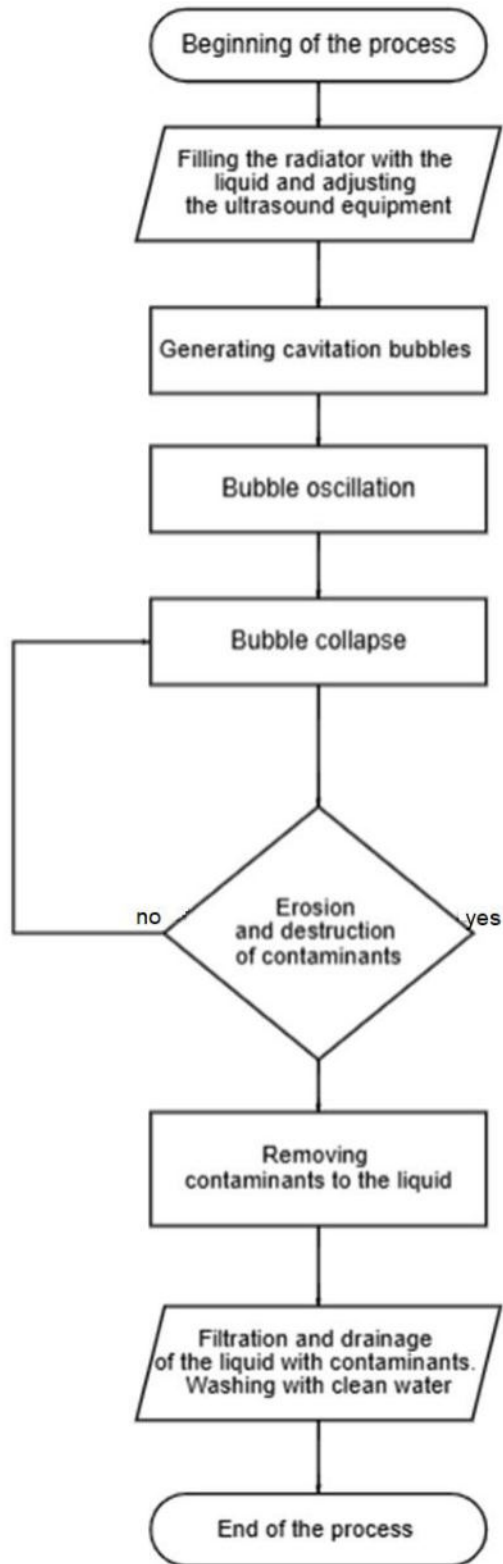


Fig. 4. – Stages of cleaning the radiator tubes with ultrasound

The proposed flowchart visually represents the ultrasonic cleaning process for radiators, highlighting key stages and the sequence of actions to achieve maximum efficiency. The diagram simplifies the understanding of the process, making it more accessible for analysis and practical implementation. It clearly outlines the critical parameters that need to be considered for effective radiator cleaning.

## Conclusion

The conducted analysis confirms that ultrasonic cavitation has significant potential for effective and safe cleaning of car radiator tubes. The main advantage of ultrasonic cleaning lies in its ability to break down contaminants at the molecular level through microjets and shockwaves generated by the collapse of cavitation bubbles. This process allows the removal of even the most stubborn deposits deeply embedded in the tube walls, without causing significant mechanical impact on the radiator material. As a result, the risk of tube damage is reduced, which is especially important for car radiators, where the strength and durability of the structure are crucial for the stable operation of the engine cooling system.

Unlike existing studies, future work will focus on detailed control of parameters such as the position of the ultrasonic emitter and the stability of air saturation in the liquid, to achieve uniform cleaning along the entire length of the tubes. It is expected that these improvements will enhance the repeatability of results, allow for more precise control of the cavitation process, and increase the overall reliability of the method.

## References

- [1] Semeshin A. L., Mokretsov N. A. Modern technologies for repairing radiators of the internal combustion engine cooling system // *Agrotechnics and energy supply*. - V. 1, Issue. 1., 2014 - pp. 351-356.
- [2] Bhogare R.A., Kothawale B.S. A review on applications and challenges of nanofluids as coolant in automobile radiator. // *International journal of scientific and research publications*, Vol. 3, Issue 8, 2013 – p. 1-11.
- [3] Barrow R. E., Lee R. J. Cavitation damage of materials. // *Materials Science*, Vol.15, Issue 2, 1980, - p. 123-135.
- [4] Chahine G. L., Hsiao C.T. Modeling cavitation dynamics in fluids. // *Journal of Fluid Mechanics*, Vol. 617, Issue 2, 2008 – p. 105-132.
- [5] Lauterborn W., Kurz T. Physics of bubble oscillations. // *Reports on Progress in Physics*, Vol.73 Issue 10, 2010, p. 106501.
- [6] Mardonov B.T., Sherov K.T., Toirov, M.S., Makhmudov L.N., Yakhshiev Sh.N., Kongkybayeva A.N., Shezhau K. Features of Engineering Methods of Research Results on Butt Welding on Metal Pipelines. // *Material and Mechanical Engineering Technology*, Vol. 2024, Issue 1 2024, - p. 3–8. DOI: [https://doi.org/10.52209/2706-977X\\_2024\\_1\\_3](https://doi.org/10.52209/2706-977X_2024_1_3)
- [7] Balamurugan K., Sivakumar M. (2016). Advances in sonochemical cavitation reactors for water and wastewater treatment. // *Ultrasonics Sonochemistry*, Vol.32, 2016 – p.1-14.
- [8] Mindubayeva F., Niyazova Y., Nigmatullina R., Sadykova D., Akhmaltdinova L., Salikhova Y., Kadyrova I., Akhmetova M., Sabirova D. Membrane serotonin transporter as a Biomarker of Pulmonary arterial hypertension in children with Congenital Heart Defect. // *Research Journal of Pharmacy and Technology*. Vol. 13, Issue 5, 2020. – p.2435-2438. doi: <http://dx.doi.org/10.5958/0974-360X.2020.00436.9>
- [9] Ashokkumar, M., & Grieser, F. Sonochemistry and cavitation: Handbook of Nanotechnology. 2007 – 921 p.
- [10] Akhmaltdinova L., Kolesnichenko S., Lavrinenko A., Kadyrova I., Avdienko O., Panibratov L. Influence of Pathogen Type on Neonatal Sepsis Biomarkers. Wiley // *International Journal of Inflammation*. Vol. 2021, Issue 2. – p.1- 7. doi: <http://dx.doi.org/10.1155/2021/1009231>
- [11] Flannigan D.J., Suslick, K.S. Plasma formation and temperature during single-bubble cavitation. // *Nature*, Vol. 434, Issue 7029, 2005. – p. 52-55.
- [12] Ospanov O., Yeleuov G., Kadyrova I., Bekmurzinova F. The life expectancy of patients with metabolic syndrome after weight loss: study protocol for a randomized clinical trial (LIFEXPE-RT). // *Trials*, Vol. 20, 2019 – p. 1-7.
- [13] Ilesaliev D.I. Design of Ultrasonic Technology to Improve the Efficiency of Car Exhaust Gas Cleaning System // *Material and Mechanical Engineering Technology*, Vol. 6. Issue 2, 2024. – p. 3-7
- [14] Pak I. Experimental Study of the Ultrasonic Muffler Efficiency for Improving the Exhaust Gas Cleaning System of Internal Combustion Engines of Automobile // *Material and Mechanical Engineering Technology*, Vol. 6. Issue 2, 2024. – p. 53-63.
- [15] Kyzylbaeva E.Zh., Kukeshva A.B., Kunaev V.A. Mathematical model of plate movement in thixotropic mud. // *Material and Mechanical Engineering Technology*, Vol. 2, Issue 2, 2020. – p. 26-30.
- [16] Sakhapov R. L. Method of Cleaning Internal Combustion Engine Radiator Tubes with Ultrasound/ *Material and Mechanical Engineering Technology*, Vol. 6. Issue 2, 2024. – p. 18-24.
- [17] Flannigan D.J., Suslick K. S. Plasma formation and temperature during single-bubble cavitation. // *Nature*, Vol. 434, Issue 7029, 2005, - p. 52-55.
- [18] Kadyrov A., Bembek M., Sarsembekov B., Kukeshva A., Nurkusheva S. The Influence of the Frequency of Ultrasound on the Exhaust Gas Purification Process in a Diesel Car Muffler. // *Appl. Sci*. Vol.14, Issue 12, 2024. – p. 1-19. <https://doi.org/10.3390/app14125027>
- [19] Sarsembekov B.K., Kadyrov A.S., Kunayev V.A., Issabayev M.S., Kukeshva A.B. Experimental Comparison of Methods for Cleaning Car Exhaust Gas by Exposure Using Ultrasound and Laser Radiation. // *Material and Mechanical Engineering Technology*., 2024, Vol.3, 2024 – p. 44–53.
- [20] Kukeshva A., Kadyrov A., Kryuchkov Y. Establishing the parameters of the operation mode of the electric pulse automobile muffler. // *Journal of Applied Engineering Science*. Vol. 22, Issue 1, 2024. – p.89–99. doi: 10.5937/jaes0-45196

- [21] Kadyrov A.S., Amangeldiev E.A. New specifications of the theory of ground cutting //Periodico Tche Quimica. Vol. 166 Issue 31, 2019 – p. 922-936.
- [22] Kadyrov A.S., Kunaev V.A., Georgiadi I.V. Prospects for Processing of Ferrous Metallurgical Waste Based on Arcelormittal Temirtau Experience. // Metallurgist, Vol. 62, Issue 1-2, p. 22–28.
- [23] Kadyrov A., Sarsembekov B., Ganyukov A., Zhunusbekova Z., Alikarimov K. Experimental research of the coagulation process of exhaust gases under the influence of ultrasound. // Communications – Scientific Letters of the University of Zilina, 2021, Vol.23, Issue 4, 2021. – p. 288-298. doi: <https://doi.org/10.26552/com.C.2021.4.B288 B298>
- [24] Ibatov M.K., Kadyrov A.S., Pak I.A., Kadyrova I.A., Askarov B.Sh. Results of experimental studies of the operation of capacitive equipment for ultrasonic cleaning of exhaust gases of motor vehicles // Coal, Vol. 2, Issue 1127, 2020 - pp. 73-78.
- [25] Moldabaev B., Sinelnikov K., Kukeshva A. Justification of the method of vehicle engine radiator ultrasonic cleaning. // Communications - Scientific Letters of the University of Zilina, Vol. 27, Issue 1, 2025. – p. 75-84, doi: <https://doi.org/10.26552/com.C.2025.015>
- [26] Kadyrov A., Sakhapov R., Ganyukov A., Sinelnikov K., Kurmasheva B., Suyunbaev Sh. Studying the process of transport equipment cooling system ultrasonic cleaning //Communications - Scientific Letters of the University of Zilina, Vol. 24, Issue 4, 2022. – p. 288-300, doi: <https://doi.org/10.26552/com>

### Information of the authors

**Sinelnikov Kirill**, PhD, Abylkas Saginov Karaganda Technical University  
e-mail: [coolzero7777@gmail.com](mailto:coolzero7777@gmail.com)

**Moldabaev Baurzhan** PhD student, Abylkas Saginov Karaganda Technical University  
e-mail: [baurmoldabaev62@mail.ru](mailto:baurmoldabaev62@mail.ru)

**Zhunusbekova Zhanar Zhumashevna**, PhD, Abylkas Saginov Karaganda Technical University  
e-mail: [zhzhzh\\_84@mail.ru](mailto:zhzhzh_84@mail.ru)

**Kukeshva Aliya**, PhD, Abylkas Saginov Karaganda Technical University  
e-mail: [aliya.kukeshva@bk.ru](mailto:aliya.kukeshva@bk.ru)

## Research and Optimization of Designs of External Gear Pumps

Berg A.S.<sup>1</sup>, Reshetnikova O.S.<sup>1\*</sup>, Krasnov A.O.<sup>1</sup>

Abylkas Saginov Karaganda Technical University, Karaganda, Kazakhstan

\*corresponding author

**Annotation.** Gear hydraulic machines are a type of volumetric hydraulic machines that are widely used in various industries. Their main purpose is to convert mechanical rotational energy into hydraulic energy (pumps) or vice versa (hydraulic motors). The performance of gear hydraulic machines depends on tribological properties such as hardness, wear resistance, strength, viscosity, surface roughness, lubricity. This article discusses the problems of gear pumps, namely their tribological properties associated with designs and materials of manufacture. There are several basic designs of gear pumps, each of which has its own characteristics, advantages and disadvantages. They ensure stable operation of systems that require fluid transfer with constant flow and pressure. However, their performance characteristics largely depend on the tribological properties of working elements such as gears, bearings and sealing devices. Wear and damage to these elements can significantly reduce the efficiency of the pump, lead to its breakdown or increased energy consumption. Various designs of gear pumps are considered, their characteristics, operating principles, liquid flows, advantages and disadvantages of various pump designs are studied.

**Key words:** gear pumps, design, characteristics, fluid flow, tribological properties

### Introduction

Tribological properties of gear pumps refer to the characteristics associated with friction, wear and lubrication in mechanisms that ensure their durability, operating efficiency and reliability. These properties are especially important for gear pumps, as they operate at high pressures and are often subject to intense friction between working parts.

**Table 1.** Factors influencing tribological properties and methods of their improvement

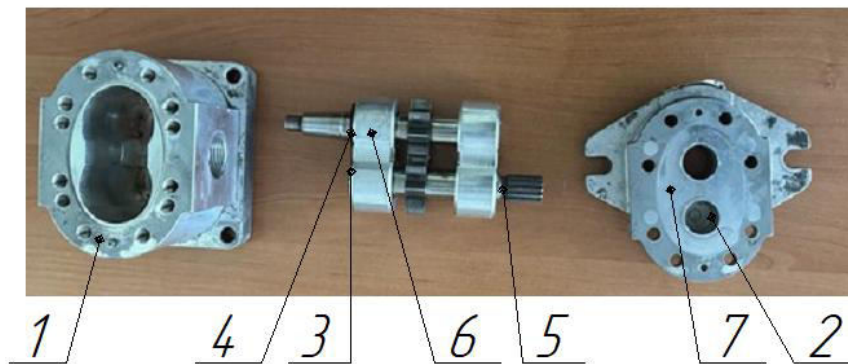
Factors Affecting Tribological Properties	Description	Reasons	Methods of increasing
Friction	Resistance to movement between surfaces. In gears, it occurs when they interact.	Reduced friction improves efficiency, reduces overheating and wear.	Use of lubricants, improvement of surface treatment, coatings.
Wear	Resistance of materials to damage during prolonged contact.	Minimizing wear increases service life and stabilizes pump operation.	Use of wear-resistant materials, improvement of surface quality.
Lubrication	Friction protection using liquid or solid lubricants.	Proper lubrication reduces friction and wear, improving operating efficiency.	Use of synthetic oils, additives, nanomaterials for coating.
Service life	The time during which the pump operates efficiently without significant breakdowns.	Improving tribological properties extends service life and reduces repair costs.	Improving the quality of lubrication and coating, optimizing operating conditions.
Efficiency (Coefficient of Performance)	Pump efficiency, the ratio of useful work to energy expenditure.	Reducing friction and wear improves efficiency, reducing energy loss and increasing productivity.	Reduced friction and increased precision in machining of working parts.
Resistance to loads	The ability of the pump to operate under high pressure and loads.	Improved tribological properties help the pump operate under extreme conditions.	Use of stronger materials, improved lubrication and coating.
Leaks	Fluid loss through gaps between teeth and other parts of the pump.	Reducing leaks improves operating stability and productivity.	Elimination of design defects, improvement of tightness and accuracy.
Performance stability	Maintaining stable pump operation without significant fluctuations in efficiency.	Improving tribological properties contributes to stable and efficient operation.	Use of improved lubricants, improved surface treatment of teeth.

The factors influencing tribological properties in this study are friction, leakage and performance stability.

Gear pumps are widely used in many industries due to their reliability, simplicity of design, compactness and efficiency [1, 2]. Gear pumps are positive displacement pumps. Gear pumps are typically used to pump high viscosity liquids: fuel oils, petroleum, lubricating oils, paints, acids and alkalis, alcohols and solvents, the rotation is transmitted by the driving gear [3 – 6]. The rotation of the driven gear is produced by contact with the driving gear, the liquid is transported from the suction side to the discharge side of the pump (from the inlet channel to the outlet channel) [7]. A gear pump moves liquid by repeatedly enclosing a fixed volume in interconnected gears, transmitting it mechanically to ensure a smooth, pulse-free flow proportional to the rotation speed of its gears [8]. In this case, tight contact is formed between the teeth, as a result of which the reverse transfer of liquid from the discharge cavity to the suction cavity is impossible.

The choice of the object of study is determined by the following factors:

- these units have a set of basic parts and components that is very common in mechanical engineering practice, namely: shafts, gears, bearing supports, friction units (Figure 1);
- gear pumps are characterized by a wide range of operating modes, which means a large variety of different combinations of loads on the machine parts of the unit, up to the maximum possible;
- the practice of operating gear pumps in the CIS countries and abroad, as well as the analysis of foreign and domestic literary publications, shows that they experience premature failures.



1 - housing; 2 - bearing supports; 3 - seals; 4 - thrust bearings; 5 - driving pinion shaft; 6 - driven pinion shaft; 7 - housing cover.

Fig. 1. - Typical design components of gear pump

Reliability and durability of units are primarily determined by the loaded state of their constituent structural elements, parts, and assemblies. At present, methods for calculating the loaded state of parts and assemblies for various purposes have been developed quite deeply and are supported by a wide range of normative and technical documentation, including: GOSTs, industry standards, methods, etc., allowing you to set the required service life for most units and mechanisms containing typical machine parts: shafts, gears, bearing supports, friction units, etc..

### 1. Methodology

Gear pumps are mechanisms consisting of two gears in engagement, placed in a tightly enclosing housing. The pump operates on the principle of transferring liquid by working chambers from the suction cavity to the opposite discharge cavity and then squeezing the liquid out of the working chambers of the displacer.

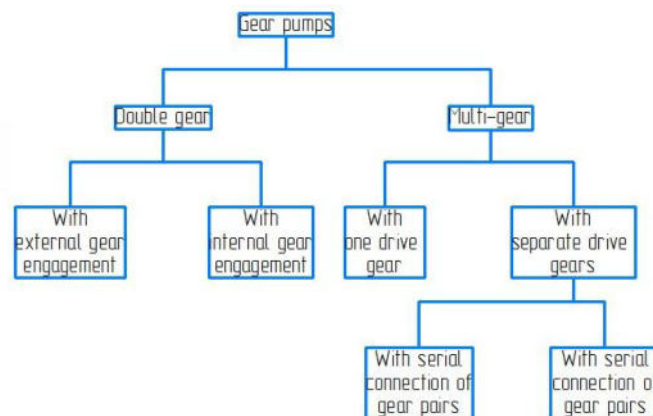
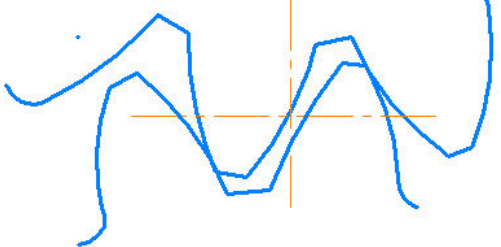
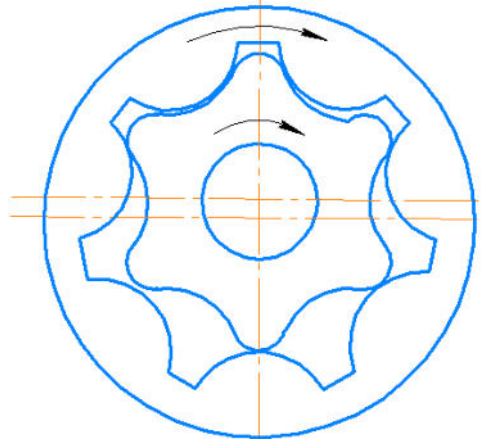
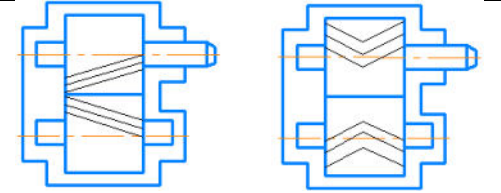


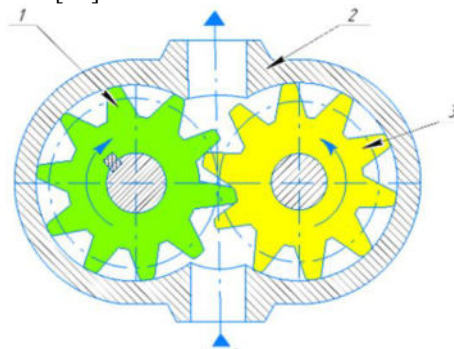
Fig. 2. - Classification of gear pumps

In gear pumps, the working chamber is the cavity between adjacent gear teeth, and the displacer is the gear tooth. Depending on the need, the following designs of gear pumps are used, each of which has its own characteristics, advantages and disadvantages (Figure 2, Table 2).

**Table 2.** Types of gear pump designs, their advantages and disadvantages.

Pump type	Scheme	Advantages	Flaws
<p><b>External Gear Pumps:</b> These pumps use two counter-rotating gears to pump fluid, which is trapped between the gear teeth and transferred through the pump body.</p>		<p>Simple design, high reliability, wide range of liquids</p>	<p>Not suitable for use with liquids containing solid particles as they may cause wear on gears. Require precision manufacturing to ensure stable operation. Limited in pressure range (usually no more than 20-30 bar).</p>
<p><b>Internal Gear Pumps:</b> One of the gear elements (internal gear) is placed inside the outer gear, and the fluid is captured between the teeth and transferred through the pump. This is a type of design where the gears are not driven in one axis, which helps reduce flow pulsations.</p>		<ul style="list-style-type: none"> <li>- High stability of outlet pressure and low flow pulsations.</li> <li>- Higher working pressure than external gears.</li> <li>- Higher flow density and greater productivity.</li> </ul>	<ul style="list-style-type: none"> <li>- More complex and expensive design.</li> <li>- High demands on the precision of gear manufacturing.</li> <li>- Reduced durability when working with contaminated liquids.</li> </ul>
<p><b>Hexagonal Tooth Pumps:</b> These pumps have gears with teeth that are angled (hexagonal teeth). This reduces flow pulsations and improves power transmission.</p>		<p>Reduced flow pulsations. Higher efficiency and less friction than conventional gear pumps. Suitable for working with viscous liquids.</p>	<p>Complex design and high demands on manufacturing precision. May require more expensive materials for durability. There may be problems with tightness.</p>

There are several designs of gear pumps. External gear pumps come in various configurations, distinguished by the number and arrangement of gears. Some designs feature two (Figure 3), three, or four gears in a line, while others have three or four gears surrounding a central drive gear [14]. This simplifies production, maintenance and repair. Such designs provide a high efficiency due to minimal friction losses. They can work with various types of liquids, including viscous and abrasive ones [15].



1 - driving gear; 2 - housing; 3 - driven gear (displacer)

**Fig. 3 -** Design of a gear pump with two external gears [14]

There are also diagrams of gear pumps with three gears located on one axis (Figure 4).

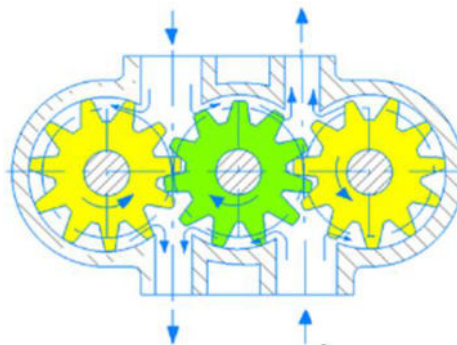
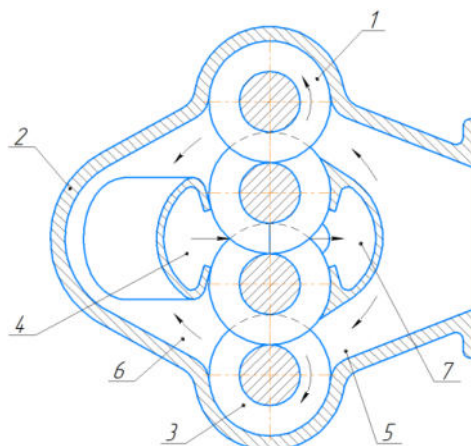


Fig. 4. - Three-gear pump with external gearing [14]

Gear pumps with external engagement and three gears are advisable to use in hydraulic drives where it is necessary to have two hydraulic lines with independent pressure, since this pump has two inlet and outlet openings, that is, one pump can provide the necessary fluid flow in two circuits at once [15].

There are designs with 4 gears located on one axis (Figure 5). Such a design increases the amount of energy that the pump consumes to pump a certain volume of liquid.



1 – drive gear; 2 – housing; 3 – plane; 4, 5 – suction channels; 6, 7 – discharge channels

Fig. 5. - Four-gear pump with external engagement with gears on one axis [9]

There are also known designs with six gear wheels, three on each driven and drive shaft (Figure 6). In such a pump, several gears are located on one drive shaft, each of which rotates the driven gear on the drive shaft. The suction and discharge lines of such pumps are usually separated, but can also be combined in a special design. Multistage pumps are used to increase the pressure or feed the unit.

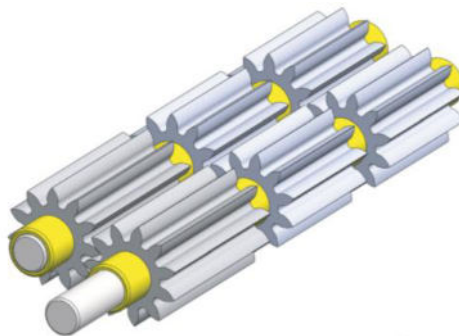


Fig. 6. - Driven and driven shaft of the pump under consideration of multistage gear pumps with external engagement [10]

To increase pressure, gear pairs are installed in series, to increase productivity (feed) - in parallel. By installing the second stage in series, we can almost double the pressure at the pump outlet. However, this will lead to a decrease in the efficiency of the machine, since the feed of each previous stage must be greater than the required feed of the subsequent stage to ensure a reliable supply of power. To get rid of excess liquid at the outlet of each stage, an overflow valve is used.

To increase productivity, multi-gear pumps with three or more gears placed around a central axis are used.

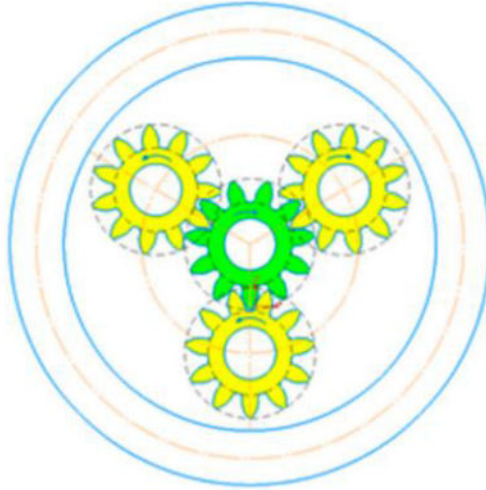


Fig. 7. - Multi-gear pump located around a central axis [11]

Another common type of pump is centrifugal pumps due to their simple design, high performance and ability to pump large volumes of liquid. However, like any mechanism, they have their drawbacks: sensitivity to cavitation, low efficiency, etc. Table 3 shows comparative characteristics of the use of a gear pump.

Table 3. Comparative characteristics of a gear pump and a centrifugal pump.

Characteristic	Centrifugal pump	Gear pump
Operating principle	Transfer of energy to a liquid by centrifugal forces	Movement of liquid by engagement of gears
Performance	High at high costs	High at low cost
Pressure	Low and medium	High
Pulsations	Tall	Low
Efficiency	Depends on the operating mode	High
Self-priming	No	Limited
Viscosity of the pumped liquid	Low and medium	Tall
Dimensions	Big ones	Compact

In order to improve tribological properties, a new design of a multi-gear pump with 3 or more driven gears placed around the central axis is proposed.

Pressure pulsation during fluid delivery is an integral characteristic of a gear pump with external engagement [12]. Flow pulsation, i.e. delivery occurs in portions equal to the volume of the chambers. The trapped volume, which they try to get rid of using the unloading grooves of the follower drive and other things, leads to sharp pressure drops in the tooth engagement zone. Pressure surges generate increased noise and vibration [13]. Flow pulsation can be represented graphically (Figure 8).

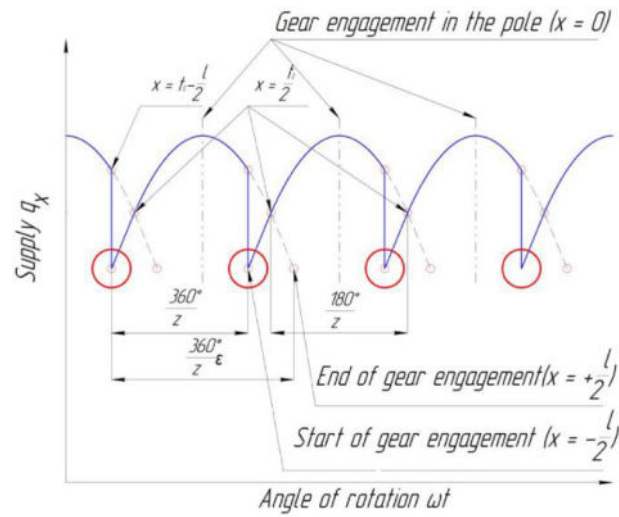
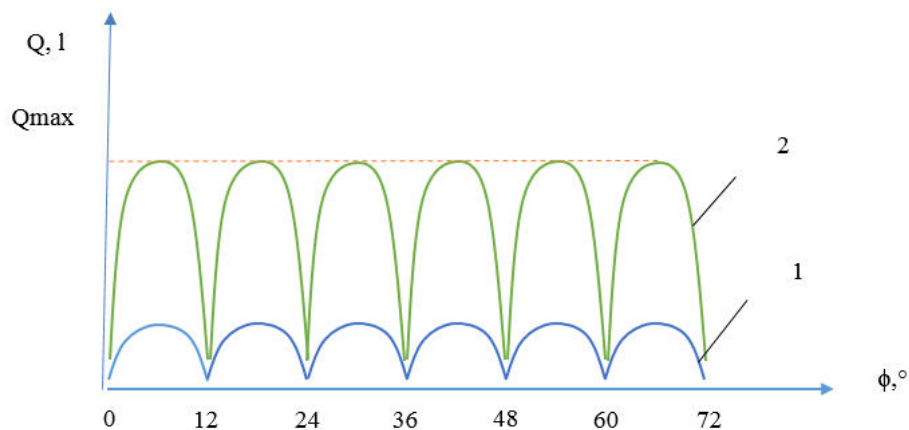


Fig. 8. - Flow pulsation graph [15, 16]

The study will examine the kinematic systems of multi-gear pumps, which is the main axis of this proposal, as well as its idea. The basis for the final optimization of the prototype and the creation of a useful mathematical apparatus from the industrial point of view, capable of accurately selecting pumps for given output parameters, will be the shape of the tooth and the dimensions of the pump parts.

## 2. Results and Discussions

During the research work, the parameters selected will be such parameters as the shape of the tooth and the dimensions of the pump parts, which will form the basis for the final optimization of the prototype and the creation of a useful mathematical apparatus from the industrial point of view, capable of accurately selecting pumps for the specified output parameters. The distribution of the same stresses that are used in the classic gear pump will allow the use of less critical materials or the application of greater forces, which will further popularize these designs.



1 – supply of fluid for engagement 1; 2 – supply of fluid for engagement 1

Fig. 9. - Fluid flow pulsation graph

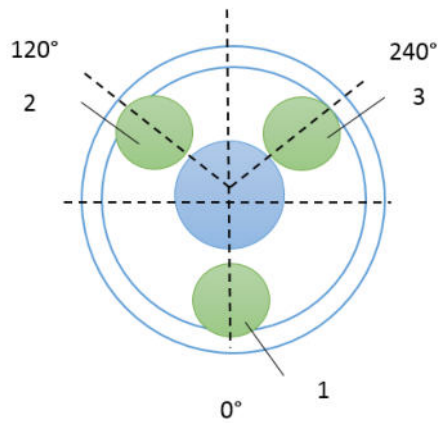
As can be seen from the graph (Figure 9), the feedgear pump is uneven, since simultaneously volumes (equal to the volume of the depressions) are forced into the system, limited by the parameters of the teeth and the housing.

It is known that the reduction of pressure unevenness depends on the number of gear teeth and the angle of engagement of the teeth. The greater the number of teeth, the less the unevenness of the feed, but the less the feed itself, which is undesirable.

The number of teeth of the drive gear was taken to be  $z_1 = 30$ . Then  $\phi = 360/30 = 12^\circ$  is the angle of rotation of the tooth at which the displacement of the moved volume of liquid by the cavity of the tooth occurs.

- for three driven gears the offset of the axes is equal to:

$\alpha = \phi/3 = 12^\circ/3 = 4^\circ$ . Consequently, the axes of the driven gears are shifted by angles of  $4^\circ$  and  $8^\circ$ , respectively (Figures 10, 11).



1, 2, 3 – driven gears

Fig. 10. - 4 gear pump

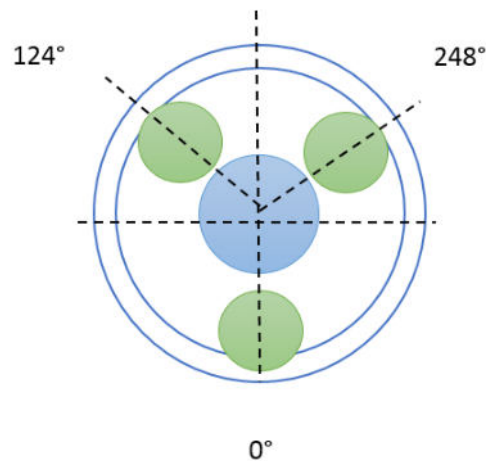


Fig. 11. - 4-x gear pump with offset driven gear axes

Advantages of the three-gear pump design:

- in such a design, the load on each of the gears is distributed more evenly. In a classic two-gear pump, the entire load falls on two gears (driven and leading), which can lead to their rapid wear. When adding a third gear, the load is distributed between three teeth, which reduces the mechanical stress on each of them;

- the presence of three driven gears increases the number of working cycles per unit of time. This can increase the pump's productivity, as the number of captured and pumped portions of liquid per one shaft revolution increases. For pumps designed for high volumes of pumped liquids, this significantly increases the efficiency of operation;

- pumps with three driven gears distribute the fluid flow more evenly, which reduces pressure pulsations. Pulsations can cause additional vibrations and noise, as well as unpredictable system behavior, which is important for precise or sensitive installations;

- the load is distributed evenly and the teeth contact is more even, the pump will wear out more slowly than a pump with fewer driven gears. This extends the life of the unit, which is important in heavy-duty applications such as oil or chemical fluid pumps;

- three-gear driven pumps are less likely to experience sudden pressure surges and, as a result, have reduced vibration and noise, especially at high speeds. This makes them more suitable for applications where low noise levels are required.

By using multiple driven gears, fluid flow parameters can be controlled more precisely, which is especially important for precision systems such as hydraulic and lubrication systems where it is important to maintain stable pressure and fluid flow.

Another important issue when designing a gear pump is the correct choice of material, which significantly affects the durability, efficiency and cost of the equipment. The optimal material must have a set of properties that ensure reliable operation of the pump under specific operating conditions.

Basic requirements for materials for pump housings:

- the material must be resistant to the effects of the pumped liquid (water, acids, alkalis, etc.);

- the housing must withstand internal pressure and mechanical loads.
  - the material must be resistant to abrasive wear, especially when pumping solids;
  - good thermal conductivity facilitates heat removal from the working parts of the pump;
  - the material should be easy to process using traditional methods (casting, machining).
- Table 4 presents standard materials of construction for gear pumps.

**Table 4.** Standard materials for gear pump construction.

Material	Example of construction	Advantages and disadvantages
Cast iron	 [17]	<ul style="list-style-type: none"> <li>- Widely used due to its low cost and good casting properties.</li> <li>- Has sufficient strength and corrosion resistance in fresh water and neutral environments.</li> <li>- Not recommended for aggressive environments.</li> </ul>
Steel	 [18]	<ul style="list-style-type: none"> <li>- Used for the production of pump bodies operating in more aggressive environments or at high pressures.</li> <li>- Alloy steels have increased strength, corrosion resistance and wear resistance.</li> </ul>
Bronze	 [19]	<ul style="list-style-type: none"> <li>Used for pump bodies handling sea water or other aggressive media.</li> <li>- Has high corrosion resistance and good antifriction properties.</li> </ul>
Brass	 [20]	It is used for the production of small pumps and parts requiring high corrosion resistance.
Polymer materials	 [21]	Used for the production of chemical pump bodies and pumps for the food industry. They have high corrosion resistance, are lightweight and low cost.

An analysis of standard materials for gear pump designs and previously conducted studies [21] showed that the use of aluminum will reduce the weight of a multi-gear pump without reducing the strength properties of the structure.

On the chart Figure 12 It is clear that the greatest weight reduction (16%) is observed in polycarbonate, followed by aluminum with 14% and cast iron with 12%. Although polycarbonate shows the greatest weight savings, the choice of material should take into account not only this parameter, but also other factors such as strength, manufacturability and cost. Aluminum, as the optimal material for the manufacture of pump parts, is proposed based on the best balance between weight and strength, as well as taking into account the technological aspects of production.

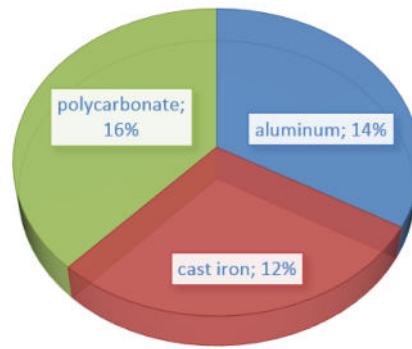


Fig. 12. - Histogram of the dependence of weight change depending on the selected material

This graph highlights the importance of material selection and design optimization to achieve lighter, more efficient pumps [11, 22 - 24].

### Conclusions

An analysis of gear pump designs and possible materials for their manufacture showed that the design of a gear pump with three driven gears around a central axis is a structurally improved version of a classic gear pump. This solution allows for increased productivity, reduced pulsation, reduced wear and extended service life of the device, and also ensures more stable and uniform operation of the system. Such pumps are especially effective in cases where high productivity and durability are required, as well as reduced vibration and noise. This makes them suitable for use in more complex and demanding operating conditions. Further, a study and modeling aimed at the tooth profile and fluid flow in the pump will also be carried out. The use of aluminum for the design of a multi-gear pump will reduce the weight of the structure, material consumption and, as a result, economic costs.

### References

- [1] Kayal Lakshmanana, Fabrizio Tessicini, Antonio J. Gil, Ferdinando Auricchio A fault prognosis strategy for an external gear pump using Machine Learning algorithms and synthetic data generation methods *Applied Mathematical Modelling*, 2023, Volume 123, 348-372
- [2] Emma Frosina, Adolfo Senatore, Manuel Rigosi Study of a High-Pressure External Gear Pump with a Computational Fluid Dynamic Modeling Approach *Energies* 2017, 10, 1113
- [3] Fnu Rituraj, Andrea Vacca gear pumps operating with non-Newtonian fluids: Modeling and experimental validation *Mechanical Systems and Signal Processing*, 2018, Volume 106, 284-302
- [4] Sherov AK, Myrzakhmet B., Sherov KT, Absadykov BN, Sikhimbayev MR Method for selecting the location of the clearance fields of the landing surfaces of gear pump parts with a biaxial connection *NEWS of the Academy of Sciences of the Republic of Kazakhstan* 2022, 1, 159 - 166
- [5] Thomas Ransegnola, Xinran Zhao, Andrea Vacca A comparison of helical and spur external gear machines for fluid power applications: Design and optimization *Mechanism and Machine Theory*, 2019, Volume 142, 103604
- [6] Xiaoru Hao, Xiaojun Zhou, Xiaoguang Liu, and Xiaohu Sang Flow characteristics of external gear pumps considering trapped volume *Advances in Mechanical Engineering* 2016, Volume 8, Issue 10, 1 - 13
- [7] Keith R. Mobley *Fluid Power Dynamics Chapter 3 - Hydraulic Pumps*. – Elsevier: Imprint Butterworth-Heinemann, 2000, pp. 25-46
- [8] Richard W. Hanks *Fluid Dynamics (Chemical Engineering) Encyclopedia of Physical Science and Technology (Third Edition)*, Academic Press, 2003, 45-70
- [9] Khramtsov AA, Galperovich LG, Klebanov BM, Borisova MR, Klyuev ON Multi-gear pumps. Patent of the USSR 836387 dated 07/06/81
- [10] Davide Guerra, Marco Polastri, Mattia Battarra, Alessio Suman, Emiliano Mucchi, Michele Pinelli Design Multistage External Gear Pumps for Dry Sump Systems: Methodology and Application *Mathematical Problems in Engineering* 2021, Volume 1, 1 - 11
- [11] Zharkevich, O.; Nikonova, T.; Gierz, Ł.; Berg, A.; Berg, A.; Zhunuspekov, D.; Warguła, Ł.; Łykowski, W.; Fryczyński, K. Parametric Optimization of a New Gear Pump Casing Based on Weight Using a Finite Element Method. *Appl. Sci.* 2023, 13, 12154. <https://doi.org/10.3390/app132212154>
- [12] Wengang Xu, Zhiying Wang, Zheng Zhou, Chuang Sun, Junhui Zhang, Ruqiang Yan, Xuefeng Chen An advanced pressure pulsation model for external gear pump *Mechanical Systems and Signal Processing* 2023, Volume 187, 109943
- [13] Antonino Bonanno, Francesca Pedrielli A Study on the structureborne noise of hydraulic gear pumps *Proceedings of the JFPS International Symposium on Fluid Power* September 2008, 641-646

- [14] Zharkevich O., Nikonova T., Gierz Ł., Berg A., Berg A., Zhunuspekov D., Warguła Ł., Łykowski W., Fryczyński K. Parametric Optimization of a New Gear Pump Casing Based on Weight Using a Finite Element Method. *Appl. Sci.* 2023, 13, 12154. <https://doi.org/10.3390/app132212154>
- [15] Yudin Y. M. *Shesterennyye Nasosy*; Mashinostroenie: Moscow, Russia, 1964. (In Russian) [Google Scholar]
- [16] Sanchugov V., Rekadze P. New Method to Determine the Dynamic Fluid Flow Rate at the Gear Pump Outlet. *Energies* 2022, 15, 3451. <https://doi.org/10.3390/en15093451>
- [17] Pump body NC 60/125 | Snail 60/125A Cast iron <https://kommash.info/korpus-nasosa-nts/>
- [18] Industrial Water Pump Cast Iron Body [https://ru.made-in-china.com/co\\_dycastings/product\\_Steel-Casting-Industrial-Water-Pump-Body-Water-Pump-Housing\\_uohhhuunsy.html](https://ru.made-in-china.com/co_dycastings/product_Steel-Casting-Industrial-Water-Pump-Body-Water-Pump-Housing_uohhhuunsy.html)
- [19] Single-block pump with high pressure bronze body [https://ru.made-in-china.com/co\\_jskangqiao/product\\_High-Pressure-Bronze-Casing-Monoblock-Pump\\_ysrnegihig.html](https://ru.made-in-china.com/co_jskangqiao/product_High-Pressure-Bronze-Casing-Monoblock-Pump_ysrnegihig.html)
- [20] Brass pump body 201908014 <https://sillan.kz/p99265165-latunnyj-korpus-nasosa.html>
- [21] Plastic Pumps Housing Water Jet 100p Waterproof Switch Electric Motor 1HP Water Pump [https://ru.made-in-china.com/co\\_elestar/product\\_Plastic-Pumps-Body-Jet-100p-Waterproof-Switch-Electric-Motor-1HP-Water-Pump\\_uoinuyiung.html](https://ru.made-in-china.com/co_elestar/product_Plastic-Pumps-Body-Jet-100p-Waterproof-Switch-Electric-Motor-1HP-Water-Pump_uoinuyiung.html)
- [22] Zharkevich, O.; Nikonova, T.; Gierz, Ł.; Reshetnikova, O.; Berg, A.; Warguła, Ł.; Berg, A.; Wieczorek, B.; Łykowski, W.; Nurzhanova, O. Improving the Design of a Multi-Gear Pump Switchgear Using CFD Analysis. *Appl. Sci.* 2024, 14, 5394. <https://doi.org/10.3390/app14135394>
- [23] Zharkevich, O.; Reshetnikova, O.; Nikonova, T.; Berg, A.; Berg, A.; Zhunuspekov, D.; Nurzhanova, O. CFD-FEM Analysis for Functionality Prediction of Multi-Gear Pumps. *Designs* 2024, 8, 115. <https://doi.org/10.3390/designs8060115>
- [24] Nikonova T., Gierz Ł., Berg, A., Turla V., Warguła Ł., Yurchenko V., Abdugaliyeva G., Zhunuspekov D., Wieczorek B., Robakowska M., et al. Comparative Analysis of Strength Fatigue Properties and Abrasive Wear Resistance for a New Composition of Polymer Concrete Coated with Metal Alloy Powders // *Coatings* 2023, 13, 586. <https://doi.org/10.3390/coatings13030586>

#### Information of the authors

**Berg Alexandra Sergeevna**, PhD, assistant, Abylkas Saginov Karaganda Technical University  
e-mail: [kibeko\\_1995@mail.ru](mailto:kibeko_1995@mail.ru)

**Reshetnikova Olga Stasisovna**, doctor PhD, senior lecturer, Abylkas Saginov Karaganda Technical University  
e-mail: [olga.reshetnikova.80@mail.ru](mailto:olga.reshetnikova.80@mail.ru)

**Krasnov Alexandr Olegovich**, Master's student, Abylkas Saginov Karaganda Technical University  
e-mail: [alexandr.kr.05.07.01@gmail.com](mailto:alexandr.kr.05.07.01@gmail.com)

## Investigating the Thermal Performance of Wheat Straw Insulation in Cement Hollow Blocks

Patil P.J.\*<sup>1</sup>, Pawar R.Sh.<sup>2</sup>, Kardekar N.B.<sup>3</sup>, Kamble D.A.<sup>4</sup>, Yadav R.Sh.<sup>5</sup>

<sup>1</sup>Abhinav Education Society's COET, Pune, India

<sup>2</sup>Bharati Vidyapeeth's JNIO, Pune, India

<sup>3</sup>JSPMCOE, Pune, India

<sup>4</sup>Directorate of Technical Education, Mumbai, India

<sup>5</sup>Marathwada Mitramandal College of Engineering, Pune India

\*corresponding author

**Abstract.** A building's carbon footprint could be reduced by using wheat straw, a sustainable agricultural material, as insulation in cement hollow blocks. To evaluate its thermal performance, four test walls were constructed: one without insulation and three with varying levels of compacted wheat straw. Measurements revealed that walls insulated with wheat straw experienced significant reductions in heat flow (82.80% - 38.95%) compared to non-insulated walls. This indicates that wheat straw is an effective insulation material. The insulated walls also demonstrated improved thermal performance, with lower U-values and higher R-values. Notably, the highest compaction density of wheat straw achieved the greatest energy savings (82.80%). These findings suggest that wheat straw is a promising, eco-friendly solution for enhancing the thermal insulation of cement hollow blocks, leading to significant energy savings and environmental benefits in the construction sector.

**Keywords:** wheat straw, thermal resistance, hollow brick, construction material

### Introduction

The growing energy demands of buildings are a pressing global challenge. Passive thermal management strategies, such as improved building insulation, are essential for reducing energy consumption and mitigating the associated environmental impacts. The construction industry is responsible for 30-40% of worldwide energy use and contributes significantly to greenhouse gas emissions.

Renovation and construction projects often consume significant amounts of energy and materials, contributing to environmental degradation. India, facing severe pollution problems, is particularly affected by the energy-intensive nature of its building sector. Improving building insulation is a key strategy for reducing energy consumption for heating, cooling, and air conditioning. High-performance thermal materials are essential for energy savings. Building materials are important in global efforts to conserve energy and protect the environment. Eco-friendly buildings utilize natural and renewable resources, such as locally available agricultural residues, offering numerous benefits.

Despite the prevalence of inappropriate agricultural waste disposal, a readily available solution exists in fiber-rich agricultural residues, which are widely used in global construction. These residues are often burned, representing a missed opportunity for sustainable utilization. According to the Food and Agriculture Organization (FAO, 2019), the burning of wheat and rice paddy residues alone amounted to 92 Mt and 87.5 Mt in 2017. India, for example, generated an average of 521 Mt of agricultural residue annually, including Mt from rice and 114 Mt from wheat. The use of straw in construction dates back to the pre-Harappan era of the Indus Valley civilization, where straw fibers were used as a reinforcement material for mud and clay structures.

Building materials play a crucial role in energy conservation and environmental protection. Ecofriendly buildings often use natural, renewable resources like agricultural waste. Thermal conductivity of agricultural residues, such as maize husk and wheat straw, is comparable to that of artificial insulations like mineral wool and polystyrene. This suggests that agricultural waste can be a sustainable and effective insulation material.

Wheat straw, a common agricultural waste, is often burned, contributing to air pollution. Due to its low density, porous structure, and excellent insulation properties, straw has a long history of use in construction. Its high silica content prevents decomposition, and it is widely available in many regions.

Previous research has demonstrated the superior performance of natural and renewable materials for building insulation compared to traditional materials. Present research explores the wheat straw as a sustainable insulation option by filling concrete hollow bricks with varying densities. The thermal conductivity and resistance of the filled bricks will be evaluated to assess their effectiveness. The potential environmental benefits, such as fuel savings, reduced energy costs, and pollution mitigation, associated with building insulation will also be determined. This research contributes to the development of sustainable construction practices by promoting the use of natural, renewable materials for improved building energy efficiency.

### 1. Methodology

To evaluate the impact of compacted wheat straw density on thermal conductivity, a test rig with four identical external side walls was constructed, as shown in Figure 1. These walls were made from cement hollow

bricks, the specifications of which are provided in Table 1. The table details four walls (W1, W2, W3) filled with compacted wheat straw at varying densities, and one control wall (W4) containing empty hollow bricks. Each brick measured 390 mm x 140 mm x 140 mm and had two internal chambers measuring 88 mm x 78 mm x 110 mm.

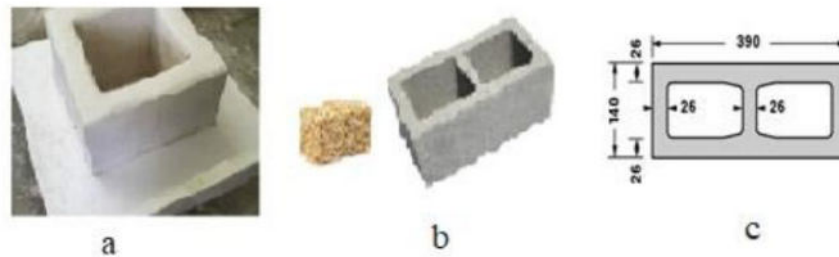


Fig. 1. - a - Test chamber walls b-Straw bell and Brick c- Hollow brick details

### 1.1 Wheat Straw Compaction

To establish different compaction levels, wheat straw was first loaded; un compacted, in chambers of two clay hollow bricks. Subsequently, the straw was loaded again with maximum pressure. The mass of extracted straw from each chamber was measured individually, resulting in average masses of 37.7 g (un compacted) and 94.37 g (maximum compaction). An intermediate compaction level of 65.5 g was established by averaging the previous measurements.

### 1.2 Brick Preparation

To create different compaction levels, wheat straw was initially loaded in chambers of two clay bricks without compression. The straw was then loaded again with maximum pressure. The mass of extracted straw from each chamber was measured individually, resulting in average masses of 37.7 g (uncompressed) and 94.37 g (maximum compaction). An intermediate compaction level of 65.5 g was established by calculating the average of these two measurements.

Table 1. Specifications of four walls of test rig.

Sr. No	Cement brick wall with high compaction straw (W1) wall	Cement brick wall with moderate compaction straw wall (W2)	Cement brick wall with low compaction straw wall (W3)	Cement brick wall with no straw wall (W4)
Straw Density (Kg/m <sup>3</sup> )	125	90	50	-
Size of Wall (mm)	780X560	780X560	780X560	780X560

## 2. Test Rig Construction

The test rig consisted of 32 bricks bonded together with sand-cement mortar. To prevent heat transfer, the corner cavities were filled with polystyrene, and the top and bottom were insulated with 15 cm thick polystyrene sheets. The final dimensions of the model were 780 mm x 560 mm x 560 mm (length, width, height), and it was maintained in a controlled temperature environment.

### 2.1 Temperature Measurement Techniques

A data logger thermometer measured the internal and external surface temperatures of the walls every 5 minutes for 3 hours during each test. Another thermometer was used to collect data for calculating the U- value, with measurements taken over 3 replications of 3 hours each.

### 2.2 Thermal Transmission Coefficient (U-value)

The U-value, measured in W/m<sup>2</sup>·K, indicates how well a wall resists heat transfer. This study used a U-value meter to measure heat loss over three-hour periods. A wall with a lower U-value is considered to be better insulated.

### 2.3 Thermal Resistance (R-value)

Thermal resistance (R-value), the reciprocal of U-value and expressed in m<sup>2</sup> °C/W, was calculated using Equation (1), whereas R and U are thermal resistance and thermal transmittance (W/m<sup>2</sup> °C) respectively:

$$R = 1/U \tag{1}$$

### 2.4 Heat Flux (q)

The amount of heat flowing through the walls was measured using sensors and a thermometer. Equation (2) was used to calculate the total heat flow based on the internal and external temperatures..

$$q = (T_i - T_e) \tag{2}$$

### 2.5 Testing in open Environment without heaters

"The test rig was located on the rooftop of a four-story building at the Abhinav campus in Wadwadi, India. The experiments were conducted during the hot months of April and May. The testing chamber was oriented according to the geographical axes. Data was collected over ten days within the fully enclosed experimental chamber."

### 3. Environmental Considerations and Energy savings

This study evaluated the potential reduction in pollutants, energy savings, and cost savings associated with the investigated model. Equations (3) and (4) were used to calculate the energy savings (S) and energy savings ratio (SR) based on the measured heat flow (q) through the insulated and non-insulated walls (W/m<sup>2</sup>). Additionally, equation (5) was employed to estimate the total annual energy savings for a hypothetical building with a specified surface area (A):

$$S = q_1 - q_i \tag{3}$$

$$S(\%) = [(q_1 - q_i)/q_1] \times 100 \tag{4}$$

$$S_1 = AS \tag{5}$$

This analysis examines the potential cost savings associated with wheat straw insulation in cement hollow bricks, considering the entire energy chain from power generation to household consumption. Thermal power plants, which are the primary source of electricity generation, have an inherent efficiency of only 30- 40%. The remaining energy is lost as heat, emphasizing the importance of efficiency. Electricity transmission and distribution lines also experience energy losses due to resistance and other factors, typically ranging from 8-15%. To account for both power plant inefficiencies and transmission/distribution losses, we use a conservative estimate of 27.6% overall efficiency. A typical 1500 sqft house with 1600 sqft of wall surface area was considered for estimating cost savings.

### 4. Results and Discussion

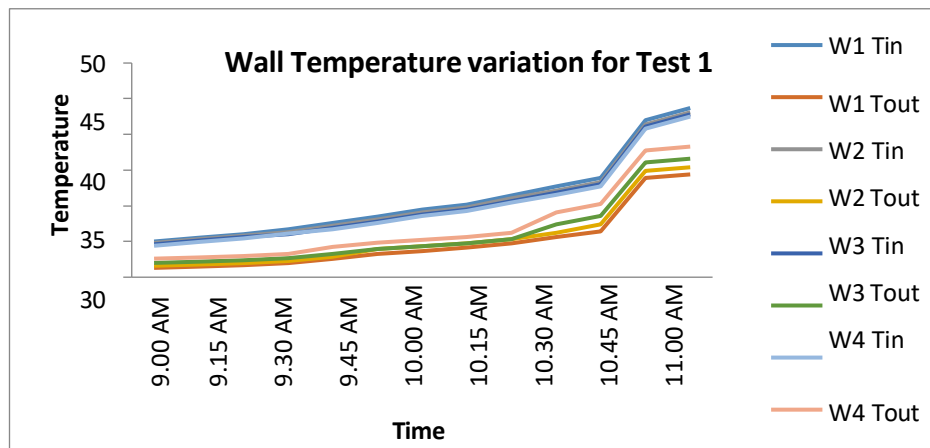


Fig. 2. Wall surface temperatures during test 1

#### 4.1 Performance of straw for Heat Transfer

Figure 2 to 5 show the temperature variations for different walls. The external temperature difference between the walls ranged from 4°C to 6°C. The heat transfer values were highest for W4 and lowest for W1, indicating that W1 had the greatest resistance to heat flow. Wall W4 experienced large heat loss, while W1 had the lowest heat loss. The slopes of the temperature curves for the insulated walls were shallower than for the non-insulated wall, indicating the effectiveness of wheat straw insulation. Wall W4 has highest heat loss and poorest thermal behavior, while wall W1 has lowest heat loss and superior thermal behavior. This shows a positive correlation between straw compaction and thermal insulation efficiency.

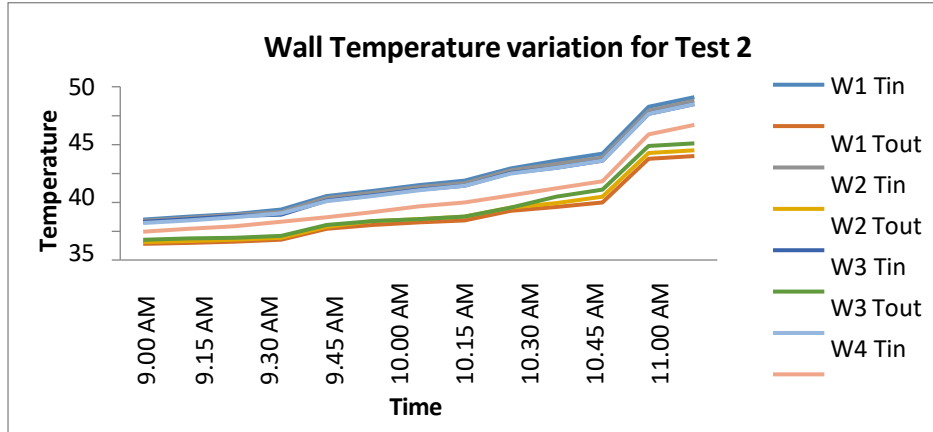


Fig. 3 Wall surface temperatures during test 2

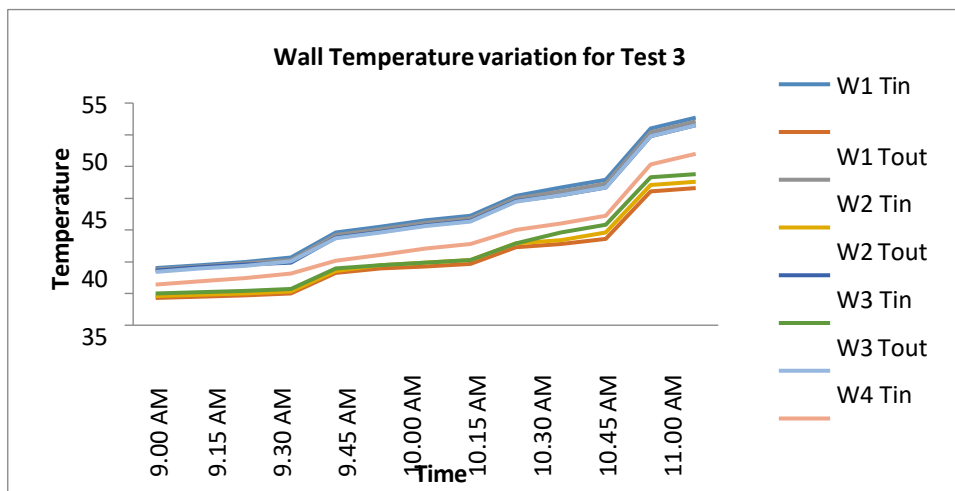


Fig. 4. Wall surface temperatures during test 3

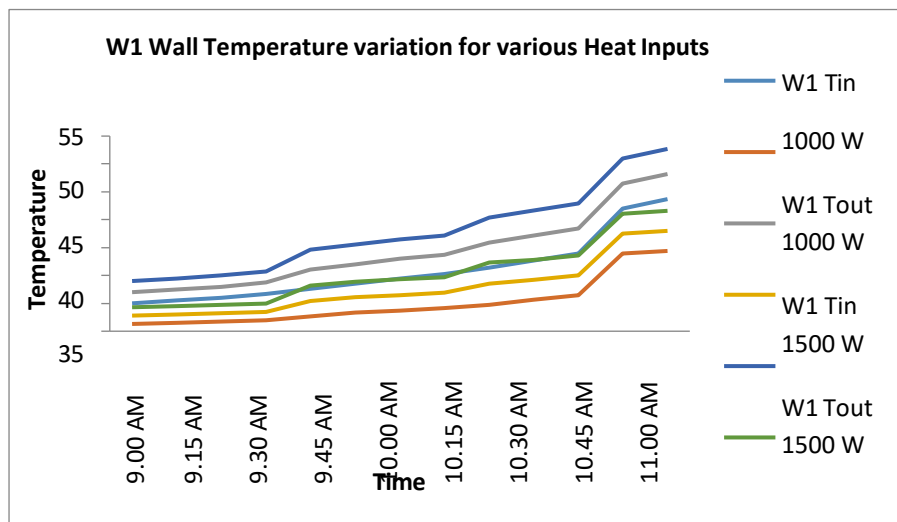


Fig. 5. Wall (W1) surface temperatures during three tests conducted

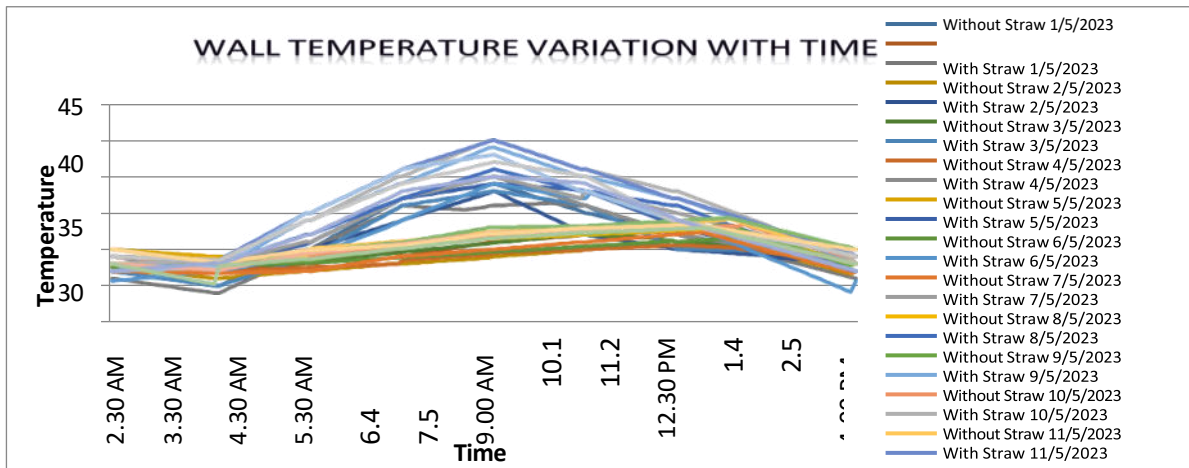


Fig. 6. Wall surface temperature variation for 15 days during open environmental testing

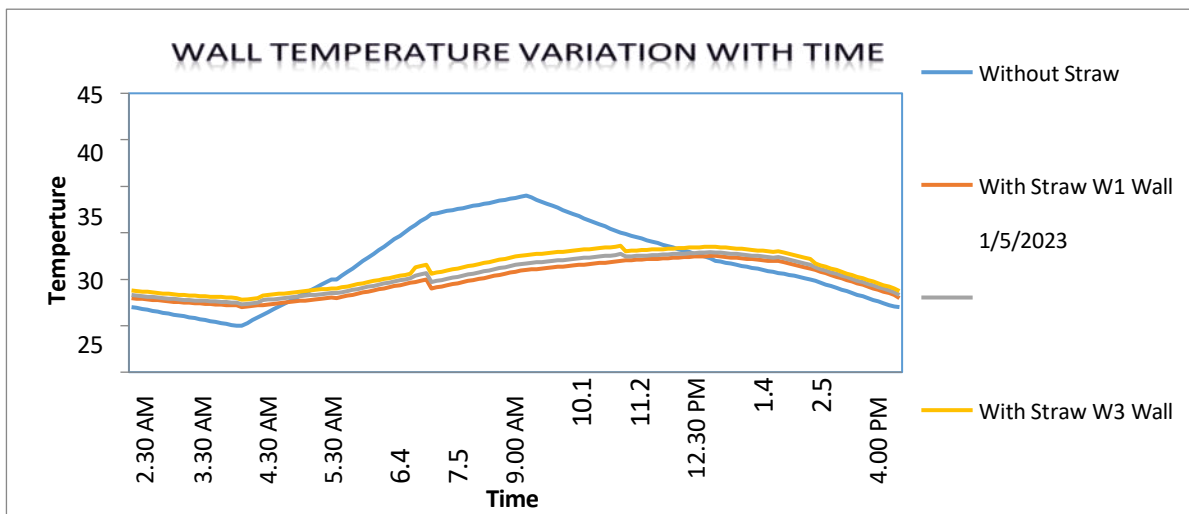


Fig. 7. Wall surface temperature variation for one day during open environmental testing

Figure 6 and 7 show the temperature variation for insulated and non-insulated walls during open environmental testing. The non-insulated wall had a much higher temperature variation (16°C) compared to the insulated wall (6°C). This indicates the effectiveness of the insulation material in reducing heat transfer and maintaining a more stable internal temperature.

Figure 8 shows the R-values for each wall. Wall W1, with the densest straw compaction, had the highest R-value, indicating its superior ability to resist heat flow. The analysis shows that higher compaction density leads to lower thermal conductivity, heat flow, and U-value, resulting in improved thermal insulation and reduced energy consumption.

The incorporation of compacted wheat straw insulation into cement hollow bricks offers substantial environmental benefits by enhancing energy efficiency and reducing greenhouse gas emissions, reinforcing its position as a sustainable building material. Compared to the uninsulated control wall (W4), walls W1, W2, and W3, insulated with wheat straw, exhibited significant reductions in heat flow. These reductions were 82.80%, 66.96%, and 35.74% for W1, W2, and W3, respectively. This translates to improved building energy efficiency by minimizing unwanted heat gain during summer and heat loss during winter. The U-value, a metric quantifying a wall's thermal transmittance, displayed significant reductions in W1, W2, and W3 walls compared to W4 (Table 2). Lower U-values indicate greater resistance to heat transfer, further enhancing building energy efficiency. The R-value, a metric representing thermal resistance, demonstrated significant increases in W1, W2, and W3 walls compared to W4. These increases were 82.80%, 66.96%, and 35.74% for W1, W2, and W3, respectively. Higher R-values signify a greater ability to retain heat within the building, leading to reduced energy consumption for heating purposes. As evidenced, the construction industry can achieve significant reductions in fuel and energy consumption by adopting wheat straw insulation. This translates to lower operational costs and a diminished environmental footprint.

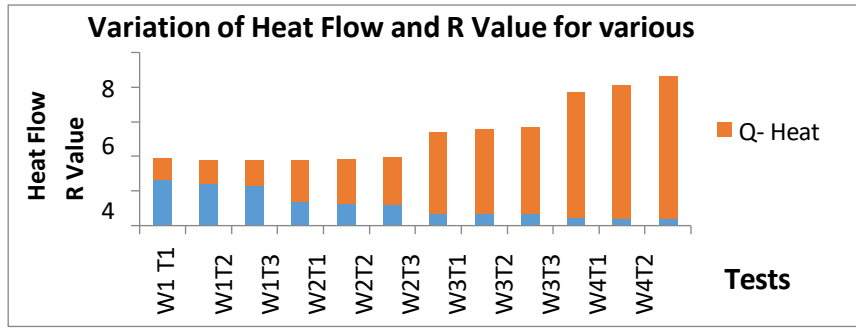


Fig. 8. Analysis of the R-value of the walls in relation to the Heat Transfer for three tests

Table 2. Measured U-value and the computed R-value for the walls

Sr. No.	Wall Type and Test Number	U-value W/m <sup>2</sup>	R-value m <sup>2</sup> /W	Q Watts	% Reduction in comparison with W4
1	W1 T1	0.38	2.631579	1.254	82.8054
2	W1 T2	0.41	2.439024	1.353	82.3276
3	W1 T3	0.43	2.325581	1.419	82.7309
4	W2 T1	0.73	1.369863	2.409	66.9683
5	W2 T2	0.79	1.265823	2.607	65.9483
6	W2 T3	0.83	1.204819	2.739	66.6667
7	W3 T1	1.42	0.704225	4.686	35.7466
8	W3 T2	1.49	0.671141	4.917	35.7759
9	W3 T3	1.52	0.657895	5.016	38.9558
10	W4 T1	2.21	0.452489	7.293	0
11	W4 T2	2.32	0.431034	7.656	0
12	W4 T3	2.49	0.401606	8.217	0

4.2 Performance of straw for Fuel and cost savings

Increasing the compaction density of wheat straw insulation significantly improves its effectiveness in reducing thermal energy loss from the walls. This leads to enhanced building thermal performance and potential energy cost savings for heating and cooling. An effectiveness ratio (SR) was calculated for each insulated wall (W1, W2, and W3) across three test runs, comparing their performance to the non-insulated wall (W4). Wall W1 exhibited the highest energy savings with an average SR of 82.80%. Walls W2 and W3 demonstrated lower effectiveness, with SR values of 66.967% and 35.74%, respectively. The greater energy savings observed in W1 are attributed to its higher straw density and lower porosity. This results in reduced air gaps within the insulation, hindering heat transfer through the wall.

Table 3. Energy, fuel and cost savings for the assumed sample house

Sr. No	Wall Type and Test Number	Energy savings (S) (W/m <sup>2</sup> )	Energy saving ratio (SR) W	Cost saving for 1500sqft house (Rs/year)
1	W1 T1	6.039	82.80543	15110.71
2	W1 T2	6.303	82.32759	14895.87
3	W1 T3	6.798	82.73092	14752.64
4	W2 T1	4.884	66.96833	12604.2
5	W2 T2	5.049	65.94828	12174.51
6	W2 T3	5.478	66.66667	11888.05
7	W3 T1	2.607	35.74661	7662.778
8	W3 T2	2.739	35.77586	7161.475
9	W3 T3	3.201	38.95582	6946.631

This section explores the potential economic and environmental benefits of using different wheat straw configurations (W1, W2, and W3) in a typical residential building with a 1200 sqft living space. To evaluate the cost-effectiveness and environmental impact, we estimated the energy, fuel, and cost savings associated with each wall type (W1, W2, and W3) based on data from the three test runs for the different straw compaction densities.

Table 6 summarizes the projected savings. Wall W1 (highest compaction) consistently demonstrated the greatest energy savings across all three tests, making it the most energy-efficient option. For a typical 15

sqft single-story house with 1600 sqft of wall surface area, the energy savings from Wall W1 were  $6.798 \times 148.64 = 1.0104$  kW, resulting in an estimated cost savings of approximately Rs 4 per kWh. Wall W1 emerged as the leader with the highest average fuel savings. Based on the average energy saving capacity and the total building area, an estimated annual energy savings of 3777.67 W can be expected for the prototype building.

### 4.3 Performance of straw for pollutants reduction

This section examines the potential of wheat straw insulation to mitigate pollutant emissions associated with building energy consumption. As highlighted by research, modern society faces significant environmental challenges linked to energy use. Table 4 (Ebrahimi & Keshavarz, 2015) illustrates the emission rates of the three primary pollutants per unit of energy generated by burning coal. Notably, CO<sub>2</sub> emissions are the highest, followed by NO<sub>x</sub> and CO.

**Table 4.** Greenhouse gas emissions of CO, CO<sub>2</sub>, and NO<sub>x</sub>

Green House Gases	CO	CO <sub>2</sub>	NO <sub>x</sub>
Emissions (g/KWh)	0.9	900	6

The experiment demonstrates a direct correlation between the reduction in CO, CO<sub>2</sub>, and NO<sub>x</sub> emissions and the fuel and energy savings achieved in the prototype building with insulated walls (W1, W2, and W3). The findings suggest that utilizing wall W1 (highest compaction) can potentially reduce CO, CO<sub>2</sub>, and NO<sub>x</sub> emissions by nearly double compared to walls W2 and W3. These results indicate that wheat straw insulation, particularly with higher compaction density, can contribute to environmental improvements by lowering energy consumption and consequently reducing greenhouse gas and air pollutant emissions. This aligns with sustainable building practices aimed at minimizing environmental impact.

### Conclusion

This study investigated the effectiveness of wheat straw as an insulating material for fired clay hollow bricks. The findings strongly support the use of compacted wheat straw in sustainable building practices.

- enhanced thermal performance: Compared to non-insulated walls, wheat straw insulation, especially with higher compaction, significantly improved thermal performance. This translates to reduced heat transfer and increased energy efficiency within buildings;
- energy savings and cost reduction: The improved thermal performance of highly compacted wheat straw (W1) led to substantial energy savings in the modeled building, potentially resulting in annual cost savings of up to Rs 15110.71;
- environmental advantages: By lowering energy consumption, wheat straw insulation contributes to reduced greenhouse gas emissions and decreased air pollution, aligning with sustainable building principles.

This research supports the use of compacted wheat straw as a sustainable and environmentally friendly building material. It offers significant benefits in terms of improved thermal performance, reduced energy consumption, and minimized environmental impact. Encouraging its widespread adoption in the construction sector holds immense potential for contributing to a more sustainable future.

### References

- [1] Janowska Renkas, E., Król, A., Pochwała, S., Pałubski, D., Adamska, M., Klementowski, I., 2022. The fire resistance and heat conductivity of natural construction material based on straw and numerical simulation of building energy demand. *Energies* 15 (3), 1155.
- [2] Platt, S.L., Walker, P., Maskell, D., Laborel-Préneron, A., 2019. Re-baling straw for better insulation. *Academic Journal of Civil Engineering* 37 (2), 32–36.
- [3] Jun. Platt, S., Maskell, D., Walker, P., Laborel-Préneron, A., 2020. Manufacture and characterisation of prototype straw bale insulation products. *Construct. Build. Mater.* 262,
- [4] Rabbat, C., Awad, S., Villot, A., Rollet, D., Andrès, Y., 2022. Sustainability of biomass-based insulation materials in buildings: current status in France, end-of-life projections and energy recovery potentials. *Renew. Sustain. Energy Rev.* 156, 111962.
- [5] Ramukevičius, D., Šadzevičius, R., Skominas, R., Gurskis, V., 2021. Field studies of temperature distribution in a straw building wall. In: 10th International Scientific Conference: Rural Development 2021.
- [6] Rojas, M.P., Grimaldo, J.M., Fuentes, C.D., 2020. Physical thermal properties and comparative analysis of the ecological straw constructive modules. *J. Phys. Conf.* 1708 (1). Feb. [7] Sabapathy, K.A., Gedupudi, S., 2021. In situ thermal characterization of rice straw envelope of an outdoor test room. *J. Build. Eng.* 33, 101416.
- [7] Koh, C.H., Kraniotis, D., 2021. Hygrothermal performance, energy use and embodied emissions in straw bale buildings. *Energy Build.* 245, 111091. Aug 15th.
- [8] C.H., Kraniotis, D., 2020. A review of material properties and performance of straw bale as building material. *Construct. Build. Mater.* 259, 120385. Oct 30th.

- [9] Scrucca, F., et al., 2020. Energy and carbon footprint assessment of production of hemp hurds for application in buildings. *Sep Environ. Impact Assess. Rev.* 84, 11. Art. no. 106417.
- [10] Thomson, A., Dick, K., Walker, P., 2021. Steady-state and dynamic hygrothermal performance of rendered straw bale walls. In: *Proceedings of the Institution of Civil Engineers-Construction Materials*, vol. 174, pp. 298–308.
- [11] Dec. Tlajji, G., Pennec, F., Ouldboukhitine, S., Ibrahim, M., Biwole, P., 2022. Hygrothermal performance of multilayer straw walls in different climates. *Construct. Build. Mater.* 326, 126873. Apr 4th.
- [12] Tlajji, G., Ouldboukhitine, S., Pennec, F., Biwole, P., 2022. Thermal and mechanical behavior of straw- based construction: a review. *Construct. Build. Mater.* 316, 125915. Jan.
- [13] Li, K., et al., 2020. Analysis on energy saving and thermal insulation performance of improved straw brick in northern cold area. *Arabian J. Geosci.* 13 (16), 807.
- [14] Walker, P., Thomson, A., Maskell, D., 2020. Straw bale construction. In: *Nonconventional and Vernacular Construction Materials*. Elsevier, pp. 189–216.
- [15] Yang, L., Yang, J.J., Liu, Y., An, Y.G., Chen, J.H., 2021. Hot box method to investigate U-values for straw bale walls with various structures. *Energy Build.* 234, 110706. Mar 1st.
- [16] Abanomi, W.M., 2021. The effect of straw bale on thermal performance of buildings in hot and arid regions, riyadh city as A case study. *Emirates Journal for Engineering Research* 26 (3).
- [17] Ahmadi, R., Souri, B., Ebrahimi, M., 2020. Evaluation of wheat straw to insulate fired clay hollow bricks as a construction material. *J. Clean. Prod.* 254, 120043, 11, May.
- [18] Marques, B., Tadeu, A., Almeida, J., Ant'onio, J., de Brito, J., 2020. Characterisation of sustainable building walls made from rice straw bales. *J. Build. Eng.* 28, 101041
- [19] Cornaro, C., Zanella, V., Robazza, P., Belloni, E., Buratti, C., 2020. An innovative straw bale wall package for sustainable buildings: experimental characterization, energy and environmental performance assessment. *Energy Build.* 208, 109636.

### **Information of the authors**

**Patil Prashant Jagannath, PhD**, Abhinav Education Society's COET  
e-mail: [pjpatil1776@gmail.com](mailto:pjpatil1776@gmail.com)

**Pawar Rohini Shankar, ME**, Associate Professor, Bharati Vidyapeeth's JNIOT  
e-mail: [15rohini pawar@gmail.com](mailto:15rohini pawar@gmail.com)

**Kardekar Nitin Babanrao, PhD**, Associate Professor, JSPMCOE  
e-mail: [nitinkardekar.n@gmail.com](mailto:nitinkardekar.n@gmail.com)

**Kamble Dhanpal Ananda, PhD**, Assistant, Director, Directorate of Technical Education  
e-mail: [kambled@gmail.com](mailto:kambled@gmail.com)

**Yadav Rahul Shuvaji, PhD**, Associate Professor, Marathwada Mitramandal College of Engineering  
e-mail: [rahulyadav@mmcoe.edu](mailto:rahulyadav@mmcoe.edu)

## Carbon Aerogels Derived from Industrial Wastes and Biomass Sources: Characteristics, Characterization, and Applications

Muhammad Hashami<sup>1,2,3</sup>, Auyelkhanzy Molder<sup>1,2</sup>, Auyelkhanzy Madina<sup>1</sup>

<sup>1</sup>Al-Farabi Kazakh National University, Almaty, Kazakhstan

<sup>2</sup>Institute of Combustion Problems, , Almaty, Kazakhstan

<sup>3</sup>Institute of Higher Education Mirwais Khan Nika Zabul, Qalat City, Afghanistan

Corresponding email: mg.hashami2010@gmail.com

**Abstract.** Biomass derived carbon aerogels (BDCAs) have become a major area of interest because of their high potential for functionality and novel structure, which makes them potential candidates for environmentally friendly next generation carbonaceous materials. This review discusses the synthesis route for developing porous carbon structures from renewable biomass such as cellulose, lignin, hemicellulose and chitosan through sol-gel processes, freeze-drying, supercritical drying, carbonization and activation. Moreover, reorganizes BDCAs according to their precursors by describing common features and possible applications of cellulose-based, lignin-based, hemicellulose-based, and chitosan-based aerogels. In addition, characterization methods such as SEM, BET analysis, FTIR and XRD are explained the surface morphology, pore structure and chemical constitution of the aerogels. Due to high surface area, lower thermal conductivity and high electrical conductivity, the BDCAs are suitable for energy storage applications, catalysis and environmental application. This review also supports the role of BDCAs for the development of new sustainable technologies and the reduction of negative environmental effects of conventional materials.

**Keywords:** Biomass, carbon aerogels, water treatment, energy storage, porous aerogels.

### Introduction

In recent years BDCAs have attracted much more attention of scientists due to their unique properties and potential applications. These materials have synthesized from industrial wastes [1], biomass sources such as agricultural waste, forestry waste and other renewable organic sources, which make them an environmentally friendly alternative to conventional carbon-based materials [2, 3]. Their functional advantages combined with their renewable origin emphasize their potential to play a significant role in sustainable technological advancement. Sol-gel, lyophilization, supercritical drying, carbonization and activation techniques are used to synthesize BDCA by converting natural renewable precursors such as cellulose, lignin or chitosan into a carbon-based porous structure. The process of obtaining BDCAs involves, carbonization of biomass precursors, followed by the removal of non-carbon elements, which results a highly porous [4], lightweight, and conductive material production. High specific surface area (SSA), which can exceed 2500 m<sup>2</sup>/g is one of the key advantages of BDCAs. These characteristics combined with low density and excellent electrical conductivity of BDCAs, make them appropriate solution across energy, environmental and industrial applications, including super capacitors [5], catalysis [2], environmental remediation [6]. For instance, BDCAs have shown great ability to facilitate rapid ion transport and electron transfer, make them important as electrode materials in supercapacitors and batteries. The porosity and functionality of the BDCA surface allow the synthesis of materials with specific properties tailored for specific applications [4]. These materials can also exhibit tunable physical and physical properties, representing a stable and versatile class of materials with a wide range of potential applications. These versatile characteristics are particularly important in areas such as water treatment, where BDCAs can be used as adsorbents to remove pollutants from wastewater [6]. Keirabadi et al, 2019 investigated carbon aerogel derived from alginate modified with protonated cross-linked chitosan to remove nitrate from water. In addition, their biocompatibility and degradability make them suitable for drug delivery systems and tissue engineering in biomedical applications [7]. Manipulation of the structure and properties by changing the precursor and synthesis method allows the synthesis of materials with a given functionality [8]. with combination of large surface area, low density and superior conductivity as well as the ability to tailor their properties, make them crucial for future technological advancements, as shown in (Figure 1) many studies describing the versatile usage of BDCAs. As research in this area continues to tailor, their biocompatibility and degradability will make them suitable for biomedical applications such as drug delivery systems and tissue engineering scaffolds [9].

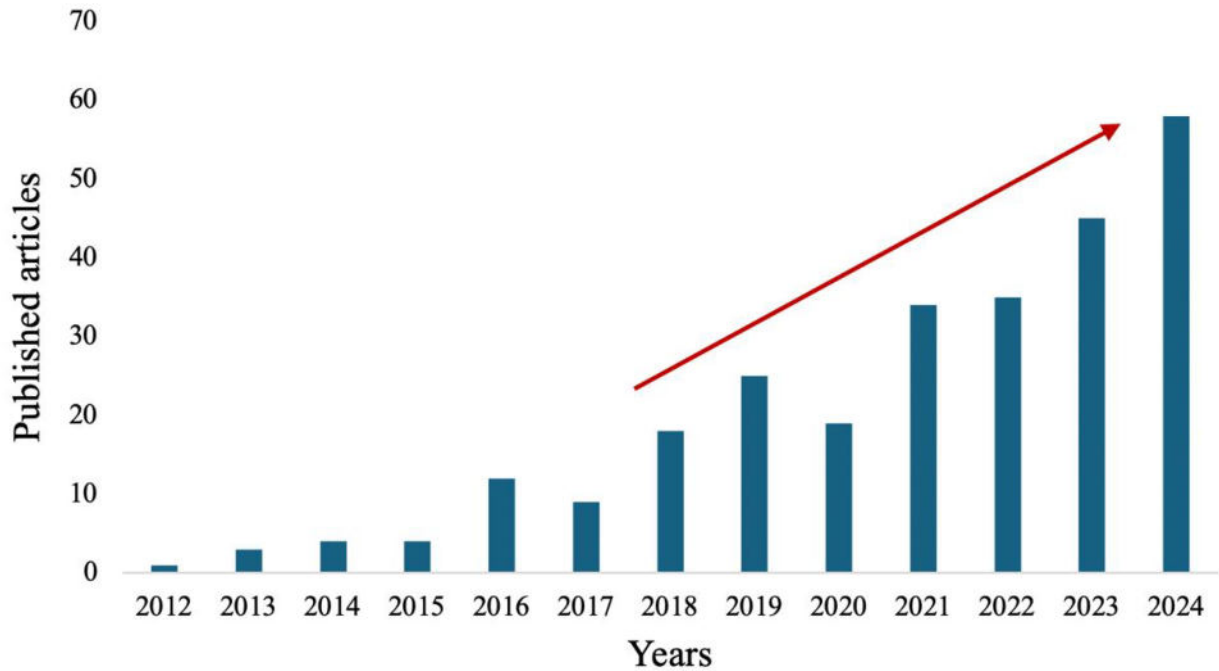


Fig. 1. - A scheme of published articles about BDCAs. Taken from Scopus

This review underscores synthesis of carbon aerogels (CAs) from agriculture sources, examining their properties, synthesis processes, their significance and potential impact across various fields, highlighting the need for further research and exploration of their multifaceted applications, represents a comprehensive overview of the synthesis, characteristics, and applications, focusing on the green synthesis methods as versatile and efficient approaches for their production. As shown in (Fig. 2) many studies have been done on synthesis of these materials from biomass agriculture wastes, such as oil palm, rice husk, and coconuts which explore the versatility and promise of these particles in potential applications. However, most of the studies have centered around their catalytic, energy storage, and supercapacitors applications thus, the need for research on biomedical, diagnostic/therapeutic and water treatment applications of these materials necessary to be given more attention.

## 1. BDCAs

BDCAs are novel class of materials derived from renewable resources and eco-friendly alternatives for traditional aerogels. These materials recycle from natural precursors, which are both economical and sustainable. BDCAs in contrast to traditional aerogels that could use synthetic or non-renewable components is an example of green chemistry, suitable for a variety of high-performance applications due to their lightweight, large surface area, and superior porosity [2, 10, 11]. which aims to reduce environmental impact and improve functional efficiency [2, 12].

### 1.1. Types of CAs

BDCAs categorized based on the primary natural polymers from which they are derived, each of them offers distinct properties. Cellulose-based aerogels are the most widely studied one, celebrated for their lightweight structure and high mechanical strength, particularly well-suited for thermal insulation applications due to their low thermal conductivity and stability. Lignin derive carbon aerogels are known with high carbon yields and efficient for using in energy storage systems to utilize the intrinsic carbon richness of lignin. In addition, hemicellulose and chitosan-based aerogels are known for their improved thermal stability and high electrical conductivity, making them valuable in electrochemical systems and energy storage devices [6, 13].

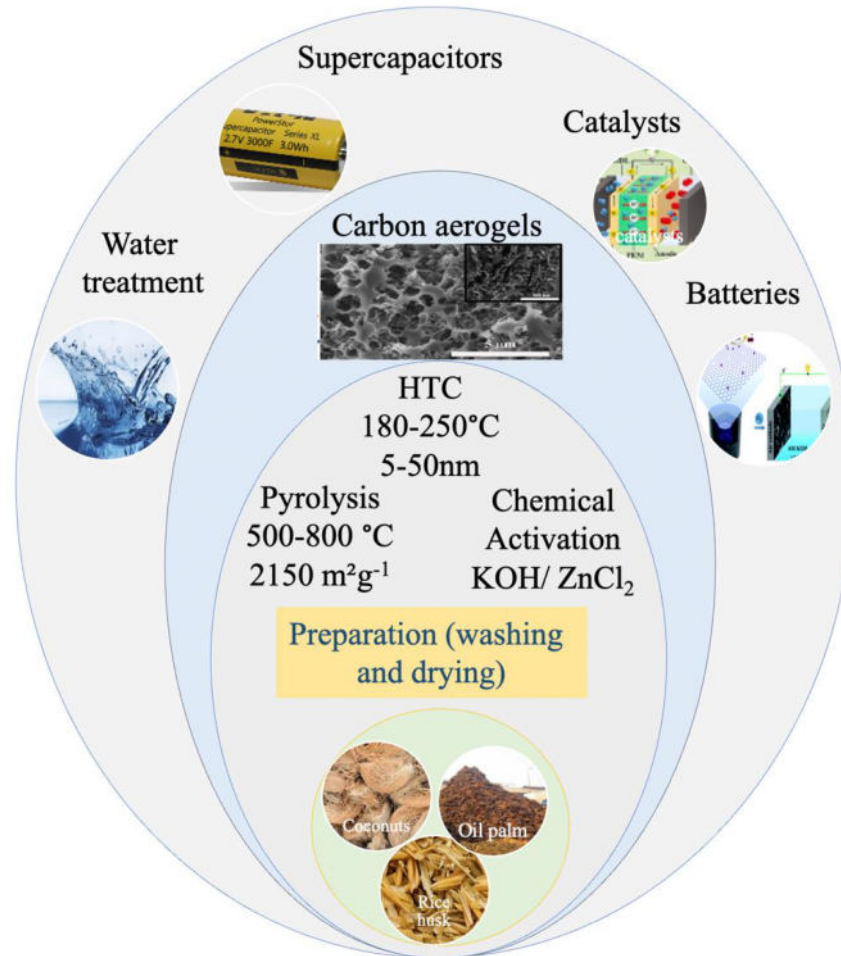
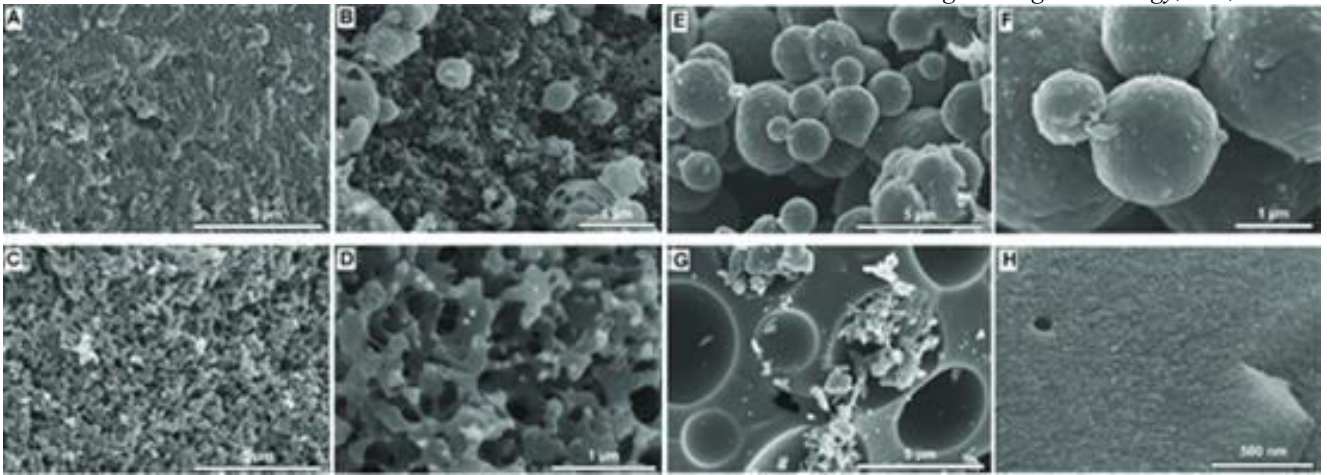


Fig. 2. - Graphical abstract of CAs taken from biomass agriculture wastes and their potential applications

## 1.2. Characterization

Characterization of BDCAs plays a crucial role in understanding and optimizing their properties for target applications. These aerogels are usually evaluated based on their surface morphology, pore structure, chemical composition and crystalline structure. Microscopies such as SEM and TEM techniques play an important role in visualizing the complex nanostructures and pore size distribution of BDCAs, required for applications requiring high surface interaction such as adsorption and catalysis. The surface morphology and porous structure of CAs prepared with different lignin to cross-linker ratios were examined by Karaaslan et al., 2022 (Fig. 3) [14]. It depends on the composition of aerogels, the structure of pores and the shape of carbon particles changed significantly. Samples with lower lignin to cross-linker ratios (CA-L87 and CA-L81) showed a three-dimensional porous network structure composed of interconnected particles (Fig. 3A-D), which is typical for CAs with mesopores (2-50 nm). On the other hand, the samples CA-L68 and CA-L56 had no visible mesoporous network structure but composed of either spherical carbon particle with sizes ranging from (1-3  $\mu\text{m}$ ) or micron-size pores (Fig. 3E-G). Interestingly, higher magnification SEM images revealed that CA-L68 and CA-L56 samples had secondary carbon particles with less than 50 nm and additional surface features suggesting the presence of micropores (Fig. 3F-H).



**Fig. 3** - SEM images of lignin CAs; (A, B) CA-L87, (C, D) CA-L81, (E, F) CA-L68, and (G, H) CA-L56, showing the effect of lignin content on surface morphology microstructure and porosity taken from [14]

Brunauer-Emmett-Teller (BET) analysis is frequently employed for assessing of SSA, the total pore volume ( $V_t$ ) was obtained from the nitrogen adsorption isotherm at ( $p/p_0 \sim 0.99$ ) and the specific surface area was determined using the BET method [14]. Increased surface area and pore size which shown in (Table 1), provides insights into the aerogel's capacity for adsorption make them crucial for environmental remediation, gas adsorption and industrial application [11].

The crystalline structure and degree of graphitization of these aerogels are often examined using X-ray Diffraction. The X-ray diffraction pattern of the CAs before surface modification is shown in (Fig. 4a). As expected, the carbon phase peaks can be seen at  $2\theta=23^\circ$  which corresponds to the (002) plane and the broad peaks at  $2\theta$  of about  $43^\circ$  corresponds to the (100) plane reflection [15]. As the level of graphitization directly impacts these properties. this characterization is valuable for applications where electrical conductivity and thermal stability is required. Spectroscopies such as FTIR and Raman Spectroscopy are used Complementing these techniques to analyze the functional groups present in the carbon aerogels materials, lead a deeper understanding of chemical composition. For instance, FTIR spectra of lignin aerogels and CAs were recorded from ( $600$  to  $4,000\text{ cm}^{-1}$ ) at a resolution of ( $4\text{ cm}^{-1}$ ) using a Bruker Invenio-spectrometer. FTIR spectra of lignin and aerogels with different lignin contents confirmed the structural changes of lignin after crosslinking reaction (Fig. 4b). The peaks characteristic to lignin's hydroxyl (O-H) stretching at ( $3,400\text{ cm}^{-1}$ ) and aromatic skeletal vibrations at ( $1,595\text{ cm}^{-1}$ ) and ( $1,510\text{ cm}^{-1}$ ) shifted in the spectra of all aerogels after the reaction. For the region corresponding to C-H stretching of methyl and methylene groups, the intensity of ( $2,935\text{ cm}^{-1}$ ) peak increased, and a new peak appeared at ( $2,877\text{ cm}^{-1}$ ) [14]. This information is crucial for tailoring the aerogels to exhibit specific surface chemistry conducive to enhanced catalytic activity or selective adsorption [9].

**Table 1.** Comparison of surface area and pore size of CAs based on their precursor materials

Type of BDCA	SSA ( $\text{m}^2\text{g}^{-1}$ )	Pore Size (nm)	Reference
Cellulose-based Cas	200 – 900	2-50	[10]
Lignin-based Cas	300 – 700	1-30	[6, 16]
Hemicellulose-based Cas	150 – 600	5-20	[13]
Chitosan-based Cas	200 – 800	2-40	[16]
Mixed Biomass (e.g., Cellulose-Lignin)	400 - 1,000	1-60	[2]
Activated Biomass Cas	1,000 - 2,500 (after activation)	0.5-10	[9, 11]
Alginate-based Cas	470	2-50	[7]

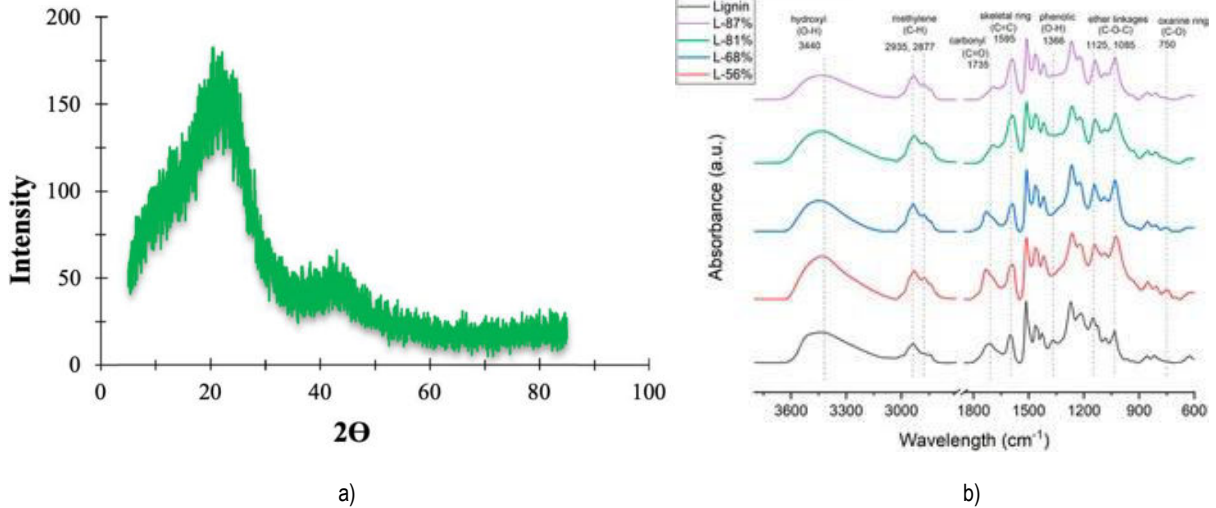


Fig. 4 - a. XRD pattern of the CAs before surface modification [7] and b. FTIR spectra of lignin aerogels with different crosslinker to lignin ratios corresponding to 44, 68, 81, and 87 wt % of lignin (all spectra normalized with skeletal vibration band of lignin at 1,510 cm<sup>-1</sup>) taken from [14].

### 1.3. Applications

As shown in (Fig. 5), their combination of unique properties and synthesis methods allows them to function effectively in a variety of applications. Their stability increases their attractiveness for use in energy storage [12, 14], catalysis [17, 18], thermal insulation [10], and environmental remediation [7, 17, 19], meeting both performance and environmental requirements (Table 2). CAs act as electrode materials which can rapidly store large amounts of charge in supercapacitors, enhancing efficiency in energy consumption [14]. Improvement in conductivity and large surface area can lead to increase energy storage capacity and cycling stability which is highly useful in supercapacitors and batteries. These materials provide stable and durable anodes or cathodes for batteries, increasing battery life and reliability [12].

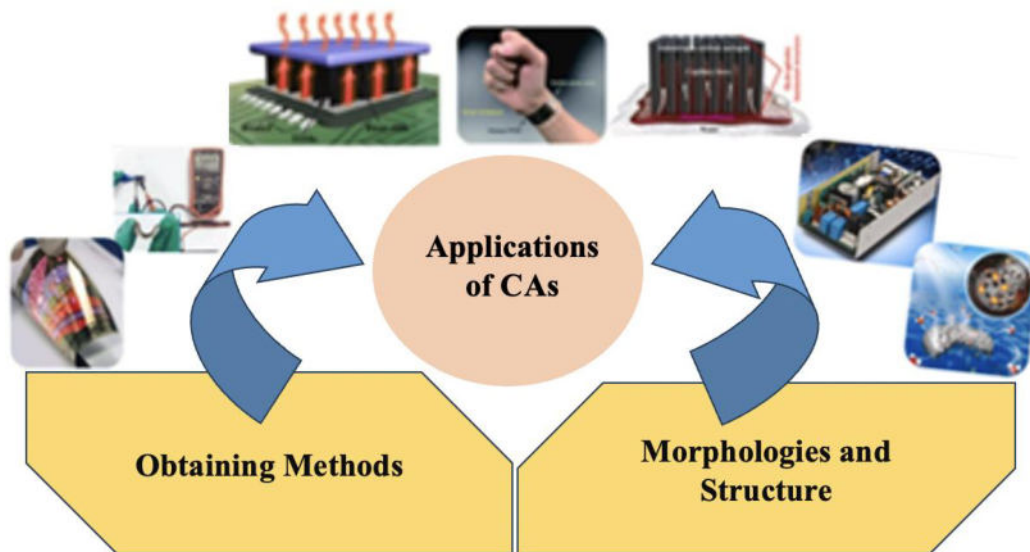


Fig. 5 - Versatile applications of CAs.

In electro-catalysis, BDCAs are highly valued for their performance in oxygen reduction reactions (ORR) and oxygen evolution reactions (OER), which are crucial in fuel cells and metal-air batteries. Due to the open structure and surface activity of CAs, energy transformations through the catalytic reactions can be carried out with high rates. This efficiency arises from their capacity to facilitate quick and frequent movement of large quantities of mass, together with a large number of active sites that enhance the performance of fuel cells and batteries [2]. Cellulose-derived CAs have low thermal conductivity and high thermal stability, making them suitable for use in energy-efficient construction materials. In addition, thermal insulation characteristics make these materials appropriate for applications in

temperature-sensitive electronic devices, assisting heat dissipation management. CAs has high insulating properties without adding significant weight, especially valuable in current construction where lightweight is considered as priority [10].

**Table 2.** BET analysis for BDCAs with comparison of synthesis methods and applications

№	Synthesis method	Type of aerogels	SSA (m <sup>2</sup> g <sup>-1</sup> )	Porosity	Application	Ref.
1	Hydrothermal carbonization and activation	BDCAs	700-1200	Hierarchical microporous	ORR/OER bifunctional oxygen electrodes	[2]
2	Freeze-drying and carbonization	Renewable biomass-based aerogels	300-800	Mesoporous to macroporous	Structural design and functional regulation	[6]
3	Sol-gel method with mannitol addition	Carbonaceous aerogel/mannitol composites	500-900	Stable, interconnected	High thermal-energy-release and shape stabilization	[9]
4	Template-assisted carbonization	Sustainable CAs	400-1000	Mesoporous/macroporous	Energy storage applications	[12]
5	Gelation and freeze-drying	Biomass-based aerogels for insulation	600-1100	Ultra-low density	Building insulation materials	[13]
6	Alkaline activation of softwood kraft lignin	Lignin-derived CAs	700-1200	Mesoporous	Supercapacitor electrodes	[14]
7	Pyrolysis of biomass precursors	CAs for gas adsorption	300-1200	Microporous to mesoporous	Gas adsorption and separation	[11]
8	Hydrogel synthesis and freeze-drying	Cellulose aerogels	400-800	Nanoporous structure	Thermal insulation	[10]
9	Hydrothermal treatment and modification	Alginate-derived CAs	500-1000	Modified mesoporosity	Nitrate removal in water	[7]
10	Pyrolysis and chemical activation	Activated cellulose aerogels	600-1000	Interconnected microporous	Dye treatment in wastewater	[17]
11	Carbonization and activation	Rice husk ash-derived aerogels	200-500	Microporous	Primary cells and energy storage	[20]
12	Thermochemical treatment of biomass	Softwood-derived CAs	800-1200	High porosity	Hydrophobic/oleophilic sorbents	[19]

BDCAs have been used as a removal for pollutants through their adsorption abilities, suitable for environmental remediation application. These materials may promptly engage with a pollutant and remove it due to their high porosity; therefore, may be used in water and air purification for instance as absorbents of oil/ water mixtures [19]. as they have been effective in the water purification by discharging oil, heavy metals, organic dyes and gaseous toxins from the water. Here, CAs play a positive role of protecting the environment the mitigation of pollution by enhancing fast adsorption of the pollutants, which makes them sustainable approach for pollution management [11, 19].

## Conclusion

BDCAs offer a novel category of materials that can be derived from renewable biomass raw materials and offer a sustainable replacement for carbon-based materials. The review emphasized synthesis methods and properties such as high specific surface area, low density and good electrical conductivity of BDCAs in relation to their use in energy storage, catalysis, and environmental remediation applications. Analytical techniques have been employed for understanding important features regarding the structural and chemical nature of BDCAs to ensure that they are nearly perfectly tailored for the required performance. Thus, increasing the role and relevance of BDCAs in the development of innovative technologies is the further development of research and the overall flexibility and eco-friendliness of BDCAs. Future studies should aim to improve their performance and explore new areas of application in order for BDCAs to contribute significantly to global challenges such as energy efficiency and environmental sustainability. After all, BDCAs hold major promise for advancing innovation in materials science and promoting a more sustainable future.

## References

- [1] Asim N., Badiei M., Alghoul M. A., Mohammad M., Fudholi A., Akhtaruzzaman M., Sopian K. (2019). Biomass and industrial wastes as resource materials for aerogel preparation: Opportunities, challenges, and research directions. *Ind. Eng. Chem. Res.* 58 (38): 17621–17645.

- [2] Jiao Y., Xu K., Xiao H., Mei C., Li J. (2023). Biomass-derived carbon aerogels for ORR/OER bifunctional oxygen electrodes. *Nanomaterials*, 13 (17): 2397.
- [3] Lesbayev B., Auyelkhanzy M, Ustayeva G., Yeleuov M., Rakhymzhan N., Maltay A., Maral Ye. (2023). Recent advances: Biomass-derived porous carbon materials. *South African Journal of Chemical Engineering*, 43(1): 327-336.
- [4] Lesbayev B.T., Rakhymzhan N., Ustayeva G., Maral Ye., Atamanov M.K., Auyelkhanzy M., Zhamash A. (2024). Preparation of nanoporous carbon from rice husk with Improved textural characteristics for hydrogen sorption. *J. Compos. Sci.*, 8(2): 74.
- [5] Lesbayev B., Auyelkhanzy M., Ustayeva G., Yeleuov M., Rakhymzhan N., Maral Y., Tolynbekov A. (2023). Modification of Biomass-Derived Nanoporous Carbon with Nickel Oxide Nanoparticles for Supercapacitor Application. *Journal of Composites Science*, 7:20.
- [6] Chen L., Yu X., Gao M., Xu C., Zhang J., Zhang X., Cheng Y. (2024). Renewable biomass-based aerogels: from structural design to functional regulation. *Chem. Soc. Rev.*, 53: 7489-7530.
- [7] Kheirabadi N. R., Tabrizi N. S., Sangpour P. (2019). Removal of nitrate from water by alginate-derived carbon aerogel modified by protonated cross-linked chitosan. *Journal of Polymers and the Environment*, 27: 1642-1652.
- [8] Lee J. H., Park S. J. (2020). Recent advances in preparations and applications of carbon aerogels: A review. *Carbon*, 163: 1-18.
- [9] Liu H., Qian Z., Wang Q., Wu D., Wang X. (2021). Development of renewable biomass-derived carbonaceous aerogel/mannitol phase-change composites for high thermal-energy-release efficiency and shape stabilization., *ACS Applied Energy Materials*, 4(2): 1714-1730.
- [10] Sen S., Singh A., Bera C., Roy S., Kailasam K. (2022). Recent developments in biomass derived cellulose aerogel materials for thermal insulation application: A review. *Cellulose*, 29(9): 4805-4833.
- [11] Zhang L., Lei Y., He P., Wu H., Guo L., Wei G. (2022). Carbon material-based aerogels for gas adsorption: fabrication, structure design, functional tailoring, and applications. *Nanomaterials*, 12(18): 3172.
- [12] Li M., Pang B., Dai S., Cui Y., Wu Y., Li H., Luo B. (2024). Sustainable biomass-derived carbon aerogels for energy storage applications. *Chemical Engineering Journal*, 156693.
- [13] Wang Y., Rasheed R., Jiang F., Rizwan A., Javed H., Su Y., Riffat S. (2021). Life cycle assessment of a novel biomass-based aerogel material for building insulation. *Journal of Building Engineering*, 44: 102988.
- [14] Karaaslan M. A., Lin L. T., Ko F., Rennecker S. (2022). Carbon aerogels from softwood kraft lignin for high performance supercapacitor electrodes. *Frontiers in Materials*, 9: 894061.
- [15] Liu Y., Nguyen L. D., Truong-Huu T., Liu Y., Romero T., Janowska I., Pham-Huu C. (2012). Macroscopic shaping of carbon nanotubes with high specific surface area and full accessibility. *Materials Letters*, 79: 128-131.
- [16] Wang R., Feng Y., Li D., Li K., Yan Y. (2024). Towards the sustainable production of biomass-derived materials with smart functionality: A tutorial review. *Green Chem.*, 26: 9075-9103.
- [17] Tran K.A., Nguyen L.L.T., Huy N.N., Do N.H.N., Le K.A., Le P.K. (2023). Synthesis of cellulose aerogel and its derived activated carbon as an effective adsorbent for dye treatment in water. *International Journal of Environmental Science and Technology*, 20(12): 13717-13728.
- [18] Li S., Hou D., Jia S., Lan G., Sun W., Li G., Feng W. (2024). Highly ordered carbon aerogels: Synthesis, structures, properties and applications. *Carbon*, 218: 118669.
- [19] Sankaranarayanan S., Lakshmi D. S., Vivekanandhan S., Ngamcharussrivichai C. (2021). Biocarbons as emerging and sustainable hydrophobic/oleophilic sorbent materials for oil/water separation. *Sustainable Materials and Technologies*, 28: e00268.
- [20] Hossain A., Maroof I., Mahmud M. F. (2021). Waste to Energy: Potential of using activated carbon and rice husk ash in primary cells (Doctoral dissertation, Department of Mechanical and Production Engineering (MPE), Islamic University of Technology (IUT), Board Bazar, Gazipur, Bangladesh).

### Information of the authors

**Muhammad Hashami**, master student, Faculty of Chemistry and Chemical Technology, Al-Farabi Kazakh National University,

**e-mail:** [mg.hashami2010@gmail.com](mailto:mg.hashami2010@gmail.com)

**Auyelkhanzy Moldir**, PhD, Acting Associate Professor of the Department of Chemical Physics and Materials Science, Faculty of Chemistry and Chemical Technology, Al-Farabi Kazakh National University  
[auyelkhanzy@gmail.com](mailto:auyelkhanzy@gmail.com), [auyelkhanzy.m@kaznu.kz](mailto:auyelkhanzy.m@kaznu.kz)

**Auyelkhanzy Madina**, Master of engineering sciences, Lecturer of the faculty of pre-university education, Al-Farabi Kazakh National University

**e-mail:** [m.auyelkhanzy@gmail.com](mailto:m.auyelkhanzy@gmail.com)